

Imperial College London

Department of Chemical Engineering and Chemical Technology

Forward Osmosis for Desalination
and
Water Recovery

By

Nur Muna Mazlan

Supervisor: Prof. Andrew G. Livingston

A thesis submitted for the degree of Doctor of Philosophy of Imperial
College London and the Diploma of Imperial College London

2016

I certify that the work in this thesis is my own and that the work of others
is appropriately acknowledged

“The copyright of this thesis rests with the author and is made available under a Creative Commons Attribution Non-Commercial No Derivatives licence. Researches are free to copy, distribute or transmit the thesis on the condition that they attribute it, that they do not use it for commercial purposes and that they do not alter, transform or build upon it. For any reuse or redistribution, researches must make clear to others the licence terms of this work”

Abstract

In recent years, there has been an increased interest in forward osmosis (FO) from academic research and industry with a rising number of FO academic publications in the last decade. The common perception of FO as a low energy process compared to reverse osmosis (RO) sparked interest in this area. Nevertheless, there are some major challenges that need to be addressed before FO can be successfully implemented as an effective technology. Some of these challenges are addressed in this dissertation, starting with the assessment of FO as a low energy process. A modelling approach was used to assess the energy consumption of various FO hybrid processes and provide a detailed comparison with RO for desalination, in an effort to answer the critical question: Is FO truly a low energy process compared to RO? Results showed that there was practically no difference in specific energy consumption (SEC) between standalone RO, and FO with nanofiltration (NF) draw solution (DS) recovery; this can be generalised for any pressure-driven membrane process used for the DS recovery stage in a hybrid FO process, such as UF or RO. It was also found that even if any or all of the membranes considered, FO, RO or NF, were perfect (i.e. had infinite permeance and 100% rejection), it would not improve the SEC significantly. Furthermore, in order to reduce the higher membrane footprint required by FO hybrid processes, internal concentration polarisation (ICP) within the support has to be greatly reduced or eliminated. Hence, any advantage possessed by the FO hybrid process derives from the lower fouling propensity of FO, lower pretreatment costs arising from reduced fouling, use of draw solutes which can be recovered with low cost thermal energy sources and specific applications where RO cannot compete. Inspired by this insight, subsequent work was performed to study the multifaceted interactions alongside membrane and process parameters involved in the fouling of FO membranes, specifically the HTI TFC and CTA membrane. The chapter on organic fouling behaviour of structurally and chemically different FO membranes revealed that fouling on the HTI TFC membrane was more significant compared to

HTI CTA in both membrane orientations, arising from a variety of factors associated with surface chemistry, membrane morphology and structural properties. Interestingly, it was observed that in FO mode, membrane surface properties dominated over fouling layer properties in determining fouling behaviour, with some surface properties (e.g. surface roughness) having a greater effect on fouling than others (e.g. surface hydrophilicity). In PRO mode, structural properties of the support played a more dominant role whereby fouling mechanism was specific to the foulant size and aggregation as well as the support pore size relative to the foulant. Whilst pore clogging was observed in the TFC membrane due to its highly asymmetric and porous support structure, fouling occurred as a surface phenomenon on the CTA membrane support layer, indicating that the latter's structure was more symmetric in relation to the foulant (alginate) studied. Besides pore clogging, the severe fouling observed on the TFC membrane in PRO mode was due to a high specific mass of foulant adsorbed in its porous support. A new method was successfully introduced to quantify the density of the fouling layer and correlate it with hydrodynamic conditions and fouling behaviour of the membranes studied. It was observed that a trade-off between enhanced membrane performance and fouling mitigation is apparent in these membranes, with both membranes providing improvement in one aspect at the expense of the other. Hence, significant development in their surface and structural properties are needed to achieve good anti-fouling properties without compromising flux performance. Measured fouling densities on the studied surfaces suggest that there is not a strong correlation between foulant-membrane interaction and fouling density. Cleaning results suggest that physical cleaning was more efficient on the CTA membrane compared to the TFC membrane. Further, they implied that despite different mechanisms of fouling and quantities of foulant adsorbed in FO membranes, FO is a resilient process with high cleaning efficiencies and fouling reversibility. Finally, to address the challenge of ICP, a novel method of fabricating FO membranes was developed by interfacially polymerising a free-standing, salt rejecting polyamide (PA) film using a floating technique and directly depositing this layer onto an open mesh fabric. By doing this,

the need for a phase inversion support was entirely eliminated. The fabrication method resulted in the successful formation of a defect-free, salt-rejecting FO membrane with significantly reduced or eliminated ICP, attributed to large open mesh sizes and straight channels in the fabric support. Interestingly, it was observed that even in the absence of ICP, flux was limited by the support layer at lower effective open areas of the mesh fabric. At higher mesh sizes and effective open areas, the effect of the fabric support became less significant and FO performance was likely governed by diffusion through the PA film, limited by its structure and transport properties. A trade-off between surface roughness and thickness of the PA film was observed, which is linked to the mechanism of film formation at the bulk interface. It was proposed that the design of FO membranes with ideal supports should also include tailoring the PA film properties in order to achieve superior FO performance. Additionally, the use of supports with higher percentage open areas or porosities should be considered.

Acknowledgments

I would like to thank everyone who have contributed to the process of developing and completing this thesis. I would like to thank my academic supervisor Professor Andrew G. Livingston for his guidance and support throughout the course of my PhD. It has been an enriching experience working and learning from you. I would like to acknowledge the financial support provided throughout my PhD by CIMB Foundation, as part of the CIMB Regional Scholarship award.

A special thanks to my colleagues and friends who have been tremendously supportive, in both professional and personal capacities. Thank you Dimitar, Zhiwei, Santanu, Keeran, Boram, Patrizia, María and other colleagues not mentioned here for always being there to offer guidance, advice and support. Thank you for all the collaborative work that developed during the PhD and for your friendship.

To my dear friends who have always been there through good and challenging times. Thank you - Débora, Marta, Evelina, Naoko, Ilyas, Syma, Çiğdem, Sharon and others unnamed here. To my friends back home, Aster, Feli, Rohene, Pei Ling, Jolene, Agki, Rupini, Raani and others, thank you for the amazing times in school and for your support and friendship over the years.

To my school teachers and university lecturers, thank you for inspiring.

To my dear family and family friends who have been supportive of my decisions and who have contributed much to this journey, A. Joy, U. John, Anushya, Anita, U. Patrick, A. Anne, and others not mentioned here, thank you. A special thanks to both my grandmothers who have had a great influence in my life.

Last but not least, a big thank you to my parents, who have always believed in me and allowed me to follow my heart. To my father, for an adventurous childhood and lessons on kindness, generosity and communal living. To my mother, for leading by example and nurturing

practical skills on problem-solving, independence, resilience and living with a social conscience; for always being supportive.

To home where I grew up and became, Malaysia. To my present home, where I morphed and matured, the UK, it's amazing how place moulds you. To writers, poets, philosophers who have inspired. To nature, the universe and beyond, for this wonderful existence and opportunity to understand some of the mysteries of this physical world.

“And I say that life is indeed darkness save when there is urge,
And all urge is blind save when there is knowledge,
And all knowledge is vain save when there is work,
And all work is empty save when there is love;
And when you work with love you bind yourself to yourself, and to one another, and
to God.”

Khalil Gibran.

Publications

Parts of this thesis have been published or submitted for publication:

Nur Muna Mazlan, D. Peshev, and A.G. Livingston, Energy Consumption for Desalination -A Comparison of Forward Osmosis with Reverse Osmosis, and the Potential for Perfect Membranes. *Desalination* (2015) - *in Press*.

Nur Muna Mazlan, Patrizia Marchetti, H A Maples, Boram Gu, Santanu Karan, A Bismarck and A.G. Livingston, Organic Fouling Behaviour of Structurally and Chemically Different Forward Osmosis Membranes- A study of Cellulose Triacetate and Thin Film Composite Membranes. *J. Membr. Sci.* (2016) - *under review*.

Table of Contents

1	Research motivation and thesis structure	1
2	Literature review	5
2.1	Introduction	5
2.2	Advantages and Challenges of Forward Osmosis	7
2.3	Energy Consumption in Forward Osmosis	9
2.3.1	Does FO Hybrid Processes Consume Less Energy than RO?	9
2.3.2	Leveraging low-cost Thermal Energy for FO Draw Solution Recovery	11
2.4	Membrane Development for Forward Osmosis	11
2.4.1	Tailor-made Membranes for Forward Osmosis.....	14
2.4.2	Structural Properties of the FO Membrane Support Layer	18
2.4.3	Selectivity of the FO Membrane Active Layer- Mitigating Reverse Solute Flux ..	21
2.5	Fouling in Forward Osmosis Membranes	23
2.5.1	Low Fouling Propensity of Forward Osmosis	23
2.5.2	Fouling Mitigation- Membrane Surface Properties.....	26
2.6	Draw Solution Development for Forward Osmosis	28
2.6.1	Classification of Draw Solutes and their Applications.	28
2.6.2	Selection Criteria for Optimal Draw Solutes.....	31
2.6.3	Does the Choice of Draw Solute Improve Energy Consumption?.....	35
2.7	Modeling Membrane Performance in Forward Osmosis	35
2.7.1	Solution-Diffusion Model Describing Transport across a Semi-Permeable Selective Layer in Forward Osmosis.....	36
2.7.2	Mathematical Description of Transport in Forward Osmosis- Mass Transfer Resistances.....	38
2.8	Applications where Forward Osmosis can potentially outperform Other Technologies .	44
3	Project objectives	48
3.1	Objective 1	49
3.2	Objective 2.....	50
3.3	Objective 3.....	51
4	Energy Consumption for Desalination - A Comparison of Forward Osmosis with Reverse Osmosis, and the Potential for Perfect Membranes.....	52
4.1	Introduction	52
4.2	Process Modelling and Simulation	55
4.2.1	Process Flow Diagrams and Unit Operations	55
4.2.2	Process Models.....	55
4.2.2.1	RO Desalination.....	55

4.2.2.1.1	Pretreatment Effects	58
4.2.2.1.2	Pressure Drop Effects	58
4.2.2.2	FO Desalination	62
4.2.3	Simulation Tools.....	64
4.3	Results and Discussion.....	65
4.3.1	Pretreatment Effects	65
4.3.2	Selection of Optimal Process Configuration for RO Desalination.....	66
4.3.3	Energy Consumption for SWRO.....	72
4.3.4	Energy Consumption for FO Desalination	80
4.3.5	Comparison of Energy Consumption between FO and RO Desalination	84
4.3.6	Model Sensitivity	90
4.4	Conclusions	92
5	Organic Fouling Behaviour of Structurally and Chemically Different Forward Osmosis Membranes- A study of Cellulose Triacetate and Thin Film Composite Membranes	94
5.1	Introduction	94
5.2	Materials and Methods.....	96
5.2.1	FO Membranes	96
5.2.2	Organic Foulant.....	96
5.2.3	Test Solutions	96
5.2.4	Membrane Pretreatment	97
5.2.5	Membrane Characterisation	98
5.2.5.1	Scanning Electron Microscopy (SEM)	98
5.2.5.2	X-ray Photoelectron Spectroscopy (XPS).....	99
5.2.5.3	Contact Angle	99
5.2.5.4	Atomic Force Microscopy	99
5.2.5.5	Zeta Potential.....	100
5.2.5.6	Intrinsic properties.....	100
5.2.6	Foulant Characterisation	101
5.2.6.1	Hydrodynamic Diameter and Surface Charge	101
5.2.6.2	Specific Mass of Foulant Adsorbed	101
5.2.6.3	Fouling Layer Density	102
5.2.7	FO Cross-flow Setup.....	103
5.2.8	Fouling and Cleaning Procedure	104
5.2.9	Data Analysis	105
5.2.9.1	Baseline Data.....	108
5.2.9.2	Fouling Data.....	108
5.3	Results and Discussion.....	110

5.3.1	Membrane Characterisation	110
5.3.1.1	Physical Structure	110
5.3.1.2	Chemical Composition	112
5.3.1.3	Intrinsic Properties	115
5.3.2	Baseline Data Analysis Results	119
5.3.3	Factors Affecting Fouling Behaviour	122
5.3.3.1	Membrane Type and Orientation	122
5.3.3.2	Fouling Layer Characteristics	129
5.3.3.2.1	Fouling Density	129
5.3.3.2.2	Specific Mass of Foulant Adsorbed	132
5.3.3.3	Membrane Surface Properties.....	132
5.3.3.3.1	Surface Roughness	132
5.3.3.3.2	Surface Hydrophilicity	137
5.3.3.3.3	Surface Charge.....	137
5.3.3.3.4	Surface Chemical Heterogeneity.....	140
5.3.4	Cleaning and Fouling Reversibility	141
5.3.5	Effect of TFC Membrane Support Structure	143
5.3.5.1	On Fouling and Cleaning Behaviour in PRO mode.....	143
5.3.5.2	On Critical Flux Behaviour in PRO mode.....	145
5.4	Conclusion	146
6	Towards Mitigating the Challenge of Internal Concentration Polarisation.....	150
6.1	Introduction	150
6.2	Materials and Methods	152
6.2.1	Chemicals and Materials	152
6.2.2	Membrane Preparation.....	152
6.2.3	Commercial FO membranes	154
6.2.4	FO Test Solutions	155
6.2.5	Intrinsic Membrane Properties.....	155
6.2.6	Membrane Characterisation	156
6.2.6.1	Scanning Electron Microscopy (SEM)	156
6.2.6.2	X-ray Photoelectron Spectroscopy (XPS).....	156
6.2.6.3	Atomic Force Microscopy	156
6.2.6.4	UV Spectrometry.....	157
6.2.7	FO Experimental Setup	157
6.2.8	FO Experimental Procedure	160
6.3	Results and Discussion	161
6.3.1	The Ideal Support Layer.....	161

6.3.2	Membrane Characterisation	163
6.3.2.1	Scanning Electron Microscopy (SEM)	163
6.3.2.2	X-ray Photoelectron Spectroscopy (XPS).....	166
6.3.2.3	Atomic Force Microscopy	166
6.3.3	FO Performance of In-House Membranes.....	167
6.3.3.1	Factors Contributing to Performance Results following ICP Mitigation	170
6.3.3.1.1	The Low Flux Phenomenon	170
6.3.3.1.2	Limiting Effect of the Polyamide Film	173
6.3.3.2	Rethinking the Structural Parameter – ICP Relationship	176
6.4	Conclusion	178
7	Overall conclusions.....	179
8	Future directions.....	183
9	Appendices.....	198

List of Figures

Figure 2.1: (a) Number of FO academic publications and (b) number of citations of FO publications between 1997 to April 2016. Figures adapted from the Web of Science database.	6
Figure 2.2: Schematic comparing (A) an RO process (RO_1) with a hybrid FO–RO process (FO– RO_2). [Reprinted from Shaffer et al. [1]]	10
Figure 2.3: SEM image of the HTI CTA membrane	16
Figure 2.4: SEM image of the HTI TFC membrane.....	18
Figure 2.5: Fouling and cleaning of a HTI CTA membrane with a model organic foulant (alginate). [Reprinted from Mi et al. [2]].	25
Figure 2.6: Figure showing a conceptual illustration of the effect of reverse draw solute diffusion on cake-enhanced osmotic pressure (CEOP) in FO mode for different draw solute sizes: (a) NaCl and (b) dextrose. [Adapted from Lee et al. [5]].	26
Figure 2.7: Schematic diagrams of antifouling mechanisms: (a) pure water layer; (b) electrostatic repulsion; (c) steric repulsion. [Reprinted from Kang et al. [110]].	28
Figure 2.8: Relationship between osmotic pressure and viscosity for different draw solutions. [Reprinted from Shaffer et al. [1]].	34
Figure 2.9: Illustration of the effect of external and internal concentration polarisation on the concentration profiles and effective driving force across an asymmetric FO membrane in (a) FO mode (AL-FS) and (b) PRO mode (AL-DS). [Adapted from McCutcheon et al. [92]].	44
Figure 4.1: Desalination process flowsheets considered in this work for comparison of SEC. (A): RO desalination process with UF membrane pretreatment. (B): FO desalination process with UF membrane pretreatment and various draw solution (DS) recovery methods.	57
Figure 4.2: Flat rectangular channel model of the SW module feed channel with feed spacer [Adapted from Geraldès et al. [148]].	60
Figure 4.3: Typical (A) single-stage RO configuration with 8 spiral wound modules per pressure vessel; (B) two-stage tapered RO configuration with 6 spiral wound modules per pressure vessel	

and an array ratio of 2:1; (C) two-stage tapered RO configuration with 6 spiral wound modules per pressure vessel and an array ratio of 3:2..... 68

Figure 4.4: SEC versus axial pressure drop for different SWRO configurations at 50% and 75% product recovery..... 70

Figure 4.5: ASPEN process flowsheet for (A) membrane pretreatment with UF; (B) single-stage RO with ERD; (C) two-stage RO with ERD and array ratio=3:2 71

Figure 4.6: (A) Effect of mass transfer coefficient on SEC and product recovery; (B) Change in SEC with increasing mass transfer coefficient in a single-stage RO at 50% recovery..... 74

Figure 4.7: Specific energy consumed versus product recovery for single-stage and two-stage RO with and without an ERD. Pretreatment energy and effects of pressure drop included. 78

Figure 4.8: Contribution of pretreated feed, axial and transmembrane pressure components on SEC in a single-stage RO..... 79

Figure 4.9: Change in SEC with increasing membrane permeance as the thermodynamic limit is approached in a single-stage RO at 50% recovery. ΔP was gradually decreased from 65 bar to 53 bar (i.e. near thermodynamic limit, whereby $\Delta P=53$ bar and $\Delta \Pi_{\text{retentate,exit}}=49$ bar). At $\Delta P=53$ bar and product recovery=50%, the specific membrane area required is plotted as a function of permeance. 79

Figure 4.10: Overall cost savings for a 2-stage RO relative to a single-stage RO, considering both energy and membrane costs. 80

Figure 4.11: ASPEN process flowsheet for FO desalination followed by NF for recovery of draw solution..... 82

Figure 4.12: (A) Process configuration for FO with single-stage NF recovery; (B) Process configuration for FO with two-stage NF recovery. 82

Figure 4.13: Effect of increasing membrane permeance and decreasing solute resistivity for diffusion within the FO membrane support layer, on specific membrane area and SEC in an FO with single-stage NF recovery process at 50% product recovery. 83

Figure 4.14: Comparison of SEC and specific membrane area between FO with NF recovery, FO with two-stage NF recovery, single-stage RO, two-stage RO, FO-UF, and FO-Distillation at 50% and 75% product recovery. Energy contributions from the pretreatment stage, LPP, HPP, ERD and distillation are shown in each process. 89

Figure 5.1: SEM micrographs of cross-section and aerial views of the TFC membrane top layer [(a), (c)] before and [(b), (d)] after soaking in DIW.	98
Figure 5.2: (a) Schematic of the lab scale forward osmosis experimental setup, and (b) schematic of the FO cross-flow cell with cell dimensions.	104
Figure 5.3: SEM image and schematic representation of (a,c) HTI CTA membrane and (b,d) HTI TFC membrane used in this study. Schematic not drawn to scale.	111
Figure 5.4: SEM images of pristine membranes after soaking in water: (a) TFC top surface, (b) CTA top surface, (c) TFC bottom surface and (d) CTA bottom surface.	112
Figure 5.5: Survey spectra and narrow scan results of X-ray photoelectron spectra measured from the top surface of CTA membrane. (A) Survey, (B) C 1s and (C) O 1s spectra.	113
Figure 5.6: Survey spectra and narrow scan results of X-ray photoelectron spectra measured from the top surface of polyamide TFC membrane. (A) Survey, (B) C 1s, (C) O 1s and (D) N 1s spectra.	114
Figure 5.7: (a) NaCl rejection and (b) pure water permeance of HTI CTA and TFC membranes under RO experimental conditions.	117
Figure 5.8: Figure showing the quality of fitting between calculated and experimental baseline fluxes for (a) HTI CTA and (b) HTI TFC membranes.	121
Figure 5.9: Schematic summarising the factors affecting fouling behaviour of the membranes investigated in this chapter.	122
Figure 5.10: Comparison of fouling behaviour on HTI TFC and CTA membranes in (a) FO mode and (b) PRO mode.	124
Figure 5.11: SEM micrographs of pristine, fouled and cleaned CTA membranes; (a-c) top surface, (d-f) bottom surface, and (g-h) cross-sectional micrographs.	126
Figure 5.12: SEM micrographs of pristine, fouled and cleaned TFC membranes; (a-c) top surface, (d-f) bottom surface, and (g-j) cross-sectional micrographs.	127
Figure 5.13: Schematic representation of foulant deposition on (a) CTA active surface, (b) CTA support surface, and (c) TFC active surface.	128

Figure 5.14: Profile view of (a) TFC active surface with a ridge-and-valley structure and (b) CTA support surface.....	128
Figure 5.15: Effect of membrane type and orientation on fouling density at different cross-flow velocities.	130
Figure 5.16: Computational Fluid Dynamics (CFD) results showing the velocity magnitude and velocity field in the FO cell at a height of 1 mm from the membrane surface.	131
Figure 5.17: Variation in cross-flow velocity with radial distance from centre of cell at a height of 1 mm from the membrane surface. The plot was developed from CFD data obtained from simulations run under specified conditions mimicking hydrodynamic conditions in the FO cell.	131
Figure 5.18: AFM images of the active and support layer surfaces of HTI TFC (a,b) and CTA (c,d) membranes.	135
Figure 5.19: Surface roughness dependence on length scale for the HTI CTA membrane. ...	136
Figure 5.20: Schematic representation of the estimated surface roughness measured by the AFM probe and the actual surface roughness of the polyamide surface. [Adapted from Karan et al. [194]].	136
Figure 5.21: Zeta potential on (a) CTA and TFC top surface; (b) CTA top and bottom surfaces, as a function of pH with solutions representing baseline conditions (0.5 mM NaCl), feed solution before (0.5 mM NaCl, 0.5 mM CaCl ₂) and after foulant addition (0.5 mM NaCl, 0.5 mM CaCl ₂ , 2.0 mM Alginate).	139
Figure 5.22: Structural formula of sodium alginate and calcium alginate, following the complexation of sodium alginate with Ca ²⁺ ions. [Adapted from Ichiura et al. [203]].	140
Figure 5.23: Flux recovery of fouled CTA and TFC membranes in FO and PRO mode, after cleaning with DIW at 60 L.h ⁻¹ for 15 minutes.....	142
Figure 5.24: (a-d) Fouling behaviour and flux recovery of the HTI TFC membrane in PRO mode under various cleaning conditions at 2 h, 5 h, 16 h and 27 h, and (e) Specific mass of alginate adsorbed within the porous support at 2 h, 5 h, 16 h and 27 h of fouling in PRO mode.	144
Figure 5.25: Flux behaviour of the TFC membrane in PRO mode with a 0.25 M-1.0 M NaCl DS and 50 mM NaCl FS. 200 mg.L ⁻¹ alginate and 0.5 mM CaCl ₂ were added to the fouling FS. A critical flux behaviour is observed between 0.25 M and 0.50 M DS.	146

- Figure 6.1: Schematic of the apparatus used for floating PA film formation and deposition onto a fabric support..... 154
- Figure 6.2: Schematic of (a) lab-scale U-tube FO experimental setup and (b) U-tube FO cell configuration..... 159
- Figure 6.3: Comparison of the HTI TFC membrane flux performance using the FO cross-flow setup in Chapter 5 and the new U-tube experimental setup in this chapter..... 160
- Figure 6.4: Schematic of an FO membrane with a dense active layer for rejection of foulants and salt ions, and an ideal support layer with low tortuosity, reduced thickness and high porosity to provide direct diffusion paths for water and salt transport. 162
- Figure 6.5: Cross-sectional SEM image showing the elimination of a phase inversion support in the (a) in-house fabricated FO membrane, compared to conventional phase-inversed membranes, such as the HTI (b) cellulose triacetate (CTA) and (c) thin film composite (TFC) FO membrane. The in-house fabricated membrane utilised an open mesh fabric to provide mechanical support, eliminating the need for a phase inversion support. 163
- Figure 6.6: SEM image of a Nylon 6,6 support (mesh size = 15 μm and effective open area for water transport = 10% of total fabric), (a)-(b) before and (c) after of PA film deposition. The SEM image shows (a)-(b) a precision engineered open support with large mesh size and low tortuosity, and (c) a continuous PA film formed by interfacial polymerisation, physically adhered on the support. (d) A close-up showing a continuous PA film formed between a Nylon 6,6 fabric fibre and the open mesh. (e) Typical ridge-and-valley morphology of the interfacially polymerised PA film on the Nylon 6,6 mesh support. (f) Cross-sectional SEM image of the in-house membrane. 165
- Figure 6.7: SEM image of the (a) smoother PA film formed with 3 wt% MPD and 0.15 wt% TMC, and (b) rougher PA film formed with 6 wt% MPD and 0.3 wt% TMC..... 165
- Figure 6.8: AFM images of the polyamide film with (a) 3 wt% MPD, 0.15 wt% TMC, (b) 6 wt% MPD, 0.3 wt% TMC and on (c) a commercial HTI TFC membrane..... 167
- Figure 6.9: Water flux and NaCl rejection of in-house membranes made on i) 10 μm mesh size, 2% open area, ii) 15 μm mesh size, 10% open area and iii) 20 μm mesh size, 14% open area N6,6 fabrics; with corresponding effective mesh open areas of 0.3 cm^2 , 1.3 cm^2 and 1.7 cm^2 , respectively. DIW and 1 M NaCl were used as the feed and draw solutions..... 168

Figure 6.10: Water flux and NaCl rejection of an in-house membrane (10 μm mesh size and 2% open area), before and after prewetting with methanol. DIW and 1 M NaCl were used as the feed and draw solutions, respectively. 171

Figure 6.11: Schematic showing two membranes with identical 'S' parameter, i.e. equivalent thickness δ , porosity ε and tortuosity $\tau = 1$, but varying pore size D_p . Figure (a) exhibits a larger pore size, allowing for higher solute diffusivities within the pore channel, whereas smaller pore sizes in (b) result in a lower solute diffusivity. 177

List of Tables

Table 2.1: Table showing recent FO membrane developments. [Adapted from Zhao et al. [25]].	13
Table 2.2: Standard operating conditions for testing flatsheet ODMP membranes in forward osmosis. [Adapted from Cath et al. [85]].	14
Table 4.1: Properties of 8-inch by 40-inch spiral wound module FilmTec SW30HR-380. [Adapted from Geraldtes et al. [148]].	61
Table 4.2: Energy consumption for UF membrane pre-treatment for desalination	66
Table 4.3: Process conditions used to simulate pressure drop and SEC at 50% and 75% product recoveries for the optimal configurations selected for comparison of SEC with FO.	70
Table 4.4: Summary of process calculations for SWRO at a water recovery of 50%, membrane rejection of 100%, $Q_F=12.85 \text{ m}^3 \text{ h}^{-1}$, $\Delta P=59.5 \text{ bar}$, $L_p = 3.5 \times 10^{-12} \text{ m}^3 \text{ m}^{-2} \text{ Pa}^{-1} \text{ s}^{-1}$.	73
Table 4.5: FO with $\text{CO}_2\text{-NH}_3$ DS recovery energy data for a single vacuum distillation column. [Adapted from McGinnis et al. [39]].	86
Table 4.6: Process conditions (applied pressure, feed and draw solution concentrations) used in the comparison of SEC for various RO and FO hybrid desalination processes.	90
Table 5.1: XPS results of the CTA and TFC active surfaces.	115
Table 5.2: Experimental conditions used in this study for RO, fouling and cleaning experiments.	118
Table 5.3: Analysis of variance (ANOVA) showing effects of membrane type and methanol pretreatment on membrane permeance and rejection	119
Table 5.4: Table summarising output parameters obtained from the regression model and the membrane permeance measured under RO conditions.	122
Table 5.5: Effect of membrane type and orientation on specific mass of alginate adsorbed during fouling.	132

Table 6.1: Properties of the N6,6 open mesh fabrics used as membrane supports in this study.	153
Table 6.2: XPS results of the polyamide floating film made from 3 wt% MPD and 0.15 wt% TMC. [Adapted from Karan et al. [194]].	166
Table 6.3: Membrane performance and structural parameters of the in-house membranes and other FO membranes available in literature and commercially	169

Symbols and Abbreviations

Abbreviations

AFM	Atomic force microscopy
CA	Cellulose Acetate
CAB	Cellulose acetate butyrate
CAP	Cellulose acetate propionate
CEOP	Cake enhanced concentration polarisation
CFD	Computational fluid dynamics
CP	Concentration polarisation
CTA	Cellulose triacetate
DIW	Dionized water
DS	Draw solution
ECP	External concentration polarisation
ERD	Energy recovery device
ESI	Electronic supplementary information
FO	Forward osmosis
FS	Feed solution
GO	Graphene oxide
HPP	High pressure pump
HTI	Hydration Technology Innovations
ICP	Internal concentration polarisation
IEP	Isoelectric point
IP	Interfacial polymerisation
IPA	Isopropyl alcohol
LPP	Low pressure pump
MBR	Membrane bioreactor
MD	Membrane distillation
MNP	Magnetic nanoparticles
MPD	M-phenylenediamine
MWCNT	Multiwalled carbon nanotube
N 6,6	Nylon 6,6
NC	Nanocomposite
NF	Nanofiltration
NP	Nanoparticles
ODMP	Osmotically driven membrane process
PA	Polyamide
PAA	Polyacrylic acid
PAA-NP	Polyacrylic acid-nanoparticles
PAH	Poly(allylamine hydrochloride)

PAI	Polyamide-imide
PAN	Polyacrylonitrile
PBI	Polybenzimidazole
PDA	Polydopamine
PEG	Polyethylene glycol
PEI	Polyethyleneimine
PES	Polyethersulfone
PET	Polyethylene terephthalate
PRO	Pressure retarded osmosis
PSf	Polysulfone
PSS	Poly(sodium 4-styrene-sulfonate)
PVP	Polyvinylpyrrolidone
RMS	Root mean square roughness
RO	Reverse osmosis
S	Structural Parameter
SEC	Specific energy consumption
SEM	Scanning electron microscope
sPPSU	Sulfonated polyphenylenesulfone
SW module	Spiral wound module
SWRO	Seawater reverse osmosis
TFC	Thin film composite
TMC	Trimesoyl chloride
UF	Ultrafiltration
UPP	Ultrafiltration permeate pump
WHO	World Health Organisation
XPS	X-ray photoelectron spectroscopy

Roman symbols

A_{cell}	Cross sectional area of the feed and draw solution channels, m^2
A_{m}	Membrane area, m^2
$A_{\text{m,s}}$	Specific membrane area, $[\text{m}^2(\text{m}^3 \cdot \text{h}^{-1})^{-1}]$
B	Salt permeability coefficient, $\text{L} \cdot \text{m}^{-2} \cdot \text{h}^{-1}$
c	Molar concentration, $\text{mol} \cdot \text{L}^{-1}$
C	Mass concentration, $\text{g} \cdot \text{L}^{-1}$
CO_2	Carbon dioxide
D	Solute diffusion coefficient, $\text{m}^2 \cdot \text{s}^{-1}$
d_{h}	Hydraulic diameter of the feed channel (m)
D_{h}	Hydraulic diameter, m
f_{ES}	Fractional energy savings
G_{SEC}	Gain in energy savings
h	Channel height, m

i	van't Hoff factor
J_P	Permeate flux, $L.m^{-2}.h^{-1}$
J_s	Solute flux, $g.m^{-2}.h^{-1}$
J_w	Water flux, $L.m^{-2}.h^{-1}$
k	External mass transfer coefficient, $m.s^{-1}$
K	Solute resistivity for diffusion within porous support layer, $s.m^{-1}$
L	Channel length, m
L_p	Membrane permeance, $m^3.m^{-2} Pa^{-1} s^{-1}$
m	Amortized membrane price per unit area, $Pa.m^3.m^{-2}.h^{-1}$
m_A	Amortized membrane unit cost, $£.m^{-2}.h^{-1}$
m_{norm}	Dimensionless membrane price
NH_3	Ammonia
P	Hydraulic pressure, Pa
P_f	Feed side pressure, Pa
P_{SMC}	Penalty due to the increase in membrane area
Q_D	Draw solution flowrate, mol (solvent+solute). s^{-1}
Q_F	Feed flowrate, mol (solvent+solute). s^{-1}
Q_P	Permeate flowrate, mol (solvent+solute). s^{-1}
Q_{PP}	Pure water permeate flowrate in FO, mol (solvent+solute). s^{-1}
Q_R	Retentate flowrate, mol (solvent+solute). s^{-1}
R	Membrane rejection, %
R_g	Universal gas constant= $8.314 J.K^{-1}.mol^{-1}$
S	Structural parameter, μm
T	Temperature, K
t	Thickness, m
W_{eq}	Equivalent work, $kWh.m^{-3}$
W_{pump}	Pump work, W
x	Position down the feed flow path
X_i	Molar fraction of the solute
Y	Product recovery
v_f	Fluid velocity, $m.s^{-1}$
$v_i(P, T, X_i)$	Molar volume of mixtures and solvent as a function of pressure, temperature and molar fractions of the solute, supplied by the thermophysical properties engine, $m^3.mol^{-1}$

Greek symbols

ϕ_{MgSO_4}	Corrected van't Hoff factor for MgSO_4 solution = 1.2
ϕ_{NaCl}	Corrected van't Hoff factor for NaCl solution = 1.64
K_λ	Factor to take into consideration pressure losses in the feed tubes and module fittings
β	Conversion factor, $\text{Pa}\cdot\text{m}^3\cdot\text{kWh}^{-1}$
ΔP	Transmembrane pressure difference, Pa
$\Delta \pi$	Osmotic pressure difference across the membrane, Pa
$\Delta \pi_1$	Osmotic pressure difference between the permeate and feed side of the FO stage, Pa
$\Delta \pi_2$	Osmotic pressure difference between the draw and retentate side of the FO stage, Pa
ε	Porosity
ε_P	Energy price, $\text{£}\cdot\text{kWh}^{-1}$
η	Solution kinematic viscosity, $\text{m}^2\cdot\text{s}^{-1}$
μ	Solution dynamic viscosity, $\text{Pa}\cdot\text{s}$
π	Osmotic pressure, Pa
ρ	Fluid density, $\text{kg}\cdot\text{m}^{-3}$
τ	Tortuosity

Dimensionless groups

N_R	Norm of residuals
Re	Reynolds Number
Sc	Schmidt
Sh	Sherwood number
λ	Friction factor

Chapter 1

1 Research motivation and thesis structure

Forward osmosis (FO), a relatively new technology compared to conventional membrane technologies such as reverse osmosis (RO) is being increasingly researched for potential applications in desalination and water treatment, amongst others. It utilises an osmotic pressure difference ($\Delta\pi$) between a less concentrated feed and a more concentrated draw solution to drive water across a selectively permeable membrane, whilst rejecting the transport of most solute molecules. Whereas, RO employs the application of a hydraulic pressure difference which exceeds the osmotic pressure difference across a semi-permeable membrane ($\Delta P > \Delta\pi$) to effect a separation. Following the extraction of water from the feed solution in FO, the product water is separated from the draw solution using different recovery methods. The draw is then recycled to facilitate a continuous FO operation.

The abundance of seawater makes it a good prospect for improving the world's water supply and has resulted in desalination gaining popularity as an attractive technology for the provision of clean water. Seawater reverse osmosis (SWRO) has been the leading desalination technology since the 1970's and involves the separation of pure water from seawater (typically 35 to 42 g.L⁻¹ of dissolved solutes). However, SWRO is an energy intensive process and despite major improvement in its energy consumption, there is still motivation for further reduction. This encouraged the investigation of FO as a potential low energy alternative for desalination. In the area of water treatment, FO is being investigated as a low fouling alternative to conventional membrane bioreactors and as a pretreatment step to improve the permeate quality produced by RO. The ability of FO to remove trace organic compounds, boron and dissolved organic material ensures the production of safe potable water.

FO requires strategic research to assess its viability for use on a commercial or industrial scale. Despite extensive study on the potential of FO as a low energy alternative to RO for major applications such as desalination and water treatment, there is a gap in the literature on a realistic assessment of the energy consumption of FO processes along with the draw solution (DS) recovery stage. Due to the osmotic driving force used to drive separation in the FO stage, there has been a notion that FO is a low-energy process, with an initial optimism that the correct selection of draw solutes will lead to greater energy savings compared to RO. In an attempt to provide greater clarity on the potential of FO, Chapter 4 of this thesis models and compares the practical energy consumption and membrane area requirements of FO hybrid processes with RO quantitatively, taking the process factors such as pressure drop, pre-treatment, specific module configuration and different draw solution recovery methods into account. Importantly, an attempt is made to answer the question, does FO offer advantages over RO for seawater desalination; and specifically, does it consume less energy per unit water produced? Further, it is a commonly held belief among researchers that it would be of great benefit if it were possible to develop the “perfect desalination membrane” i.e. one with infinite permeance and 100% salt rejection. Indeed, this has been the main focus of membrane research efforts in FO which are principally directed towards developing new FO membranes; and there is also substantial effort in new RO membranes, driven by the promise of graphene and other 2D materials. This raises a further important question- if it were possible to make both FO and RO membranes “perfect”, would this impact on the specific energy consumption (SEC) and on the relative advantages of FO vs. RO? Chapter 4 presents and discusses the answers to these questions. To the author’s best knowledge, there hasn’t been any study in literature specifically analysing the energy consumption of these processes taking various process conditions and process flow schemes into account. Moreover, the modelling approach in Chapter 4 enables the integration of custom models and unit operations in process simulation software namely, Aspen Plus. It is hoped that

the results from this chapter will help realign the direction of FO membrane research and applications more strategically.

Inspired by the results in Chapter 4 and other publications in literature demonstrating the advantages and potential of FO to mitigate fouling over pressure-driven membrane processes [1-9], it was decided that a fouling study would be conducted to analyse the multifaceted interactions involved in the fouling and cleaning of FO membranes of varying chemical and structural properties. Although current literature collectively concludes that FO has a higher fouling reversibility compared to pressure-driven membrane processes resulting from the absence of hydraulic pressure, there is a lack of quantitative evidence linking the properties of the fouling layer formed under FO conditions with fouling behaviour and hydrodynamic conditions of the process. Moreover, membranes utilised in most FO fouling studies are predominantly commercially available asymmetric cellulose triacetate (CTA) membranes from Hydration Technology Innovations (HTI, Albany, OR) [2-5, 7, 10-21], as no TFC-FO membranes were commercially available until recently. HTI has in recent years, commenced commercial production of a TFC membrane with a tailor-made support structure to suit FO applications, which is claimed to have superior fluxes and anti-fouling properties compared to the CTA membrane. Since TFC membranes are the current state-of-the-art for FO due to their higher water permeability and salt rejection compared to CTA [22], it is of interest to conduct systematic research on the performance and fouling behaviour of the HTI TFC membrane, which has not yet been widely studied. TFCs are prone to fouling due to their high surface roughness, available carboxyl groups on the membrane surface [23] and porous structure of the support layer. In Chapter 5, the gaps mentioned above are addressed by conducting a systematic study on the organic fouling and cleaning behaviour of the novel HTI TFC and CTA membranes, using calcium alginate as a model foulant.

Besides addressing concerns regarding the energy consumption and fouling propensity of FO, a major challenge in the development of successful FO membranes is the elimination of the severely flux-limiting internal concentration polarisation (ICP) bottleneck. ICP is known to be exponentially dependent on flux and as a result, fluxes in FO exhibit a self-limiting behaviour. The presence of severe ICP in conventional phase inversion FO membranes results in a significant reduction in the effective osmotic driving force across these membranes, leading to higher membrane areas required to achieve a specific product recovery. Moreover, FO hybrid processes require significant membrane areas due to the number of unit operations and stages required in both the FO and DS recovery stages. This would increase the capital costs for FO hybrid systems, making them less competitive with commercially available technologies. One solution to reducing the FO footprint is to improve the productivity per m^2 of membrane, which can be achieved by mitigating ICP. Chapter 6 investigates a novel method of fabricating FO membranes, which eliminates the need for a conventional phase inversion support. Instead, an open mesh fabric with large open mesh sizes and straight transport channels (i.e. $\tau \approx 1$) was used to provide mechanical support for the polyamide (PA) selective layer, which was formed independently. The work performed in Chapter 6 was intended to provide a simple yet effective method for the fabrication of FO membranes with significantly reduced or eliminated ICP.

Chapter 2

2 Literature review

2.1 Introduction

Forward osmosis (FO), more conventionally known as osmosis, is a physical phenomenon that has been exploited since the beginning of mankind for its functional use in food preservation and other applications [24]. Today, the applications of FO have diversified and become more prominent as a means to resolve pressing environmental, social and economic issues due to a rising population and depleting resources especially at the water-energy nexus. An increased interest from academic research and industry has been shown [24, 25]. There has been a rising number of FO academic publications and citations from the early 2000's up to April 2016 (Figure 2.1). Earlier studies focused on the potential application of FO in the food, water and energy sectors [24]. Besides extensive research on the potential of FO in desalination and water treatment applications, latest studies have focused on specific applications of FO in areas where RO cannot compete [1]. These include hybrid FO systems for desalination of high-salinity feed waters with thermolytic draw solute recovery and high trace organic compound content wastewaters [26-28], FO as a pretreatment process to conventional desalination processes [29-33] and FO as a pretreatment process for improving permeate quality produced by reverse osmosis [34-37]. When developing FO technologies and applications, an important consideration is the sustainable development and deployment of long-term solutions for water and energy shortages, due to the limited availability of these resources [38].

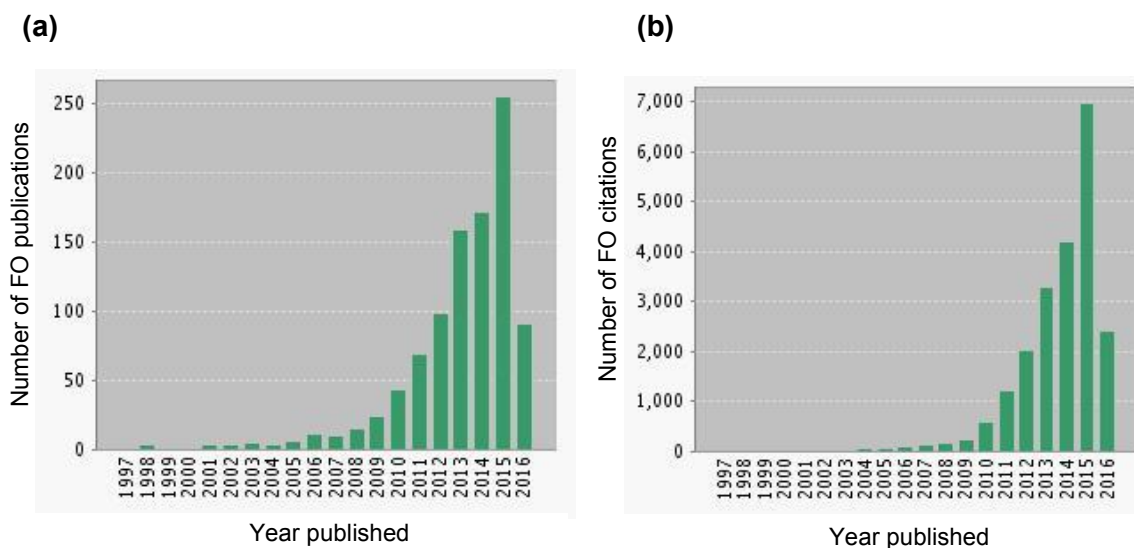


Figure 2.1: (a) Number of FO academic publications and (b) number of citations of FO publications between 1997 to April 2016. Figures adapted from the Web of Science database.

This review aims to address the key challenges of FO at present including energy efficiency, membrane development, characterisation and performance, fouling phenomena, the use of optimal draw solutes and suitable applications for FO. It also attempts to clarify the position of FO as a low energy and cost efficient alternative to reverse osmosis (RO), laying out its limitations and specifying cases where FO can potentially outperform other technologies.

FO can be defined as the transport of water across a selectively permeable membrane from a region of higher water potential to a region of lower water potential due to a difference in osmotic pressure. The more concentrated draw solution is circulated on the permeate side of the membrane and draws the water molecules from the less concentrated feed solution. The membrane allows for the water molecules to pass through but rejects the transport of most solute molecules. FO uses an osmotic pressure difference ($\Delta\pi$) rather than a hydraulic pressure difference (ΔP) as the driving force for the transport of water through the membranes which

results in the concentration of the feed stream and dilution of the concentrated draw solution [24].

A combination of operating principles used in FO and RO result in a process used mainly for power generation, known as pressure retarded osmosis (PRO) [25]. In PRO, a hydraulic pressure is applied on the draw solution side in the opposite direction of the osmotic pressure gradient. However this pressure difference is still lower than the osmotic pressure difference, ($\Delta\pi > \Delta P$) thus maintaining a net water flux in the direction of the concentrated draw solution. Similarly, RO employs the concept of applying a hydraulic pressure difference, but the applied pressure exceeds the osmotic pressure difference, ($\Delta P > \Delta\pi$). The general equation used for water transport in FO, PRO and RO is

$$J_P = L_p(\Delta\pi - \Delta P)$$

Equation 2.1

Whereby J_P is the permeate flux ($L \cdot m^{-2} \cdot h^{-1}$), L_p the water permeability constant ($L \cdot m^{-2} \cdot h^{-1} \cdot bar^{-1}$), $\Delta\pi$ the osmotic pressure difference (bar) and ΔP the hydraulic pressure difference (bar).

Following the extraction of water from the feed stream in FO, the product water is separated using various means from the draw solution which is recycled to facilitate a continuous FO operation [38].

2.2 Advantages and Challenges of Forward Osmosis

FO offers many potential benefits in applications where RO cannot compete. For example, depending on the form of energy used for draw solution (DS) recovery, FO hybrid processes may offer lower consumption of electrical energy compared to pressure driven membrane

processes, from operating the DS recovery stage at low pressures and low temperatures [26-28]. This is highly dependent on the development of suitable draw solutes and their regeneration methods [23-25, 39]. Draw solute recovery should operate with low-cost energy, for example, using low grade heat from thermal power plants. Regeneration is not always necessary and if a draw solute that adds value to the extracted water is used, the dilute draw solution can be readily used, with new draw solutes introduced to the system to create an additional product, such as personal hydration packs developed by HTI. If the objective is to concentrate the feed stream, then a low value and abundant draw solution such as seawater can be used. This has been demonstrated in the case of osmotic dilution of seawater feed to RO whilst reducing the volume of impaired water [38, 40].

Due to the low fouling propensities and high fouling reversibility of FO membranes, alongside high rejection of solutes and a wide range of contaminants, FO can provide an effective pretreatment to improve the permeate quality of RO [34-37]. Additionally, FO has the ability to pretreat feed waters for desalination, by removing both dissolved organic material and dissolved inorganic scalants from the feed water, in addition to suspended contaminants [29-33].

Other potential benefits of FO include its application in the liquid food and pharmaceutical processing industries where the physical properties (e.g. colour, odour, taste and nutrition) of the feed can be maintained without affecting its quality as it does not require high temperatures or pressures [24]. FO can also be potentially used in medical applications where it can assist in the release of drugs with low oral bioavailability (i.e. poor solubility or permeability) using osmotic pumps [24, 41, 42].

However, there remain several critical challenges with FO that need to be addressed before it can be successfully implemented as commercially viable and practical technology.

These challenges include i) development of highly permeable and selective FO membranes with ideal support structures to eliminate internal concentration polarisation (ICP), ii) development of ideal draw solutes capable of generating high osmotic pressures at low viscosities, iii) development of low energy draw solution recovery methods, iv) design and operation of FO modules with effective mass transfer to reduce external concentration polarisation (ECP), v) development of FO fouling mechanisms, models and mitigation methods, vi) further development of FO hybrid processes to enhance energy savings, process efficiencies, promote diversification of sources, and reduce environmental impact.

2.3 Energy Consumption in Forward Osmosis

2.3.1 Does FO Hybrid Processes Consume Less Energy than RO?

Forward osmosis (FO) has been investigated as a potentially lower energy alternative to pressure-driven membrane processes, due to the elimination of hydraulic pressure as the driving force, reduced fouling propensity and high fouling flux recovery. However, recent studies [1, 43] have shown by closer analysis that the hybrid FO-RO process cannot outperform the standalone RO process in terms of energy consumption. Shaffer et al. [1] demonstrated this by using simple thermodynamic calculations based on the theoretical minimum energy of separation, to compare a standalone RO process with an FO-RO process. Similarly, Mc Govern et al. [43] provided a thermodynamic comparison of the theoretical and actual energy requirements for FO-RO and standalone RO. Both studies concluded that the FO-RO process cannot outperform RO as the efficiency of an optimal draw regeneration process in FO and that of a standalone RO process are unlikely to differ significantly. Moreover, the osmotic pressure of the brine solution in the FO recovery stage has to be slightly higher than a standalone RO process for the same percentage recovery, in order to overcome the brine osmotic pressure in the FO stage and enable effective separation across the FO unit (Figure 2.2).

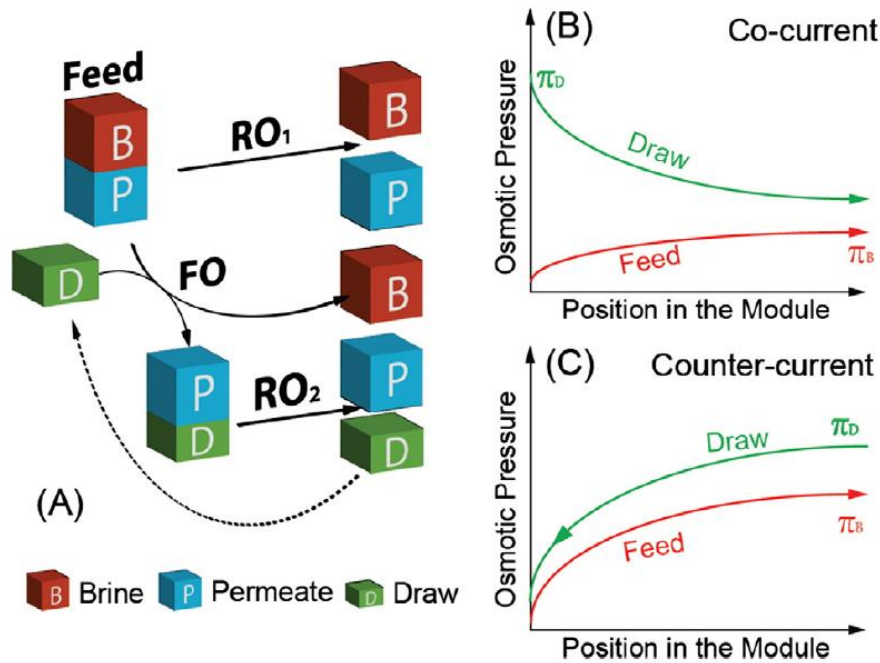


Figure 2.2: Schematic comparing (A) an RO process (RO_1) with a hybrid FO–RO process (FO– RO_2). The blocks with letters B, P, and D represent the brine, permeate, and draw solutions, respectively. The composite block with letters B and P represents the feed solution for both systems, while the block with letters P and D indicates the diluted draw solution that needs further separation by RO_2 . The size of the blocks is proportional to the solution volume. Both RO_1 and FO– RO_2 have the same product recovery. Figures (B) and (C) illustrate the osmotic pressures of the feed and draw solutions in FO in a co-current (B) and counter-current flow module (C). [Reprinted from Shaffer et al. [1]]

Despite the limitations in energy savings for FO hybrid processes, there still exists an opportunity to provide energy cost savings for these processes, by leveraging low-cost thermal energy draw solution (DS) recovery methods.

2.3.2 Leveraging low-cost Thermal Energy for FO Draw Solution Recovery

Although the draw solution (DS) dilution step in forward osmosis hybrid processes places the draw recovery stage at an energetic disadvantage, innovative DS recovery methods can be utilised to save energy costs. One such method is using alternative low-cost thermal energy, for example, low-grade heat to regenerate a draw solution of thermolytic salts by separating the more volatile components from the product water [26, 44]. Additionally, FO can be combined with membrane distillation (MD) as a pretreatment step for sewer mining to reduce fouling by organic and particulate matter which is otherwise more severe in a standalone MD process. Besides achieving a TOC removal up to 98% and water recovery up to 80%, the energy consumption of this hybrid process could be further compensated by utilising industrial waste heat, solar or geothermal energies. This makes the process attractive in arid areas where solar energy and other forms of low-grade heat are abundant and readily available [28].

2.4 Membrane Development for Forward Osmosis

Earliest studies on FO were performed using thin film composite (TFC) RO membranes [24] as there were no tailor-made FO membranes available. Upon realising the limitations of the TFC RO membrane for FO applications, more studies were conducted on developing membranes specifically for FO use (Table 2.1). The most extensively researched and used amongst these membranes are i) cellulosic membranes and i) thin film composite (TFC) membranes.

The main challenge for developing an ideal FO membrane involves improving the permeance of these membranes whilst maintaining high rejections of feed and draw solutes, mitigating mass transfer limitations within the support and remaining mechanically robust. Achieving these goals

involves tailoring the support and active layers of the membrane to promote ideal mass transfer conditions and mitigate solute transport across the selective layer.

Year	Membranes	Materials	Preparation methods	Reference
2005	Capsule wall membrane	Cellulose acetate or ethyl cellulose	Dip-coating, phase inversion	[42]
2007	Hollow fiber NF	Polybenzimidazole (PBI)	Dry-jet wet phase inversion	[45, 46]
2008	Flat sheet cellulose acetate membrane	Cellulose acetate	Phase inversion and then annealing at 80–95 °C	[47]
2009	Dual-layer hollow fiber NF	PBI–PES/PVP	Dry-jet wet phase inversion (i.e. coextrusion technology)	[48, 49]
2010	Hollow fiber	PES substrates, polyamide active layer	Dry-jet wet spinning and interfacial polymerization (IP)	[50, 51]
2010	Hollow fiber NF	Cellulose acetate	Dry-jet wet spinning	[52]
2010	Flat sheet double-skinned	Cellulose acetate	Phase inversion, and then annealing at 85 °C	[53]
2010	Flat sheet TFC polyamide	Polysulfone (PSf) support, Polyamide active layer	Phase inversion and IP	[22, 54]
2010	Double dense-layer membrane	Cellulose acetate	Phase inversion	[55]
2011	Modified RO	PSf support modified by polydopamine	Chemical coating	[56]
2011	Flat sheet composite	Cellulose acetate cast on nylon fabric	Phase inversion	[57]
2011	Flat sheet composite	PAN substrate, multiple PAH/PSS polyelectrolyte layers	Layer-by-layer assembly	[58]
2011	Positively charged hollow fiber	PAI substrate treated by PEI	Chemical modification	[59]
2011	Nanoporous PES	PES cast on PET fabric	Phase inversion	[60]
2011	Cellulose ester membrane	Cellulose ester	Phase inversion	[61]
2011	Flat sheet nanofiber TFC	PES nanofiber support, polyamide active layer	Electrospinning and IP	[62]
2012	Positively charged flat sheet	PAI substrate treated by PEI	Chemical modification	[63]
2012	Flat sheet TFC polyamide	PES/SPSf substrate, polyamide active layer	Phase inversion and IP	[64]
2012	Hollow fiber TFC	PES substrate, polyamide active layer	Phase inversion and IP	[65]
2013	Flat sheet TFC polyamide	PAN/CA nanofiber support, polyamide active layer	Electrospinning and IP	[66]
2013	Flat sheet TFC polyamide	PSf substrate, Jeffamine modified polyamide active layer	Surface chemical modification	[67]
2013	Mixed matrix flat sheet	PES/ multiwalled carbon nanotube (MWCNT) substrate, polyamide active layer	Phase inversion and IP	[68]
2013	Thin film nanocomposite	PSf–TiO ₂ nanocomposite substrate, polyamide active layer	Phase inversion and IP	[69]
2013	Carbon nanotube immobilised hollow fiber	PAI substrate with MWCNT immobilized PEI fibres	Dry-jet wet spinning, vacuum filtration and chemical post-treatment	[70]
2014	Flat sheet TFC polyamide	PSf substrate on PE mesh, polyamide active layer	Phase inversion and IP	[71]
2014	Flat sheet TFC polyamide	PSf substrate, PEG functionalised polyamide active layer	Surface modification	[72]
2014	Layer-by-layer GO flat sheet	Hydrolysed PAN substrate, GO poly(allylamine hydrochloride)	Phase inversion and layer-by-layer assembly	[73]

		(PAH) bilayers on both sides of hPAN		
2014	Flat sheet TFC polyamide	Cellulose acetate propionate (CAP)/ cellulose acetate butyrate (CAB) substrate, polyamide active layer	Phase inversion, IP and post-treatment	[74]
2014	Flat sheet nanofiber TFC	PET/PVA nanofiber support, polyamide active layer	Electrospinning and IP	[75]
2015	Flat sheet double-skinned	Cellulose acetate propionate (CAP), polyamide active layer	Phase inversion and IP	[76]
2015	Flat sheet TFC polyamide	PDA coated PSf substrate, polyamide active layer	Chemical coating	[77]
2015	Thin film nanocomposite	PSf substrate, polyamide active layer with amine-functionalised titanate nanotubes (NH ₂ -TNT)	Phase inversion, IP and chemical modification	[78]
2015	Hollow fiber composite biomimetic membrane	PES substrate, polyamide active layer embedded with aquaporin-incorporated proteoliposomes	Surface modification	[79]
2015	Flat sheet TFC polyamide	PSf/GO substrate, polyamide active layer	Phase inversion and IP	[80]
2016	Thin film nanocomposite	PSf with layered double hydroxide nanoparticles (LDH-NPs) blended substrate, polyamide active layer	Phase inversion and IP	[81]
2016	Flat sheet TFC polyamide	Hydrolysed PAN substrate, GO incorporated polyamide active layer	Surface modification	[82]
2016	Mesh reinforced flat sheet TFC polyamide	Sulfonated polyphenylenesulfone (sPPSU) substrate on PET mesh, polyamide active layer	Phase inversion and IP	[83]
2016	Mixed matrix flat sheet membrane	CA-functionalised porous carbon nanofiber (CNF) substrate	Phase inversion	[84]

Table 2.1: Table showing recent FO membrane developments. [Adapted from Zhao et al. [25]].

Increased research interest in the development of FO membranes resulted in more membranes being fabricated and tested under different experimental conditions i.e. different feed and draw solution compositions and concentrations, temperatures, cross-flow rates and operating pressures. However, in osmotically driven membrane processes (ODMP), the operating conditions and membrane properties play important roles in mass transport and process performance. This brings about the need for testing membranes using a standard protocol to ensure the different membranes available in literature can be compared on the same basis. Cath et al. developed a standard methodology for testing ODMP membranes [85]. After performing tests on two commercial flat sheet membranes in seven independent laboratories, the study revealed that membranes tested under the same protocol yielded similar performance results. The standard operating conditions used to test the flat sheet ODMP membranes in FO are

presented in Table 2.2. Following the development of the standard methodology, more studies have adopted this approach to align their results with others in literature [71, 86]. For the purpose of reviewing the wide scope of available literature on membrane development in FO, the following subsections will discuss results of studies performed both, with and without the standard protocol.

Experimental conditions	Value	Units	Notes
Testing modes: FO (active layer facing feed solution) and PRO (active layer facing DS solution)			
Feed and DS temperatures	20	°C	
Draw solution concentration	1	M NaCl	58.44 g.L ⁻¹
NaCl Feed concentration	0	M NaCl	Deionized water
Feed and DS pH	Unadjusted		As close to neutral and within the appropriate range for the polymer tested
Feed and DS cross-flow velocity	0.25	m.s ⁻¹	<ul style="list-style-type: none"> • Feed and DS flow rates defined by multiplying cross-flow velocity by cross section area of the flow channel perpendicular to flow direction • No spacers in the feed or DS flow channel • Co-current flow
Feed and DS pressures	< 0.2 (3)	bar (psi)	Keep as low as possible and similar on both sides of the membrane
Membrane orientation			Tests should be conducted in FO and PRO modes

Table 2.2: Standard operating conditions for testing flatsheet ODMP membranes in forward osmosis. [Adapted from Cath et al. [85]].

2.4.1 Tailor-made Membranes for Forward Osmosis

Cellulosic Membranes

Following the breakthrough by Loeb et al. in developing cellulose acetate (CA) RO membranes via phase inversion [87], various advances have been made for the use of CA in developing FO

membranes. Chung's membrane research group developed several hollow fiber and flat sheet cellulose-based membranes for FO applications [52, 53, 55, 61]. The use of CA is attributed to its relatively good hydrophilicity which favours high water flux and reduces fouling propensity, good mechanical strength and good resistance to degradation by chlorine and other oxidants [25]. The CA membranes developed by Chung's research group had a double-skin or selective layers formed on the top and bottom of a middle porous support layer which is claimed to reduce ICP and salt leakage due to the improved salt rejection properties of the double-skin [53, 55]. It was also observed that the interaction between the polymer and casting substrate for substrates with different hydrophilicities had an effect on the morphology of the membrane formed during phase inversion [55]. A study by Sairam et al. used the same phase inversion method for the preparation of a CA flat sheet composite FO membrane on nylon woven fabric using different pore-forming agents at different annealing temperatures [57]. This study found that the presence of the pore forming agent, $ZnCl_2$ resulted in improved fluxes and an NaCl rejection of 95% compared to lactic acid and maleic acid [57]. Cellulosic membranes have also been used in PRO applications for power generation [88, 89].

The commercially available Hydration Technology Innovations (HTI) cellulose triacetate (CTA) membrane has been widely used in literature for a variety of FO studies until recently. Lately, new TFC FO membranes are beginning to take centre stage with overall improved membrane performance. The HTI CTA membrane has a top rejecting layer followed by a relatively thin and less dense support layer made of cellulose triacetate embedded with a polyester mesh for added mechanical strength. CTA is prevalent throughout the membrane as a denser layer on the rejecting side and a looser layer on the support side. The total thickness of the membrane is approximately 50 μm (Figure 2.3).

The drawback of the CA membrane is its poor resistance to hydrolysis [90, 91] which can be minimized by adjusting the pH of the feed and draw solutions in the range of 4-6, and maintaining a working temperature of 35°C or less [91]. The CA membrane also exhibits lower permeance and rejection compared to TFC membranes [71, 92, 93].

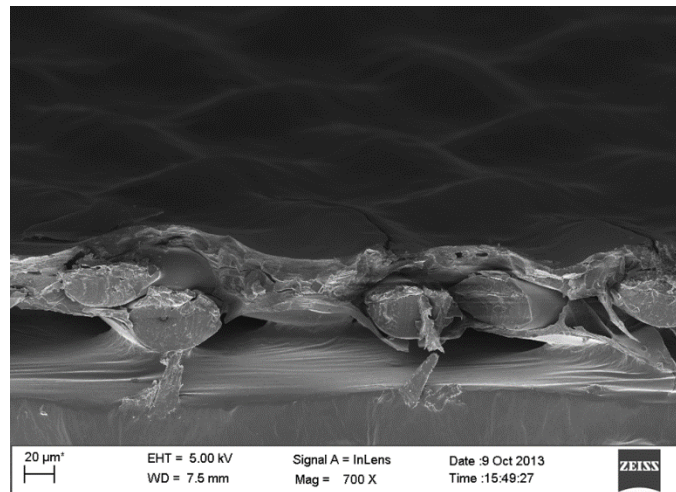


Figure 2.3: SEM image of the HTI CTA membrane

Thin Film Composite (TFC) Membranes

TFC membranes are the current state-of-the-art for FO because they have a higher water permeance and salt rejection compared to CTA membranes. This has been shown in previous studies whereby fabricated TFC FO membranes demonstrated three to four times higher permeance and improved salt rejection compared to the HTI CTA membrane [22, 94]. Wei et al. reported a pure water permeance of $1.78 \text{ L}\cdot\text{m}^{-2}\cdot\text{h}^{-1}\cdot\text{bar}^{-1}$ and NaCl rejection of 93.4% for a TFC membrane, compared to $0.46 \text{ L}\cdot\text{m}^{-2}\cdot\text{h}^{-1}\cdot\text{bar}^{-1}$ permeance and 92.4% rejection for the HTI CTA membrane [94]. Since the start of TFC FO membrane development, research has been focused on optimizing the support structure of the TFC membrane to mitigate internal concentration polarisation. Yip et al. developed a high-performance thin-film composite membrane which consists of a selective polyamide rejection layer formed by interfacial polymerization on top of a

polysulfone (PSf) support formed on a 40 μm polyester nonwoven fabric by phase inversion [22]. It was found that optimisation of the membrane performance was largely dependent on the formation of the substrate layer, whereby a support layer with a mixture of finger-like and sponge-like morphologies gave an enhanced membrane performance. High water fluxes (18 $\text{L}\cdot\text{m}^{-2}\cdot\text{h}^{-1}$ in FO mode with DIW feed solution and 1.5 M NaCl draw solution) were reported with a salt rejection $> 97\%$. The membrane exhibited a pure water permeance of $1.58 \text{ L}\cdot\text{m}^{-2}\cdot\text{h}^{-1}\cdot\text{bar}^{-1}$ compared to $0.36 \text{ L}\cdot\text{m}^{-2}\cdot\text{h}^{-1}\cdot\text{bar}^{-1}$ for the HTI CTA membrane. The high water flux was directly linked to the thickness, porosity, tortuosity and porous structure of the polysulfone support layer [22]. A further study was conducted by Tiraferri et al. which confirms the initial hypothesis that optimal forward osmosis membranes consist of a mixed-structure support layer with a thin sponge-like layer sitting on top of highly porous macrovoids [54].

In recent years, HTI has commenced commercial production of a TFC membrane with a tailor-made support structure to suit FO applications. The HTI TFC membrane (Figure 2.4) is an asymmetric membrane with finger-like morphology, reinforced with a polyester mesh similar to the mesh-embedded CTA membrane. However, the polyester mesh is oriented towards the bottom of the support layer, creating additional macroscopic pores around the mesh lines on the bottom surface [71]. The total thickness of the membrane is $\sim 100 \mu\text{m}$. The HTI TFC membrane demonstrated fluxes superior to the HTI CTA membrane [86] and other FO membranes available in literature. Following the commercial availability of this membrane, a further study was performed by Stillman et al. [71] to understand the influence of mesh-incorporation on the formation of support structures and the final FO performance. The flux performance of their best performing membrane exceeded the HTI TFC membrane.

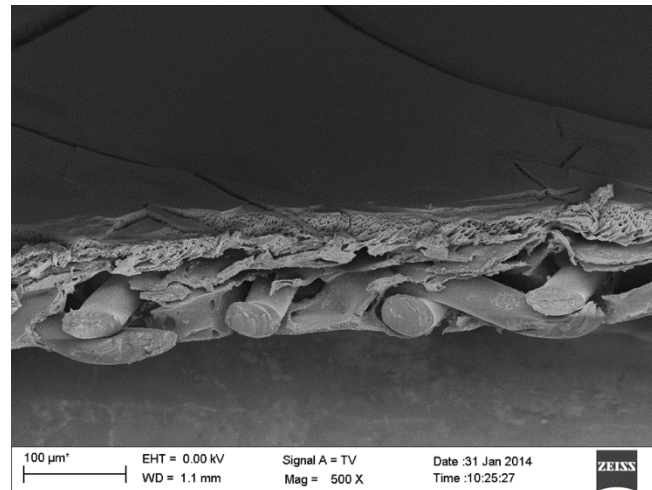


Figure 2.4: SEM image of the HTI TFC membrane

Besides the flat sheet TFC membranes presented above, hollow fiber thin film composites have also been used in FO. These membranes were fabricated using phase inversion for the preparation of the porous substrate and interfacial polymerization for the preparation of the polyamide rejection layer. Wang et al. [51] developed a novel TFC hollow fiber membrane with an ultrathin polyamide layer via interfacial polymerization of MPD and TMC on the outer (#A-FO) and inner (#B-FO) surface of a porous PES substrate. They found that #B-FO achieved a high flux of $32 \text{ L.m}^{-2}.\text{h}^{-1}$ using a 0.5 M NaCl draw solution and DIW feed at $23 \text{ }^{\circ}\text{C}$ in the AL-DS configuration, although NaCl rejection was compromised at 91%. This membrane exhibited a pure water permeance of $2.19 \text{ L.m}^{-2}.\text{h}^{-1}.\text{bar}^{-1}$. It was suggested that the optimal FO membrane support structure should possess a very thin sponge-like layer in a thin and highly porous substrate [50, 51]. Hollow fiber membranes have also been used in PRO applications for power generation [65].

2.4.2 Structural Properties of the FO Membrane Support Layer

Internal concentration polarisation (ICP) is a major challenge in FO which greatly limits process performance [92, 95, 96] due to the lowering of the effective osmotic pressure across the

selective layer. It arises as a result of poor shear in the porous support, leading to a diffusive boundary layer being formed with a resistance to solute transport within the support [54]. This boundary layer is a consequence of dilution of the draw solution (FO mode) or concentration of the feed solution (PRO mode) in the support, as water permeates across the membrane active layer, resulting in a concentration profile from the bulk solution across the support layer to the inner surface of the active layer. This concentration profile results in a reduction of the effective osmotic pressure difference.

The extent of ICP greatly relies on the support structural properties which should be tailored to minimise the resistance to solute diffusion within the support layer. This is done by tailoring the support layer to be thin, highly porous, and minimally tortuous. Support hydrophilicity can also influence the extent of ICP, whereby, commonly used hydrophobic supports such as polysulfone and polyester decrease the effective porosity of the support as they are not fully wetted by water [97]. Hence, a prewetting step is usually performed to ensure the support is fully wetted prior to membrane testing. The support layer properties along with the solute diffusivity, make up the solute resistivity to diffusion within the porous support layer, K , whereby:

$$K = \frac{t\tau}{D\varepsilon} = \frac{S}{D} \text{ [unit: s. m}^{-1}\text{]}$$

Equation 2.2

whereby, D is the solute diffusion coefficient ($\text{m}^2 \cdot \text{s}^{-1}$), t , τ and ε are the thickness (m), tortuosity and porosity of the support layer, respectively, and S is the structural parameter of the support (m).

Earlier research debated whether finger-like or sponge-like structures were more suitable for the mitigation of ICP and improved FO performance. A clear consensus was not achieved, with

some studies claiming that the degree of hydrophilicity in the membrane support structure possess a much stronger influence on flux performance in FO, despite forming a sponge-like, macro-void free structure [98]. Other studies claimed that a support layer with a mixed-structure of a sponge-like layer sitting on top of highly porous macrovoids gave enhanced membrane performance [22, 54]. A further study performed by Wang et al. [64] attempted to fabricate a high performance TFC FO membrane using a PES-sulfonated PSf alloyed porous support layer with enhanced hydrophilicity. The best performing membrane exhibited water fluxes of $17 \text{ L}\cdot\text{m}^{-2}\cdot\text{h}^{-1}$ and $32 \text{ L}\cdot\text{m}^{-2}\cdot\text{h}^{-1}$ with a DIW feed and 1.0 M NaCl draw in FO and PRO mode, respectively [64]. This membrane had a reported pure water permeance value of $0.77 \text{ L}\cdot\text{m}^{-2}\cdot\text{h}^{-1}\cdot\text{bar}^{-1}$ and an NaCl rejection of 96.5%.

Besides efforts to reduce the structural parameter of TFC membranes made with the conventional phase inversion method [22, 54], recent studies [62, 66, 99] have transitioned to developing desired FO supports which has also led to significant decreases in the membrane structural parameter. These studies formed TFC membranes by interfacially polymerizing a polyamide film directly on an electrospun support. Bui et al. developed an electrospun nanofiber supported thin film composite membrane whereby, the polyamide selective layer was polymerized in situ onto a PSf-PET electrospun nanofiber support. The best membranes exhibited two to five times higher water flux with over 100 times lower salt flux compared to the HTI CTA membrane following the addition of SDS [99]. Song et al. fabricated a nanofiber composite FO membrane by interfacially polymerizing a polyamide film on a minimally tortuous polyethersulfone (PES) nanofiber support sitting on a non-woven fabric [62]. This membrane exhibited water fluxes six times higher than the commercial HTI CTA membrane with an NaCl rejection of 97%. It is likely the best performing FO membrane currently available in literature. The membrane had a pure water permeance of $1.7 \text{ L}\cdot\text{m}^{-2}\cdot\text{h}^{-1}\cdot\text{bar}^{-1}$ compared to $0.39 \text{ L}\cdot\text{m}^{-2}\cdot\text{h}^{-1}\cdot\text{bar}^{-1}$ for the HTI CTA membrane. It should be cautioned that supports with very low structural

parameters are likely to be less mechanically robust and hence, measures to improve the mechanical strength of these membranes should be taken to ensure they can withstand any hydrodynamic stresses in FO operation.

Despite present achievements of reduced membrane structural parameters and improved fluxes, there is still further opportunity for improvement and a few important questions that need addressing: Does the S parameter always provide a good indication of ICP? Are some of the terms describing the S parameter more dominant than others in influencing ICP behaviour? If ICP was successfully eliminated, will transport through the membrane approach the ideal theoretical flux or will it be limited by the properties of the polyamide layer and external concentration polarisation? In Chapter 6 of this thesis, some answers to these questions are discussed in an attempt to improve on the current understanding of ICP and the role of the support layer in influencing FO performance.

Besides improving support properties, a key to developing FO membranes with superior transport properties is ensuring high membrane selectivity to mitigate any solute diffusion across the active layer.

2.4.3 Selectivity of the FO Membrane Active Layer- Mitigating Reverse Solute Flux

A limiting factor affecting FO performance is the back permeation of solutes from the draw solution through the membrane active layer into the feed solution, known as reverse solute flux. As a result, draw solutes accumulate at the membrane surface on the feed side resulting in a reduction in the osmotic pressure difference across the membrane. The ratio of water flux to salt flux, $\frac{J_w}{J_s}$, provides a measure of the volume of water produced per mass of solute lost from the draw side. $\frac{J_w}{J_s}$ is a function of the selectivity of the active layer $\left(\frac{A}{B}\right)$ and the ability of the draw solute to generate an osmotic pressure (iRT) [100, 101]:

$$\frac{J_w}{J_s} = \frac{A}{B} iRT \text{ [unit: L. g}^{-1}\text{]}$$

Equation 2.3

whereby, J_w is water flux ($\text{L. m}^{-2} \cdot \text{h}^{-1}$), J_s is the solute flux ($\text{g. m}^{-2} \cdot \text{h}^{-1}$), A and B are the water ($\text{L. m}^{-2} \cdot \text{h}^{-1} \cdot \text{bar}^{-1}$) and salt ($\text{L. m}^{-2} \cdot \text{h}^{-1}$) permeability coefficients, i is the number of dissolved ionic species created by the draw solute (e.g. 2 for NaCl), R is the ideal gas constant ($\text{L. bar. K}^{-1} \cdot \text{mol}^{-1}$) and T is the absolute temperature (K).

The reverse solute flux is independent of the S parameter and the bulk draw solution concentration. It is solely dependent on the selectivity of the active layer which is determined by the ratio of $\left(\frac{A}{B}\right)$. Hence, an ideal FO membrane would be one tailored to maximize the $\left(\frac{A}{B}\right)$ ratio. Highly selective polyamide films would enable the use of smaller, lower molecular weight draw solutes with higher diffusivities such as NaCl, MgCl_2 and $\text{NH}_3\text{-CO}_2$ [24, 102]. Due to their good diffusivities, small draw solutes are ideal for mitigating ICP and producing high osmotic pressures at low viscosities. Ammonia-carbon dioxide ($\text{NH}_3\text{-CO}_2$) is one such example of a promising draw solute which can be recovered thermally with low energy costs [26, 103]. However, due to the small molecular size of the ammonia-carbon dioxide draw solute [102, 104], it suffers from more severe reverse solute flux compared to NaCl [102]. Thus, it is paramount to develop highly selective polyamide films for FO membranes to enable effective rejection of draw solutes. Improved selectivity also has the added benefit of decreasing forward solute flux and hence, preventing the accumulation of feed solutes in the draw solution, which could lead to precipitation or permeation into the final product water [102].

Due to the intrinsic properties of the polyamide film, a high selectivity cannot be achieved without compromising on water permeance. Hence, an ideal FO membrane will have a moderately high

water permeance without compromising selectivity, with improved structural properties to mitigate ICP.

2.5 Fouling in Forward Osmosis Membranes

2.5.1 Low Fouling Propensity of Forward Osmosis

Membrane fouling is an undesirable phenomenon as it decreases process performance and increases operating costs. Fouling in FO involves adsorption and deposition of organic and inorganic contaminants, microbial species and colloidal particles on the membrane surface or in the membrane support, depending on the orientation of the FO membrane. The cake layer which is formed following the deposition of these components, creates a hydraulic resistance and cake-enhanced concentration polarisation which results in the reduction of the osmotic driving force [5, 105].

FO offers a potential solution to mitigate fouling with various publications over the past decade demonstrating its advantages over pressure-driven membrane processes [1-9]. These studies conclude that the lower fouling propensity and high fouling reversibility in FO is attributable to the less-compact fouling layer formed, resulting from the absence of hydraulic pressure. The loosely-packed fouling layer enables almost complete flux recovery following a simple cleaning step by increasing shear rate (Figure 2.5) [2], suggesting that chemical cleaning may be avoided. High fouling reversibility is also observed with scaling by gypsum [11] and silica [12].

Besides increasing cross-flow velocities, other hydrodynamic strategies to mitigate fouling in FO have been adopted and successfully applied, including spacers placed near the membrane surface to reduce fouling [13, 14], use of flow pulsation [13], and use of air bubbles [2].

The reversibility of fouling in FO enables the treatment of raw feed waters with high fouling potential, such as those heavily laden with natural and effluent organic matter [15]. FO has been employed in osmotic membrane bioreactor (OMBR) systems for sludge and wastewater treatment due to its low fouling potential [4, 8]. A long term study (up to 28 days) conducted on the OMBR in submerged configuration showed that fluxes were recoverable up to approximately 90% of the initial permeate flux by applying osmotic backwashing [4]. This study indicates that membrane fouling does occur in FO, especially in long term applications, albeit with high potential for reversibility. Other studies showed that a steady water flux was maintained during wastewater treatment [13, 15] and sludge dewatering [16].

Observed flux decline behaviour in FO changes dramatically with the type of organic foulant, size of colloidal foulant, and type of draw solution employed to generate the osmotic driving force. Reverse salt diffusion from the draw side to the feed side exacerbates a phenomenon known as the cake-enhanced osmotic pressure (CEOP) within the fouling layer. The accumulation of draw solutes within the cake layer increases the effective osmotic pressure on the feed side, thus resulting in an overall decline in net osmotic driving force and permeate flux. A draw solute with a smaller hydrated radius is (e.g. NaCl) causes CEOP more readily than one with a larger hydrated radius (e.g. dextrose) as can be seen in Figure 2.6 [5].

Critical flux in FO has been studied using direct microscopic observation to detect large foulants or visible fouling layers on the membrane surface. Critical flux can be defined as the permeate flux when membrane fouling becomes noticeable. Studies conducted by Wang et al. and Zhao et al. showed that critical flux was observed only when the membrane surface was partially covered with a layer of foulant, suggesting that it may have an inherent correlation with the visible layer [106, 107]. In one of the studies [106], it was observed that the FO mode

experienced significantly less fouling compared to PRO mode, which could be attributed to the lower fluxes in the former, consistent with the critical flux concept.

As presented in Section 2.3, the limitations to energy savings posed by the DS recovery stage in FO hybrid processes make the lower fouling propensity in FO an important benefit over RO, as it can result in the reduction or elimination of pre-treatment and chemical cleaning. Hence, fouling mechanisms in FO need to be further understood and fouling mitigation methods improved, in order for FO to be successfully implemented. In Chapter 5 of the thesis, the physicochemical mechanisms involved in the organic fouling and cleaning of cellulose acetate and thin film composite FO membranes are investigated to better understand the various factors affecting the fouling behaviour of these membranes.

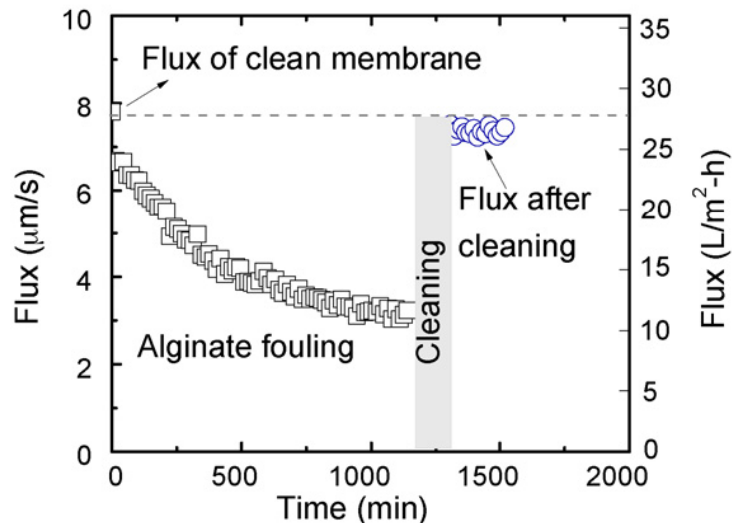


Figure 2.5: Fouling and cleaning of a HTI CTA membrane with a model organic foulant (alginate). The fouling test was conducted at a cross-flow velocity of $8.5 \text{ cm}\cdot\text{s}^{-1}$ and temperature of $25.5 \text{ }^\circ\text{C}$. The feed solution consisted of $200 \text{ mg}\cdot\text{L}^{-1}$ of alginate, 50 mM NaCl , and 0.5 mM CaCl_2 . Cleaning involved rinsing with 50 mM NaCl at an increased cross-flow velocity ($21 \text{ cm}\cdot\text{s}^{-1}$) for 15 min. [Reprinted from Mi et al. [2]].

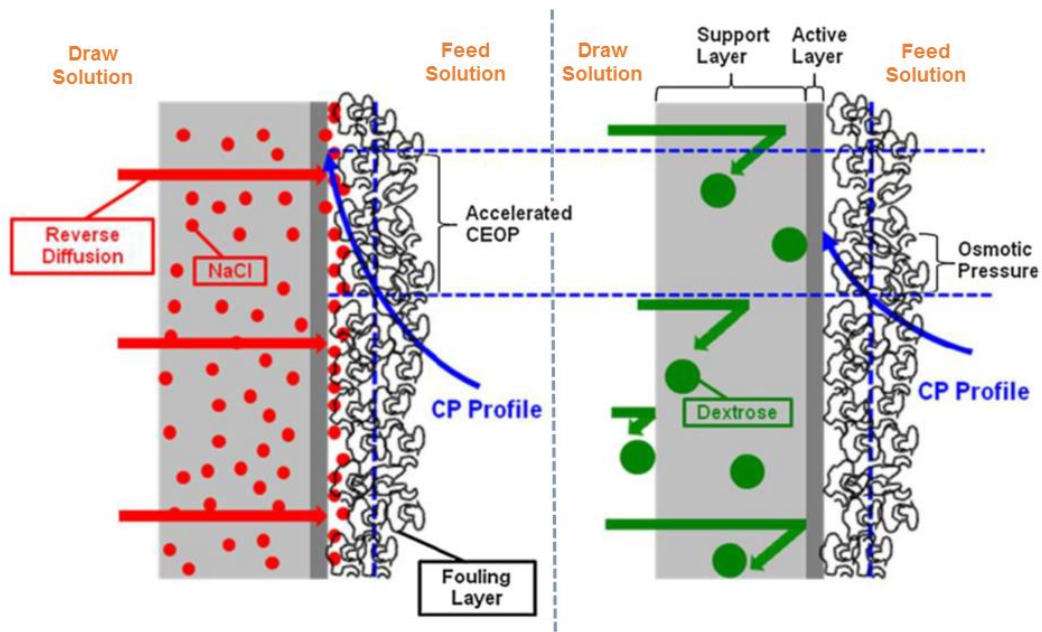


Figure 2.6: Figure showing a conceptual illustration of the effect of reverse draw solute diffusion on cake-enhanced osmotic pressure (CEOP) in FO mode for different draw solute sizes: (a) NaCl and (b) dextrose. [Adapted from Lee et al. [5]].

2.5.2 Fouling Mitigation- Membrane Surface Properties

Besides the effects of hydrodynamic conditions on the fouling propensity in FO, interactions between the foulant and membrane surface also contribute to the severity of fouling [23]. Hence, FO membrane surfaces need to be tailored to improve hydrophilicity, exhibit inert surface chemistry and a smooth morphology in order to be fouling resistant.

Rising interest in the potential and use of TFC membranes for forward osmosis, has resulted in a few studies utilising these membranes for fouling mitigation studies. These studies investigated the surface modification of the membrane active layer [67, 72, 108]. A commonly used method is the grafting of hydrophilic polymers, such as polyethylene glycol (PEG), onto the membrane surface to form a polymer brush, which exhibits a steric hindrance to foulant adhesion [67, 72, 108, 109]. The PEG-modified membrane exhibits significantly improved hydrophilicity and reduction in foulant adhesion, reduced flux decline and almost complete

fouling reversibility [67], albeit at the expense of reduced membrane permeance due to the hydraulic resistance imposed by the grafted polymer.

Besides surface modification of TFC FO membranes, there are some widely used anti-fouling mechanisms (Figure 2.7) in RO which can be adapted to FO when modifying membrane surfaces with anti-fouling properties. Improvements can be made to the interfacial polymerisation (IP) step by selecting new monomers which contain more functional or polar groups to increase surface hydrophilicity and decrease surface roughness. The IP process can also be improved by introducing organic modifiers, chemical coupling, grafting, or introducing more active hydrophilic groups such as $-\text{NH}_2$ [110].

Surface modification by physical methods include surface adsorption with surfactants or charged electrolytes and surface coating with water soluble molecules, block co-polymers or dendrimers. Chemical methods include hydrophilization with hydrophilizing acids, radical grafting, chemical coupling with high molecular weight molecules etc. Surface modification can also be performed using hybrid FO membranes with inorganic particles (e.g. TiO_2 , SiO_2 , Zolite A and silver) by direct coating or incorporating inorganic particles during IP (e.g. TFN). The self-cleaning and anti-bacterial fouling potential of these materials can be very useful to prevent bio-fouling [110]. Further studies performed on surface modification of membranes for improved fouling resistance are described in a review by Rana et al. [111].

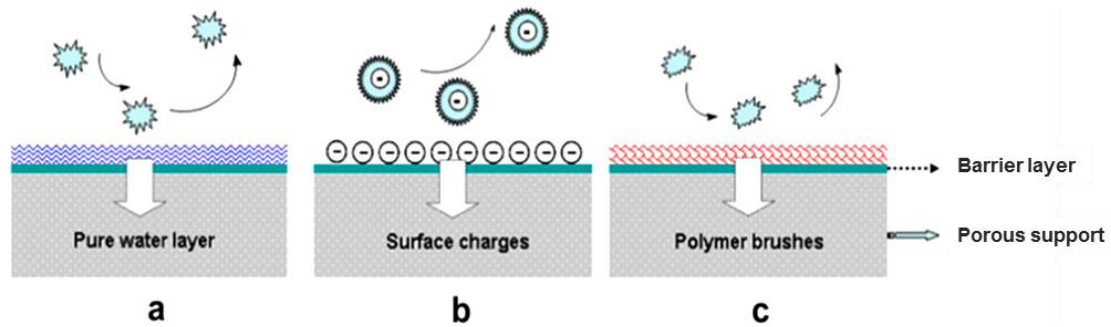


Figure 2.7: Schematic diagrams of antifouling mechanisms: (a) pure water layer; (b) electrostatic repulsion; (c) steric repulsion. [Reprinted from Kang et al. [110]].

2.6 Draw Solution Development for Forward Osmosis

Two important criteria central to the success of forward osmosis (FO) are the design and fabrication of a suitable membrane, and the use of a suitable draw solute. As the main source of driving force in the FO process, the careful selection of a suitable draw solute is crucial as it determines the overall energy consumption of the process depending on the regeneration method selected, and affects the performance of the FO stage, particularly where ICP is concerned. This section of the review will discuss the different aspects of draw solutes affecting FO performance, the selection criteria and suggestions for the optimal draw solution (DS), the implications of DS choice on energy consumption, the classification of DS and its use in various modern applications and the regeneration methods available for DS recovery.

2.6.1 Classification of Draw Solutes and their Applications.

Draw solutes can be divided into inorganic-based, organic-based and other categories such as polyelectrolytes and magnetic nanoparticles (MNPs), and polymer-based draw solutes. Inorganic-based DS are usually composed of electrolyte solutions although non-electrolyte solutions are sometimes considered [112]. Achilli et al. [104] has tested fourteen inorganic DS suitable for FO applications using a hybrid FO-RO process with an RO system design software

simulating DS regeneration. The DS were tested for their effects on pure water flux and reverse salt flux. Along with the costs associated with the FO and RO processes, they found a group of seven high-ranking DS based on performance and replenishment costs. Different properties of the selected DS indicate that their specific use would depend on the application and membrane type [104]. The study suggested that $MgCl_2$ may be the best DS for most water and wastewater applications due to its resistance to form precipitates at pH lower than 9, hence lowering the risk of scaling. However, Tan et al. [113] observed that $MgCl_2$ and $CaCl_2$ exhibited lower-than-expected water fluxes compared to NaCl and KCl when used in the hybrid FO-NF process for desalination, due to more severe concentration polarisation effects. Of all the draw solutes tested, $MgSO_4$ gave the best FO rejection of 99.99%, albeit at the cost of lower fluxes. Phuntsho et al. [114] evaluated the performance of nine commonly used inorganic fertilisers as potential DS in fertigation. The results of the study indicated that draw solutions of KCl, $NaNO_3$ and KNO_3 performed best in terms of water flux while $NH_4H_2PO_4$, $(NH_4)_2HPO_4$, $Ca(NO_3)_2$ and $(NH_4)_2SO_4$ had the lowest reverse solute flux. Besides the DS mentioned above, other commonly used inorganic DS include NaCl and ammonia-carbon dioxide (NH_3-CO_2). These draw solutes are preferred for their small molecular weight, low toxicity and high diffusivity. In addition, NH_3-CO_2 can be recovered using low cost thermal energy sources for the DS recovery stage.

Organic-based DS include fructose and glucose which have been used in applications such as production of nutrient drinks, emergency water supply in life boats and emergency relief situations during natural disasters [115-117]. Organic DS are usually non-electrolyte compounds that can generate appreciable osmotic pressures due to their solubility in water. Other organic DS include polyethylene glycol 400 (PEG), ethanol, albumin and 2-methylimidazole-based compounds [112].

Besides the draw solutions mentioned, other categories include polyelectrolytes and magnetic nano-particles (MNPs), ionic polymer hydrogel particles, micelles close to the Krafft point and dendrimers, amongst others. Hydrophilic MNPs have received attention as a novel draw solute [118-120]. It was discovered that the hydrophilicity and particle size were crucial in determining FO performance [120]. Their advantages are attributed to the high surface-area-per-volume ratio and larger size compared to inorganic salts and organic molecules, which enabled their recovery using magnetic fields and low pressure membrane processes such as NF or UF [112]. It was found that the MNPs agglomerate when recycled using magnetic separators [121]. This phenomenon could be minimized by ultrasonication [122] which affects the magnetic properties of the particles and reduces their recovery efficiency. UF was employed to recover the draw solute successfully where large particle sizes were used. Polyacrylic acid (PAA) MNPs achieved osmotic pressures of up to 71 bar which makes them attractive for desalination applications [118].

There is a need to sustainably manage RO concentrate from desalination processes in order to minimize its adverse effects on the environment. There have been efforts made to use RO brine as DS in a dual-stage FO process [119] and hybrid FO-RO process [123]. In the first case, FO is used to concentrate proteins using MNPs as the DS. Subsequently, RO brine is used as the DS in a second FO stage to recover the MNPs. The second case involves FO as a pre-treatment step for RO desalination whereby RO brine is used as the DS to concentrate impaired water in order to minimise its volume for further treatment. The diluted brine is then recovered using an RO desalination process.

The use of ionic polymer hydrogel particles has been investigated as a potential DS for desalination [118]. These hydrogels have the ability to draw water from the saline feed due to their highly concentrated hydrophilic groups causing them to swell. They also have the

advantage of reversible volume change whereby they can release the water by de-swelling in response to certain environmental stimuli such as temperature, light, pressure or pH. This makes the polymer hydrogel easy to recover at a lower energy cost compared to thermal recovery or membrane-based recovery processes. It was later discovered that light-absorbing carbon particles enhanced heating and dewatering of the polymer hydrogel particles [124].

2.6.2 Selection Criteria for Optimal Draw Solutes

FO performance is characterized by permeate productivity, reverse solute flux selectivity and energy efficiency for DS recovery. The challenge is selecting or developing a suitable DS with characteristics that promote high water flux and product recovery, low reverse salt flux, and recoveries at low energy costs.

Various approaches towards selecting a suitable DS for FO applications have been proposed [104, 112, 125, 126]. The criteria for selection are i) highly soluble and able to generate high osmotic pressures at low viscosities, ii) inexpensive, non-toxic, inert and can be regenerated using simple, efficient techniques, and iii) large enough to minimise reverse solute flux yet small enough to mitigate ICP.

The osmotic pressure of a DS can be described using Morse's derivation of the van't Hoff equation, for dilute ionic solutions:

$$\pi = icRT = i \left(\frac{n}{V} \right) RT \text{ [unit: bar]}$$

Equation 2.4

Whereby i is the van't Hoff factor or the number of dissolved ionic species created by the draw solute (e.g. 2 for NaCl), c is the molar concentration (mol. L^{-1}) equivalent to the ratio of moles

of solute, n , to the volume of solution, V , R is the universal gas constant ($\text{L} \cdot \text{bar} \cdot \text{K}^{-1} \cdot \text{mol}^{-1}$) and T is the absolute temperature (K).

For a wider range of concentrations, a more general form of the equation can be used to describe osmotic pressure of a solution:

$$\pi = CRT \left(\frac{1}{M_w} + A_2 C + A_3 C^2 + \dots \right) \text{ [unit: bar]}$$

Equation 2.5

Whereby C is the mass concentration of the solute ($\text{g} \cdot \text{L}^{-1}$), M_w is the molecular weight of the solute ($\text{g} \cdot \text{mol}^{-1}$), R is the universal gas constant ($\text{L} \cdot \text{bar} \cdot \text{K}^{-1} \cdot \text{mol}^{-1}$), T is the absolute temperature (K), A_2 and A_3 are the second and third virial coefficients that capture the solute-solvent interactions [127].

From Equation 2.4, it can be deduced that in order to achieve a high osmotic pressure, a high solubility is required of the draw solute to obtain a high n or M value. Additionally, ionic solutes which can dissociate fully to produce more ionic species and increase the i value are favourable. Simple multivalent ionic solutes are suitable candidates. Small molecular weight solutes are also preferred due to their ability to generate high osmotic pressures at reduced viscosities. This is expressed by Equation 2.5 whereby the osmotic pressure is inversely proportional to the molecular weight of the solute. Figure 2.8 shows that low molecular weight inorganic solutes can generate osmotic pressures greater than 100 bar at solution viscosities close to that of pure water (i.e. 1 cP). On the other hand, polymer and nanoparticle based solutions require very high solute concentrations which lead to unacceptably high viscosities, due to their large size, in order to achieve appreciable osmotic pressures [1, 112, 128]. High solution viscosities are

undesirable as they lead to increased pressure losses along the module, thus increasing energy requirements.

Higher DS temperatures give improved water fluxes due to reduced solution viscosity and enhanced mass transfer effects. However, water flux can only be enhanced by temperature to a certain critical point beyond which the onset of membrane scaling results in flux decline [112].

Due to their sizes, small inorganic solutes exhibit higher mobilities and diffusivities which can mitigate the flux limiting effects of ICP and lead to higher overall fluxes. As flux is exponentially dependent on draw solute concentration and diffusivity, the selection of a draw solute with high diffusivities is critical, as even a small difference can have a significant effect on flux [104]. Large draw solutes such as nanoparticles have lower diffusivities which limit their transport in the support structure of FO membranes, and results in limited applications for treating real feed waters.

Although small and simple dissolved inorganic ions and thermolytic salts such as NaCl, MgCl₂ and NH₃-CO₂ are preferred as effective draw solutes for FO applications, the small sizes of these salts result in more severe reverse salt flux compared to nanoparticle or polymer-based draw solutions. However, the trade-off between improved ICP and lower selectivity is being addressed with the recent development and commercialisation of TFC FO membranes, which exhibit higher reverse salt flux selectivity [22, 101, 129].

Other factors to be considered when selecting a suitable draw solute include the presence of scale precursor ions (e.g. Mg²⁺, Ca²⁺, Ba²⁺, SO₄²⁻ and CO₃²⁻) whereby in the case of feed and draw solutions containing these ions, the use of draw solutions likely to cause scaling (e.g. CaCl₂, KHCO₃, MgSO₄, NaHCO₃ and Na₂SO₄) is strictly limited to applications involving pure

feed solutions (e.g. food concentration). Draw solutions containing scale precursor ions are not recommended for typical environmental engineering applications due to the complex ion matrix of the feed solution [104].

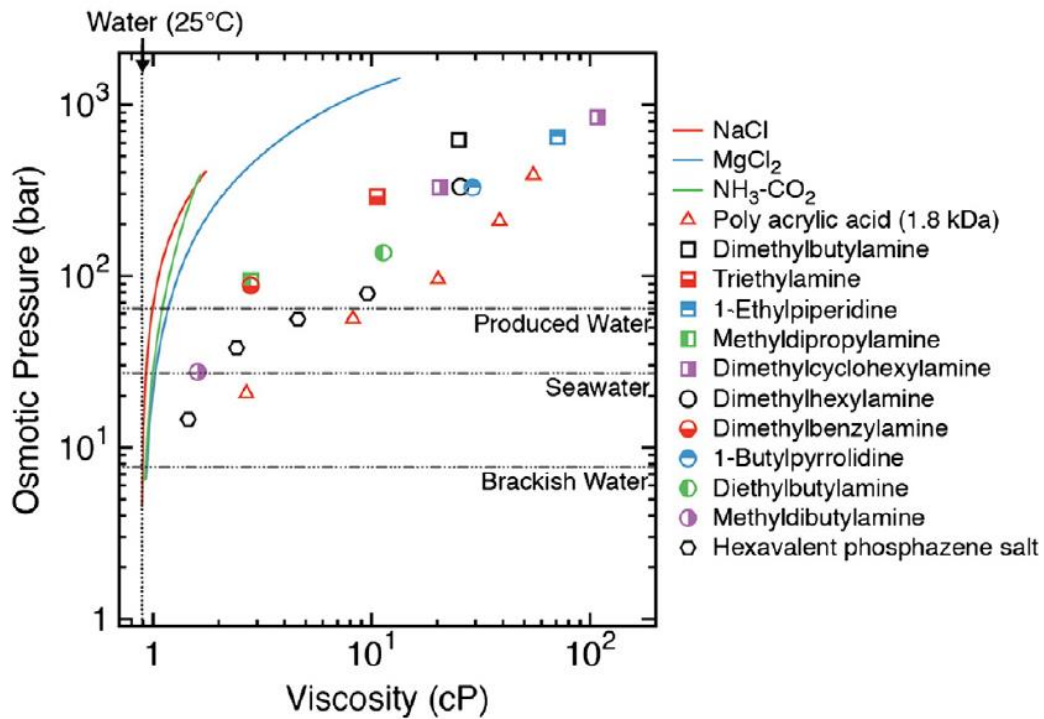


Figure 2.8: Relationship between osmotic pressure and viscosity for different draw solutions. Solid curves represent draw solutions consisting of simple, small ions. Red open triangles indicate a draw solution with polyacrylic acid (MW= 1800 Da) [130]. Black open hexagons represent a draw solution with a hexavalent phosphazene salt as the draw solute [131]. All other symbols represent draw solutions with different tertiary amines and dissolved carbon dioxide as switchable polarity solvents for draw solutes [132, 133]. Solid curve data were simulated at 25 °C. Aqueous solutions of ammonia carbamate were modelled to represent ammonia–carbon dioxide. The vertical dotted line indicates the viscosity of pure water at 25 °C. The horizontal lines show the representative osmotic pressures of three feed solutions: shale gas produced water (64.8 bar), seawater (27 bar), and brackish water (7.7 bar). [Reprinted from Shaffer et al. [1]].

2.6.3 Does the Choice of Draw Solute Improve Energy Consumption?

Although there has been extensive research on finding the ideal draw solute [104, 118, 120, 124, 126, 129-132] which can reduce energy consumption of the DS recovery stage, novel draw solutes are limited in their potential for energy savings. The reason for this limitation is that the energy required for the recovery of draw solutes in the DS recovery stage cannot be less than the minimum energy required for separation in the FO stage, at a specific product recovery. Hence, regardless of the choice of draw solute, including those capable of generating higher osmotic pressures at lower concentrations, energy consumption in the DS recovery stage will not vary significantly at a given product recovery if a pressure-driven membrane process is used, since SEC is governed primarily by the osmotic pressure of the brine which is a direct function of the recovery in FO. Consequently, using larger draw solutes that can be recovered with a typically low-pressure and low-energy membrane process like UF does not result in further energy savings compared to RO, as the same brine concentration factor will be required to achieve the osmotic pressure needed to drive the FO stage at a given recovery. Novel draw solution recovery methods that seek improvement in energy efficiency are limited to applications that involve high osmotic pressure requirements where RO cannot compete, such as desalinating high-salinity feed waters using thermolytic salts, which can be recovered with low-cost thermal energy sources. Further research into DS development should be focused on these specific applications, besides applications with strategically chosen DS intended for use as the final product [114].

2.7 Modeling Membrane Performance in Forward Osmosis

FO membranes are commonly asymmetric membranes consisting of a selective layer and a porous support layer. The solution-diffusion model is used to model transport through the selective layer which is considered as a dense, symmetric film or membrane. For the support

layer, transport is described using the diffusion-convection model. The coupling of these models describes solute and water transport in forward osmosis. This section presents the derivation of the solution-diffusion and diffusion-convection models for FO water and solute flux, taking into account concentration polarisation effects.

2.7.1 Solution-Diffusion Model Describing Transport across a Semi-Permeable Selective Layer in Forward Osmosis

The solution-diffusion model has been used to model transport in reverse osmosis, dialysis, gas permeation and pervaporation. It can also be extended to describe transport across a selective layer in FO. In the solution-diffusion model, a separation is achieved due to the differences in the amount of material that dissolves in the membrane and the rate at which the material diffuses through the membrane down a concentration gradient. The underlying assumption in this model is that the pressure within a membrane is uniform and the chemical potential gradient across the membrane is expressed only as a concentration gradient. It assumes that when a pressure is applied across a dense membrane, the pressure everywhere within the membrane is constant at the high pressure value i.e. the membrane transmits pressure in the same way as liquids. It is also assumed that the chemical potential of the feed and permeate solutions are in equilibrium with the adjacent membrane surfaces. Consequently, the pressure difference across the membrane is expressed as a concentration gradient within the membrane, resulting in a Fickian expression for flux:

$$J_P = \frac{D_i(c_{io(m)} - c_{il(m)})}{l}$$

Equation 2.6

Whereby D_i is the diffusion coefficient of component i ($\text{m}^2 \cdot \text{s}^{-1}$), $(c_{i(o(m))} - c_{i(l(m))})$ is the concentration difference of component i across the membrane surface ($\text{mol} \cdot \text{m}^{-3}$), and l is the membrane thickness (m).

Substituting the concentration difference adjacent to the membrane surface with the appropriate expressions for bulk concentration and chemical potential for incompressible fluids, and rearranging Equation 2.6, yields the expression:

$$J_P = \frac{D_i K_i c_{i(o)} v_i (\Delta\pi - \Delta p)}{lRT}$$

Equation 2.7

Whereby K_i is the absorption coefficient equivalent to the ratio of the activity coefficient in the bulk solution to that at the membrane surface, $c_{i(o)}$ is the bulk molar concentration of component i ($\text{mol} \cdot \text{m}^{-3}$), v_i is the molar volume of component i ($\text{m}^3 \cdot \text{mol}^{-1}$), $\Delta\pi$ and Δp are the osmotic and applied pressure differences across the membrane, respectively (bar).

Equation 2.7 can be simplified to describe water flux across the membrane:

$$J_P = L_p (\Delta\pi - \Delta p)$$

Equation 2.8

Where L_p is equal to $\frac{D_i K_i c_{i(o)} v_i}{lRT}$ and is known as the water permeability constant ($\text{L} \cdot \text{m}^{-2} \cdot \text{h}^{-1} \cdot \text{bar}^{-1}$).

Under FO conditions, Δp is negligible. Hence, Equation 2.8 can be written as

$$J_p = L_p(\Delta\pi)$$

Equation 2.9

Whereby J_p is the permeate water flux ($\text{L} \cdot \text{m}^{-2} \cdot \text{h}^{-1}$).

Similarly, a simplified expression for solute flux can be derived:

$$J_s = \frac{D_s K_s}{l} (c_{so} - c_{sl})$$

Equation 2.10

And can be simplified as:

$$J_s = B(c_{so} - c_{sl})$$

Equation 2.11

Whereby J_s is the salt flux ($\text{mol} \cdot \text{m}^{-2} \cdot \text{s}^{-1}$), B is equal to $\frac{D_s K_s}{l}$ and is the salt permeability constant ($\text{m} \cdot \text{s}^{-1}$), $(c_{so} - c_{sl})$ is the salt concentration difference across the membrane ($\text{mol} \cdot \text{m}^{-3}$).

A detailed description of the solution-diffusion model is given by Wijmans et al. [134].

2.7.2 Mathematical Description of Transport in Forward Osmosis- Mass Transfer Resistances

In practice, the severe effects of ICP result in the self-limiting behaviour of water flux in FO, whereby effective osmotic pressure at the membrane surface is exponentially dependent on flux. Additionally, when the membrane support layer is facing the feed solution (PRO mode),

fouling in the support layer increases the severity of ICP by reducing porosity of the support, thereby resulting in a coupled effect of fouling and ICP in FO [135]. This transport limiting phenomenon along with external concentration polarisation effects, which are not described by the solution-diffusion model in Section 2.7.1, need to be factored in to provide a realistic model that describes the actual water transport across the membrane in FO.

To include the effects of concentration polarisation, water and solute transport in FO is modelled by the solution-diffusion model coupled with diffusion-convection transport in the membrane support layer. Applying the solution-diffusion model to the dense rejection layer and assuming active layer facing draw solution (AL-DS) configuration (i.e. PRO mode):

$$J_P = L_p(\pi_{D,m} - \pi_{F,m}) \text{ [unit: L. m}^{-2}\text{. h}^{-1}\text{]}$$

Equation 2.12

$$J_S = B(C_{D,m} - C_{F,m}) \text{ [unit: g. m}^{-2}\text{. h}^{-1}\text{]}$$

Equation 2.13

Where L_p (L. m⁻². h⁻¹. bar⁻¹) and B (m. s⁻¹) are the water and solute permeability coefficients, respectively; J_P is the volumetric flux of water (L. m⁻². h⁻¹); J_S is the mass flux of solute (g. m⁻². h⁻¹); $C_{D,m}$ and $\pi_{D,m}$ are the solute concentration (g. L⁻¹) and osmotic pressure (bar) of the draw solution at the membrane surface, respectively; $C_{F,m}$ and $\pi_{F,m}$ are the solute concentration and osmotic pressure of the feed solution, at the interface of the FO support layer and the rejection layer, respectively.

In the support layer, the convective transport of solute into the support ($J_P C$) and that due to the solute back-transport through the rejection layer (J_S) have to be balanced by the solute diffusion away from the support:

$$J_P C + J_S = D_{eff} \frac{dC}{dx}$$

Equation 2.14

Where C ($\text{g} \cdot \text{L}^{-1}$) is the solute concentration in the porous support layer at a distance x from the interface between the rejection layer and the support layer, and D_{eff} ($\text{m}^2 \cdot \text{s}^{-1}$) is the effective diffusion coefficient of the solute. In a porous support layer with a porosity of ε , D_{eff} is related to the solute diffusion coefficient, D , by

$$D_{eff} = \varepsilon D$$

Equation 2.15

The boundary conditions for Equation 2.14 are:

$$C = C_{F,m} \quad \text{at} \quad x = 0$$

Equation 2.16

and

$$C = C_{F,b} \quad \text{at} \quad x = l_{eff} = \tau l$$

Equation 2.17

Where l is the actual thickness of the FO support layer, l_{eff} is the effective thickness of the support layer, and τ is the tortuosity of the support layer.

Solving Equation 2.12 - Equation 2.17 results in:

$$\ln \left[\frac{C_{F,m} + B(C_{D,m} - C_{F,m})/L_p(\pi_{D,m} - \pi_{F,m})}{C_{F,b} + B(C_{D,m} - C_{F,m})/L_p(\pi_{D,m} - \pi_{F,m})} \right] = \frac{J_P}{K_m} \quad (\text{PRO mode})$$

Equation 2.18

where K_m is the mass transfer coefficient, given by

$$K_m = \frac{D_{eff}}{l_{eff}} = \frac{D}{\left(\frac{\tau \cdot l}{\varepsilon}\right)} = \frac{D}{S} \quad [\text{unit: m} \cdot \text{s}^{-1}]$$

Equation 2.19

The structural parameter, S , is an important property of the membrane as it describes the structural properties and severity of ICP within the membrane support. A lower S value is preferred as it reflects a thinner, less tortuous and more porous support, which provides less resistance to solute diffusivity within the support layer. S is given by

$$S = \frac{\tau l}{\varepsilon} \text{ [unit: m]}$$

Equation 2.20

The solute resistivity to diffusion within the support layer, K , is given by

$$K = \frac{1}{K_m} = \frac{S}{D} = \frac{t\tau}{D\varepsilon} = \frac{t_{eff}}{D_{eff}} \text{ [unit: s. m}^{-1}\text{]}$$

Equation 2.21

If we assume that the osmotic pressure of a solution is proportional to its concentration, Equation 2.18 can be simplified to:

$$\ln \left[\frac{\pi_{F,m} + \left(\frac{B}{L_p}\right)}{\pi_{F,b} + \left(\frac{B}{L_p}\right)} \right] = J_P K$$

Equation 2.22

Where the osmotic pressure $\pi_{F,m}$ at the support-rejection layer interface can be determined from Equation 2.12.

Hence, water flux in PRO mode can be expressed as,

$$J_P = \frac{1}{K} \ln \left(\frac{L_p \pi_{D,m} - J_P + B}{L_p \pi_{F,b} + B} \right) \text{ [unit: L. m}^{-2}\text{. h}^{-1}\text{]} \quad (\text{PRO mode})$$

Equation 2.23

Similarly, water flux in FO mode can be expressed as,

$$J_P = \frac{1}{K} \ln \left(\frac{L_p \pi_{D,b} + B}{L_p \pi_{F,m} + J_P + B} \right) \quad [\text{unit: L} \cdot \text{m}^{-2} \cdot \text{h}^{-1}] \quad (\text{FO mode})$$

Equation 2.24

It should be noted that Equation 2.23 and Equation 2.24 work well for solutes obeying the van't Hoff equation at low solute concentrations. For solutes at high concentrations whereby a non-linear osmotic pressure-concentration relationship exists, an iterative method to solve for the water flux is used. This is further elaborated in Tang et al. [135].

In FO, both ECP and ICP occur simultaneously and their combined effects have been explained by models developed by McCutcheon and Elimelech [92, 95]. After modifying and rearranging Equation 2.23 which describes ICP effects and its relation to water flux and other membrane constants, and assuming negligible salt permeability coefficient (B), the effects of concentrative ICP and dilutive ECP on water flux in PRO mode can be expressed as

$$J_P = L_p \left[\pi_{D,b} \exp\left(-\frac{J_P}{k}\right) - \pi_{F,b} \exp(J_P K) \right] [\text{unit: L} \cdot \text{m}^{-2} \cdot \text{h}^{-1}] \quad (\text{PRO mode})$$

Equation 2.25

Similarly, the effects of dilutive ICP and concentrative ECP on water flux in FO mode can be expressed as

$$J_P = L_p \left[\pi_{D,b} \exp(-J_P K) - \pi_{F,b} \exp\left(\frac{J_P}{k}\right) \right] [\text{unit: L} \cdot \text{m}^{-2} \cdot \text{h}^{-1}] \quad (\text{FO mode})$$

Equation 2.26

The negative terms $\left(-\frac{J_P}{k}\right)$ and $(-J_P K)$ in Equation 2.25 and Equation 2.26 represent the dilution of the draw solution from the permeate flux into the draw side, whereas the positive terms $(J_P K)$ and $\left(\frac{J_P}{k}\right)$ indicate the concentration of the feed solution from the permeate loss to the draw side. It can be seen from these equations that flux in FO is self-limiting, whereby the effective osmotic pressure at the membrane surface is exponentially dependent on flux and concentration polarisation.

In Equation 2.25 and Equation 2.26, k is the external mass transfer coefficient:

$$k = \frac{Sh \cdot D}{D_h} \text{ [unit: m} \cdot \text{s}^{-1}\text{]}$$

Equation 2.27

Sh is the dimensionless Sherwood number, D is the solute diffusion coefficient ($\text{m}^2 \cdot \text{s}^{-1}$) and D_h is the hydraulic diameter (m).

The combined effects of ECP and ICP on the effective driving force across an asymmetric FO membrane is shown in Figure 2.9 and mathematically described by Equation 2.25 and Equation 2.26. Note that external concentration polarisation (ECP) is neglected on the outer support layer side of the membrane as it is assumed that the thickness of the external boundary layer is negligible compared to the structural parameter of the membrane. Hence, the contribution of ICP dominates over the effect of ECP. This assumption holds true for the membranes and experimental conditions applied in this work, whereby the thickness of the external boundary layer was < 5% that of the structural parameter under all the conditions studied. Moreover, water permeating the backing layer of the membrane already contains some concentration of the draw

solute, which mitigates the polarisation effects on the support side since pure water is not entering the bulk solution at the support surface [24, 93].

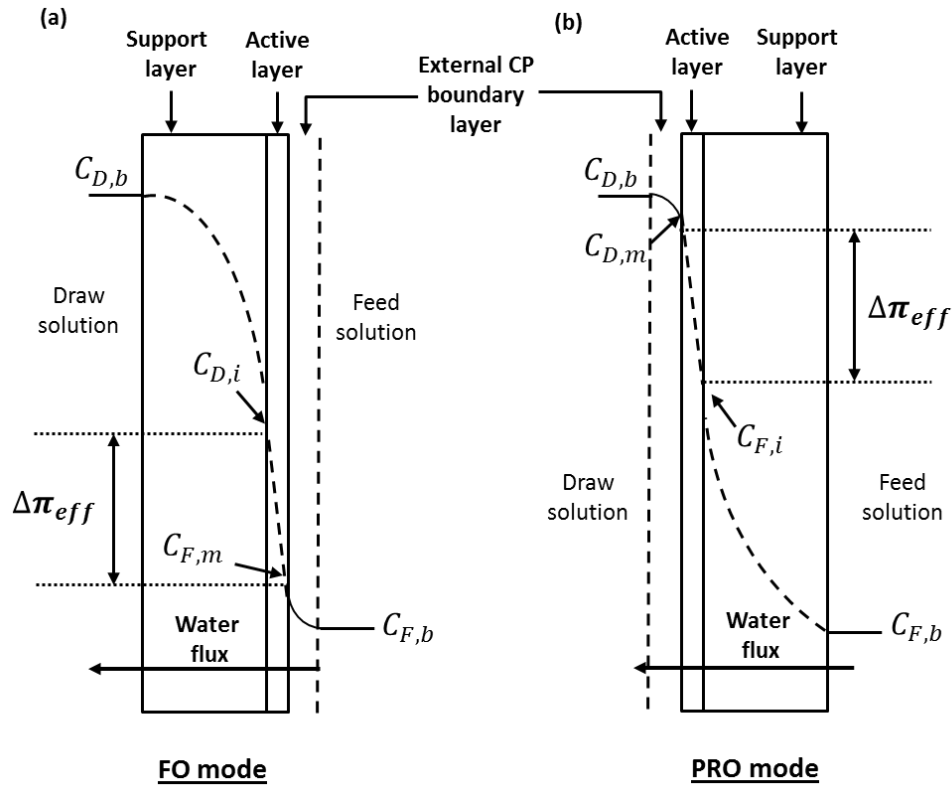


Figure 2.9: Illustration of the effect of external and internal concentration polarisation on the concentration profiles and effective driving force across an asymmetric FO membrane in (a) FO mode (AL-FS) and (b) PRO mode (AL-DS). [Adapted from McCutcheon et al. [92]].

2.8 Applications where Forward Osmosis can potentially outperform Other Technologies

As discussed in Section 2.3, the hybrid FO process with a membrane-driven DS recovery stage does not consume less energy than a standalone RO process and as such, cannot be

considered as a low-energy alternative to RO for desalination and other applications, unless a low energy draw solution regeneration method is used such as distillation using low grade heat.

Despite the energy limitations of the FO hybrid process, FO can outperform or enhance the performance of a standalone RO process in specific applications, for example, in cases where the feed solution is challenging to treat due to high salinities, high fouling potential or the presence of specific contaminants. In the case of high salinity feed waters such as seawater RO concentrate, oil and gas produced water, industrial wastewater and landfill leachate [1], FO has the potential to treat the feed water at osmotic pressures that exceed the operating pressure limits in an RO module. This is achieved by using thermolytic salts as the draw solution which can be recovered using low-temperature distillation processes [28], by leveraging low-cost thermal energy [136], such as low-grade heat from industrial processes, solar energy or geothermal energy. Thermolytic salts with vapour pressures much higher than water, allow for more efficient separation as they are more volatile and can be vaporised at relatively low temperatures. The result is greater energy savings compared to standalone thermal desalination technologies such as multi-effect distillation and multi-stage flash, which operate on the basis of vapourising and recovering the solvent (water), leaving the solutes and other non-volatile constituents behind [1, 137]. The ammonia-carbon dioxide system is an example of a widely researched thermolytic draw system [26, 39]. It can achieve an energy consumption of 1.2 kWh.m⁻³ for a 75% recovery desalination process, at least 50% lower than its other FO hybrid, SWRO and thermal desalination counterparts [39]. Its low molecular weight and high solubility results in high osmotic pressures at reasonable solution viscosities [93]. The ammonium salts decompose into ammonia and carbon dioxide gas upon moderate heating which can be regenerated into the draw solution [26].

FO can be used as a pretreatment step to improve the performance and permeate quality of conventional technologies used for desalination and water treatment. As a pretreatment step, FO is capable of removing i) dissolved organic material and inorganic scalants that affect the performance of conventional desalination processes and ii) trace organic compounds and boron, which undergo incomplete rejection by RO.

Current pretreatment processes for desalination are typically not designed to remove dissolved solids [138], resulting in challenges such as inorganic scaling which reduce the overall system recovery [139] and limit the system's operating pressure and productivity. Using FO as a pretreatment stage not only enables the removal of dissolved organic material, but inorganic scalants. In addition, the draw solution recovery stage which is effectively the conventional desalination process, is only exposed to the draw solution which has negligible fouling propensity. The use of FO as a pretreatment stage has been demonstrated elsewhere [30, 31]. The high fouling reversibility in FO [2] would enable it to maintain a stable performance when exposed to high fouling potential feed waters.

Although RO has been the state-of-the-art for treating wastewater and desalination feeds, one of its drawbacks is the incomplete rejection of trace organic compounds (TOCs) and boron, which results in reduced quality of the produced water. The removal of these dissolved contaminants are crucial for the production of safe potable water which can be used for human consumption and activities such as irrigation [140, 141]. FO pretreatment provides an additional barrier to reduce the concentration of these contaminants, whereby FO hybrid systems have been proven to exhibit higher rejections of TOC [34, 35] and boron [36] than standalone RO.

If the draw solution (DS) recovery stage can be eliminated and the diluted DS along with the concentrated feed are desired products, then FO is truly a low energy process. Osmotic dilution

[40] often involves the use of an impaired feed water source, such as wastewater effluent, and a saline source for the DS, such as seawater or brackish water [1]. It is desirable to concentrate the wastewater feed to aid with disposal [38], and dilute the saline draw to enable lower feed water salinity to a subsequent RO process or a reduction in brine concentration for a more environmentally friendly discharge [40]. Osmotic dilution has also been applied to fertigation [114] and applications where the dilute draw solution can be used directly as product, such as personal hydration packs and emergency water supply in life boats.

It should be noted that for all the FO applications presented in this section, especially those involving FO hybrid systems, the potential benefits gained from the use of FO have to be weighed against the cost of the membrane areas required along with associated items for the FO process.

Chapter 3

3 Project objectives

At present, there are several gaps in FO research which need to be strategically addressed. These include, firstly, the question on whether FO offers advantages over RO for seawater desalination; and specifically, if it consume less energy per unit water produced. Despite extensive study on the potential of FO as a low energy alternative to RO, there is a gap in literature on a realistic assessment of the energy consumption of FO hybrid processes. Secondly, is the need for a systematic fouling study of FO membranes, specifically factors affecting fouling behaviour and fouling reversibility of FO membranes, in particular novel TFC membranes which are the current state-of-the-art for FO. Further research is also required to address the lack of quantitative evidence in literature linking properties of the fouling layer formed under FO conditions, with fouling behaviour and hydrodynamic conditions of the process. Lastly, a major challenge in the development of successful FO membranes i.e. the elimination of the severely flux-limiting ICP bottleneck, is addressed. In this chapter, the research objectives of this thesis are presented, which are aimed at addressing the key gaps mentioned above.

3.1 Objective 1

Modelling and comparison of energy consumption in desalination for forward osmosis and reverse osmosis.

This work will focus on developing a simulation for the quantitative assessment of energy consumption in FO hybrid processes and providing a realistic comparison with the standalone RO process, using an integration of custom models and unit operations in the Aspen Plus process simulation software. Various process conditions such as pressure drop, pre-treatment and specific module configuration, along with process flow schemes incorporating different draw solution recovery methods will be considered to provide a more accurate analysis of the energy consumption of these processes. They will also be compared on the basis of membrane area requirements. The effect of a 'perfect' membrane i.e. one with infinite permeance and 100% salt rejection, on the specific energy consumption (SEC) and on the relative advantages of FO vs. RO, will also be investigated. This work will be presented in Chapter 4.

3.2 Objective 2

Study of organic fouling behaviour of structurally and chemically different commercial forward osmosis membranes

Fouling in FO is inherently different to pressure driven membrane processes due to the absence of hydraulic pressure as the driving force in the former. Fouling in FO is made more complex by the effect of membrane orientation as both the active and support layers can be oriented towards the feed solution, thus resulting in significant variation in fouling behaviour if the membranes are asymmetric. Different: i) structures; and ii) chemical composition of the active and support layers of the membranes result in different mechanisms for foulant deposition. In this work, an organic fouling study will be conducted on two commercially available HTI membranes with varying structural and chemical properties, the cellulose triacetate (CTA) and thin film composite (TFC) FO membranes. Specifically, it is of interest to analyse the performance and fouling behaviour of the HTI TFC membrane which has not yet been widely studied. This work will investigate various membrane and process parameters alongside physicochemical mechanisms involved in the fouling of these membranes in both the active layer facing feed solution (FO mode) and active layer facing draw solution (PRO mode) orientations. Specifically, the work will explore how factors such as fouling layer properties, membrane surface properties and membrane structural properties are linked to the fouling behaviour of these membranes and process hydrodynamic conditions, which are more significant in influencing fouling severity and reversibility and which provide good indicators for comparing fouling behaviour of different membranes. The implication of the results on furthering the understanding of FO fouling in addition to the current literature available will be presented. This work will be discussed in Chapter 5.

3.3 Objective 3

Development of novel forward osmosis membrane with potential for removing the internal concentration polarisation (ICP) bottleneck.

ICP poses a major challenge in the performance of FO membranes, severely limiting fluxes and increasing the membrane area required for separation. This work will focus on rethinking and reengineering the way FO membranes are fabricated in order to mitigate the effects of ICP. A new method of fabricating FO membranes involving the direct deposition of an independently formed polyamide film on a precision engineered open fabric support will be explored. The effect of removing the phase inversion support commonly used in FO membranes, on the mitigation of ICP and flux performance, will be discussed. Additionally, the role of the structural parameter (S) in determining the severity of ICP will be analysed to see if it provides a sufficiently good representation of ICP behaviour in the support layer. The FO membranes formed using this method will be characterised and tested to elucidate the effects of their intrinsic and structural properties on membrane performance. This work will be discussed in Chapter 6.

Chapter 4

4 Energy Consumption for Desalination - A Comparison of Forward Osmosis with Reverse Osmosis, and the Potential for Perfect Membranes

4.1 Introduction

Desalination is an attractive technology for the provision of clean water, due to the abundance of seawater. However, it is an energy intensive process compared to other water treatment technologies and poses an environmental challenge in terms of brine discharge. Since the 1970's, seawater reverse osmosis (SWRO) has been the leading technology for seawater desalination, and over this period there has been a large improvement in SWRO energy consumption, from as much as 20 kWh.m⁻³ in the 1970's to nearly 2 kWh.m⁻³ at 50% recovery, today [23]. The practical minimum energy for desalination of seawater at 50% recovery is 1.56 kWh.m⁻³ [23], which suggests potential for further improvement. Recently, forward osmosis (FO) has been receiving increasing interest from academia and industry as a potentially lower energy alternative to SWRO. Given that energy consumption makes up a major portion of the SWRO cost, reaching as high as ~45% of the total permeate production cost [142], it is useful to take a step back and compare the practical energy needs for RO and FO, where FO employs various draw solution recovery methods.

There have been recent publications comparing the energy consumption of a standalone RO process with the FO-RO hybrid process for desalination [1, 43]. However these studies presented a thermodynamic comparison assuming idealised conditions, and without considering process details such as pressure drop and pretreatment. In this chapter, a more detailed

comparison is carried out, taking the process factors into account. Furthermore, previous comparisons were limited mainly to the FO-RO hybrid process which the present work has extended to include other potential draw solution recovery processes. A detailed analysis is also carried out on the effects of potential improvements in membrane permeance on specific energy consumed and specific membrane area requirements for the various systems, another factor not considered in previous studies.

Published research on SWRO have investigated reducing the specific energy consumption (SEC) by optimising the membrane module [142-151] and/or using more permeable membranes [146, 152-154]. However, many of these studies have utilised modelling tools [23, 142] without process simulation tools. Most often pre-treatment energy requirements and pressure losses (if included in previous studies) were adopted from other publications or plant data, rather than being quantified by the studies themselves [23, 140, 155, 156]. Therefore, endogenous calculations on the effects of pretreatment and pressure losses in SWRO are in high demand.

For FO, the main direction of current research is towards improving intrinsic and transport properties of membranes on a molecular level [22, 46, 49, 53-55, 59, 63, 157]. However, the effects of these improvements on the energy efficiency of different FO desalination processes remain unexplored. Consequently, literature lacks comparative data on the SEC of different FO draw solution recovery processes, and how these compare with RO.

To reduce the sources of "side" factors which might compromise the comparison between RO and FO desalination, this present work utilises a unified process simulation environment, providing consistent numerical tolerances and sets of thermodynamic and physical properties models (in particular those embedded in the so called "Electrolytes NRTL" Property Method, available in Aspen's physical properties system) for all simulations. The mathematical models

for all custom (non-library) unit operations were programmed in Matlab R2012b, and embedded in the Aspen Plus V7.3 environment. The interoperability between the modelling tool, Matlab, and the process simulation suite, Aspen One, was achieved using CAPE-OPEN interface standards, according to the methodology proposed in Peshev et al. [158]. To the author's best knowledge, this is the first study which utilises Aspen Plus for simulation of FO and RO desalination processes using custom Matlab models. This customised process simulation approach allows for consistent evaluation and comparison of the energy requirements of FO and RO desalination along with the pretreatment stages, taking into consideration the effects of process configuration, thermodynamic restriction, product water recovery, draw solution recovery, membrane permeance, applied pressure, draw solution concentration, external and internal mass transfer coefficients, pressure drop and the use of energy recovery devices.

Accordingly, the objectives of the present work are:

- i) To quantify and compare SEC for desalination by RO and FO, considering for RO a range of process flow diagrams which account for the effects of pretreatment stages and pressure loss in the membrane modules, and for FO various draw solution recovery options;
- ii) To evaluate the potential for improvements in membrane permeance and rejection to reduce the SEC for both RO and FO.

4.2 Process Modelling and Simulation

4.2.1 Process Flow Diagrams and Unit Operations

Figure 4.1 (A) and Figure 4.1 (B) show the two types of desalination processes that were investigated in this chapter:

- A) Reverse osmosis (RO) with ultrafiltration (UF) pretreatment;
- B) Forward osmosis (FO) with UF pretreatment and varying draw solution (DS) recovery methods, namely (a) NF for the recovery of MgSO_4 draw solution; (b) UF for the recovery of polyacrylic acid-nanoparticles (PAA-NP) and; (c) distillation for the recovery of $\text{CO}_2\text{-NH}_3$ draw solution.

In this work, the energy consumption of SWRO is simulated at various recoveries. Results obtained are compared with FO to assess if FO has the potential for energy savings compared to RO. A fixed total pure water flowrate of $666 \text{ m}^3\cdot\text{h}^{-1}$ ($16,000 \text{ m}^3\cdot\text{d}^{-1}$), emulating a medium sized desalination plant is used as a basis for calculation. A higher product recovery ratio reduces the total volume of feed water to be pretreated (and hence the cost of pretreatment), whilst maintaining a constant permeate productivity. At higher recoveries, less seawater is discharged in the retentate and more is collected as the product water [159].

4.2.2 Process Models

4.2.2.1 RO Desalination

To estimate practical energy consumption for RO desalination operated near the thermodynamic limit ($\Delta P \approx \Delta \pi_{exit}$ at the exit of the RO pressure vessel) a model is constructed with user specified parameters and calculated variables. User specified parameters include pure water

permeance (L_p), corrected van't Hoff factor (ϕ), applied pressure difference (ΔP), solute rejection (R), external mass transfer coefficient (k), membrane area (A_m), and operating temperature (T). Calculated variables include permeate and retentate flowrates (Q_P and Q_R), permeate and retentate concentrations, osmotic pressure difference ($\Delta\pi$), energy consumption of high pressure pumps (HPP) and energy savings by energy recovery devices (ERD).

A model was developed to simulate the recovery of pure water from seawater at an initial salt concentration of 35 kg m^{-3} . HPP and ERD efficiencies were user selected. The governing equation used to calculate the permeate flowrate ($\text{mol}\cdot\text{s}^{-1}$) in RO is:

$$Q_P = \frac{L_P A_m (\Delta P(x) - \Delta\pi(x))}{v_P}$$

Equation 4.1

NaCl rejection is assumed at 100%. $\Delta\pi$ was estimated using the corrected van't Hoff equation i.e. $\Delta\pi = \phi \left(\frac{X_{M,NaCl}}{v_M} - \frac{X_{P,NaCl}}{v_P} \right) R_g T$ where $\phi = 1.64$ for an NaCl solution. ϕ is the corrected van't Hoff factor which is a product of the van't Hoff factor and the osmotic coefficient obtained from standard tables (Robinson and Stokes, 1959) [160, 161]. A constant value for this factor was assumed, averaged over the range of concentrations of solutions used in this work. The complete set of model equations is listed in Appendix A 1.

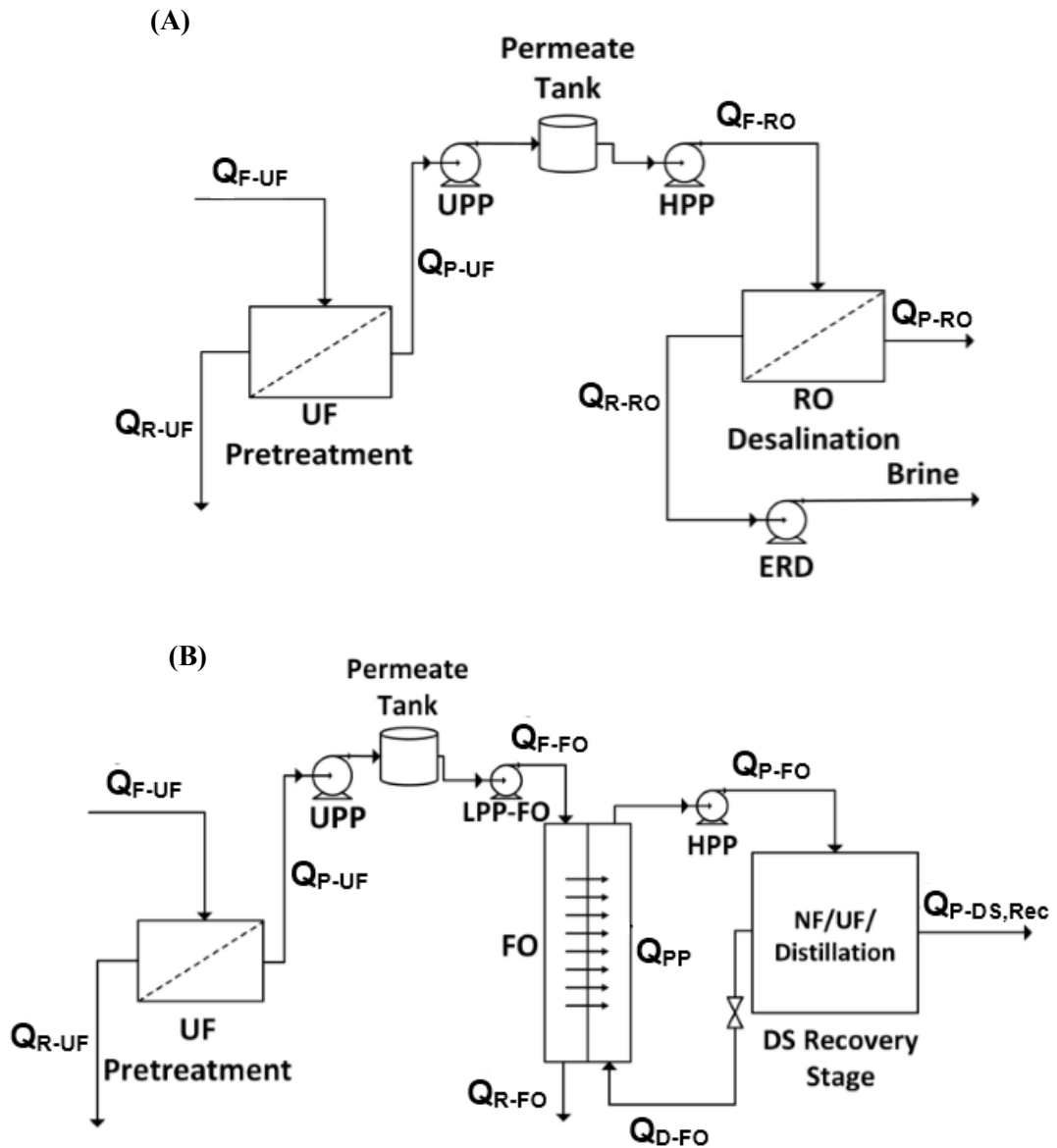


Figure 4.1: Desalination process flowsheets considered in this work for comparison of SEC. (A): RO desalination process with UF membrane pretreatment. (B): FO desalination process with UF membrane pretreatment and various draw solution (DS) recovery methods.

4.2.2.1.1 Pretreatment Effects

Pretreatment is used to produce high quality feedwater for stable and reliable performance in the RO stage.

A model for the RO desalination pretreatment step was developed to calculate the energy consumption of a submerged ultrafiltration (UF) pretreatment unit (Figure 4.5 (A)). Permeate flowrate was calculated using Equation 4.1. A membrane permeance of $3.9 \times 10^{-10} \text{ m}^3 \cdot \text{m}^{-2} \cdot \text{Pa}^{-1} \cdot \text{s}^{-1}$ based on the UF ZeeWeed® 1000 membrane was selected for use in the simulation, along with the assumption that the membrane was 100% permeable to NaCl. Membrane pretreatment was selected over conventional pretreatment given its lower sensitivity to fluctuations in feed water quality, and its ability to guarantee a low silt density index (SDI), therefore enabling operation with high and stable permeate flux over the long-term [140]. A backwash pump was included along with the assumption that the backwash flux is double the UF permeate flux, and that pressure used for backwash (1.6 bar) is double that of the low pressure (0.8 bar absolute) vacuum used to draw water through the pores of the UF fibers. Energy consumption by aeration during filtration was assumed to be ~40% of the total energy consumed by the UF pretreatment unit [162].

The energy consumed by the pretreatment stage is included in SEC calculations for comparison between RO and FO desalination.

4.2.2.1.2 Pressure Drop Effects

The energy consumption for SWRO is a function of the applied pressures and feed flowrates, which in turn are dependent on product recovery, plant configuration and frictional losses. Pressure drop across the SWRO module is a parameter which critically influences the

transmembrane driving force and, hence, the applied pressure across the membrane and overall performance of the process. For this reason, the effect of process configuration on pressure drop and energy consumption in SWRO was investigated to select the configuration which gave minimum SEC, and this minimum SEC was used for comparison with FO desalination.

A plug flow pattern was assumed in order to model the pressure, viscosity and concentration changes along the retentate channel in the SWRO modules. A typical 8-inch by 40-inch spiral wound FilmTec (SW30HR-380) module with ~30 leaves was selected for the simulation. The following underlying assumptions were made:

- i) Feed channels in the SW module are flat instead of curved due to the channel thickness being much lower than the module radius.
- ii) Pressure loss in the permeate channel is negligible. Given the selected SWRO module and typical transmembrane pressures, the average permeate velocity is low and the pressure drop is insignificant [148]. This means the pressure loss is one dimensional only in the feed side.

A schematic diagram of the flat feed channel is shown in Figure 4.2. The flat feed channel used has a length, L , height, h , and width, W . The total feed channel length, L , is assumed to be comprised of n elements in series with length, L_m , each. The seawater feed enters with an average velocity of v_f , a pressure P_f and a concentration of total dissolved solids of 35 g.L^{-1} . The properties of the FilmTec SW30HR-380 module can be seen in Table 4.1.

The pressure drop across the module was calculated using a semi-empirical pressure drop equation [163] derived for the SWRO module type of interest, given by:

$$\frac{dP_f}{dx} = \lambda \frac{\rho v_f^2}{2d_h}$$

Equation 4.2

$$\lambda = K_\lambda 6.23 Re^{-0.3}$$

Equation 4.3

Where, P_f is the feed side pressure, ρ the fluid density, v_f is the fluid velocity in the feed channel, d_h is the hydraulic diameter of the feed channel, λ is the friction factor, K_λ is a factor introduced to take into consideration pressure losses in the feed tubes and module fittings, with the average value ($K_\lambda = 2.4$) calculated using data obtained from literature based on field data from an SWRO plant in Portugal [148], and Re is the Reynolds number.

Based on the underlying equations and parameter values given in Table 4.1, the model for pressure drop was constructed as shown in Appendix A 2.

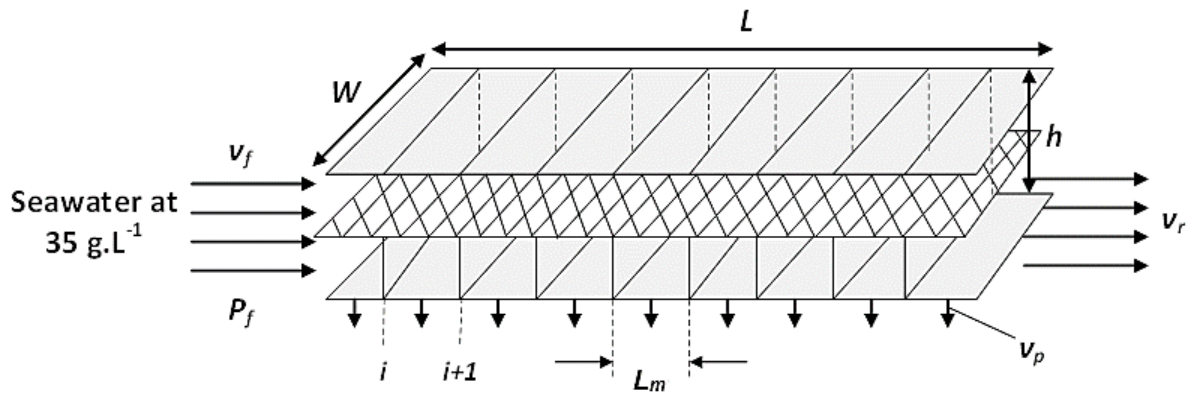


Figure 4.2: Flat rectangular channel model of the SW module feed channel with feed spacer [Adapted from Geraldes et al. [148]].

Property	Value
Effective membrane area	35 m ²
Effective membrane leaf length	0.88 m
Effective membrane leaf width	0.69 m
Feed channel height	0.0213m
Number of membrane leafs	29
Feed cross-section open area	0.0147 m ²
<i>Feed spacer^a</i>	
Height	0.737 mm
Porosity	0.9
Mesh length ^b	2.7 mm
Equivalent (hydraulic) diameter ^c	0.935 mm
<i>Operation limits</i>	
Maximum flow rate	5.1x10 ⁻³ m ³ .s ⁻¹
Minimum flow rate	1.0x10 ⁻³ m ³ .s ⁻¹
Maximum superficial feed velocity	0.35 m.s ⁻¹
Minimum superficial feed velocity	0.068 m.s ⁻¹
Maximum feed pressure	6.9 MPa

^aMesh-type spacer consisting of two layers of cylindrical filaments forming a diamond-type pattern. ^bDistance between two neighbour cylindrical filaments. ^cDefined by $4 \times$ volume of the feed channel/wetted surface [163].

Table 4.1: Properties of 8-inch by 40-inch spiral wound module FilmTec SW30HR-380.

[Adapted from Geraldès et al. [148]].

4.2.2.2 FO Desalination

The objective of the FO simulation is to model practical energy consumption for FO desalination along with the draw solution recovery step and compare results of various FO-DS recovery processes with SWRO. To do this, an FO model was constructed with user specified parameters and calculated variables. User specified parameters include pure water permeance (L_p), permeate flowrate (Q_p), corrected van't Hoff factor (ϕ), applied pressure difference (ΔP), solute rejection (R), internal and external mass transfer coefficients, and operating temperature (T). Calculated variables include membrane area (A_m), retentate flowrate (Q_R), permeate and retentate concentrations, osmotic pressure differences ($\Delta\pi$), energy consumption of high pressure pumps (HPP) and energy savings by energy recovery devices (ERD).

In all simulations, the recovery of pure water from seawater at a salt concentration of 35 kg m^{-3} in a single-stage FO was considered. Counter-current flow was assumed for all FO simulations as it provides slight improvement in flux and reduced cross migration of feed and draw solutes, relative to the co-current mode of operation [164-166]. The commercially available HTI CTA membrane with a pure water permeance of $5.56 \times 10^{-12} \text{ m}^3 \text{ m}^{-2} \text{ Pa}^{-1} \text{ s}^{-1}$ was selected as the basis for the FO simulations. The transport model used for FO was adopted from McCutcheon et al. [92]. Due to unavailability of FO module specifications for industrial scale desalination processes, the FO stage was modelled by calculating the membrane area required based on a user specified permeate flowrate and percentage recovery, as well as the log mean osmotic pressure difference. An explanation for the use of the log mean approach is provided in Appendix A 3. The governing equations used to calculate the membrane area and permeate flowrate in the FO and NF DS recovery stages respectively, are:

FO

$$A_m = \frac{(Q_{PP}) \cdot \ln\left(\frac{\Delta\pi_1}{\Delta\pi_2}\right) \cdot v_{H_2O}}{L_P \cdot (\Delta\pi_1 - \Delta\pi_2)}$$

Equation 4.4**NF (when used for DS recovery)**

$$Q_P = \frac{L_P A_m (\Delta P(x) - \Delta\pi(x))}{v_P}$$

Equation 4.5

Whereby, NaCl and MgSO₄ rejections are assumed at 100% for FO and NF stage, $\phi_{NaCl} = 1.64$ and $\phi_{MgSO_4} = 1.2$, respectively. ϕ is the corrected van't Hoff factor which is a product of the van't Hoff factor and the osmotic coefficient obtained from standard tables (Robinson and Stokes, 1959) [160, 161]. A constant value for this factor was assumed, averaged over the range of concentrations of solutions used in this work. The complete set of process equations used in the model is listed in Appendix A 3.

An 8-inch by 40-inch spiral wound FilmTec (NF90-400) module with an active surface area of 37 m² was selected for the NF simulation. Pressure drop effects for the NF stage were calculated using similar principles used for SWRO, whereby the NF module (Dow FilmTec NF90-400) operating conditions were obtained from Dow FilmTec [167].

The FO desalination stage was modelled as a single unit operation with specified inlet and outlet pressures and pressure drop values adopted from HTI bench-scale module design specifications [168], taking into account the design constraints of these modules. As FO technology is not yet commercially available on an industrial scale and data for scaled up FO

modules is not readily available, reasonable estimates were made based on laboratory data and the limited manufacturer's data which are available. Where used, the external mass transfer coefficient for the FO simulations is $k=2 \times 10^{-5} \text{ m.s}^{-1}$ and the solute resistivity to diffusion within the support layer of the FO membrane is $K=1.1 \times 10^6 \text{ s.m}^{-1}$ [92, 95, 169]. Where stated, UF pretreatment described in Section 4.2.2.1.1 was included in the total SEC for FO desalination when comparing with SEC for RO desalination.

4.2.3 Simulation Tools

There have been several studies performed on simulating energy consumption in RO desalination using mathematical models and simulation environments [23, 142, 170-175], which is not surprising given the wide application of RO in the desalination industry. On the other hand, there are at present no such simulation models and software for FO desalination processes, and so no single piece of software which contains library unit operations for both RO and FO processes together. Fortunately, the CAPE OPEN standards for software interoperability allows for efficient and fast integration of custom models and unit operations in commercially available and open source suites of chemical process simulation software. Hence, Aspen Plus was chosen as the process simulation software for simulating RO and FO desalination in this work. Further details on the procedure for integrating these models and unit operations in Aspen Plus using CAPE OPEN interface standards can be found in Peshev et al. [158].

4.3 Results and Discussion

4.3.1 Pretreatment Effects

Although increases in either membrane permeance (Section 4.3.3) and/or the number of stages will decrease the SEC required to achieve a specific product recovery within thermodynamic restrictions, a fundamental question is whether this reduction is significant when compared to the energy requirements of the pretreatment step. If the penalty due to the energy consumed in the pretreatment step is significant compared to the gain from the maximum energy savings made in the RO unit from improving membrane permeance, then there is little economic incentive in trying to improve the RO membrane permeance further. Instead, focus should be towards improving the energy efficiency of the pretreatment and post-treatment stages. The effects of pretreatment in RO desalination are presented in this section.

The simulated energy consumption for the UF unit was $\sim 0.11 \text{ kWh}\cdot\text{m}^{-3}$, which compares well with values presented in literature [155, 176]. Taking into account other pretreatment stages such as seawater intake and screening etc. [156], the total calculated energy consumption for the pre-treatment stage was $0.25 \text{ kWh}\cdot\text{m}^{-3}$. These results are summarised in Table 4.2.

Therefore, efforts to save energy can be made in the pretreatment stage which consumes energy equivalent to $\sim 13\%$ of that used in RO (assuming $\text{SEC}_{\text{RO}} = 2 \text{ kWh}\cdot\text{m}^{-3}$ i.e. the typical value of SEC for optimal RO desalination operation to date). These efforts include increasing permeance of the UF membranes, and optimising the hollow fiber UF module to improve hydrodynamics without compromising the mechanical strength of the fiber.

Type of Pretreatment Energy Consumption		Value of Pretreatment Energy Consumption (kWh.m ⁻³ of RO feed)				
UF pretreatment energy consumption	UPP energy consumed	0.024	=	0.11	=	0.25
	Backwash energy consumed	0.044				
	Aeration energy ^[162]	0.040				
Other pretreatment energy consumption	Seawater Intake ^[156]	0.084	=	0.14		
	Miscellaneous ^[156]	0.056				

Table 4.2: Energy consumption for UF membrane pre-treatment for desalination

4.3.2 Selection of Optimal Process Configuration for RO Desalination

SWRO configurations with the lowest energy consumption used in the comparison of SEC between RO and FO, were selected by comparing their pressure drops and energy consumption at various product recoveries. Three SWRO configurations were considered for this purpose (Figure 4.3 (A) to Figure 4.3 (C)) using industrial data and guidelines for designing SWRO processes recommended by Dow FilmTec [167]. Each system configuration was characterised by the number of stages, number of elements per stage and array ratio.

For a product recovery of 50%, a series of eight 35 m² elements per pressure vessel (also referred here as the basic process unit) was selected (Figure 4.3 (A)). The pressure drop calculated per pressure vessel with a feed flowrate of $Q_F=12.85 \text{ m}^3\text{h}^{-1}$ (i.e. 70% of the maximum flowrate specified per module), was 4.31 bar. The profile of feed pressure along the modules in series and the effect of varying Q_F are shown in Figures A-1 and A-2 of Appendix A 7. Pressure drop across the membrane module increased as a function of fluid velocity in the feed channel.

It was also shown that in order to operate the 8' x 40' SW30HR-380 module under the pressure drop limit of 1 bar, feed flowrate was limited to 13 m³h⁻¹ or less.

A comparison of pressure drop and SEC of the three SWRO configurations considered is shown in Figure 4.4. The process conditions used for the more efficient configurations selected for comparison with FO, at 50% and 75% product recoveries are listed in Table 4.3. It should be noted that given the maximum module operating pressure of 69 bar, the maximum achievable recovery was ~60%, after taking into account pressure loss effects. However, for simulation purposes, a higher product recovery of 75% was chosen for comparison with data available in literature for FO processes, which is explored further in Section 4.3.5.

At 50% recovery, axial pressure drop for two-stage RO is higher than single-stage due to 12 elements in series in the former compared to 8 in the latter (Figure 4.4). However, the SEC does not increase for a two-stage RO (3:2 array ratio) compared to single-stage, as the additional energy required to overcome pressure drop in the second stage is compensated by the energy savings made by the smaller volumes of feed and retentate brought to a higher pressure in the two stages. The 2:1 configuration has a higher SEC than the 3:2 configuration because the feed into the second stage of 2:1 has a higher flowrate, hence a higher pressure drop, which leads to a higher applied pressure required to overcome these losses. This is shown in Figure A-3 of Appendix A 7.

Based on these simulation results, a single stage RO configuration is selected for an SWRO process running at 50% product recovery, and a two-stage 3:2 configuration is selected for 75% product recovery. The ASPEN process flowsheets for these configurations are shown in Figure 4.5 (B) and Figure 4.5 (C).

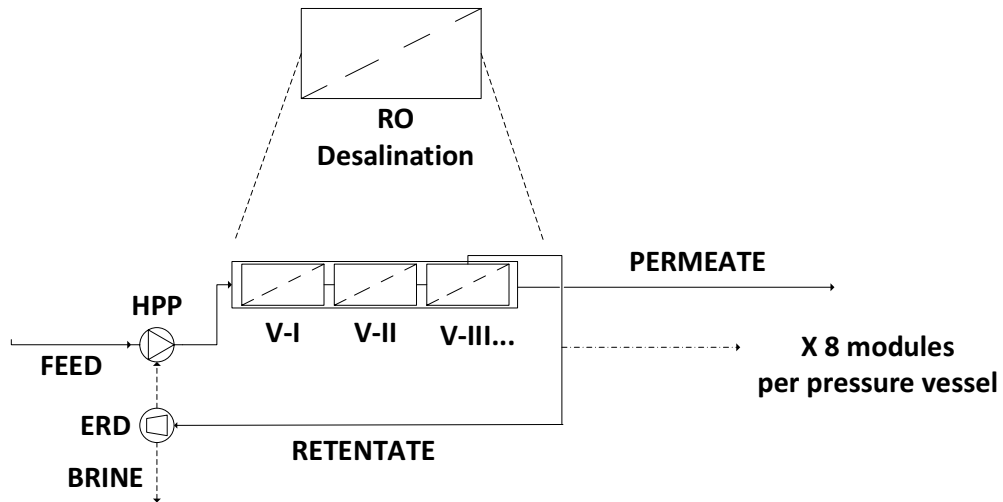


Figure 4.3 (A): Typical single-stage RO configuration with 8 spiral wound modules per pressure vessel. This configuration is used for calculation of pressure drop and SEC at 50% product recovery. Total membrane area per pressure vessel, $A_m=280 \text{ m}^2$.

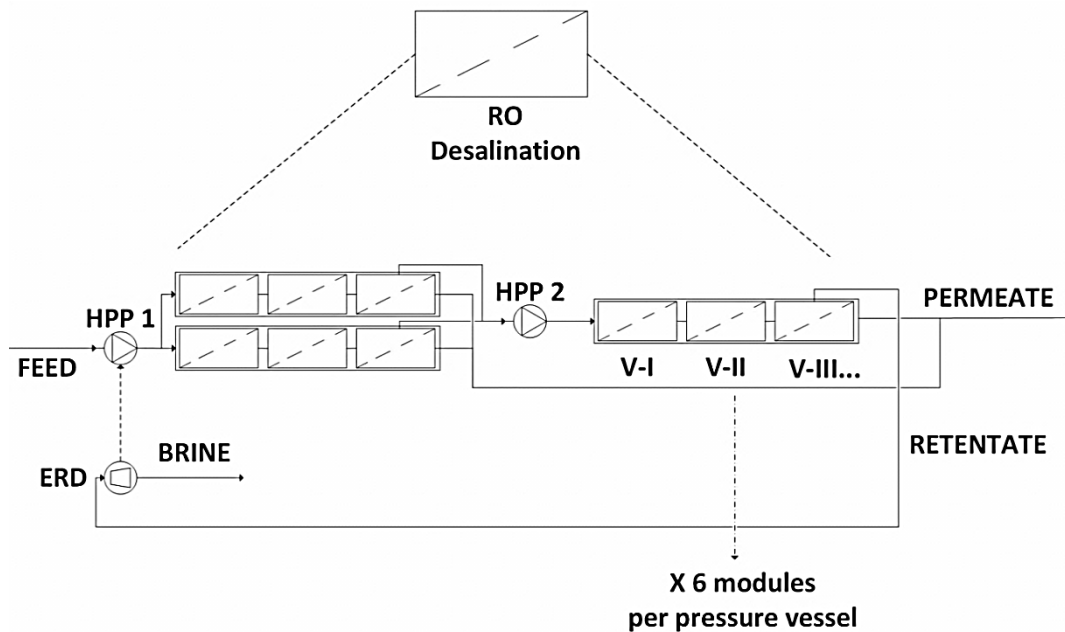


Figure 4.3 (B): Typical two-stage tapered RO configuration with 6 spiral wound modules per pressure vessel and an array ratio of 2:1. This configuration is used for calculation and comparison of pressure drop and SEC at 50% and 75% product recovery. Total membrane area per pressure vessel, $A_m=210 \text{ m}^2$.

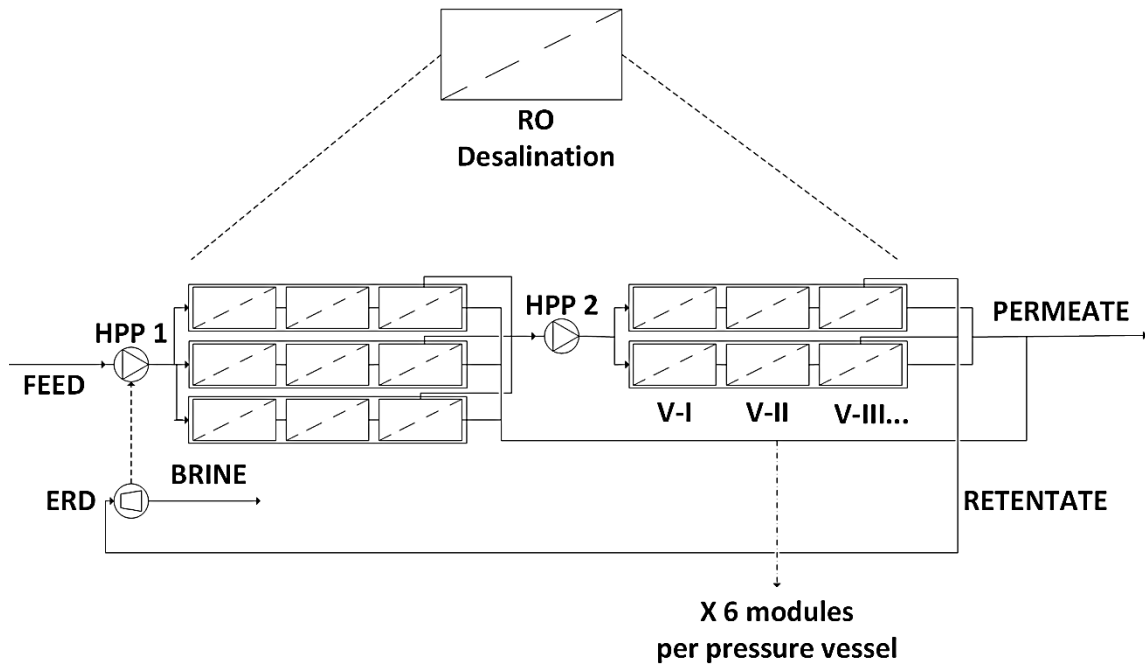


Figure 4.3 (C): Typical two-stage tapered RO configuration with 6 spiral wound modules per pressure vessel and an array ratio of 3:2. This configuration is used for calculation and comparison of pressure drop and SEC at 50% and 75% product recovery. Total membrane area per pressure vessel, $A_m=210 \text{ m}^2$.

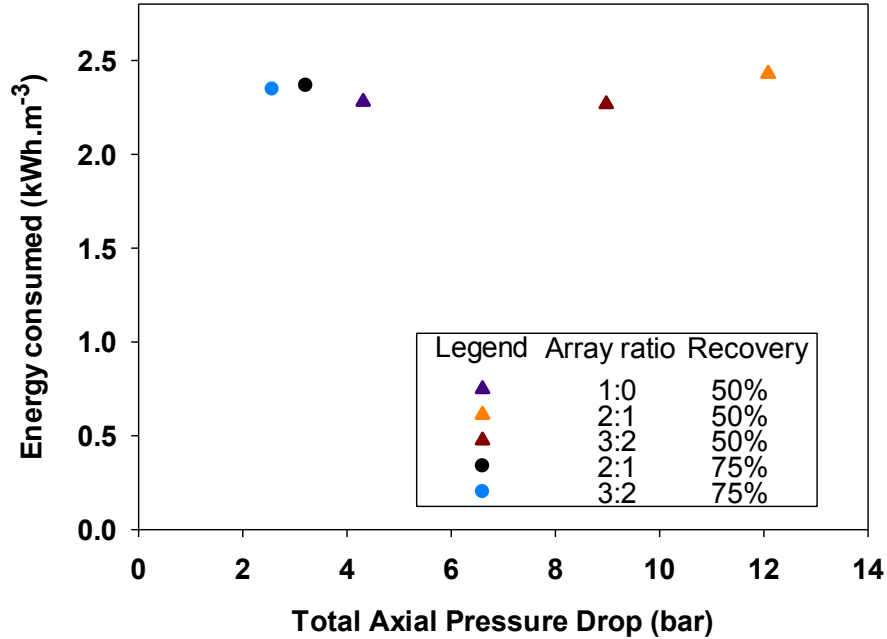


Figure 4.4: SEC versus axial pressure drop for different SWRO configurations at 50% and 75% product recovery. The single-stage and two-stage RO consist of 8 and 12 elements in series, respectively. HPP and ERD efficiencies = 100%, $L_p = 3.5 \times 10^{-12} \text{ m}^3 \text{ m}^{-2} \text{ Pa}^{-1} \text{ s}^{-1}$.

Product Recovery (%)	No. of Stages	No. of Elements per Pressure Vessel	No. of Elements in a Row	Array Ratio	Applied Pressure Difference (bar)
50	1	8	8	-	59.5
75	2	6	12	3:2	Stage 1: 56.6 Stage 2: 99.7

Table 4.3: Process conditions used to simulate pressure drop and SEC at 50% and 75% product recoveries for the optimal configurations selected for comparison of SEC with FO.

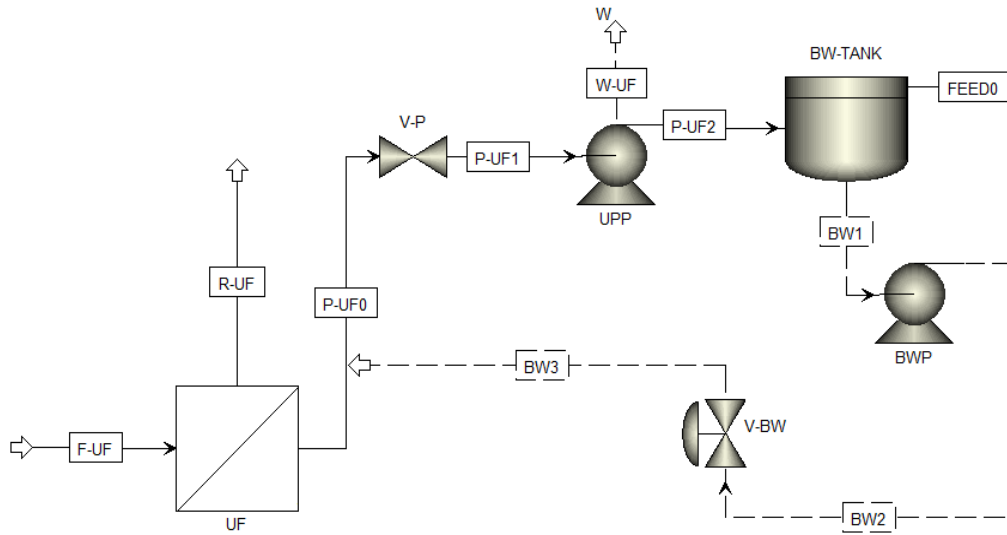


Figure 4.5 (A): ASPEN process flowsheet representation of membrane pretreatment with UF

OPTION 1

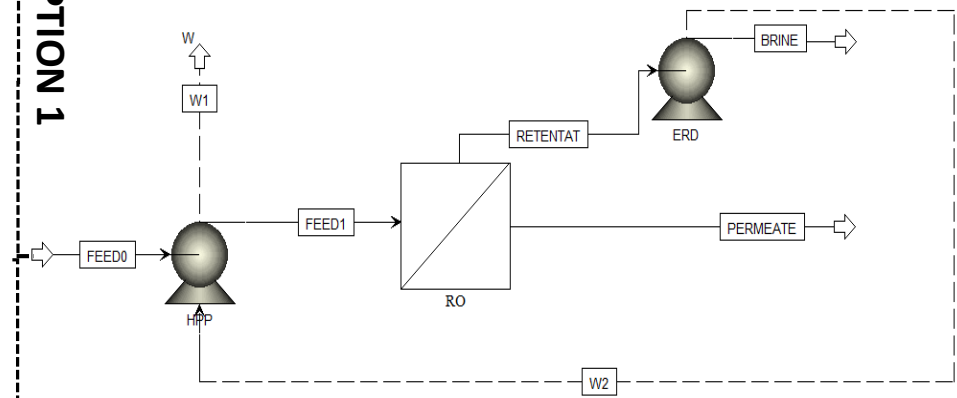


Figure 4.5 (B): ASPEN process flowsheet for single-stage RO with ERD used for process simulations with 50% product recovery

OPTION 2

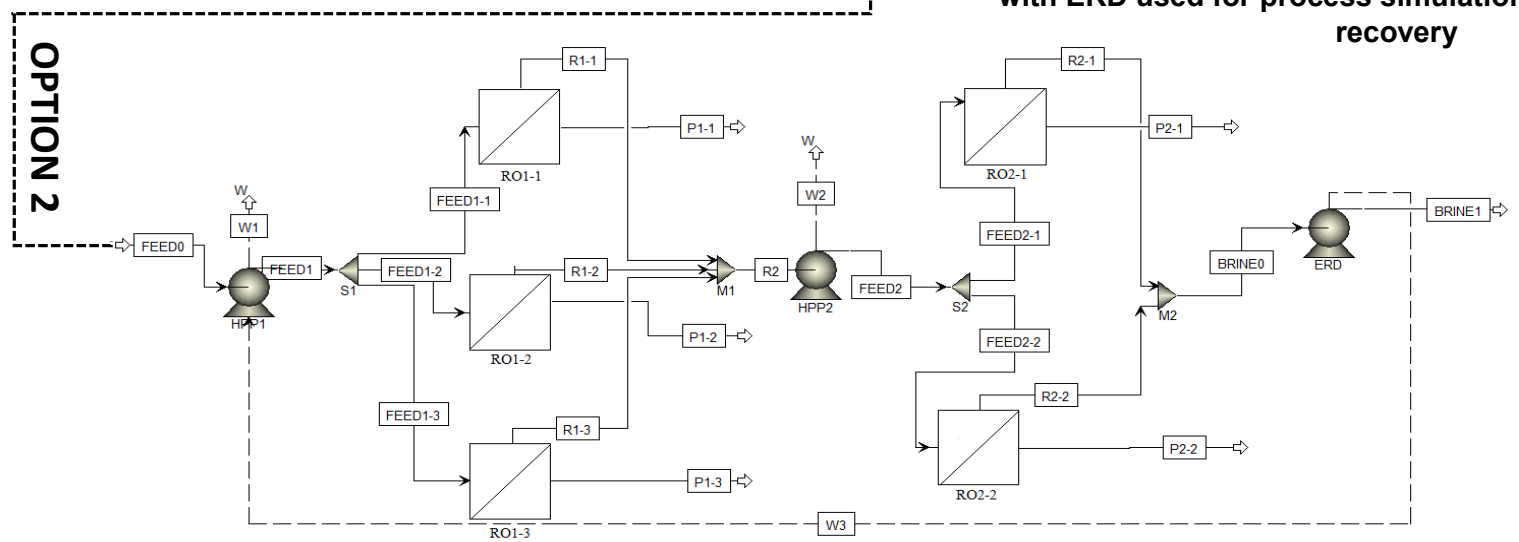


Figure 4.5 (C): ASPEN process flowsheet for two-stage RO with ERD and array ratio=3:2 used for process simulations with 50% and 75% product recovery

4.3.3 Energy Consumption for SWRO

The ASPEN process flowsheet for single-stage RO with UF pretreatment is shown in Figure 4.5 (A) and (B). Based on this configuration and model equations presented in Appendix A 1, simulation results obtained for the SWRO process are summarised in Table 4.4.

Data in Table 4.4 show that the mass transfer coefficient and pump efficiencies affect the total energy consumed by the system. Energy consumption increases as mass transfer coefficient decreases (which can be offset by increasing the effective membrane area), and concentration polarisation (CP) effects become more prominent. Membrane area is represented as the specific membrane area i.e. the membrane area required per $\text{m}^3 \cdot \text{h}^{-1}$ of permeate produced.

The effect of mass transfer coefficient (k) on SEC and product recovery at 100% pump and ERD efficiencies is shown in Figure 4.6 (A). The mass transfer coefficient was varied between 1×10^{-6} - $100 \text{ m} \cdot \text{s}^{-1}$. It was observed that a decrease in mass transfer coefficient decreased product recovery due to an increase in concentration polarisation effects and consequently caused an increase in SEC. At a product recovery of 50%, the effect of mass transfer coefficient on SEC and specific membrane area required can be seen in Figure 4.6 (B). An increase in mass transfer coefficient minimises the SEC until a limiting value of $k = 1.0 \times 10^{-4} \text{ m} \cdot \text{s}^{-1}$ is reached, after which concentration polarisation effects become almost negligible. Improvement in SEC by up to 8% is possible with an increase in k from current values typical of state-of-the-art SWRO modules. Similarly, an increase in k at constant SEC decreases the membrane area required until a limiting value of $k = 1.0 \times 10^{-4} \text{ m} \cdot \text{s}^{-1}$ is approached, whereby membrane permeance or thermodynamic effects become limiting. Current SWRO modules are already operating within this limiting area, which suggests that further increase in k can only improve the SEC further and will not have a significant effect on the membrane area.

An increase in pump and energy recovery efficiencies decreases the energy consumption of the system. The selection of HPP and ERD efficiencies in Table 4.4 was based on common values found in industrial data. For HPP used in SWRO, efficiencies can range from 30% to 90% [177] depending on the type of pump used. In Table 4.4, HPP efficiencies of 50% and 90% were chosen for comparison. ERD used for SWRO have efficiencies up to 98% [178]. Here, 90% efficiency was selected as the base case, and 100% was chosen for comparison with the base case.

The theoretical thermodynamic minimum energy (i.e. the separation energy equal in magnitude but opposite in sign to the free energy of mixing) for desalination at a recovery of 50% is 1.06 kWh m⁻³ [23]. The practical minimum energy for desalination (i.e. when $\Delta P \approx \Delta\pi_{exit}$) as predicted by the model at 100% pump and energy recovery efficiencies (excluding pressure drop and CP effects) is 1.37 kWh m⁻³. This difference is expected because the system is finite and is not operating as a reversible thermodynamic process. This practical minimum energy for desalination calculated by the model is not far behind the calculated value presented by Elimelech et al. of 1.56 kWh.m⁻³ for 50% recovery of 35 g.L⁻¹ NaCl solution at 25°C and 100% NaCl rejection [23].

Entry	Mass transfer coefficient, k (m.s ⁻¹)	η HPP (%)	η ERD (%)	Specific membrane area required [m ² (m ³ .h ⁻¹) ⁻¹]	HPP work without ERD (kW)	Net work with ERD (kW)	SEC with ERD (kWh.m ⁻³)
1.	4E-05	50	90	59.14	42.5	33.6	5.3
2.	$+\infty$	50	90	43.57	42.5	33.6	5.3
3.	$+\infty$	90	90	43.57	23.6	14.8	2.3
4.	$+\infty$	50	100	43.57	42.5	32.6	5.1
5.	$+\infty$	90	100	43.57	23.6	13.8	2.2

Table 4.4: Summary of process calculations for SWRO at a water recovery of 50%, membrane rejection of 100%, $Q_F=12.85$ m³ h⁻¹, $\Delta P=59.5$ bar, $L_p = 3.5 \times 10^{-12}$ m³ m⁻² Pa⁻¹ s⁻¹.

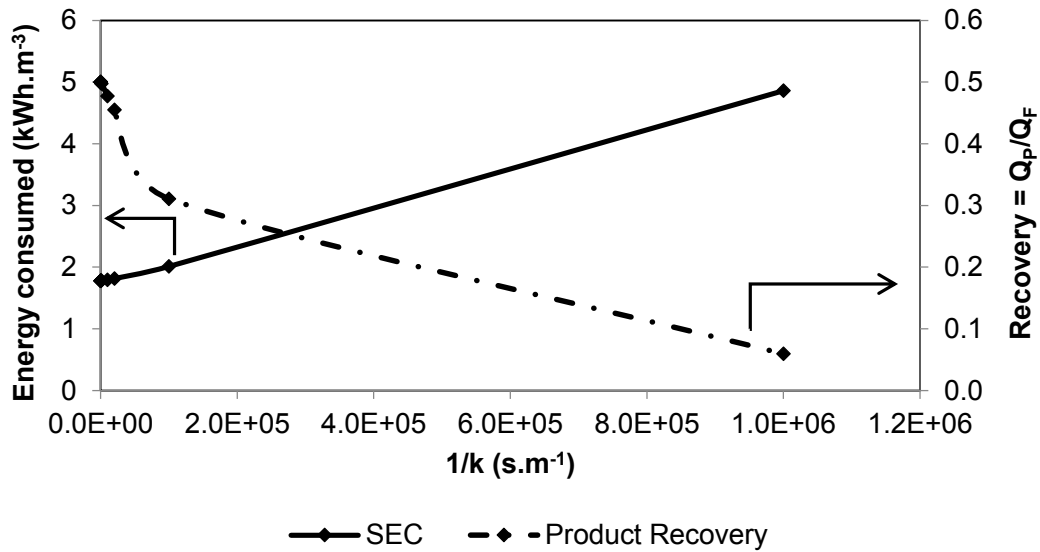


Figure 4.6 (A): Effect of mass transfer coefficient on SEC and product recovery of a single-stage SWRO at 100% pump and ERD efficiencies. $L_p=3.5 \times 10^{-12} \text{ m}^3 \cdot \text{m}^{-2} \cdot \text{Pa}^{-1} \cdot \text{s}^{-1}$ and $\Delta P=59.5 \text{ bar}$.

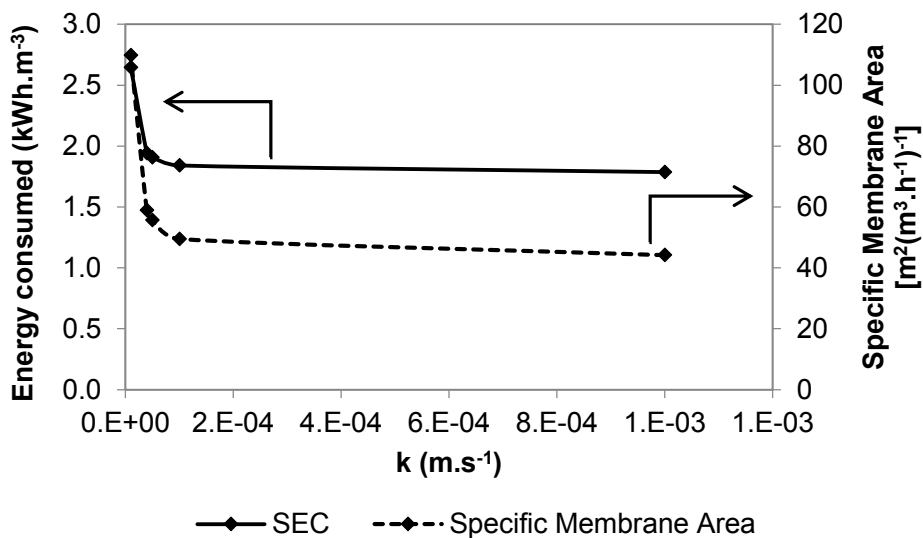


Figure 4.6 (B): Change in SEC with increasing mass transfer coefficient in a single-stage RO at 50% recovery, 100% pump and ERD efficiencies, and a specific membrane area of $44 \text{ m}^2 \cdot (\text{m}^3 \cdot \text{h}^{-1})^{-1}$. The SEC gradually decreased from $2.65 \text{ kWh} \cdot \text{m}^{-3}$ to $1.78 \text{ kWh} \cdot \text{m}^{-3}$. At $\text{SEC}=1.78 \text{ kWh} \cdot \text{m}^{-3}$ and $\text{product recovery}=50\%$, specific membrane area required is plotted as a function of mass transfer coefficient. Membrane permeance was held constant at $L_p=3.5 \times 10^{-12} \text{ m}^3 \cdot \text{m}^{-2} \cdot \text{Pa}^{-1} \cdot \text{s}^{-1}$.

Figure 4.7 shows the specific energy consumed versus product recovery calculated with and without an energy recovery device. For the single-stage RO, the theoretical global minimum for energy consumption occurs at a fractional recovery of 50%, as previously claimed in literature [142]. The specific energy consumption (SEC) of the pump was calculated as follows:

$$SEC_{pump} = \frac{\dot{W}_{pump}}{Q_P} = \frac{Q_F \cdot \Delta P}{Q_P}$$

Equation 4.6

At lower recoveries, a higher SEC was required to pressurise the feed to a pressure equal to the osmotic pressure at the exit of the module. This is due to the dominating effect of axial pressure drop as a function of higher velocities in the retentate stream (Figure 4.8). Higher pretreatment energy consumption due to increased feed flowrates at lower recoveries also contributes to this effect. With increasing product recovery, the SEC decreased due to the effect of decreasing pressure drop and pretreatment energy contribution per unit volume of permeate. However, above a certain recovery (e.g. 35% recovery in Figure 4.8), the effects of transmembrane work done by the system began to dominate. A higher increase in ΔP was required to overcome the increasing osmotic pressure, resulting in an increasing SEC with higher recoveries. At a recovery below 50%, the SEC increases despite the use of an ERD. This is because the effects of pressure drop in the system dominate over energy recovery of the retentate.

At product recoveries below 50% (Figure 4.7), it is clear that the two-stage RO consumes more energy than the single-stage RO, because it has a higher axial pressure drop. The higher axial pressure drop is caused by the higher retentate flowrate entering the second stage and an overall greater number of elements in series compared to the single-stage RO. This leads

to an increased SEC, despite energy savings made due to smaller volumes of water being brought to higher pressures.

Above 50% product recovery, the effects of pressure drop are less significant despite increasing retentate concentration and viscosity, due to the lower retentate flowrate entering the second stage. This results in higher energy savings for the two-stage RO compared to the single-stage RO at product recoveries above 50%.

Figure 4.9 shows the specific energy consumption (SEC) of a single-stage RO as the thermodynamic limit ($\Delta P = \Delta\pi_{exit}$) was approached with increasing membrane permeance at 50% recovery, mass transfer coefficient, $k=4\times 10^{-5} \text{ m}\cdot\text{s}^{-1}$, 100% pump and ERD efficiencies. The pressure difference between ΔP and $\Delta\pi_{exit}$ is due to frictional losses. It was observed that increasing the membrane permeance from the value typical of state-of-the-art SWRO membranes can improve the SEC by 18%. A recently published paper by Cohen-Tanugi et al. [179] reported a 15% reduction in SEC when the permeance was tripled. Our simulation agrees well with this value; however it was found that by increasing permeance further i.e. by eight times the current RO permeance, only 18% reduction in the SEC is achievable, after which further increases in permeance did not significantly reduce the SEC of the system.

In a postulated nanoporous graphene membrane simulated by Cohen-Tanugi et al. [180] the best performing pore exhibited full salt rejection and a membrane water permeance of $7.6\times 10^{-9} \text{ m}^3\cdot\text{m}^{-2}\cdot\text{Pa}^{-1}\cdot\text{s}^{-1}$ ($2750 \text{ L}\cdot\text{m}^{-2}\cdot\text{h}^{-1}\cdot\text{bar}^{-1}$). However, our simulation suggests that there is a limiting permeance of $2.7\times 10^{-11} \text{ m}^3\cdot\text{m}^{-2}\cdot\text{Pa}^{-1}\cdot\text{s}^{-1}$ ($10 \text{ L}\cdot\text{m}^{-2}\cdot\text{h}^{-1}\cdot\text{bar}^{-1}$) near the thermodynamic limit, beyond which the economic incentive for using more permeable membranes is low (i.e. almost negligible) and will decrease with increasing water recovery [181]. However, at conditions near the thermodynamic limit, the use of a more permeable membrane can reduce the amount of membrane area required to achieve the same product recovery (Figure 4.9). The system is however limited by concentration polarisation effects which become more limiting at higher

permeances due to the increase in permeate flux. As a result, a limiting permeance is observed, beyond which the effects of increasing permeance on membrane area become insignificant. Additionally, operation at higher fluxes would increase concern over fouling and hence the need for more fouling resistant membranes. Contrary to the findings of Cohen-Tanugi et al. [180] using molecular dynamic simulation, whereby computational results suggest that enhanced water permeance of functionalised nanoporous graphene would enable lower energy requirements and lower membrane area requirements, the findings in this chapter show that the benefits of increasing membrane permeance are limited by the thermodynamic limit and concentration polarisation effects. These findings correspond well to a recent publication by Cohen-Tanugi et al. [179] studying the potential of ultra-permeable membranes in SWRO and brackish water RO.

Data presented for the single-stage RO so far were based on flowrates and process conditions for an SWRO configuration with 8 elements per pressure vessel. In order to scale-up the basic process unit to emulate a medium sized industrial scale process producing $666 \text{ m}^3 \cdot \text{h}^{-1}$ ($16\,000 \text{ m}^3 \cdot \text{d}^{-1}$) of permeate, 104 parallel units are required with a specific membrane area of $A_{m,s} = 43.57 \text{ [m}^2(\text{m}^3 \cdot \text{h}^{-1})^{-1}]$ (Figure A-4 of Appendix A 7).

The ASPEN process flowsheet for the two-stage RO with UF pretreatment is shown in Figure 4.5 (A) and Figure 4.5 (C). The process model results for a two-stage RO with and without an ERD are shown in Figure 4.7. It can be seen that the specific energy consumed (SEC) was lower for two-stage RO compared to single-stage RO at product recoveries $\geq 50\%$. If an infinite number of stages were adopted, this would result in a reversible thermodynamic process with minimum energy consumption for desalination. However, in reality, this system is impractical if the capital costs required are not offset by the energy savings made. A cost analysis of the two-stage RO compared to the single-stage RO is presented in Figure 4.10. The method of calculation used to obtain the overall cost savings for the two-stage RO relative to the single-stage is shown in Appendix A 4. The dimensionless membrane price, m_{norm} was

calculated for seawater desalination based on a study performed by Zhu et al. [142] and details on its derivation are explained in Appendix A 4. Figure 4.10 shows that a 2-stage RO process is more cost effective (overall cost savings > 0) than a single-stage RO process when the total water recovery is greater than 50%, even with the additional membrane cost required for the 2-stage RO. Hence, a higher overall percentage recovery is favoured for a 2-stage RO in order to maximise the overall cost savings for the system.

The two-stage RO unit with a 3:2 array ratio and 6 elements per pressure vessel can be scaled up to emulate a medium sized industrial process producing $666 \text{ m}^3 \cdot \text{h}^{-1}$ ($16\,000 \text{ m}^3 \cdot \text{d}^{-1}$) of permeate, requiring 35 parallel units with a specific membrane area of $A_{m,s} = 54.47 \text{ [m}^2(\text{m}^3 \cdot \text{h}^{-1})^{-1}]$ (Figure A-5 of Appendix A 7).

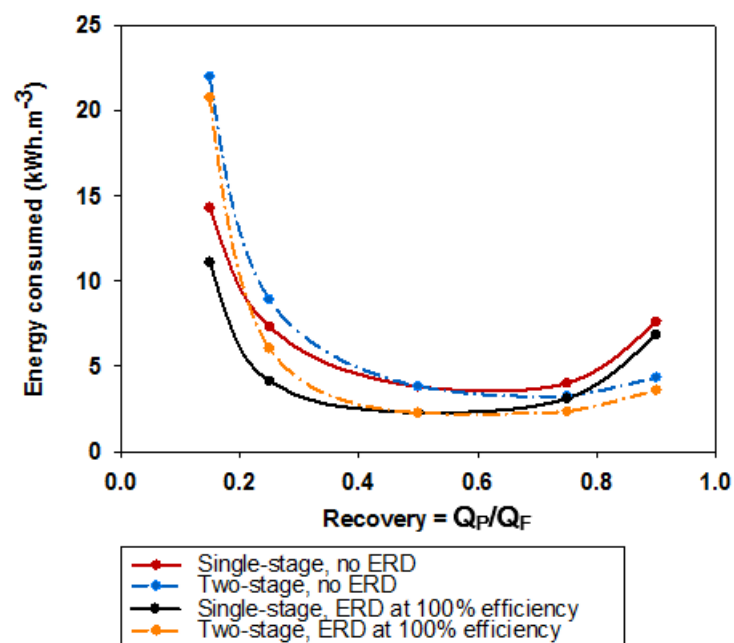


Figure 4.7: Specific energy consumed versus product recovery for single-stage and two-stage RO with and without an ERD calculated at HPP efficiency=100% and $k=+\infty \text{ m} \cdot \text{s}^{-1}$. Pretreatment energy and effects of pressure drop included.

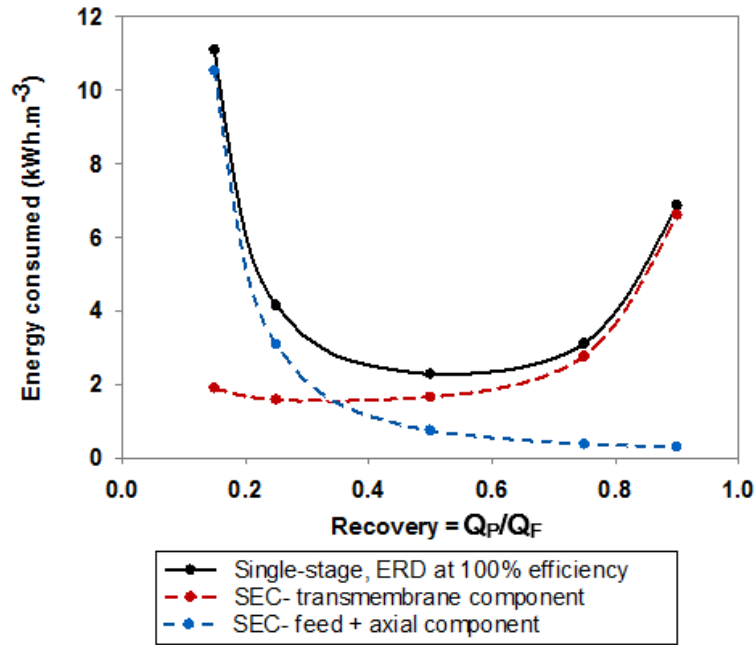


Figure 4.8: Contribution of pretreated feed, axial and transmembrane pressure components on SEC in a single-stage RO with ERD efficiency=100%.

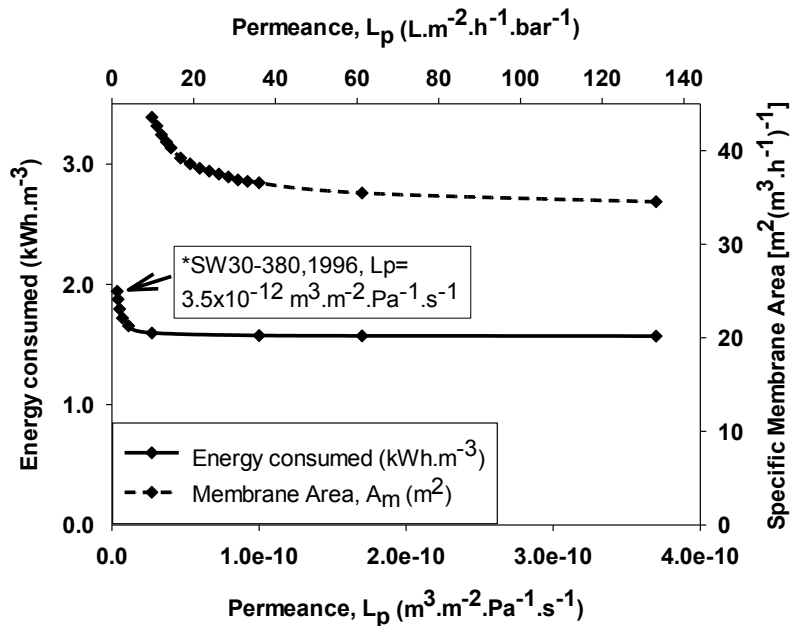


Figure 4.9: Change in SEC with increasing membrane permeance as the thermodynamic limit is approached in a single-stage RO at 50% recovery and 100% pump and ERD efficiencies. ΔP was gradually decreased from 65 bar to 53 bar (i.e. near thermodynamic limit, whereby $\Delta P=53$ bar and $\Delta\pi_{\text{retentate,exit}}=49$ bar). At $\Delta P=53$ bar and

product recovery=50%, the specific membrane area required is plotted as a function of permeance with $k=4 \times 10^{-5} \text{ m.s}^{-1}$.

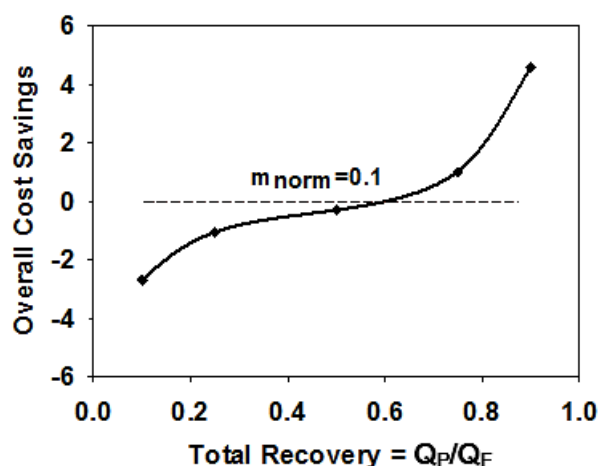


Figure 4.10: Overall cost savings for a 2-stage RO relative to a single-stage RO, considering both energy and membrane costs.

4.3.4 Energy Consumption for FO Desalination

The ASPEN process flowsheet for FO desalination followed by NF for recovery of draw solution is shown in Figure 4.11. The process configurations for the FO process with single-stage and two-stage NF recovery, are shown in Figure 4.12 (A) and Figure 4.12 (B), respectively. The inlet and outlet pressures for the FO system based on HTI's module design specifications are shown in Figure 4.11. The mass transfer coefficients in FO are not yet widely available in the literature. Values were estimated based on reported data for HTI membranes [92, 95, 169] i.e. $k=2 \times 10^{-5} \text{ m.s}^{-1}$ and $K=1.1 \times 10^6 \text{ s.m}^{-1}$, whereby K is the solute resistivity for diffusion within the porous support layer.

Permeate flux in the FO stage is driven by osmotic pressure difference between the feed and draw solutions. Hydraulic pressure is not required in the FO stage other than for recirculation of the feed and draw solutions. The specific energy consumption required for recirculation of

feed and draw solutions in the FO stage was calculated for the recirculation pumps using Equation 4.6 described in Section 4.3.3. A “perfect” membrane for FO can be defined as one with infinite permeance, negligible internal concentration polarisation and 100% rejection. At a fixed value for external mass transfer coefficient and solute resistivity for diffusion within the porous support layer of the HTI CTA membrane, the use of a more permeable membrane in FO would reduce the required membrane area for the same target product recovery as shown in Figure 4.13 (A). However, this decrease in area becomes limited by concentration polarisation effects, which become more limiting at high permeances. It can be seen that for the currently available HTI CTA membrane, a further increase in membrane permeance has negligible effect on membrane area reduction given that it is already operating under conditions whereby concentration polarisation effects are rate limiting. Hence, further savings in membrane area can only be achieved if the unwanted effects of ICP can be reduced or eliminated. This is shown in Figure 4.13 (B), whereby keeping the membrane permeance and external mass transfer coefficient constant, a decrease in solute resistivity for diffusion within the porous support layer decreases the required membrane area by 90% until a minimum value is achieved at negligible ICP effects.

It was observed that currently available NF membranes such as the Dow FilmTec NF90-400 are already operating near the thermodynamic limit (Figure 4.13 (C)) and a further increase in membrane permeance has negligible effect on the SEC. The effects of increasing permeance on membrane area are also negligible given that the NF membrane is already operating under conditions in which concentration polarisation effects are rate limiting.

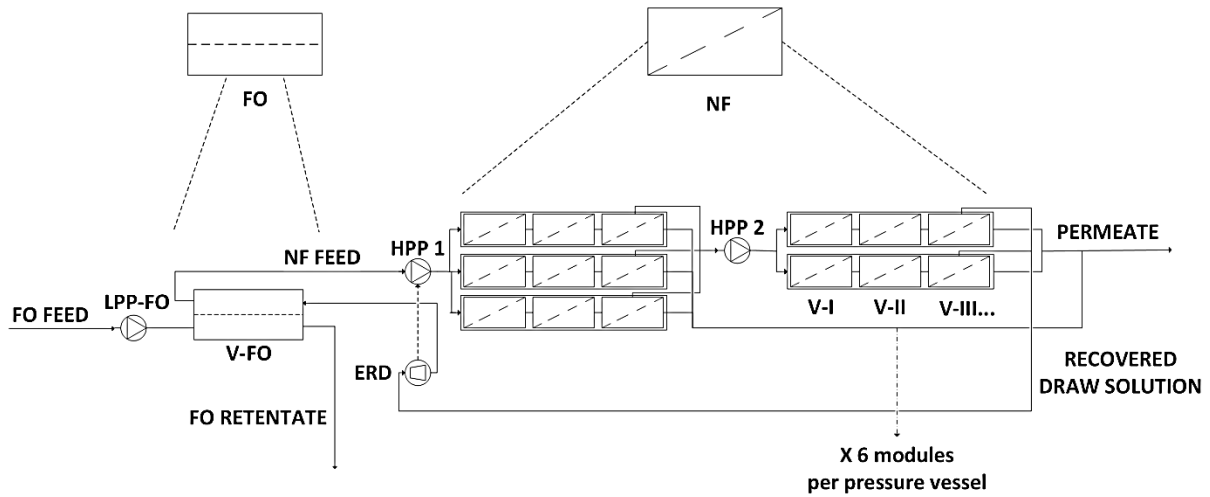


Figure 4.12 (B): Process configuration for FO with two-stage NF recovery. This configuration was considered for calculation of SEC at 50% and 75% product recovery for comparison with SWRO.

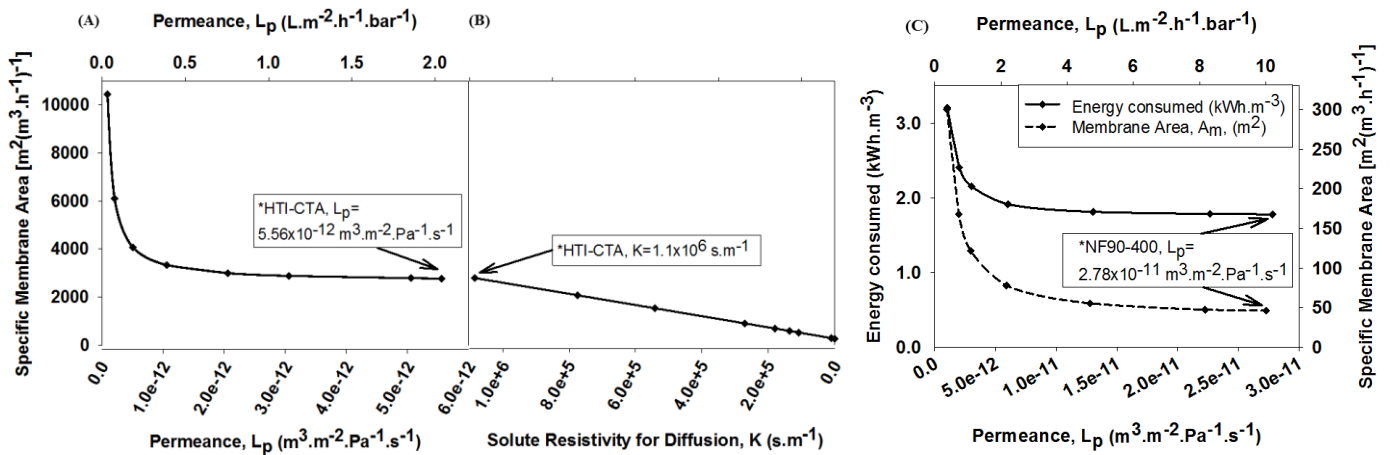


Figure 4.13: Effect of increasing membrane permeance and decreasing solute resistivity for diffusion within the FO membrane support layer, on specific membrane area and SEC in an FO with single-stage NF recovery process at 50% product recovery.

(A): FO stage- Effect of increasing membrane permeance on specific membrane area required at 50% recovery, $k=2 \times 10^{-5} m \cdot s^{-1}$ and $K=1.1 \times 10^6 s \cdot m^{-1}$.

- (B): FO stage- Effect of decreasing solute resistivity for diffusion within the support layer on specific membrane area required at 50% recovery, $k=2 \times 10^{-5} \text{ m.s}^{-1}$ and $L_p=5.56 \times 10^{-12} \text{ m}^3 \text{ m}^{-2} \text{ Pa}^{-1} \text{ s}^{-1}$.
- (C): NF stage- Change in SEC with increasing membrane permeance as thermodynamic limit is approached in a single-stage NF at 50% recovery and 100% pump and ERD efficiencies. At a fixed pressure, $\Delta P = 58 \text{ bar}$ (corresponding to pressure near the thermodynamic limit), $L_p=2.78 \times 10^{-11} \text{ m}^3 \text{ m}^{-2} \text{ Pa}^{-1} \text{ s}^{-1}$ and recovery=50%, specific membrane area required is plotted as function of permeance with $k=4 \times 10^{-5} \text{ m.s}^{-1}$.

4.3.5 Comparison of Energy Consumption between FO and RO Desalination

Figure 4.14 shows a comparison of SEC and specific membrane area between a single-stage RO, FO with NF recovery, FO with two-stage NF recovery, two-stage RO, FO-UF and FO-Distillation at 50% and 75% product recovery. The effects of pretreatment are taken into account in the energy comparison. The applied pressure, feed and draw solution concentrations used in the various processes shown in Figure 4.14, are presented in Table 4.6. It should be noted that the membrane areas calculated for the FO stage in Figure 4.14 are estimated based on an approximation for the osmotic pressure difference across the membrane using a log mean approach described in Appendix A 3. The energy consumption results obtained for SWRO are consistent with those reported in literature [23]. The energy consumption for the FO stage itself is very low i.e. 0.11 kWh m^{-3} at 50% recovery and 0.07 kWh m^{-3} at 75% recovery, because the process is driven by osmotic pressure instead of hydraulic pressure difference and the low pressure pump (LPP) used for recirculation only needs to overcome the pressure drop in the feed channel. At 50% product recovery, it can be concluded that there is no significant difference in SEC between the FO with NF recovery process and RO. Despite the similarity in SEC, it should be noted that the FO with NF recovery and FO with two-stage NF recovery processes require higher specific membrane areas

compared to RO, and this needs to be factored in when performing an overall cost comparison between FO and RO.

At 75% product recovery, there is effectively no difference in SEC between the FO with two-stage NF recovery process compared to a two-stage RO. The FO with CO₂-NH₃ DS recovery process utilising distillation had the lowest SEC compared to all other processes, albeit issues arise with purity of the product water. Key potential advantages of this process include high product recovery (e.g. 75%) at relatively low energy requirements and cost, and brine discharge minimisation. This illustrates that FO hybrid systems can provide energy cost savings for treatment of high salinity feeds if a low-cost thermal energy process is considered for the DS recovery stage [1]. The treatment of high salinity feeds is another advantage of the FO process which cannot be achieved in RO due to the limitation of maximum hydraulic pressure in RO modules.

The primary energy input for the CO₂-NH₃ recovery process is for the thermal separation of ammonia and carbon dioxide from the dilute draw solution exiting the FO membrane system. A small amount of electrical energy was used for fluid pumping. The process model and data used for this process was developed by McGinnis et al. using chemical process modelling software (HYSYS, Cambridge, MA) coupled to an electrolyte property package (OLI, Morris Plains, NJ) [39]. Process conditions include 0.5 M NaCl as the feed solution, 5 M ammonium salts (on a CO₂ basis) with a ratio of ammonia to CO₂ of 1.4 as the concentrated draw solution, 1.5 M diluted draw solution as feed to the distillation column, FO operating temperature of 25°C, reboiler steam temperature of 40°C, product recovery of 75%. Details on the specifications of the distillation column can be found in McGinnis et al. [39]. A single vacuum distillation column with steam as the heat source for the reboiler gave optimal results for energy consumption. Outputs from this modelling study include the heat duty of the distillation column, and power required by the pumps, which are expressed in terms of specific equivalent work, W_{eq} (Table 4.5). Details of the calculation of W_{eq} are presented in McGinnis et al. [39].

The FO with CO₂-NH₃ DS recovery energy data for a single vacuum distillation column is presented in Table 4.5. It should be noted that all data used in the present work was calculated using the in-house ASPEN model except for the data for FO with CO₂-NH₃ DS recovery process, for which data was adopted from McGinnis et al. [39].

Min steam temp. (°C)	Draw solution conc. (M)	Min steam press. (bar)	Column press. (bar)	Number of stages	Heat duty (MJ.m ⁻³)	Elec. duty (kWh.m ⁻³)	Gained output ratio (GOR)	Equivalent work, W _{eq} (kWh.m ⁻³)	Specific energy consumption (kWh.m ⁻³)
40	1.5	0.07	0.07	1	541.55	0.24	4.4	0.84	1.2

Table 4.5: FO with CO₂-NH₃ DS recovery energy data for a single vacuum distillation column. [Adapted from McGinnis et al. [39]].

The total SEC for this process assuming UF pretreatment prior to the FO stage was 1.2 kWh.m⁻³ (Figure 4.14). This was much lower than the SEC of RO and FO with NF recovery, albeit issues arise with purity of the product water. According to the World Health Organisation (WHO) guidelines for drinking water quality [182], the presence of ammonia above 0.2 mg.L⁻¹ in water will result in taste and odour problems, and lead to decreased disinfection efficiency by chlorine, as up to 68% of chlorine may react with the ammonia making it unavailable for disinfection. Based on literature [39], product water from the NH₃-CO₂ process may be specified to contain < 1 mg.L⁻¹ NH₃, however this would still be above the allowable limit of 0.2 mg.L⁻¹. The use of waste heat if available, instead of steam may reduce the energy cost of this process further.

Another potential DS is super hydrophilic nanoparticles (NPs) which it is claimed can be recovered efficiently using a 1kiloDalton UF membrane. It is assumed that recovery with UF will consume considerably less energy in terms of the transmembrane pressures applied compared to RO for DS regeneration [118]. However, the literature lacks actual data on this. A rough calculation of the energy consumption for the FO-UF process illustrated in Appendix A 5 shows that the energy consumed with an ERD at 75% product recovery was 3.2 kWh.m⁻³

assuming UF pretreatment prior to the FO stage. This value is similar to the FO with NF recovery process and significantly higher than the CO₂-NH₃ recovery process (Figure 4.14). The energy consumption for FO-UF is also likely to be very similar to a standalone RO and FO-RO process [1]. The reason UF and NF DS recovery systems do not save more energy than RO despite being typically low-pressure processes compared to RO, lies in the limitation posed by the osmotic pressure required in the FO stage at a specific product recovery. The osmotic pressure of the draw solution required in the FO stage to achieve a specific product recovery, must equal the osmotic pressure of the UF or NF brine in the DS recovery stage, i.e. $\pi_{(UF/NF,Brine)} = \pi_{(FO,Draw)}$. Hence, the hydraulic pressure required to produce $\pi_{(UF/NF,Brine)}$ will be similar to that required for a standalone RO process at the same product recovery. This negates the low-pressure benefits of such systems that would otherwise be attainable in a process whereby osmotic pressure was not limiting and separation was merely based on a sieving mechanism. This analysis can be applied to any pressure-driven membrane process used for the DS recovery stage and corresponds well to the recent findings of Shaffer et al. [1]. Modelling energy consumption for the NP recovery stage in ASPEN is challenging as the compounds present, along with their physical and thermo properties, do not exist in the ASPEN databank. A remaining challenge with the FO-UF process is the agglomeration of NPs during draw solution regeneration, which reduces permeate flux over time.

A further method which has been proposed for the recovery of draw solution is to use hydrophilic magnetic nanoparticles (MNPs) as a solute and recover them using a magnetic separator generating a magnetic field. At present, there is only one paper by Ge et al. [121] providing data on the power needed for MNP recovery by a magnetic field. This paper mentions the recovery of 50 mL of a magnetic nanoparticle solution in 30 min using a magnetic separator at a power of 187 W. The trapped MNPs were washed away by deionised water after turning off the electromagnet and recycled for use in a fresh draw solution. A simple calculation illustrated in Appendix A 6 shows that an exorbitant amount of energy, i.e. 1870 kWh m⁻³, was used for the recovery of the MNPs. However, the magnetic separator was not

specially designed for the study and only a very small fraction of this energy was consumed for the separation of MNPs [121]. The exact fraction of energy consumed cannot be quantified due to the lack of data available in literature at the moment. Hence, the recovery of MNPs with a magnetic separator was not used for comparison in this work but is a potential area for future research.

There is effectively no difference in SEC between the single and two-stage FO with NF recovery process and RO at 50% and 75% product recovery. Hence, the main benefit, if one exists, of the FO with NF recovery process could lie in the reduced fouling propensity of FO [1-7] which may reduce or eliminate the need for pretreatment and chemical cleaning, thus reducing costs.

Although 75% product recovery may not be practically feasible due to the pressure limitations of current RO and NF modules, these simulations were performed for purposes of comparison with the FO-Distillation process for which only data at 75% recovery was available in literature.

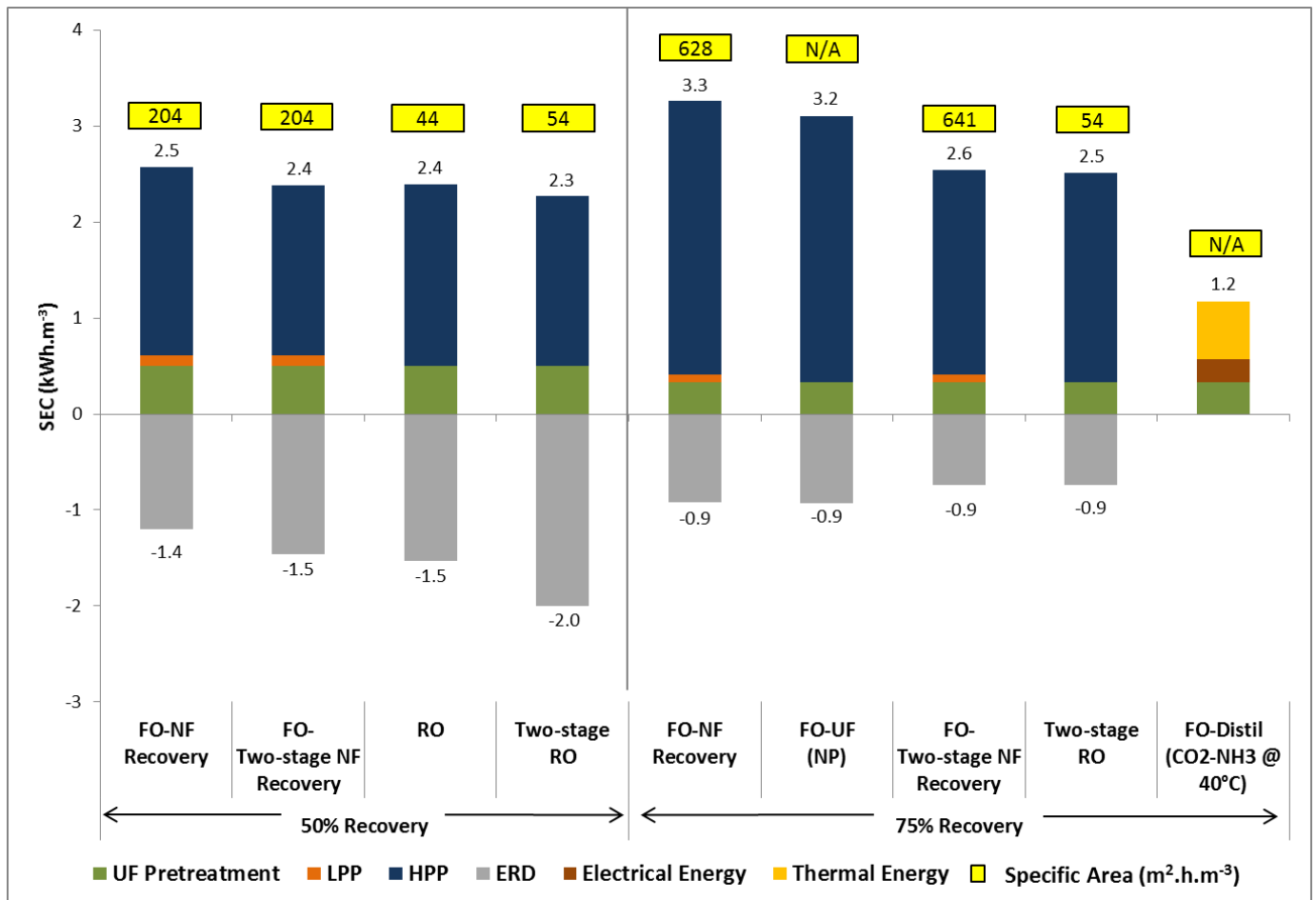


Figure 4.14: Comparison of SEC and specific membrane area between FO with NF recovery, FO with two-stage NF recovery, single-stage RO, two-stage RO, FO-UF, and FO-Distillation at 50% and 75% product recovery. Energy contributions from the pretreatment stage, LPP, HPP, ERD and distillation are shown in each process.

Process conditions	50% Rec								75% Rec								
	Single stage FO-NF		Single stage RO	FO- Two-stage NF			Two-stage RO		Single stage FO-NF		Single stage FO-UF		FO- Two-stage NF			Two-stage RO	
	FO	NF	RO	FO	NF-I	NF-II	RO-I	RO-II	FO	NF	FO	UF	FO	NF-I	NF-II	RO-I	RO-II
Applied pressure (bar)	2.0	58.0	59.5	2.0	41.7	58.7	46.8	60.8	2.0	101.0	2.0	100.0	2.0	51.2	100.5	56.6	99.7
Feed concentration (g.L ⁻¹)	35.0	105.5	35.0	35.0	108.1	152.4	35.0	49.6	35.0	100.2	35.0	N/A	35.0	100.2	220.6	35.0	49.6
Draw concentration (g.L ⁻¹)	218.3	N/A	N/A	216.2	N/A	N/A	N/A	N/A	400.8	N/A	N/A	N/A	400.5	N/A	N/A	N/A	N/A

* Applied pressure in FO stage is for circulation of feed. Feed concentration in NF draw solution recovery stage refers to MgSO₄. Feed concentration in UF DS recovery stage refers to magnetic nanoparticles (MNP). All other feed concentrations refer to NaCl. Draw concentration refers to MgSO₄ in the NF stage.

Table 4.6: Process conditions (applied pressure, feed and draw solution concentrations) used in the comparison of SEC for various RO and FO hybrid desalination processes.

4.3.6 Model Sensitivity

As with most model-based assessments, the results reported in this chapter are subject to the constraints imposed by the modelling assumptions and parameter values used in the models for RO, FO and NF. In the models used, specific values for the external mass transfer coefficient, k , solute resistivity to diffusion within the support layer, K , and membrane permeance, L_p , were selected based on the available manufacturer's and laboratory data for the modules and conditions studied. The effect of varying these parameters on the model outputs (i.e. SEC and membrane area) were explored in Figure 4.6, Figure 4.9, Figure 4.13 and Table 4.4 of this chapter, and their results discussed in Sections 4.3.3 and 4.3.4.

The external mass transfer coefficients may vary slightly if different module types and configurations were used due to differences in hydrodynamic conditions. Small variations in the mass transfer coefficients may also occur as a function of fluid properties, local feed velocities and module geometry. However, these variations are unlikely to have a significant effect on the SEC of the process from a thermodynamic perspective, whereby for SWRO, a conservative variation by a factor of two will affect the SEC by $\leq \pm 5\%$ and for NF, the same variation will affect the SEC by $\leq \pm 3\%$.

Improvements in membrane permeance from current values has an effect on energy consumption of the SWRO process, whereby an increase in permeance by a factor of eight yields a maximum variation (or reduction) in SEC by 18% before the thermodynamic limit is approached. Variation in membrane permeance from present values has a negligible effect on the SEC and membrane area requirements of the FO-NF process, as these processes are already operating under conditions where concentration polarisation and thermodynamic effects are limiting. However, the use of FO membranes with lower solute resistivity to diffusion within the porous support layer, K , can reduce membrane area requirements further. A total reduction by up to 90% is possible if internal concentration polarisation was completely eliminated (i.e. $K = 0 \text{ s.m}^{-1}$).

4.4 Conclusions

A customized simulation tool was used to estimate the SEC for RO and FO desalination by considering the effect of different process variables and a UF pretreatment step. Using a CAPE-OPEN interface standard for running Matlab scripts in ASPEN, this modelling approach provided a flexible tool for quantifying the energy consumption of desalination by simulating real process conditions.

It was concluded that there is effectively no difference in SEC between the FO with NF recovery and RO processes. Furthermore, it has been shown that even if any of the membranes, FO, RO or NF had infinite permeabilities and 100% rejection, it would not change the SEC significantly. Based on these simulations alone, FO with NF recovery cannot be considered to be competitive with RO taking into account the additional capital costs needed, unless other advantages of the process can be capitalised on. One such advantage is the apparently lower fouling propensity of FO [1-7] which may reduce or eliminate the need for pretreatment and chemical cleaning, thus reducing costs. In order to investigate if this phenomenon can be exploited, the mechanism and extent of fouling in FO compared to RO needs to be further studied and understood.

The FO-Distillation process with $\text{CO}_2\text{-NH}_3$ draw solution exhibited the lowest SEC compared to other FO and RO desalination processes. However, concerns over residual NH_3 being above the allowable limit in the product water is a challenge which remains to be resolved.

At 75% recovery, the single-stage FO-UF process with NPs as the draw solution is estimated to have a similar SEC to the FO with single-stage NF process. A two-stage UF for the nanoparticle recovery therefore may result in similar SEC as the two-stage RO and FO with two-stage NF recovery processes, albeit increasing capital costs. The lack of data in the literature makes it challenging to model the SEC for this process at varying product recoveries

and process conditions. Hence, more research is required in this area to increase the availability of data before accurate comparisons can be made with other desalination processes.

In general, it was observed that despite the type of draw solution and pressure-driven recovery method used, there is effectively no difference in energy consumption of different hybrid FO processes and the standalone RO process. This is because, the requirement for $\pi_{\text{DS Recovery, Brine}} = \pi_{\text{FO, Draw}}$ negates the benefit of using draw solutes which can be recovered by low pressure processes. This analysis can be generalised for any pressure-driven membrane process used for the DS recovery stage, although there are still opportunities for hybrid FO processes to provide energy cost savings by leveraging on low-cost thermal energy DS recovery methods such as the FO-Distillation process for recovering the $\text{CO}_2\text{-NH}_3$ DS.

Chapter 5

5 Organic Fouling Behaviour of Structurally and Chemically Different Forward Osmosis Membranes- A study of Cellulose Triacetate and Thin Film Composite Membranes¹

5.1 Introduction

Despite opinion on the low energy benefits of FO, recent studies have shown that FO generally does not consume less energy compared to the standalone RO process [1, 43]. In a recent paper [183], it was concluded that there is effectively no difference in energy consumption between FO and RO (Chapter 4). This conclusion can be generalised for any pressure-driven membrane process used for the draw solution (DS) recovery stage in FO. Hence, the advantages of FO would derive from its lower fouling propensity which this chapter investigates, and its potential to treat high salinity feeds whilst leveraging low-cost thermal energy for draw solution (DS) recovery.

Various publications have demonstrated the advantages of FO over pressure-driven membrane processes to mitigate fouling [1-9]. They conclude that the lower fouling propensity and high fouling reversibility in FO are attributed to the less-compact fouling layer formed, resulting from the absence of hydraulic pressure. The majority of these studies were conducted with commercial CTA membranes because no TFC-FO membranes were commercially available until recently. In recent years, HTI has commenced commercial production of a TFC membrane with a tailor-made support structure to suit FO applications. The HTI TFC membrane is thought to have superior performance and anti-

¹ I would like to acknowledge Patrizia Marchetti for her supervision on the Matlab coding for data analysis, Santanu Karan for the deconvolution of the XPS spectra and Boram Gu for the CFD simulation.

fouling properties [184, 185] in addition to a broad pH tolerance range compared to the CTA membrane. Despite claims of its potential, the membrane has not been widely studied.

Utilising the HTI TFC and CTA membrane, this chapter systematically investigates multiple contributing factors and interactions affecting FO fouling behaviour and propensity, using calcium alginate as a model organic foulant. It explores how factors such as fouling layer properties, membrane surface properties and membrane structural properties are linked to the fouling behaviour of these membranes and process hydrodynamic conditions, which are more significant in influencing fouling severity and reversibility and which provide good indicators for comparing fouling behaviour of different membranes. The implication of the results on furthering the understanding of FO fouling in addition to the literature currently available on the HTI TFC membrane [86, 186, 187] is presented.

From an experimental perspective, quantitative methods are introduced for the effective measurement of FO fouling layer properties such as the specific mass of foulant adsorbed and fouling layer density. These methods provide a new avenue for measuring such properties and allow for their correlation with fouling behaviour and process conditions. Various analytical and membrane characterisation techniques such as AFM and XPS, were utilised to further the understanding of the relationship between membrane surface properties and FO fouling propensity. A data analysis method using regression techniques is also introduced to evaluate fouling performance data of closed-loop systems.

In conclusion, this chapter aims to answer the question of whether the superior performance of the HTI TFC membrane resulting from its improved surface and structural properties is further reflected under fouling conditions, or if there is an underlying trade-off between such improvements in membrane properties and the membrane's ability to mitigate fouling in FO. Further, the results may suggest if indeed the HTI TFC membrane has the potential of becoming the next most widely used commercial FO membrane and the implications this may

have on the future development of FO membranes.

5.2 Materials and Methods

5.2.1 FO Membranes

The forward osmosis membranes used in this chapter were obtained from Hydration Technologies, Inc. (Albany, OR). The HTI CTA has an asymmetric structure and is made of cellulose acetate supported by an embedded polyester mesh. The total thickness of the membrane is ~50 μm . The HTI TFC membrane resembles a typical TFC membrane with a tailor-made support structure to suit FO applications. A polyester mesh is embedded in the support for added mechanical strength. The total thickness of the membrane is ~100 μm .

5.2.2 Organic Foulant

Sodium alginate (Sigma-Aldrich, Lot number: MKBL9077V) used in this work was extracted from brown algae. The foulant represents polysaccharides that constitute a major fraction of soluble microbial products in secondary wastewater effluents. Its molecular weight is specified by the manufacturers as, between 12 to 80 kDa. The foulant was received in powder form. A stock solution of 10 g.L^{-1} was prepared by dissolving the foulant in DIW. The solution was mixed for 24 hours to ensure complete dissolution of the alginate. Once dissolved, the alginate solution was stored in a sterilized glass bottle at 4 $^{\circ}\text{C}$.

5.2.3 Test Solutions

The feed solution for the fouling experiment comprised 50 mM NaCl and 200 mg.L^{-1} sodium alginate along with 0.5 mM CaCl_2 . CaCl_2 (Sigma-Aldrich), was added to the solution to form intermolecular bridges between neighbouring alginate molecules, leading to the formation of a cross-linked gel network following the complexation of alginate with the Ca^{2+} ions. The ambient pH of the alginate feed solution was pH 6.8. The draw solution for the fouling experiment comprised 4.0 M and 2.75 M NaCl for the CTA and TFC membranes respectively,

in FO mode. In PRO mode, the draw solution comprised 1.5 M and 1.15 M NaCl for the CTA and TFC membranes. Due to the varying extent of internal concentration polarisation subject to the different membranes and orientations used, different DS concentrations were needed to ensure the same initial flux of $\sim 20 \text{ L}\cdot\text{m}^{-2}\cdot\text{h}^{-1}$ was achieved for the fouling experiments. Using the same initial flux for all experiments ensures that the effect of initial flux on membrane fouling was eliminated.

5.2.4 Membrane Pretreatment

TFC membranes used in the fouling experiments were wetted with a 50% solution of methanol (VWR) for 60 min. This step is particularly important when testing TFC membranes that are less hydrophilic and are not easily wetted upon exposure to water [85]. Following methanol pretreatment, the membrane was thoroughly rinsed in DIW and soaked in a DIW bath for three hours, replacing the DIW every hour. The membrane was subsequently stored in DIW overnight prior to the fouling experiment.

Methanol and IPA were both tested as prewetting agents for the TFC membrane. There was effectively no difference in flux performance of the prewetted membranes in both solvents. Hence, methanol was selected as the prewetting agent for the TFC membrane due to its potential for greater diffusivity in the pores. The CTA membrane was not prewetted since it is easily hydrated when exposed to water. However, the membrane was soaked in DIW for 24 hours before use. Soaking the TFC and CTA membranes in water removes glycerine, a preservative used to maintain membrane durability during transportation and storage (Figure 5.1).

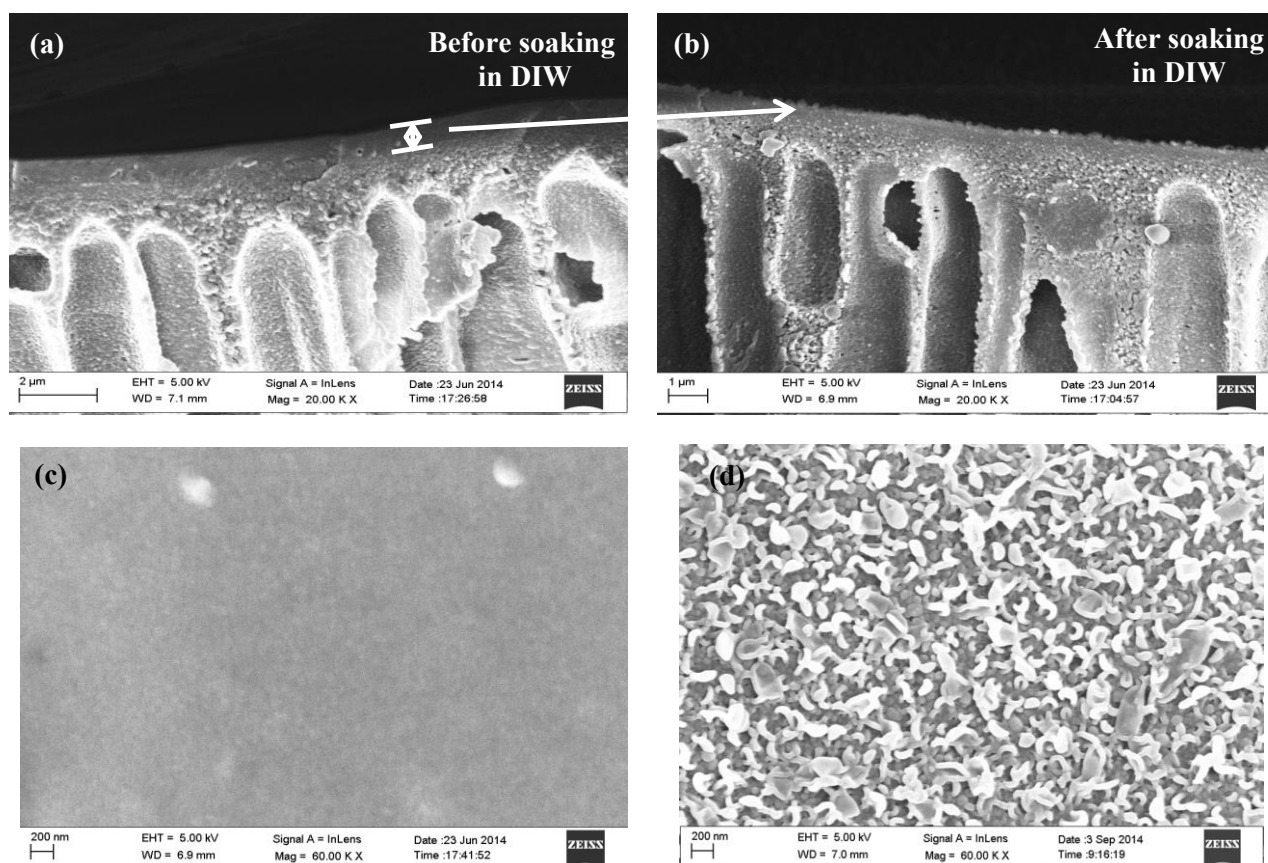


Figure 5.1: SEM micrographs of cross-section and aerial views of the TFC membrane top layer [(a), (c)] before and [(b), (d)] after soaking in DIW.

5.2.5 Membrane Characterisation

5.2.5.1 Scanning Electron Microscopy (SEM)

Aerial and cross-sectional images of the pristine, fouled and cleaned membranes were taken with a high resolution, field-emission gun scanning electron microscope (FEGSEM), LEO Gemini 1525 (Carl Zeiss). At least two locations and membrane samples were imaged to ensure reproducibility. For the cross-sectional images of the membranes, the samples were prepared by soaking in ethanol and then freeze-fractured in liquid nitrogen to preserve the pore structure, before drying in air and being carefully cut with a scissors to avoid any damage. Prior to imaging, the samples were coated with a 10 nm thick layer of chromium sputtered

(Q150T turbo-pumped sputter coater, Quorum Technologies Ltd.) under an Ar atmosphere (2×10^{-2} mbar) to achieve a minimum conductivity for reliable SEM measurements.

5.2.5.2 X-ray Photoelectron Spectroscopy (XPS)

X-ray photoelectron spectroscopy (XPS) was conducted on the TFC and CTA active surfaces by the Oxford Materials Characterisation Service and BegbrokeNano, Department of Materials, Oxford University. The survey spectra and core level XPS spectra were recorded from at least two different spots on the membrane surface of size 400 μm to ensure reproducibility. 200 Watt unmonochromated Mg X-ray excitation was used. The analyser was operated at constant pass energy of 200 eV for wide scans and 20 eV for detailed scans. Data processing was performed using CasaXps.

5.2.5.3 Contact Angle

The contact angle measurements of the active and support layers of the TFC and CTA membranes were performed with an Easy Drop Instrument (Kruess). All membranes were dried at room temperature prior to measurement. The contact angles were measured using a sessile drop method by the drop shape analysis software. The contact angle values are reported as an average of three measurements, each using a droplet volume of about 5 – 10 μL . All measurements were performed at room temperature. At least two membrane samples for each surface and three different locations per sample, were measured for reproducibility.

5.2.5.4 Atomic Force Microscopy

Atomic Force Microscopy, Dimension 3100 (Veeco Instruments Inc., New York) was used to measure the surface roughness of the active and support layers of the membranes studied. The images were captured using tapping mode with PointProbe® Plus silicon-SPM probes (PPP-NCH, Nanosensors™, Switzerland) with a typical tip radius of less than 7 nm. A sampling resolution of not more than 512 points per line and a speed of 0.2 – 1 Hz were used to capture the images. The pristine membrane was attached to a glass slide before loading onto the

holder plate. 'Gwyddion 2.38 SPM data visualisation and analysis software' was used to analyse the AFM images. An average value for surface roughness was taken from four measurements across the membrane surface and presented as root-mean-square roughness (R_{ms}). At least two membrane samples for each surface were measured for reproducibility.

5.2.5.5 Zeta Potential

The zeta potential of the membrane surface was measured using an Electrokinetic Analyzer (EKA) for Solid Surface Analysis, SurPASS (Anton Paar GmbH, Graz, Austria). The measurements were conducted by Henry Maples from the Polymer & Composite Engineering (PaCE) Group, Institute for Materials Chemistry & Research, University of Vienna. 0.5 mM NaCl was used as the electrolyte, a lower concentration than that used in the fouling solution (i.e. 50 mM NaCl) to avoid charge screening effects and enable accurate measurements of the zeta potential. 0.5 mM $CaCl_2$ was added to the test solution to observe the effects of cation adsorption on the zeta potential of the membrane surface and reflect the feed composition prior to addition of sodium alginate. Sodium alginate was added to the test solution to reflect the actual electrokinetic property of the membrane during the fouling tests. 0.05 M HCl and NaOH were used to adjust the solution pH via automatic titration. Before the beginning of each measurement or after pH adjustment of the test solution, the cell was thoroughly flushed with the test solution to remove air bubbles, provide accurate measurements and achieve the desired test solution chemistry. All zeta potential measurements were carried out at 25 ± 2 °C. The membrane surfaces were tested for reproducibility.

5.2.5.6 Intrinsic properties

The pure water permeance and salt rejection of the membranes studied were measured using an RO cross-flow rig with an applied pressure of 20 bar, temperature of 30 °C and cross-flow rate of 40 L.h⁻¹. The permeance was calculated by measuring permeate volume (V) collected per unit area (A_m) per unit time (t) per unit pressure difference (ΔP) according to the following equation:

$$L_{P,RO} = \frac{V}{A_m \cdot t \cdot \Delta P} \text{ [unit: L} \cdot \text{m}^{-2} \cdot \text{h}^{-1} \cdot \text{bar}^{-1}\text{]}$$

Equation 5.1

The salt rejection was calculated as follows:

$$R_i = \left(1 - \frac{C_{P,i}}{C_{R,i}}\right) \times 100 \text{ [%]}$$

Equation 5.2

whereby, $C_{P,i}$ and $C_{R,i}$ correspond to the concentration of salt in permeate and retentate, respectively. Three samples of each membrane were tested for reproducibility.

5.2.6 Foulant Characterisation

5.2.6.1 Hydrodynamic Diameter and Surface Charge

The hydrodynamic diameter and surface charge of calcium alginate was measured using a Zetasizer Nano ZS (Malvern Instruments, UK). An average of three measurements was taken at 30 °C, which corresponds to the temperature of the feed solution in fouling tests. The hydrodynamic diameter of calcium alginate in solution was 15±3 nm. The zeta potential of sodium alginate and calcium alginate were -56±5 mV and -20±2 mV, respectively.

5.2.6.2 Specific Mass of Foulant Adsorbed

The specific mass of alginate adsorbed per unit volume of permeate produced following the fouling experiment was calculated using the following equation:

$$\text{Specific mass of alginate, } m_{s,alg} = \frac{(C_{f,t=0} \times V_{f,t=0}) - (C_{f,t=27} \times V_{f,t=27})}{V_P} \text{ [unit: mg} \cdot \text{L}^{-1}\text{]}$$

Equation 5.3

whereby $C_{f,t=0}$ and $C_{f,t=27}$ are the foulant concentrations at the start and finish of the fouling experiments, $V_{f,t=0}$ and $V_{f,t=27}$ are the feed volumes at the start and finish of the fouling experiments, and V_p is the permeate volume.

The initial and final foulant concentrations were measured using a Total Organic Carbon Analyser, TOC-V_{CPN} (Shimadzu, UK), using the non-purgeable organic carbon (NPOC) method. At least one repeat experiment was performed for every membrane tested, and a minimum of two measurements per experiment was conducted to ensure reproducibility of results.

5.2.6.3 Fouling Layer Density

The density of the fouling layer adsorbed on the membrane surface was measured using a technique for measuring densities of biofilms [188, 189]. Following the fouling experiment, the fouled membrane was left to dry for at least 24 hours at room temperature. A known area of the fouled membrane was selected and its dry mass measured using an analytical balance. The selected membrane area was hydrated using DIW and the wet thickness of the alginate gel was measured using an Easy Drop Instrument (Kruess). Following the thickness measurement, the alginate gel was thoroughly rinsed off the membrane surface, and the cleaned membrane was dried in the oven at 80 °C for at least three hours until there was no further mass change. The mass of the dried, cleaned membrane was measured and subtracted from the mass of the fouled membrane to give the foulant mass adsorbed. Fouling density was then calculated using the following equation:

$$\frac{m_{f,d}}{\delta_{f,w} \times A_{m,s}} [\text{unit: mg. cm}^{-3}]$$

Equation 5.4

whereby $m_{f,d}$ and $\delta_{f,w}$ are the dry mass and wet thickness of the foulant, and $A_{m,s}$ is the selected area for the density measurement. At least two membrane samples for each surface were measured for reproducibility.

5.2.7 FO Cross-flow Setup

Figure 5.2 (a) shows a schematic of the experimental setup used for the FO experiments in this chapter. This setup consists of a circular stainless steel cross-flow cell with an open area of 44 cm² available for water permeation. The cross-flow cell was custom built with equally structured channels on both sides of the membrane, each 1 cm deep by 7.5 cm in diameter (Figure 5.2 (b)). No spacer was used in the channels, however, the circular geometry of the cell provides a greater degree of mixing to reduce external concentration polarisation. Feed and draw solution flow rates were fixed at 24 L.h⁻¹ using variable speed gear pumps (Micropump GJ-N23, Vancouver, USA). No hydraulic pressure was applied on either side of the membrane. The external mass transfer coefficient in the cross-flow cell at 24 L.h⁻¹ is 4.4 x10⁻⁵ m.s⁻¹. The draw solution tank was placed on a digital weighing scale (Denver S-8001) and the weight change was monitored using the Denver Transmit data transfer software. The weight change was used to calculate water flux through the membrane:

$$J_{P,FO_{t_i}} = \frac{M_{t_i} - M_{t_{i-1}}}{(t_i - t_{i-1}) \cdot \rho \cdot A_m} = \frac{\Delta M_{t_i}}{\Delta t_i \cdot \rho \cdot A_m} \text{ [unit: L. m}^{-2}\text{. h}^{-1}\text{]}$$

Equation 5.5

whereby, $J_{P,FO_{t_i}}$ is the FO permeate flux, ΔM_{t_i} is the weight change of the solution over a time interval, ρ is the solution density, A_m is the membrane area and Δt_i is the discrete time interval.

Feed and draw solution temperatures were held constant at 30±1 °C using a water bath.

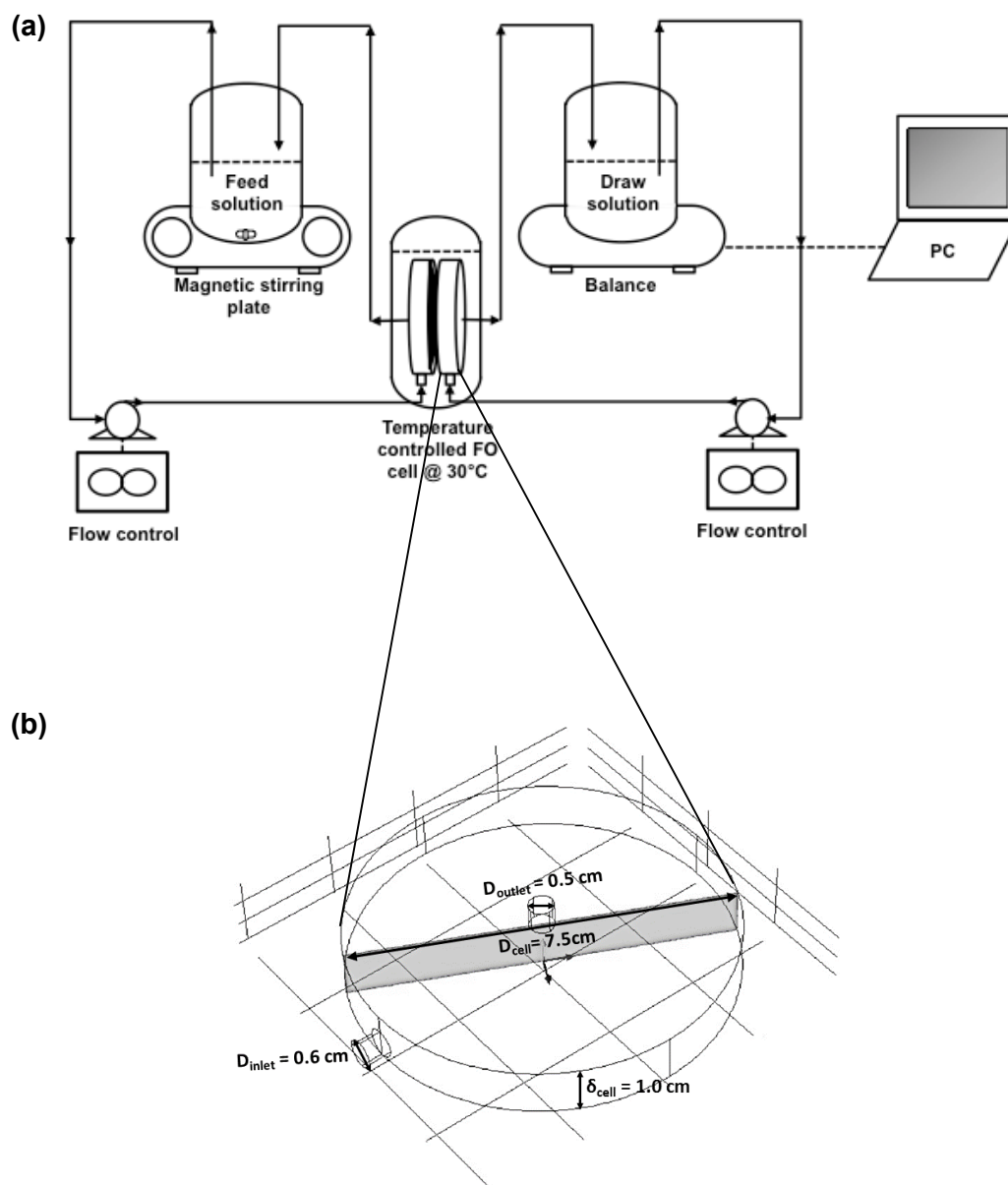


Figure 5.2: (a) Schematic of the lab scale forward osmosis experimental setup, and (b) schematic of the FO cross-flow cell with cell dimensions.

5.2.8 Fouling and Cleaning Procedure

A new membrane coupon was loaded into the FO cell before each experiment. 2 L of feed solution (without foulant) and draw solution were added to the feed and draw solution tanks. The feed and draw solutions were circulated for an hour at a fixed flowrate of $24 \text{ L}\cdot\text{h}^{-1}$ until the initial flux of the membrane was stabilised. Next, $200 \text{ mg}\cdot\text{L}^{-1}$ of foulant was added to the feed solution. The fouling experiment was run for 27 hours and a data transfer software (Denver Transmit, Germany) was

used to monitor weight change of the DS throughout the experiment, which was converted to water flux according to Equation 5.5. Baseline experiments were conducted to quantify the effect of dilution of the draw solution and corresponding decrease in driving force on flux decline. The baseline experiments followed the same procedure as the fouling experiments, only without any foulant present in the feed solution.

Cleaning experiments were conducted immediately after the fouling experiments. Unless otherwise specified, the cleaning experiments were run at $60 \text{ L}\cdot\text{h}^{-1}$ for 15 minutes with DIW as the cleaning solution. During cleaning experiments, both the feed and draw solutions were replaced with DIW to ensure there was no permeate flux through the membrane. After cleaning, flux recovery of the membrane was determined by repeating the initial flux experiment on the cleaned membrane under the same test conditions. In some cases, backwashing was performed as a cleaning mechanism for improved flux recoveries. Unless otherwise stated, backwashing was performed by replacing the draw solution with DIW and feed solution with 1 M NaCl to achieve sufficiently high back fluxes for foulant removal. The cleaning experiments were repeated using at least two different membrane samples to ensure good reproducibility of results.

5.2.9 Data Analysis

The experimental permeate flux data were analysed in terms of specific effects of fouling on the intrinsic membrane permeance, L_p , and solute resistivity to diffusion within the porous support, K . The effects of continuous dilution and concentration of the draw and feed solutions, respectively, as well as the change in concentration at the membrane surface resulting from the closed-loop batch system used, were taken into account.

The permeate flux as a function of membrane permeance and solute resistivity to diffusion is described by Equation 2.25 and Equation 2.26 for PRO and FO modes, respectively.

In Equation 2.25 and Equation 2.26, k is the external mass transfer coefficient on the active side:

$$k = \frac{Sh \cdot D}{D_h} = aRe^b Sc^c \left(\frac{D_h}{L}\right)^d \left(\frac{D}{D_h}\right) [\text{unit: m} \cdot \text{s}^{-1}]$$

Equation 5.6

Whereby, Sh , Re and Sc are the dimensionless Sherwood, Reynolds and Schmidt numbers, respectively; a , b , c and d are constants whose values depend on the system geometry, type of fluid (Newtonian or non-Newtonian) and flow regime; D is the solute diffusion coefficient ($\text{m}^2 \cdot \text{s}^{-1}$), D_h is the hydraulic diameter (m), and L is the channel length (m).

Whereas, K , described by Equation 2.21, is the solute resistivity to diffusion within the porous support layer, which provides a measure of the extent of ICP.

The external mass transfer coefficient of the cross-flow cell, k , at the cross-flow rate applied in this fouling study, was obtained experimentally using a method reported by Peeva et al. [190]. In this approach, mass-transfer coefficients of the cross-flow cell were estimated from independent measurements of the dissolution of a plate of benzoic acid into water at different cross-flow rates at 30 °C, using Equation 5.7:

$$\frac{k_{BA}A}{V}t = \ln \frac{c_b^*}{c_b^* - c_b}$$

Equation 5.7

whereby k_{BA} is the external mass transfer coefficient obtained using benzoic acid ($\text{m} \cdot \text{s}^{-1}$), A is the area of the benzoic acid disc (m^2), V is the solution volume (m^3), t is the dissolution time (s), c_b^* is the benzoic acid solubility in water at 30 °C ($\text{mol} \cdot \text{m}^{-3}$) and c_b is the benzoic acid molar concentration ($\text{mol} \cdot \text{m}^{-3}$).

Assuming that the system's hydrodynamic and geometric conditions are constant, the ratio of the solute mass transfer coefficient to the benzoic acid mass transfer coefficient can be reduced from Equation 5.6 and expressed as:

$$\frac{k_{solute}}{k_{BA}} = \left(\frac{\eta_{solute}}{\eta_{BA}} \right)^{(c-b)} \left(\frac{D_{solute}}{D_{BA}} \right)^{(1-c)}$$

Equation 5.8

whereby b and c are the Reynolds and Schmidt number exponents seen in Equation 5.6 and η is the kinematic viscosity ($\text{m}^2 \cdot \text{s}^{-1}$).

A specific $Sh = f(Re, Sc)$ correlation for the cell used in this study, where the flow is tangential, is not available, however the benzoic acid data suggested an exponent for Re of around 0.8, which justified the use of the Chilton–Colburn correlation (Equation 5.9) as a basis for calculating the mass-transfer coefficients for NaCl using Equation 5.8.

$$Sh = 0.023Re^{0.8}Sc^{0.33}$$

Equation 5.9

In order to perform these calculations, it was necessary to assume a well-mixed condition in the cross-flow cell and that turbulent flow correlations were valid for use.

Note that external concentration polarisation (ECP) is not considered on the outer support layer side of the membrane since the thickness of the external boundary layer under the present experimental conditions is much lower (i.e. < 5%) than the structural parameter of the membranes studied. Hence, it can be assumed negligible. Moreover, water permeating the backing layer of the membrane already contains some concentration of the draw solute, which mitigates the polarisation effects on the support side since pure water is not entering the bulk solution at the support surface [24, 93].

5.2.9.1 Baseline Data

The baseline permeance values (L_p) and the structural parameter (S) for the membranes studied in this work were obtained by regressing the experimental flux data for both PRO and FO modes using Equation 2.25 and Equation 2.26 for the two orientations, respectively, together with Equation 2.21. The solute diffusion coefficients, D , necessary to obtain the solute resistivity to diffusion within the support layer, K , was given as a function of solute concentration (Robinson and Stokes, 1959) [191]. The *lsqcurvefit* function was used, which solves nonlinear curve-fitting (or data-fitting) problems using a least-square approach. The external mass transfer coefficient, k , the bulk feed, $\pi_{F,b}$, and the draw solution osmotic pressures, $\pi_{D,b}$, were given as experimental input values. The quality of the fitting was calculated as the norm of residuals (see Equation 5.10):

$$N_r = \sqrt{\sum_i \left(\frac{J_i^{exp} - J_i^{calc}}{J_i^{exp}} \right)^2}$$

Equation 5.10

Whereby, N_r is the norm of residuals, J_i^{exp} is the experimental flux and J_i^{calc} is the calculated flux.

5.2.9.2 Fouling Data

Differently from the case for the baseline, the analysis of membrane permeance and solute resistivity to diffusion in the presence of fouling is more complicated. This is due to the unknown effect of fouling on both descriptors. In order to correlate the permeance decline over time with the occurrence of fouling, some assumptions were made for both FO and PRO modes and for both CTA and TFC membranes. For the CTA membrane in FO and PRO modes and the TFC membrane in FO mode, it was assumed that fouling occurs as a surface phenomenon; whereas for the TFC membrane in PRO mode, it was assumed that the foulant

is deposited within the porous support of the membrane. These assumptions were made based on physical cleaning results conducted on the CTA and TFC membranes. For the CTA membrane, high flux recoveries of 96% and 95% observed after cleaning in both FO and PRO modes, respectively, indicate that alginate fouling occurred as a surface phenomenon on the active and support layers of this membrane. For the TFC membrane, a low flux recovery in PRO mode of 37% (compared to 85% in FO mode) and the need for backflushing, indicates that fouling occurred via pore clogging of the TFC support in PRO mode. A detailed discussion on cleaning and flux recoveries of the membranes studied is presented in Section 5.3.4.

When fouling was considered as a surface phenomenon, the effective permeance was obtained by solving Equation 2.25 and Equation 2.26 for PRO and FO modes, respectively, together with Equation 2.21, with supplied values for experimental flux, J_p , external mass transfer coefficient, k , bulk feed, $\pi_{F,b}$, and draw solution osmotic pressures, $\pi_{D,b}$, and diffusion coefficients corresponding to the changing concentrations with time, D (Robinson and Stokes, 1959) [191]. The solute diffusion coefficients were used to calculate K using Equation 2.21. The structural parameter, S , also required for the calculation of K , was determined by solving Equation 2.25 and Equation 2.26, with supplied values for L_p , J_p , D , $\pi_{D,b}$ and $\pi_{F,b}$ at time 0.

When fouling was assumed to deposit within the porous support, the S parameter could no longer be considered constant. This is attributed to a reduction in the membrane porosity and an increase in the membrane tortuosity upon foulant deposition. Hence, in order to obtain the membrane permeance and the solute resistivity to diffusion within the support at each time point (t_i), one equation is not sufficient. The approximation of constant membrane permeance and solute resistivity to diffusion within the support for two consecutive time points, t_i and t_{i+1} , was made. To improve the calculation, above all, in the initial time range where the permeate flux is decreasing rapidly, the permeate flux profile was interpolated by a polynomial, and very small time intervals [$t_i - t_{i+1}$], typically 180 s, were used.

5.3 Results and Discussion

5.3.1 Membrane Characterisation

5.3.1.1 Physical Structure

Figure 5.3 shows high resolution SEM images and schematic representations of the two membranes used in this study. Both forward osmosis membranes were obtained from Hydration Technologies, Inc. (Albany, USA). The HTI CTA membrane (Figure 5.3 (a) and (c)) has a top rejecting layer followed by a relatively thin and less dense support layer made of cellulose triacetate embedded with a polyester mesh for added mechanical strength. CTA is prevalent throughout the membrane as a denser layer on the rejecting side and a looser layer on the support side. The total thickness of the membrane is approximately 50 μm . The HTI TFC membrane (Figure 5.3 (b) and (d)) is an asymmetric membrane with finger-like morphology, reinforced with a polyester mesh similar to the mesh-embedded CTA membrane. However, the polyester mesh is oriented towards the bottom of the support layer, creating additional macroscopic pores around the mesh lines on the bottom surface [71] as shown in Figure 5.4 (c). The total thickness of the membrane is $\sim 100 \mu\text{m}$.

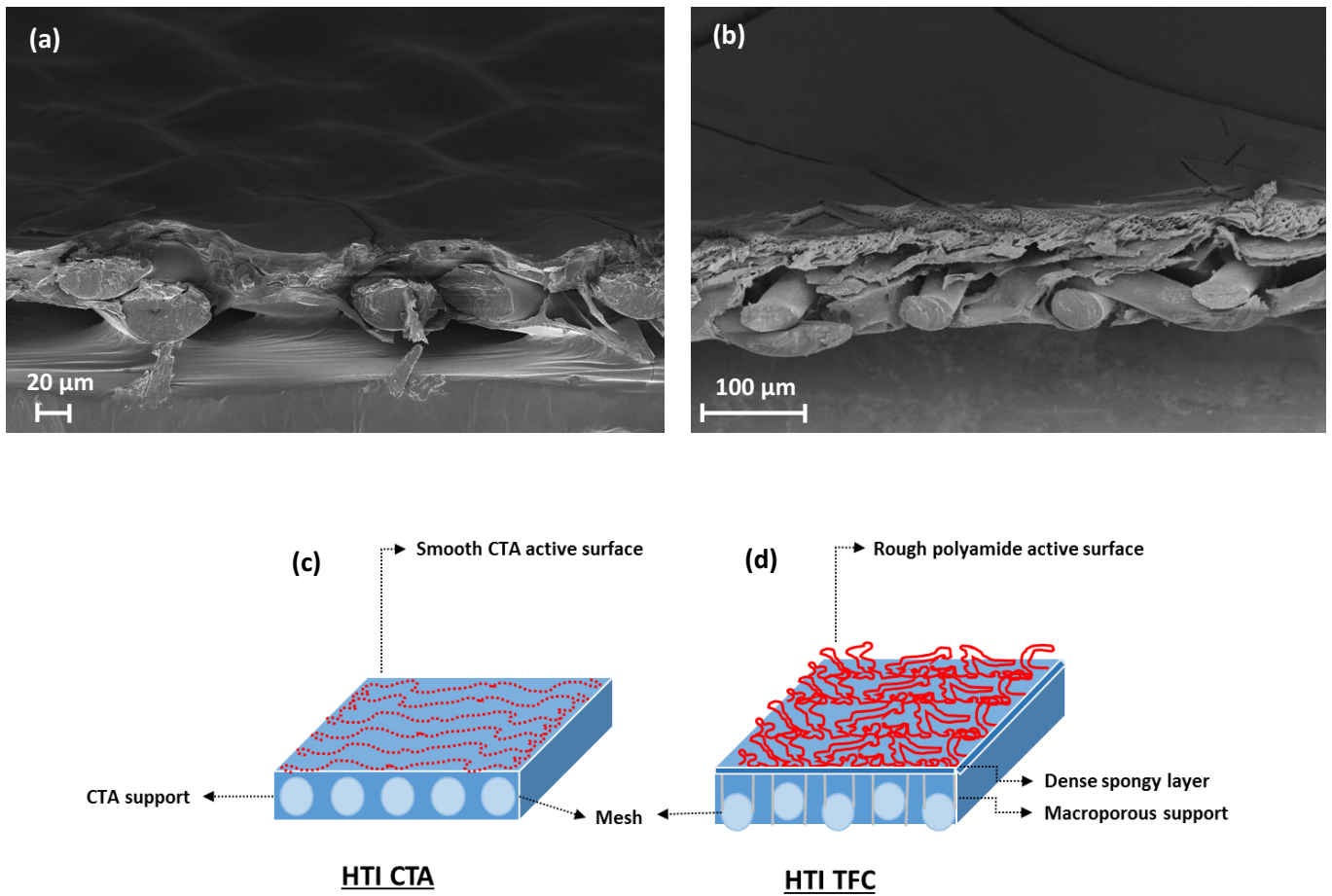


Figure 5.3: SEM image and schematic representation of (a,c) HTI CTA membrane and (b,d) HTI TFC membrane used in this study. Schematic not drawn to scale.

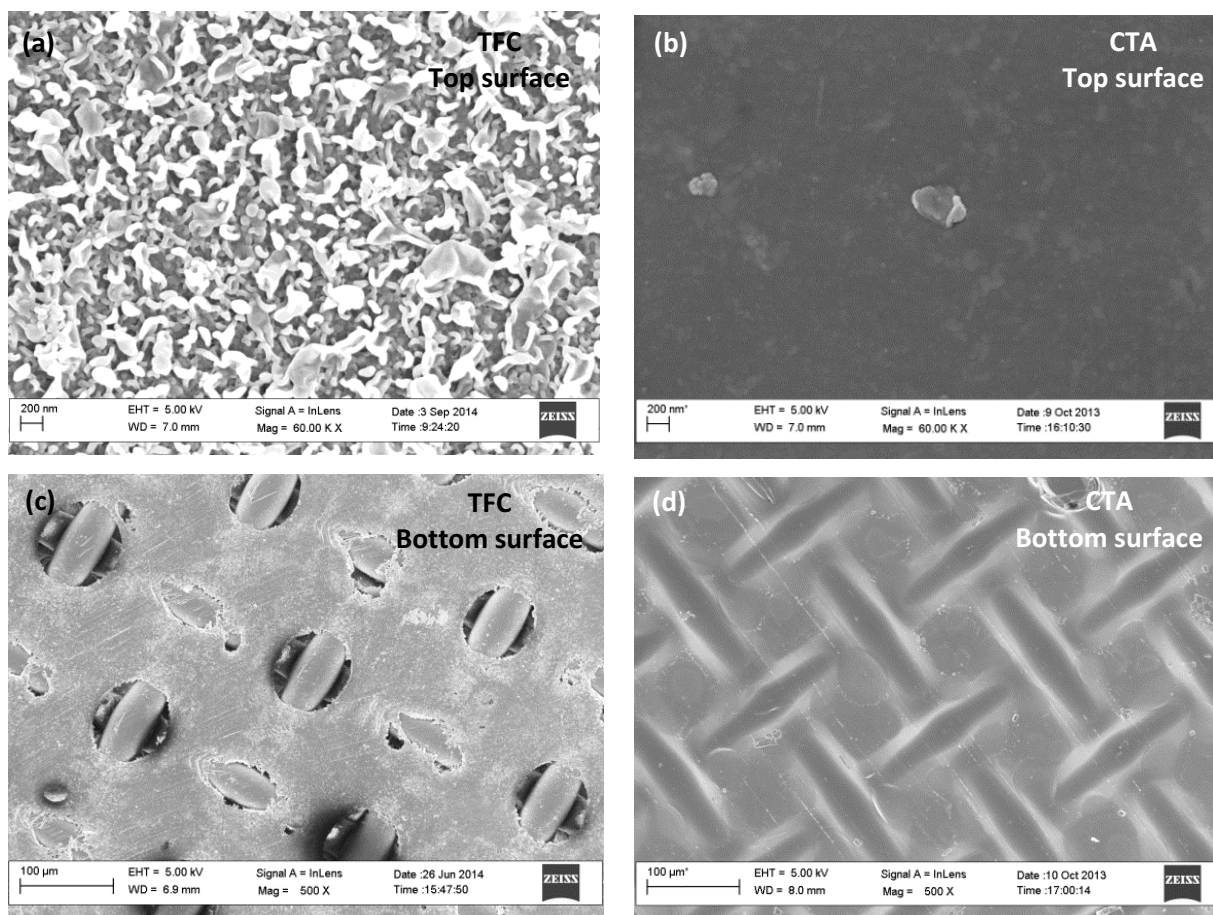


Figure 5.4: SEM images of pristine membranes after soaking in water: (a) TFC top surface, (b) CTA top surface, (c) TFC bottom surface and (d) CTA bottom surface.

5.3.1.2 Chemical Composition

An X-ray photoelectron spectroscopy (XPS) study was conducted on the TFC and CTA active surfaces to determine the differences in chemical composition of these membranes (Figure 5.5 and Figure 5.6). As expected, deconvolution of the C1 spectrum revealed the signature amide and carboxyl groups on the TFC active surface (Table 5.1). However, there was no nitrogen species or amide bond present on the CTA active surface (Table 5.1) suggesting that the CTA active layer was not formed from a typical interfacial polymerisation reaction of an acid chloride and amine derivative. In fact, the active and support layers of the CTA membrane were made from the same polymeric material by phase inversion of a precursor dope solution [25, 53, 55]. Hence, both sides are postulated to have a similar chemical composition, unlike

the TFC membrane. The XPS study also provides statistical information on the functional groups available for interaction with foulant in solution.

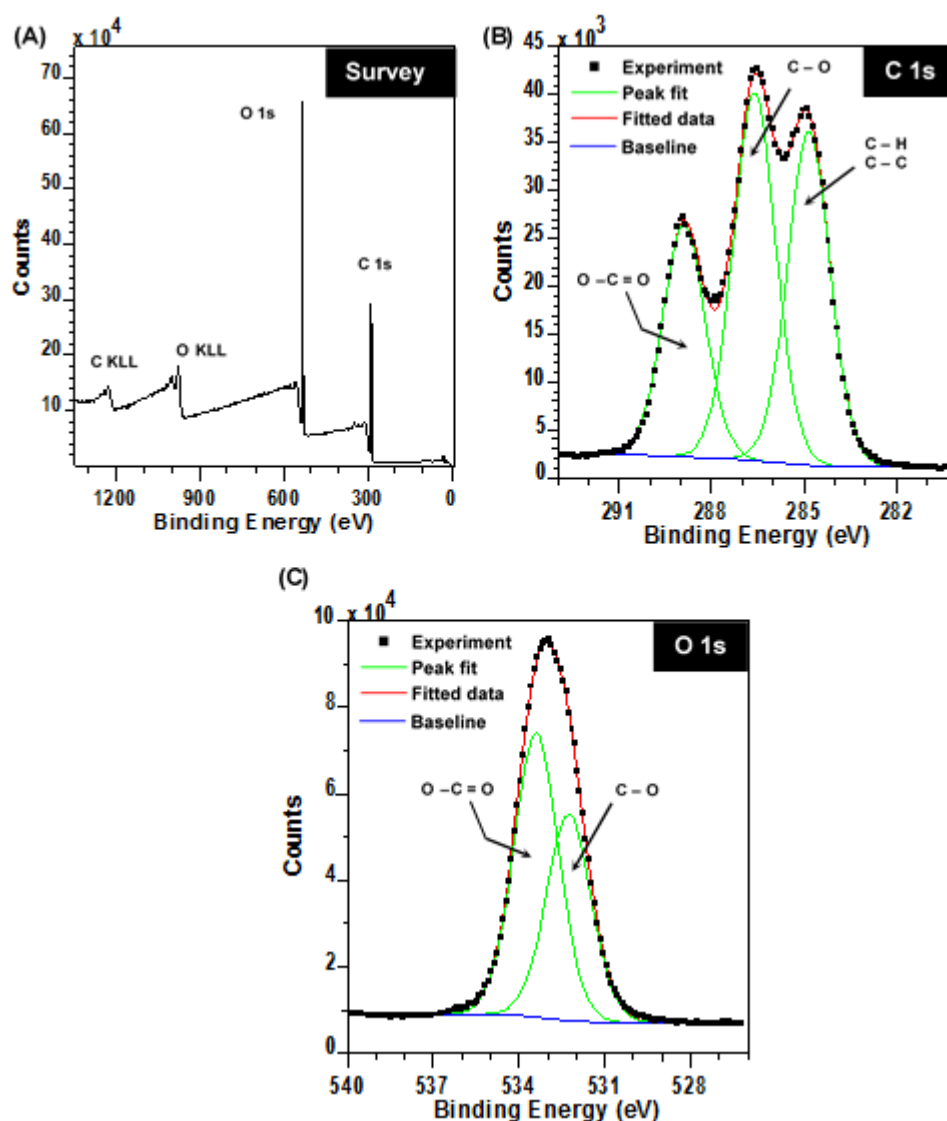


Figure 5.5: Survey spectra and narrow scan results of X-ray photoelectron spectra measured from the top surface of CTA membrane. (A) Survey, (B) C 1s and (C) O 1s spectra. Narrow scans were deconvoluted to calculate the chemical species and the corresponding binding energy.

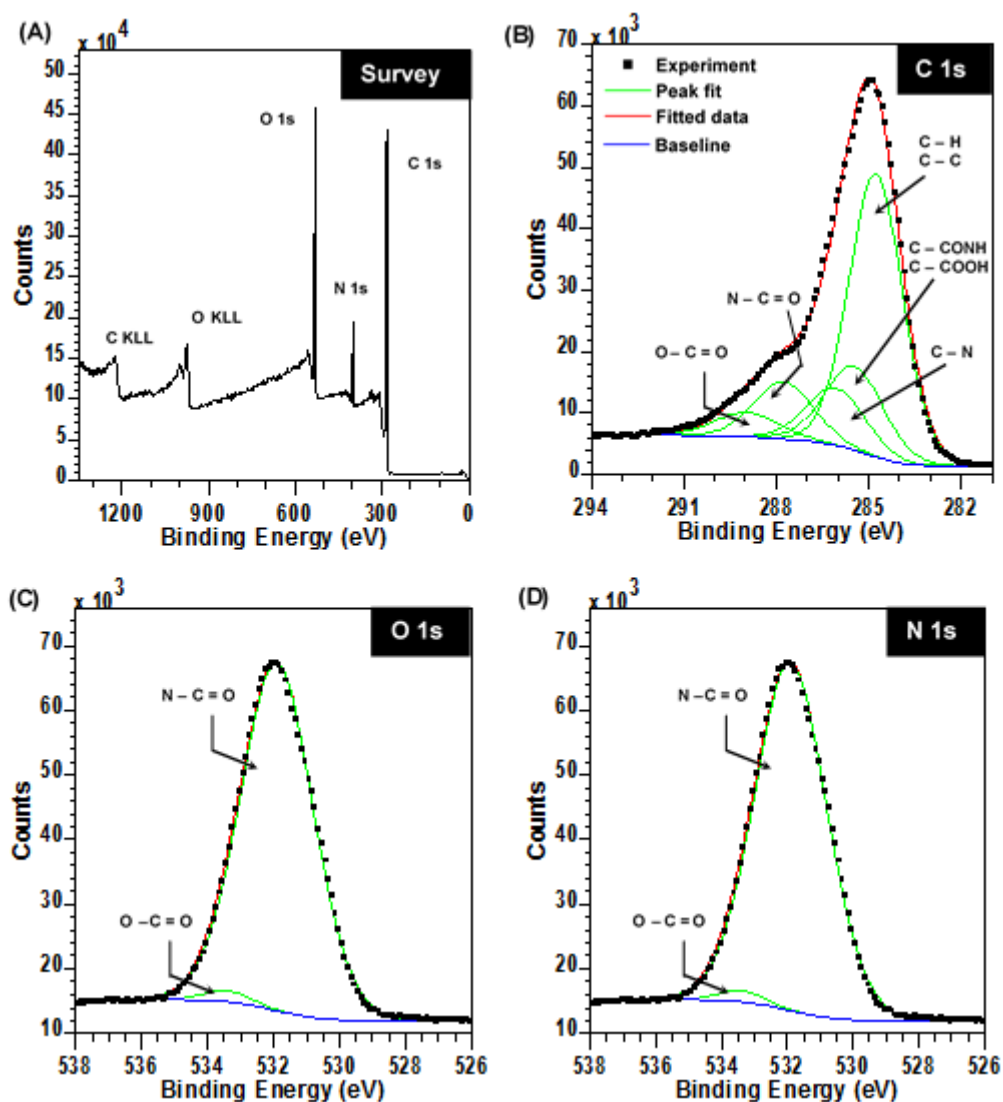


Figure 5.6: Survey spectra and narrow scan results of X-ray photoelectron spectra measured from the top surface of polyamide TFC membrane. (A) Survey, (B) C 1s, (C) O 1s and (D) N 1s spectra. Narrow scans were deconvoluted to calculate the chemical species and the corresponding binding energy.

Membranes	C1s			O1s			N1s		
	Energy (eV)	Species	(%)	Energy (eV)	Species	(%)	Energy (eV)	Species	(%)
Cellulose triacetate C: 63.8% O: 36.2%	284.8	C-H, C-C	35.7	532.3	C-O	42.1	NA	NA	NA
	286.6	C-O	39.4	533.4	O-C=O	57.9			
	288.8	O-C=O	24.9						
Polyamide TFC C: 68.7% O: 23.0% N: 8.3%	284.7	C-H, C-C, C=C	53.3	531.8	N-C=O	98.0	398.5	R-NH ₂	5.0
	285.4	C-CONH, C-COO	17.4						
	286.0	C-N	11.9	533.4	O-C=O	2.0	400.0	N-C=O	95.0
	287.7	N-C=O	11.9						
	288.8	O-C=O	5.5						

Table 5.1: XPS results of the CTA and TFC active surfaces. Binding energies and plausible species were determined from the deconvolution of C1s, O1s and N1s core level XPS spectra.

5.3.1.3 Intrinsic Properties

The intrinsic pure water permeance (L_p) and salt rejection of the CTA and TFC membranes are illustrated in Figure 5.7. The specific values are reported in Table 5.2. The CTA membrane has a lower salt rejection (97.7%) compared to the TFC membrane (99.0%), with a corresponding solute permeability coefficient of $0.34 \text{ L}\cdot\text{m}^{-2}\cdot\text{h}^{-1}$ and $0.20 \text{ L}\cdot\text{m}^{-2}\cdot\text{h}^{-1}$, respectively. This indicates that the PA rejecting layer of the TFC membrane exhibits greater selectivity over the CTA membrane.

From Figure 5.7 (b), it can be seen that the pure water permeance of the pristine TFC membrane is approximately double that of the CTA membrane. After prewetting with methanol, the permeance increases to almost three times, suggesting swelling of the polyamide network [192, 193]. Prewetting ensures that the membrane porous support is fully water saturated, especially when using TFC membranes with less hydrophilic supports. In addition to wetting the support, prewetting also swells the polyamide (PA) layer, thus increasing its permeance. This is a result of hydrogen bonding and non-polar interactions with the PA layer due to the lower polarity of methanol compared to water [192, 193]. Besides swelling of the polyamide network in methanol, a nano-scale phase separation of the polymer structure occurs when exchanged with water [194]. Upon

solvent activation, the polyamide swells and rearranges in methanol due to higher affinity (via hydrogen bonding) of the solvent to the polyamide. The adsorption of methanol increases the chain mobility as a direct result of decreasing glass transition temperature during swelling. Part of the swelling may be inwards into the nanovoid structure of the polyamide [195], along with an overall expansion of the nanofilm. When removed from methanol solution and soaked in water, a secondary structure of the nanofilm is formed, when water with a smaller molar volume replaces methanol to promote the phase separation of the “denser” region versus the “less dense and re-oriented” region. A significant increase in the ‘segmental mobility’ of the less dense regions results in enhanced permeance without compromising rejection [194]. It has been suggested that the imperfections or defects in the pretreated polyamide layer are removed because of compression effects created by the swelling of the polyamide, resulting in an overall maintained rejection (Figure 5.7 (a)).

An analysis of variance (ANOVA) was performed to analyse the statistical significance of two variables i.e. membrane type and membrane pretreatment, on the intrinsic separation properties (i.e. permeance and rejection) of the membranes studied (Table 5.3). Clearly, the type of membrane studied had a significant effect on permeance and rejection due to differences in morphology and structure of the separating and support layers, respectively. On the contrary, it was shown that pretreatment with methanol had a significant effect on permeance of the membranes but an insignificant effect on rejection, which is attributed to reasons explained previously [196, 197].

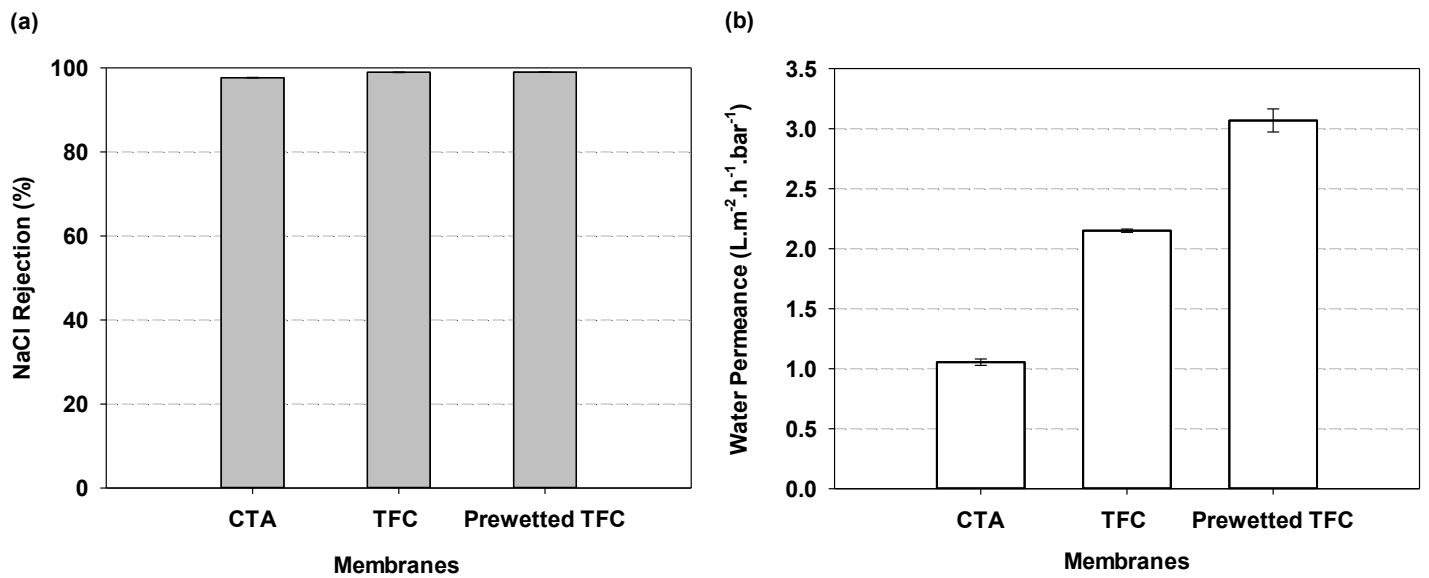


Figure 5.7: (a) NaCl rejection and (b) pure water permeance of HTI CTA and TFC membranes under RO experimental conditions with an applied pressure of 20 bar, temperature of 30 °C and cross-flow rate of 40 L.h⁻¹.

RO Experiment					
Experimental conditions	Membrane		Value	Units	
Temperature	CTA, TFC		30 ± 1	°C	
NaCl concentration			2	g.L ⁻¹	
Applied pressure			20	bar	
Recirculation flowrate			40	L.h ⁻¹	
Pure water permeance	CTA	1.05	L.m ⁻² .h ⁻¹ .bar ⁻¹		
	TFC	2.15			
	Prewetted TFC	3.07			
Salt rejection	CTA	97.7	%		
	TFC	99.0			
	Prewetted TFC	99.0			
Salt permeability coefficient	CTA	0.34	L.m ⁻² .h ⁻¹		
	TFC	0.20			
	Prewetted TFC	0.20			
Fouling Experiment					
Experimental conditions	Mode	Membrane	Value	Units	Notes
FS and DS temperatures	FO, PRO	CTA, TFC	30 ± 1	°C	N/A
DS concentration	FO	CTA	4.00	mol.L ⁻¹	NaCl
		TFC	2.75		
	PRO	CTA	1.50		
		TFC	1.15		
FS concentration	FO, PRO	CTA, TFC	50	mM	NaCl
			0.5	mM	CaCl ₂
			200	mg.L ⁻¹	Alginate
Recirculation flowrate	FO, PRO	CTA, TFC	24	L.h ⁻¹	N/A
Cleaning Experiment					
Recirculation flowrate (unless specified otherwise)	FO, PRO	CTA, TFC	60	L.h ⁻¹	DIW (unless specified otherwise)

Table 5.2: Experimental conditions used in this study for RO, fouling and cleaning experiments.

Effects	F	P-value	F crit
<i>Methanol pretreatment on TFC rejection</i>	0.485	0.558	18.513
<i>Methanol pretreatment on TFC permeance</i>	924.038	0.001	18.513
<i>Membrane type on rejection</i>	375.380	0.003	18.513
<i>Membrane type on permeance</i>	145.512	0.007	18.513

Table 5.3: Analysis of variance (ANOVA) showing effects of membrane type and methanol pretreatment on membrane permeance and rejection. Note that effects are significant when $F > F_{crit}$ and $P\text{-value} < 0.05$

5.3.2 Baseline Data Analysis Results

The model for the calculation of baseline permeance and S parameter in the CTA membrane, via regression of the experimental flux data, obtained an L_p value of $1.04 \text{ L}\cdot\text{m}^{-2}\cdot\text{h}^{-1}\cdot\text{bar}^{-1}$, with a good quality of fitting between experimental and calculated fluxes. The quality of fitting corresponds to a small norm of residuals value of 0.5, as seen in Figure 5.8 (a).

For the TFC membrane, a good quality of fitting between the experimental and calculated fluxes was not obtainable, whereby the best fit to obtain a reasonable L_p , yielded a norm of residuals value of 2.9, as seen in Figure 5.8 (b). The poor fitting is likely due to one of the following reasons:

- i) There was no single S parameter value regressed by the model which allowed for a good fitting of the fluxes in both, FO and PRO mode. This means that in order to obtain a good fitting between the experimental and calculated flux, a range of S values would have been required. However, a range of S values for a given membrane does not have an appropriate physical meaning, as the S parameter is an intrinsic property of the support and should be constant for a specific membrane.

- ii) The highly asymmetric structure of the TFC support may have caused hindered diffusion within the dense spongy layer of the support adjacent to the polyamide (PA) film, causing a great decline in solute diffusivity. The diffusivity of the solute currently used in Equation 2.21 could be much higher than the actual solute diffusivity within the dense layer of the support. This would affect the value of K in a way which is currently not captured in Equation 2.21. Hence, the range of K values currently regressed by the model may not be representative of the actual resistivity to solute diffusion within the membrane support, thus leading to a poor regression of L_p .

Since; (a) the S parameter is expected to be constant for a given support (given it is a function of the support thickness, porosity and tortuosity), and; (b) due to the lack of information on the possible phenomenon of hindered diffusion in the dense layer of the TFC membrane, it is not possible to conclusively comment on the factors affecting the regression of L_p in the TFC membrane using the current model. However, based on the permeance value regressed for the CTA membrane, which matched the experimental permeance calculated under RO conditions (Table 5.2) very well, a constant permeance for the TFC membrane before fouling is assumed, also equal to the permeance value obtained from the RO test (Table 5.2) of $3.07 \text{ L}\cdot\text{m}^{-2}\cdot\text{h}^{-1}\cdot\text{bar}^{-1}$. A summary of the output parameters obtained from the baseline regression model and the membrane permeance measured under RO conditions is presented in Table 5.4.

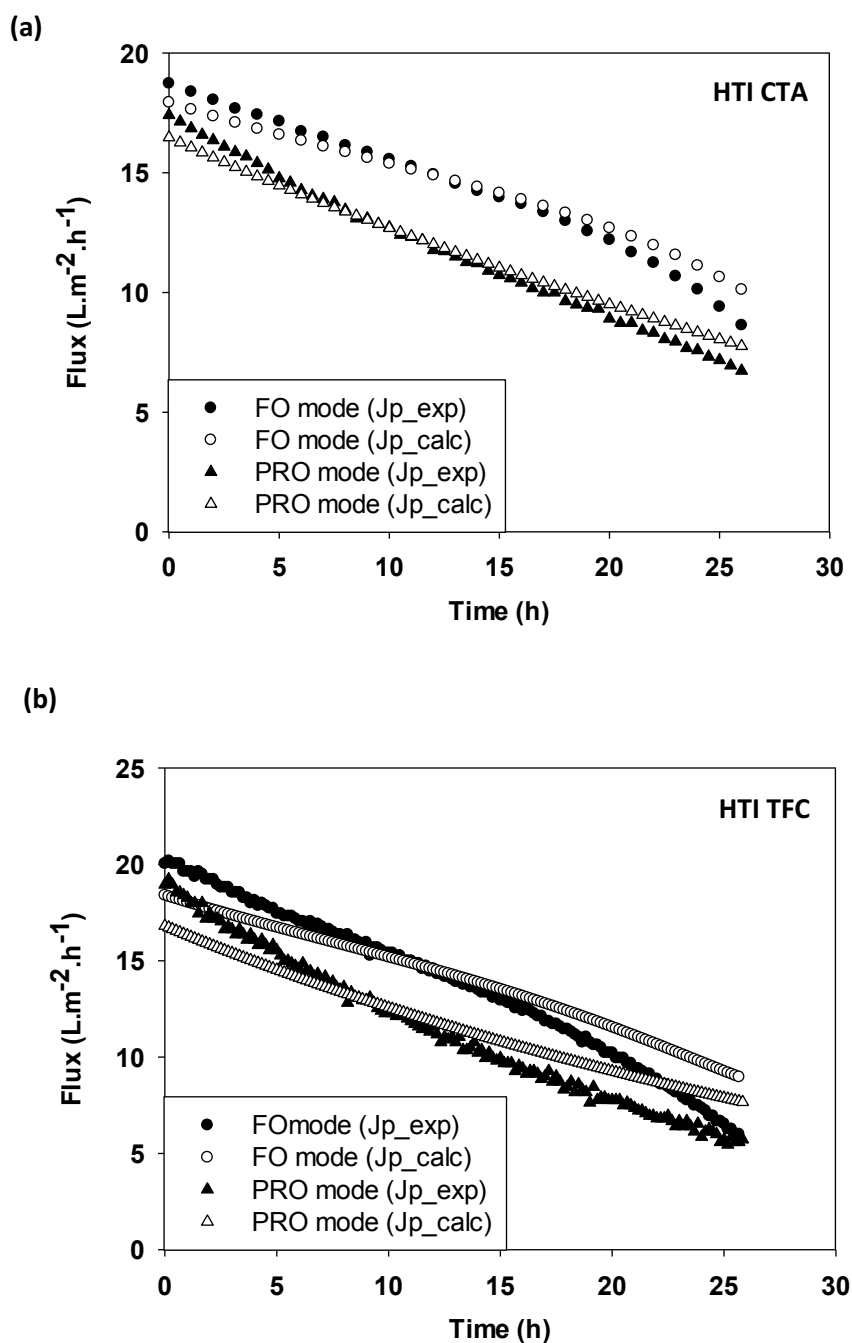


Figure 5.8: Figure showing the quality of fitting between calculated and experimental baseline fluxes for (a) HTI CTA and (b) HTI TFC membranes. The quality of fitting corresponds to a norm of residuals value of 0.5 and 2.9 for the CTA and TFC membranes, respectively.

Membrane	L_p from RO experiment ($\text{L.m}^{-2}.\text{h}^{-1}.\text{bar}^{-1}$)	L_p from regression ($\text{L.m}^{-2}.\text{h}^{-1}.\text{bar}^{-1}$)	S from regression (μm)	Norm of Residuals
CTA	1.04	1.04	842	0.5
TFC	3.07	2.36	825	2.9

Table 5.4: Table summarising output parameters obtained from the regression model and the membrane permeance measured under RO conditions.

5.3.3 Factors Affecting Fouling Behaviour

Factors affecting the fouling behaviour of the membranes investigated in this chapter are summarised in Figure 5.9 and discussed in the following sections.

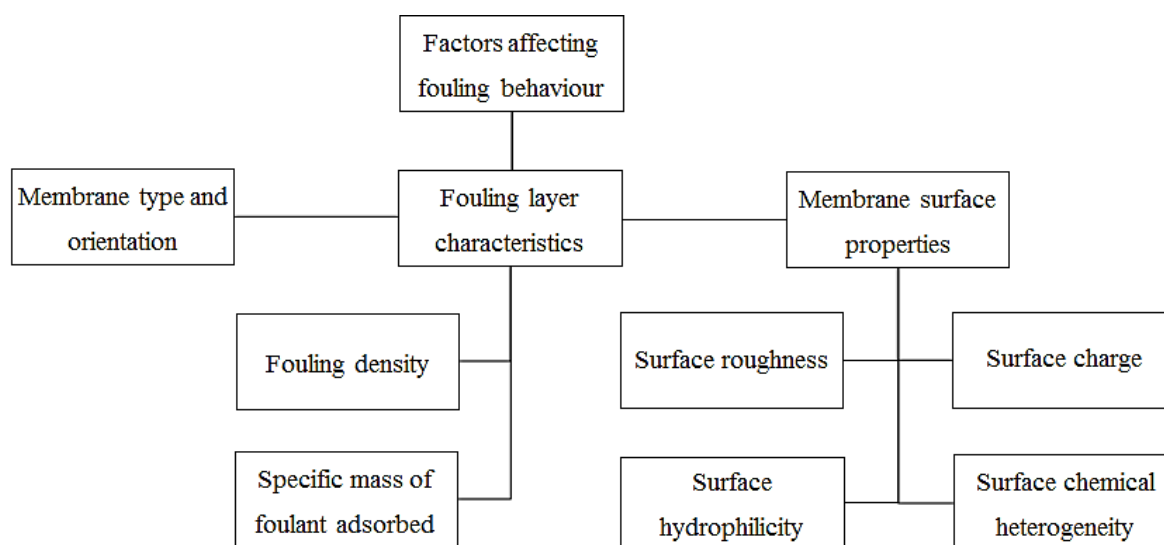


Figure 5.9: Schematic summarising the factors affecting fouling behaviour of the membranes investigated in this chapter.

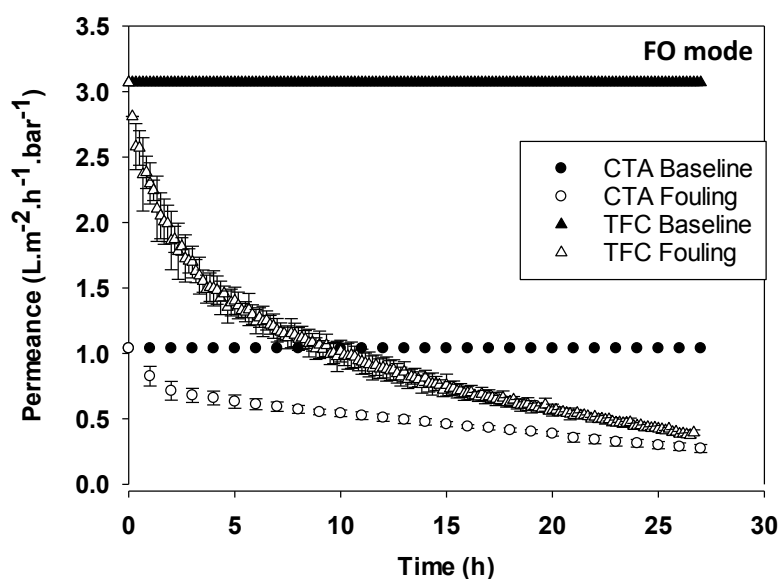
5.3.3.1 Membrane Type and Orientation

Membrane type and orientation have a significant effect on FO fouling. As both the active and support layers can be oriented towards the feed solution, fouling behaviour and the

mechanism for foulant deposition can vary significantly if the membrane is asymmetric, i.e. the active and support layers have differing i) structures and ii) chemical composition.

Figure 5.10 illustrates the baseline permeance and permeance decline due to fouling of the structurally and chemically different HTI membranes in both orientations i.e. active layer facing feed solution (FO mode) and active layer facing draw solution (PRO mode). The results shown will be discussed further in this section. The effective permeance are plotted as a function of time for baseline and fouling experiments conducted over 27 hours, using data analysis methods explained in Section 5.2.9. Further details on the baseline analysis results are presented in Section 5.3.2.

(a)



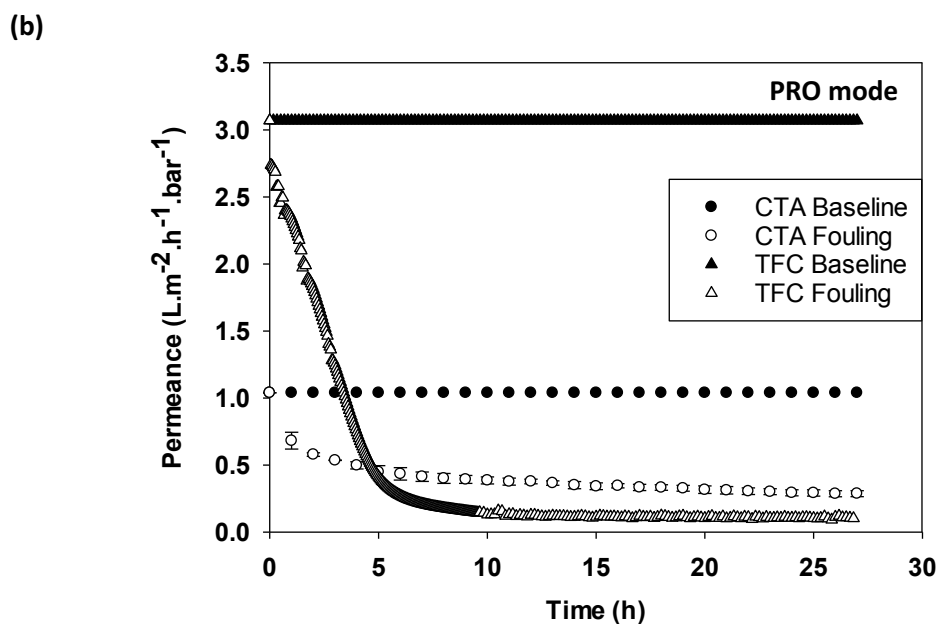


Figure 5.10: Comparison of fouling behaviour on HTI TFC and CTA membranes in (a) FO mode and (b) PRO mode. 50 mM NaCl was used as the feed solution in the baseline experiments along with 200 mg.L⁻¹ alginate and 0.5 mM CaCl₂ in the fouling experiments. The following concentrations were used for the draw solution to achieve the same initial flux, i) 4 M NaCl for CTA in FO mode, ii) 2.75 M NaCl for TFC in FO mode, iii) 1.5 M NaCl for CTA in PRO mode, and iv) 1.15 M NaCl for TFC in PRO mode.

Once the foulant is deposited on the membrane surface or in the porous support of the membranes studied, membrane permeance decreases over time due to the hydraulic resistances presented by the adsorbed foulant layer. SEM images of the membranes before and after fouling and cleaning are shown in Figure 5.11 (a-h) and Figure 5.12 (a-j).

The extent of membrane fouling is indicated by the magnitude of deviation of the fouling curve from the baseline curve in Figure 5.10. A greater extent of fouling is observed on the TFC membrane compared to the CTA membrane in FO mode (Figure 5.10 (a)). SEM images show a visible fouling layer on the surfaces of both membranes (Figure 5.11 (b) and Figure 5.12 (b))

following the 27 hour fouling experiment. It can be observed from the fouling curve in Figure 5.10 (a) that there is a greater decline in membrane permeance initially as the foulant is deposited on the membrane surface. This decline decreases with time, as a more stable, uniform fouling layer is formed across the membrane.

Fouling on the CTA membrane was comparable in both orientations (Figure 5.10 (a) and (b)). Since the active and support layers of the CTA membrane were fabricated from the same polymeric material [25, 53, 55] and are likely to be similar in chemical composition, it is proposed that foulant-membrane interactions were similar in both orientations and fouling occurred as a surface phenomenon on the CTA membrane (Figure 5.13 (a) and (b)). Surface fouling was observed on the CTA support layer in PRO mode due to the relatively smooth (Figure 5.14 (b)) and dense morphology of the support which is unlike the porous structure of the TFC support layer. It is also attributed to calcium alginate forming a highly structured gel upon aggregation. This is shown in Figure 5.11 (e) and (h), whereby a visible fouling layer was observed on the membrane surface, which was easily removed by cleaning with DIW at increased cross-flow velocity as illustrated in Section 5.3.4. However, for foulants with less significant calcium binding effects such as BSA and AHA, fouling on the CTA membrane would be more severe in PRO mode [3].

A visible fouling layer was not observed on the TFC support surface in PRO mode other than a small amount covering ~2-5% of the membrane surface shown in Figure 5.12 (e). Additionally, cleaning conditions had to be modified to include backwashing, as increasing cross-flow velocity alone was insufficient to achieve a comparable flux recovery with the CTA membrane (Section 5.3.4 and 5.3.5.1). This indicates that fouling occurred by severe internal clogging of the porous support due to the presence of macropores around the mesh lines on the bottom surface of the TFC membrane (Figure 5.4 (c)), which is reflected in the significant permeance decline compared to the CTA membrane (Figure 5.10 (b)). Internal clogging reduces the porosity of the support layer resulting in a consequent increase in structural

parameter and ICP. This results in severe flux reduction as it is exponentially dependent on the degree of ICP [135]. Following the steep decline in membrane permeance, a steady, almost constant permeance is observed after 10 hours, indicating that fluxes through the membrane are too low to effect a sufficient permeation drag, thus preventing further foulant deposition within the support.

Fouling was less severe on the TFC membrane in FO mode compared to PRO mode as it occurred as a surface phenomenon in FO mode. Besides pore clogging and the increased effect of the S parameter in PRO mode, the enhanced effects of cake-enhanced osmotic pressure [5] due to lack of shear and poor salt diffusion in the porous support may also contribute to the greater flux decline in PRO mode.

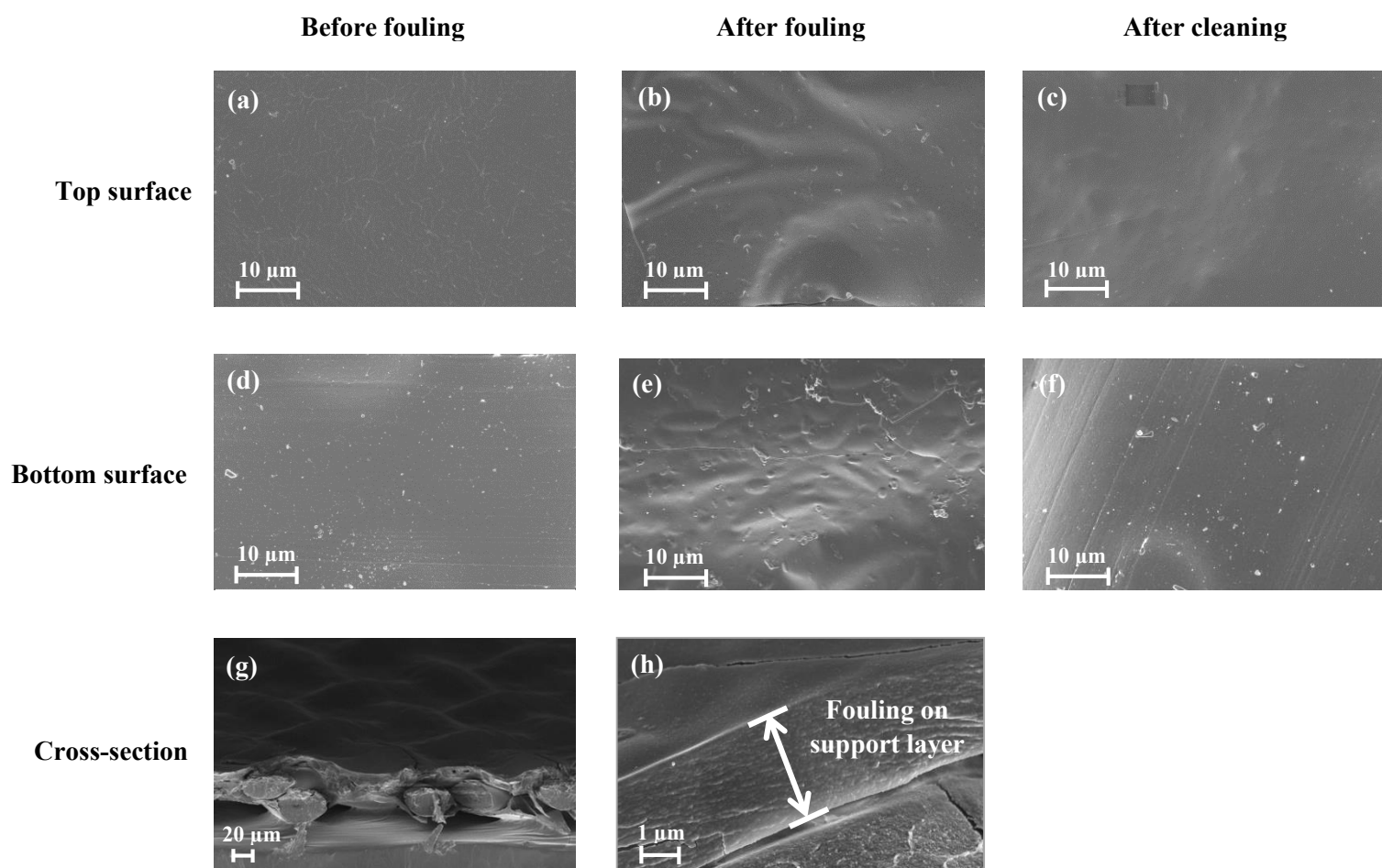


Figure 5.11: SEM micrographs of pristine, fouled and cleaned CTA membranes; (a-c) top surface, (d-f) bottom surface, and (g-h) cross-sectional micrographs.

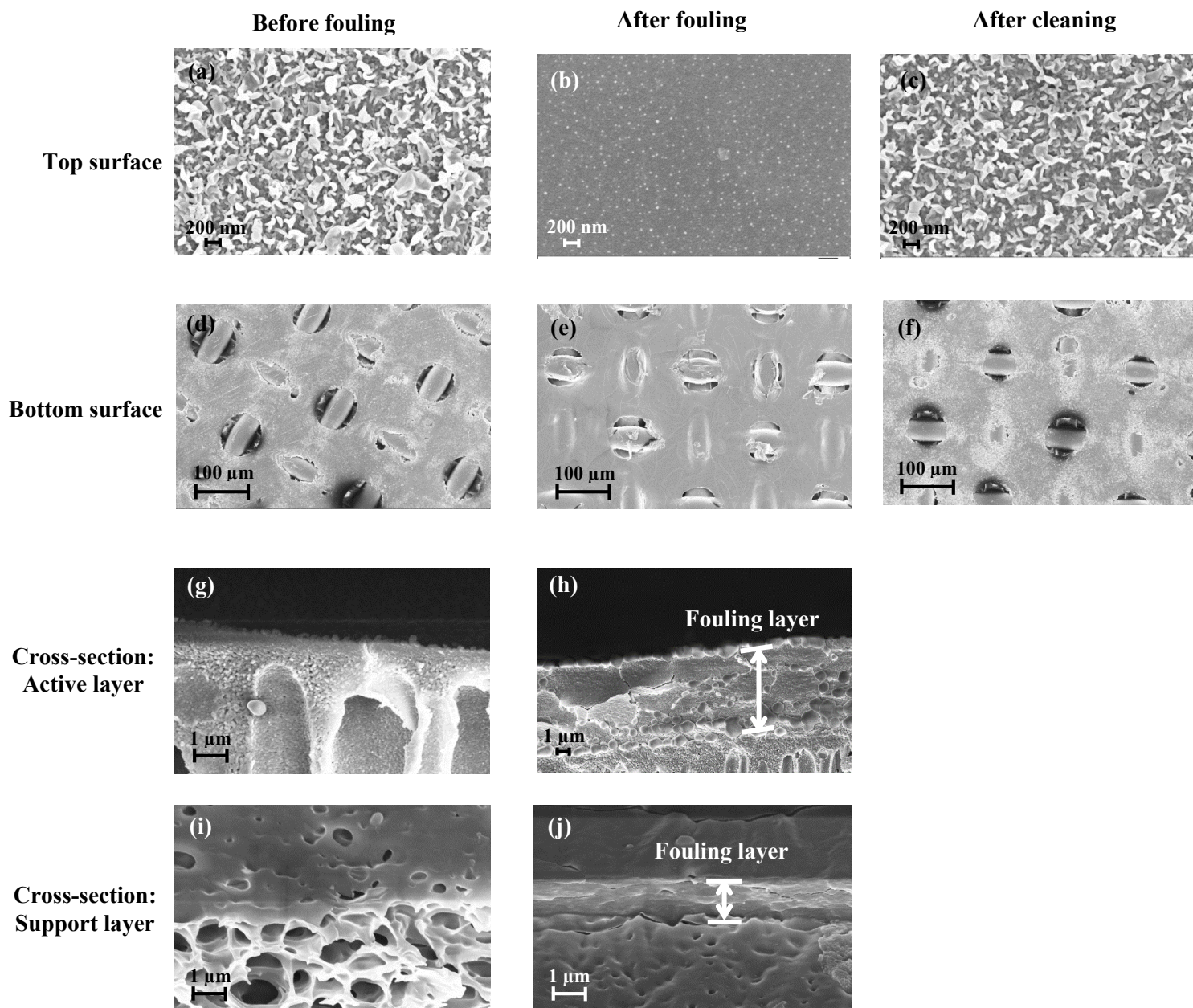


Figure 5.12: SEM micrographs of pristine, fouled and cleaned TFC membranes; (a-c) top surface, (d-f) bottom surface, and (g-j) cross-sectional micrographs. Figures (e) and (j) show the fouling layer on the TFC support surface which covered ~2-5% of the fouled membrane surface.

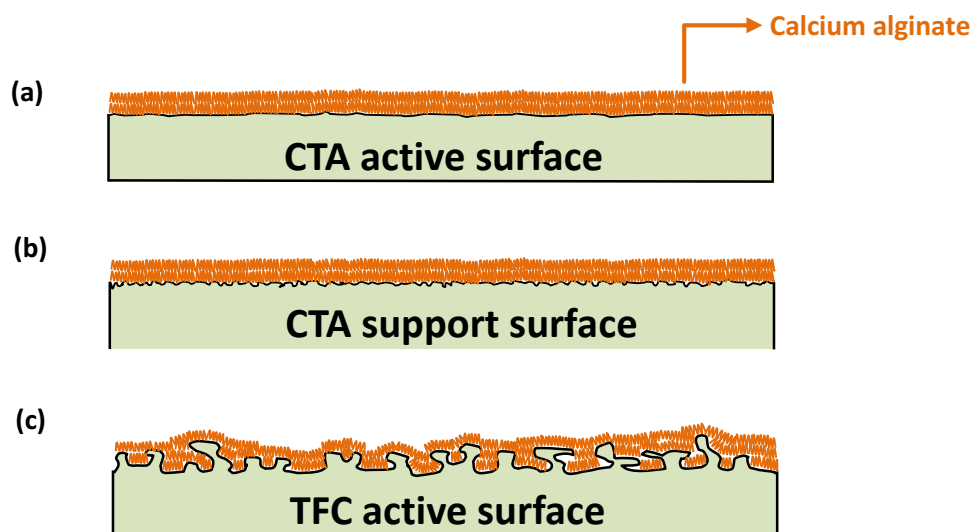


Figure 5.13: Schematic representation of foulant deposition on (a) CTA active surface, (b) CTA support surface, and (c) TFC active surface.

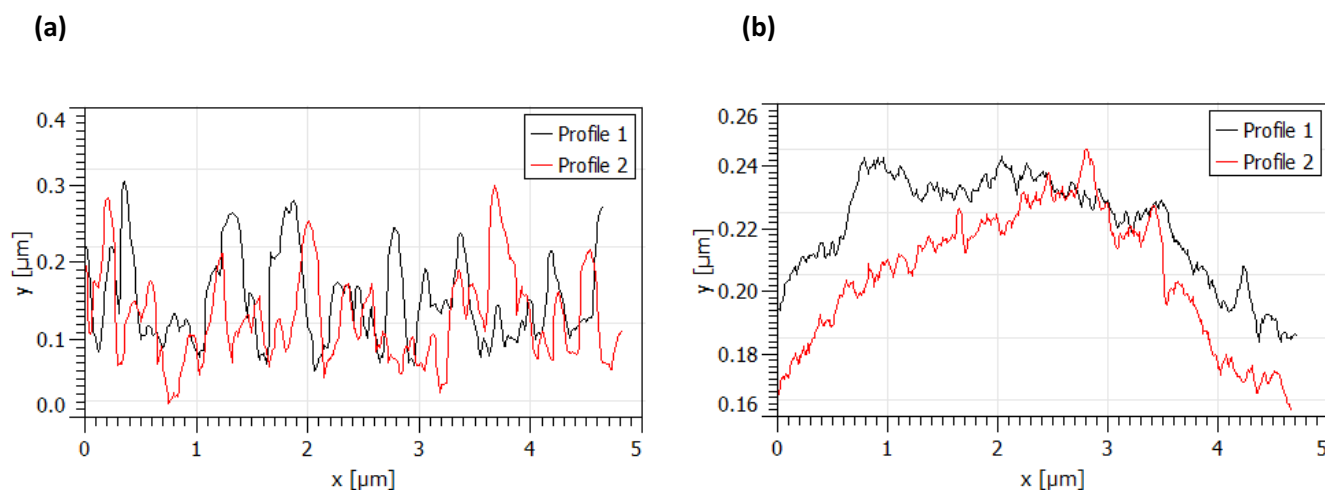


Figure 5.14: Profile view of (a) TFC active surface with a ridge-and-valley structure and (b) CTA support surface. The profile view was generated by analysing the length profile of a 5x5 μm scan size AFM image using 'Gwyddion 2.38 SPM data visualisation and analysis software'. Profile 1 and Profile 2 refer to length profiles taken from two different positions on the membrane surface.

5.3.3.2 Fouling Layer Characteristics

5.3.3.2.1 Fouling Density

Previous studies have suggested that fouling in FO is more reversible than RO due to a less compact fouling layer formed on the membrane surface as a consequence of osmotic pressure used as the driving force instead of hydraulic pressure [2, 4, 5, 135]. These inferences however, were made based on membrane performance results without being supplemented by any quantitative analysis. No effort was made to investigate the relationship between the fouling layer properties formed in FO in relation to hydrodynamic conditions, which are known to have an effect on fouling. In this section, the fouling layer density was quantified using a method explained in Section 5.2.6.3 and any correlation between fouling density and local cross-flow velocity at different radial positions in the FO cell was observed (Figure 5.15). The local cross-flow velocities were obtained from CFD simulations using the cell geometry and specified parameters representing hydrodynamic conditions in the cell. A schematic of the velocity field and magnitude at a height of 1 mm from the membrane surface (i.e. equivalent to the maximum thickness of the hydrated fouling layer) is shown in Figure 5.16.

Figure 5.15 shows the variation in fouling density with cross-flow velocity across five radial positions in the cell, starting with 0.5 cm from the centre of the membrane and radiating outwards 2.5 cm towards the edge. The cross-flow velocity decreased correspondingly from the centre to the edge of the cell as shown in Figure 5.17. Although a corresponding change in fouling density with cross-flow velocity was expected, a clear correlation was not observable. Instead, a comparable range of fouling density between 30-60 mg.cm⁻³ was observed for the CTA and TFC membranes at 1.0 cm to 2.5 cm radial distance across the cell. A clear correlation between fouling density and cross-flow velocity was not observable at these distances. The low variation in cross-flow velocity may be a reason for the insignificant effect on density, since higher cross-flow velocities have had a greater effect on fouling density [189]. The comparable range of fouling density observed on the membranes studied implies that this

property cannot be used here to explain the greater extent of fouling on the TFC top surface, which could be attributed to other factors. Fouling density measurements were not performed for the TFC membrane in PRO mode as there was no fouling layer visible on the membrane surface.

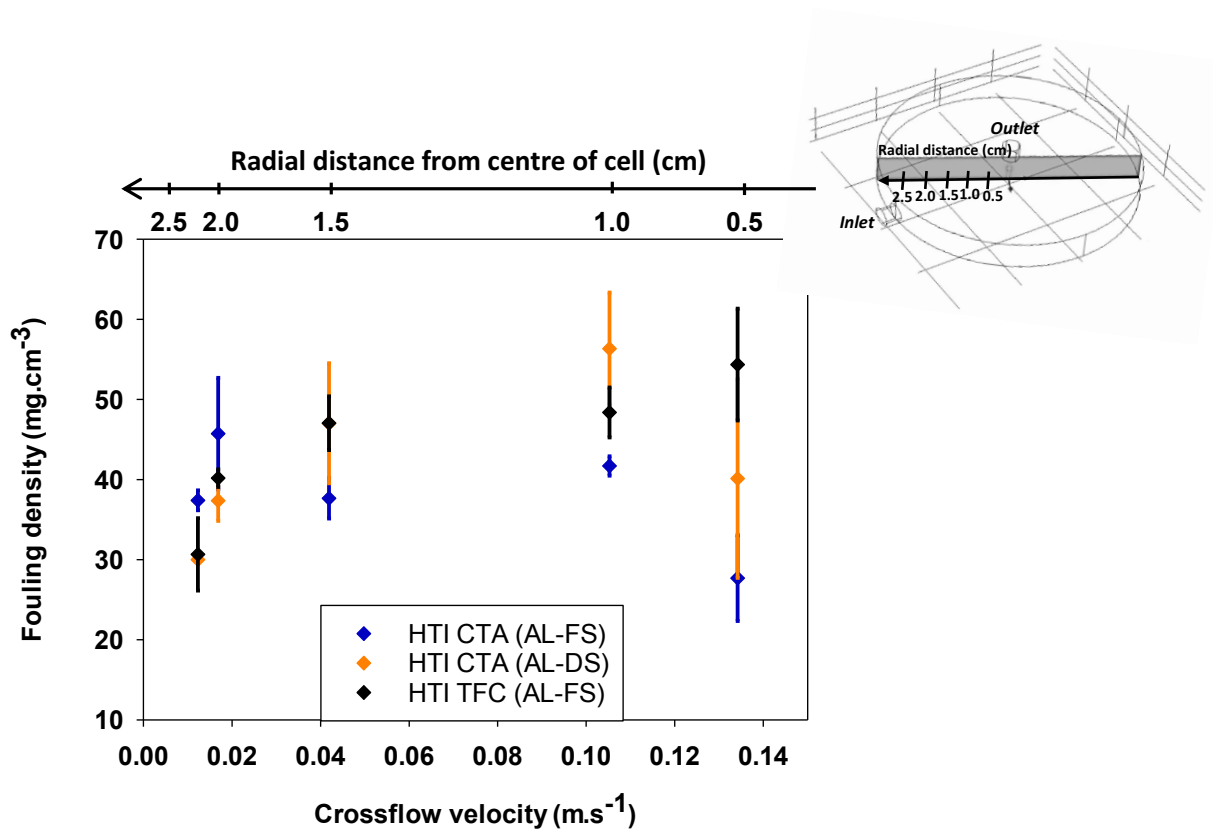


Figure 5.15: Effect of membrane type and orientation on fouling density at different cross-flow velocities.

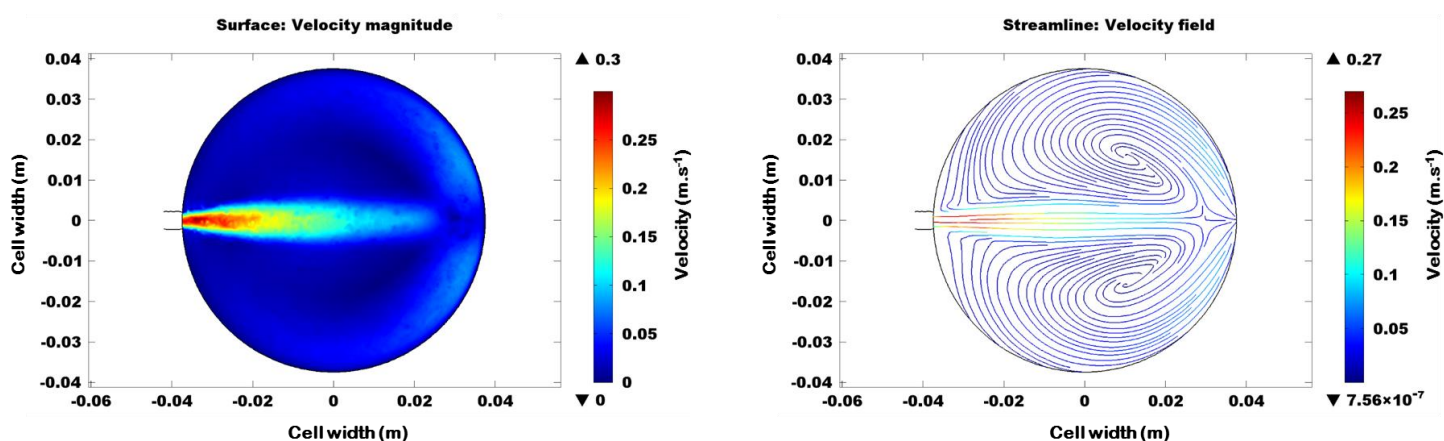


Figure 5.16: Computational Fluid Dynamics (CFD) results showing the velocity magnitude and velocity field in the FO cell at a height of 1 mm from the membrane surface.

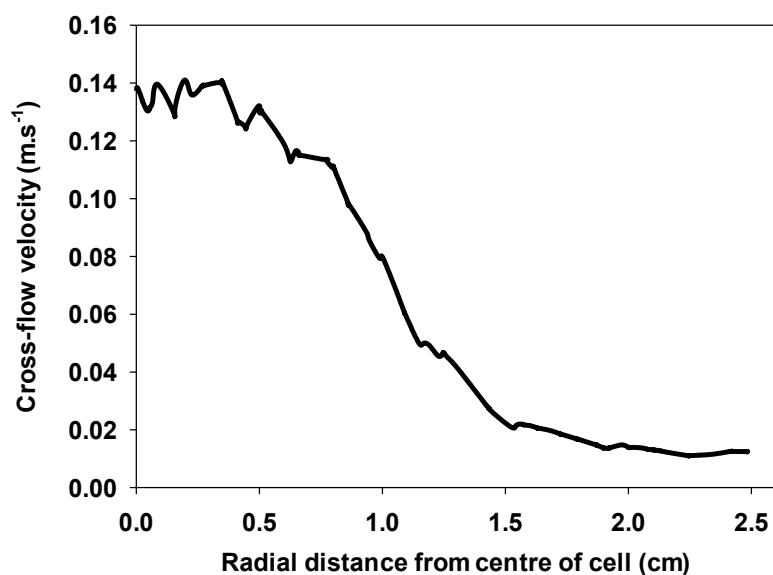


Figure 5.17: Variation in cross-flow velocity with radial distance from centre of cell at a height of 1 mm from the membrane surface. The plot was developed from CFD data obtained from simulations run under specified conditions mimicking hydrodynamic conditions in the FO cell.

5.3.3.2 Specific Mass of Foulant Adsorbed

Table 5.5 shows the total mass of alginate adsorbed per unit volume of permeate produced following the fouling experiment. It was observed that the TFC membrane in PRO mode which displayed the highest flux decline, exhibited the greatest adsorbed mass of foulant per volume of filtrate. However, despite its greater extent of fouling compared to the CTA membrane (Figure 5.10), the TFC membrane in FO mode displayed the lowest amount of alginate adsorbed per litre of permeate. This suggests that fouling of the TFC membrane in FO mode is more significantly influenced by other factors such as membrane surface properties which will be explored further in the following sections.

Membrane orientation	Membrane type	Specific mass of alginate adsorbed (mg.L ⁻¹)
FO mode	CTA	75.1±0.3
	TFC	68.0±4.2
PRO mode	CTA	84.2±2.2
	TFC	105.1±6.6

Table 5.5: Effect of membrane type and orientation on specific mass of alginate adsorbed during fouling.

5.3.3.3 Membrane Surface Properties

5.3.3.3.1 Surface Roughness

To elucidate the effect of surface roughness on the fouling behaviour of the membranes tested, AFM measurements were performed to quantify surface roughness. AFM images of the surfaces studied along with their root mean square (RMS) roughness values are shown in Figure 5.18. When comparing roughness of the different surfaces, it is important to specify the conditions used to analyse surface roughness in order to obtain the same basis for comparison

and meaningfully contribute to the analysis of fouling behaviour. Firstly, an appropriate length scale is selected, at which a meaningful correlation between surface roughness and foulant deposition can be deduced. Secondly, the peak-to-peak distance and peak-to-valley depth of the membrane surface is analysed to provide valuable information to determine if the hydrodynamic diameter of the foulant is small enough to enter the valley depth, or too large, thus resulting in deposition on the membrane surface and reducing the likelihood of valley clogging.

For the TFC membrane, four locations each measuring $2 \times 2 \mu\text{m}$ in length were selected from the $5 \times 5 \mu\text{m}$ AFM scan size (Figure 5.18 (a) and (b)). For the CTA membrane, four locations each measuring $0.5 \times 0.5 \mu\text{m}$ in length were selected from the $2 \times 2 \mu\text{m}$ AFM scan size (Figure 5.18 (c) and (d)). An average value of roughness was taken from the four locations measured and used for analysis. Although on a comparable length scale, the CTA active surface is smoother than the TFC surface, with increasing length scales however, larger, spaced out undulation features can be observed on the CTA membrane (Figure 5.19). The frequency of occurrence of these features increases with increasing length scales, resulting in an increased overall surface roughness. This demonstrates the importance of using the right length scales when comparing the roughness of different surfaces.

The TFC active layer has a uniform ridge-and-valley structure across its entire surface (Figure 5.19 (a)) with an RMS of 57.4 nm, indicating a greater roughness than the CTA membrane, RMS= 3.8 nm. In actuality, its surface roughness could be even higher as the value measured by AFM across the scanned area is limited by the probe's accessibility to the underlying polyamide surface (Figure 5.20). The TFC's rougher surface could explain the fouling behaviour results (Figure 5.10 (a)) whereby the extent of fouling was slightly greater on the TFC membrane compared to CTA in FO mode, as observed in the greater deviation in membrane permeance from the baseline during fouling. Moreover, the foulant used in this

work, calcium alginate, has a measured average hydrodynamic diameter of 15 ± 3 nm in solution. This means that on the nano scale, calcium alginate molecules are small enough to enter the valley depths of the TFC active layer and cause valley clogging, given that the peak-to-peak distance of the TFC active layer ranges from 20 nm to distances greater than 200 nm (Figure 5.14 (a)). Additionally, the peak-to-valley depth of the TFC PA layer reduces shear effects within the ridge-and-valley structure and enhances valley clogging. It is postulated that the calcium alginate molecules will first aggregate in the valleys of the TFC membrane before forming a continuous gel layer across the membrane surface, as a result of the stable "egg-box" structure formed by calcium alginate links (Figure 5.13 (c)). This renders the TFC active surface more prone to fouling by calcium alginate. A study simulating the effect of membrane surface roughness on colloid-membrane DLVO interactions [198] suggested that as particles approach closer to the membrane surface, they have a high probability of getting trapped in the valleys of the rough membrane surface. Once trapped, the particle may be shielded from cross-flow shear by the large positive asperities, resulting in enhanced initial particle deposition. The presence of an attractive energy well due to van der Waals forces of attraction surrounding each protruding asperity suggests a complex interaction between colloidal and physical (steric) interactions, which are absent on smooth surfaces [198].

The smoother active surface of the CTA membrane results in alginate aggregating and forming a continuous gel layer on the membrane surface (Figure 5.13 (a)). The comparable fouling behaviour on the active and support surfaces of the CTA membrane (Figure 5.10 (a) and (b)), can be explained partly by the similar surface roughness of both surfaces. The average RMS of the CTA support surface is 3.6 nm which is comparable to the active surface, RMS= 3.8 nm. This is not surprising, given the homogeneity of the surfaces, as demonstrated in Section 5.3.1.2. Once an initial foulant layer is deposited, the effects of surface roughness become less prominent as subsequent fouling becomes more influenced by foulant-foulant interaction.

Although the TFC support surface (RMS= 25.3 nm) is smoother than the active surface (57.4 nm), flux decline due to fouling is significantly greater in PRO mode due to pore clogging. Therefore, surface roughness is not a contributing factor to fouling in this orientation, which is more a function of the porous support structure.

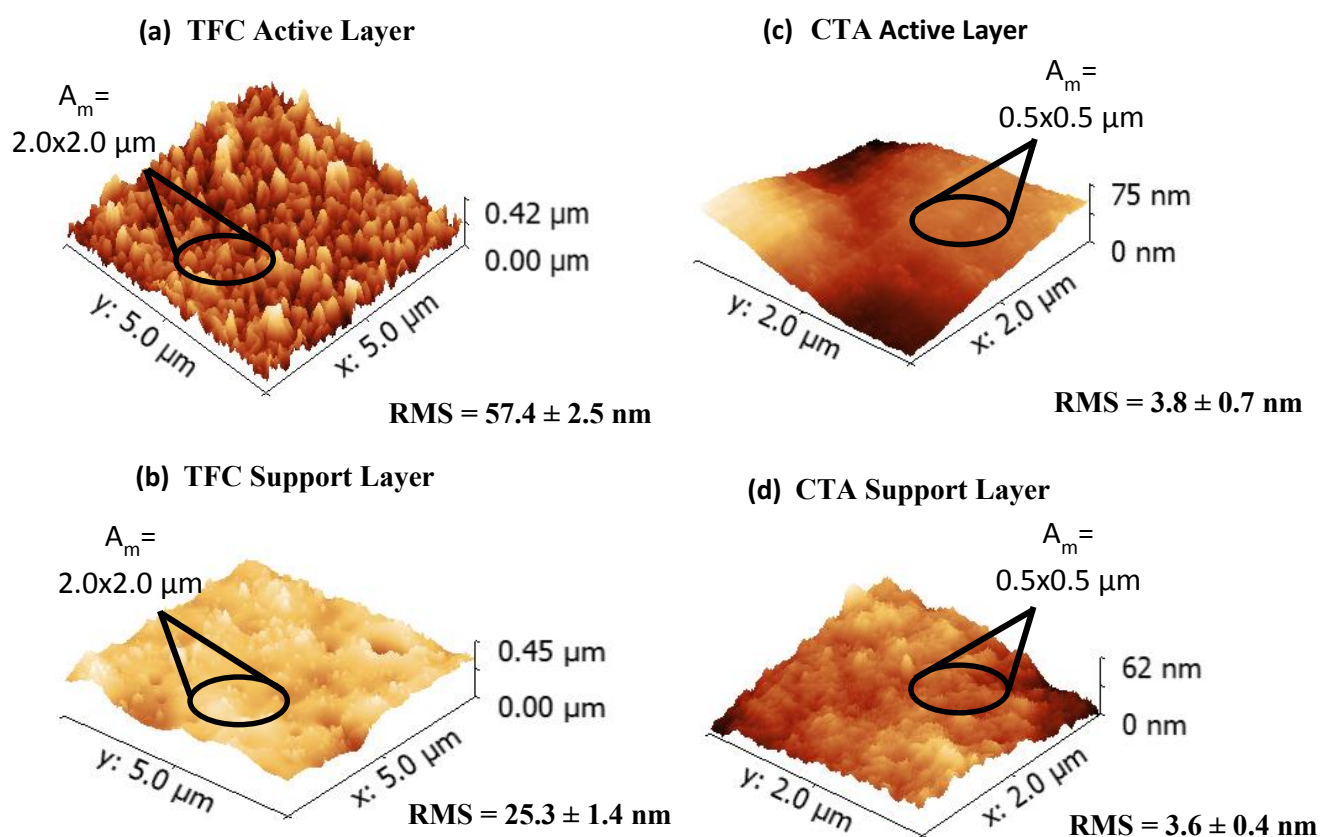


Figure 5.18: AFM images of the active and support layer surfaces of HTI TFC (a,b) and CTA (c,d) membranes. For the TFC membrane, four locations each measuring $2 \times 2 \mu\text{m}$ in size were selected from the $5 \times 5 \mu\text{m}$ scan size. For the CTA membrane, four locations each measuring $0.5 \times 0.5 \mu\text{m}$ in size were selected from the $2 \times 2 \mu\text{m}$ scan size. An average value for roughness was taken from the four measurements.

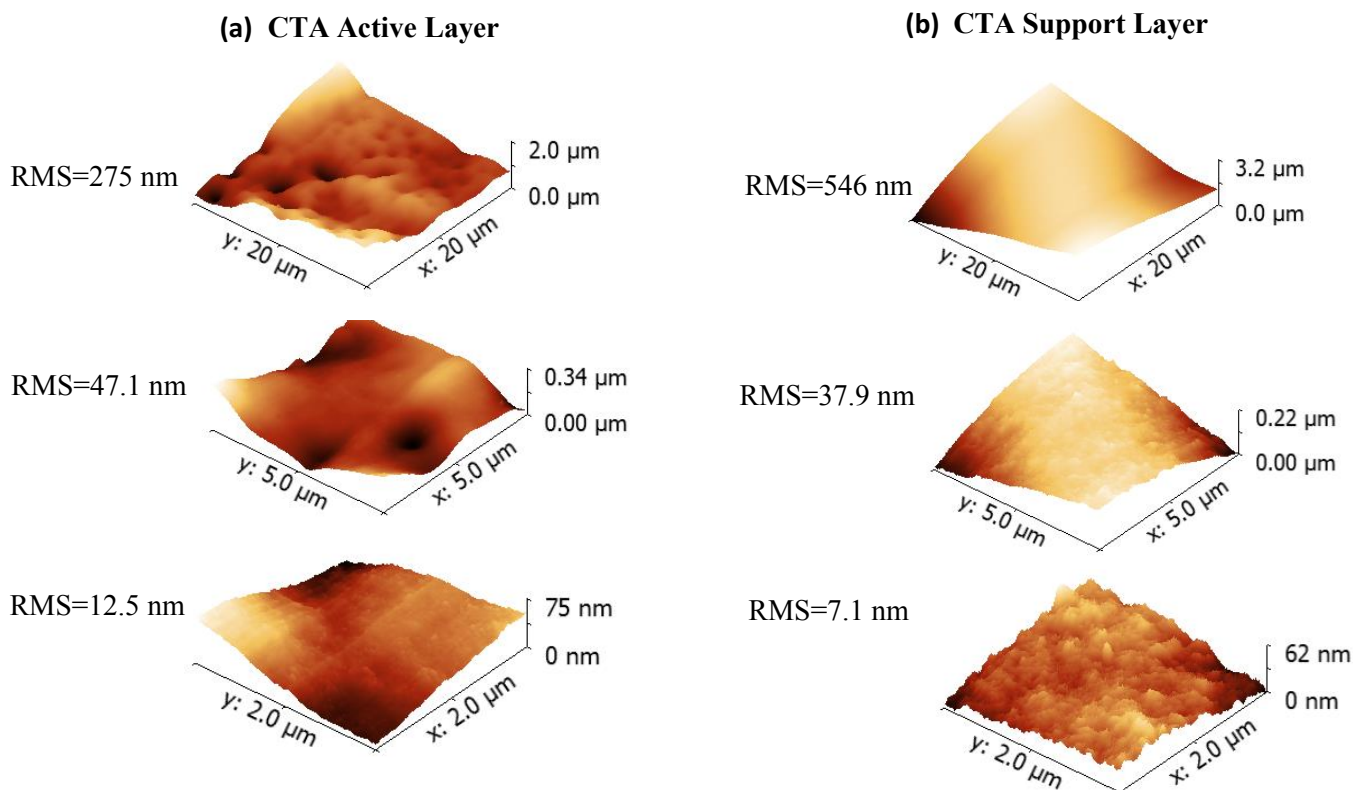


Figure 5.19: Surface roughness dependence on length scale for the HTI CTA membrane. Clear variation in surface roughness exists at different length scales. At greater length scales, larger undulation features are observed resulting in an increase in surface roughness.

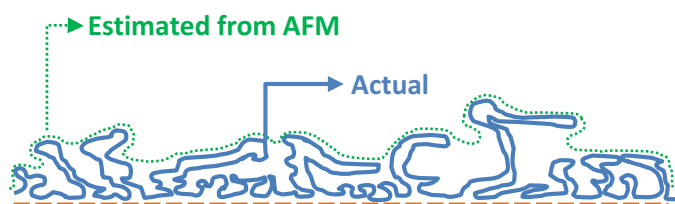


Figure 5.20: Schematic representation of the estimated surface roughness measured by the AFM probe and the actual surface roughness of the polyamide surface. [Adapted from Karan et al. [194]].

5.3.3.3.2 Surface Hydrophilicity

The CTA active and support layers had similar contact angles of $63.3\pm 1^\circ$ and $67.5\pm 2^\circ$, respectively. Amongst other factors, the similarity in surface hydrophilicity may also contribute to the comparable fouling behaviour observed on the CTA membrane (Figure 5.10 (a) and (b)). The TFC active layer has a lower contact angle of $27.4\pm 1^\circ$, suggesting that it is more hydrophilic than CTA and other high performance FO membranes [94]. However, the improved hydrophilicity of the TFC active layer is not reflected in its propensity for fouling which is greater than the CTA membrane (Figure 5.10 (a)). This suggests that surface roughness had a greater influence on alginate fouling than membrane hydrophilicity. The contact angle of the TFC support layer was not measurable as the water droplet was absorbed during measurement by the porous support.

5.3.3.3.3 Surface Charge

The electrostatic interaction between the foulant and membrane surface at different pH can be described using zeta potential. At the ambient pH of the fouling solution i.e. pH 6.8, the carboxylic acid groups of sodium alginate alone would have been almost completely deprotonated, leading to an increase in electrostatic repulsion. However, the complexation of alginate with divalent ions such as Ca^{2+} results in charge minimisation and intermolecular bridging, causing agglomeration of the alginate molecules and forming a structured gel upon deposition on the membrane surface [199]. A schematic showing the structural formula of sodium alginate and calcium alginate, following the complexation of sodium alginate with Ca^{2+} ions is shown in Figure 5.22.

At the fouling solution pH (pH 6.8), the surface charge of calcium alginate was -20 ± 2 mV, resulting in electrostatic repulsion between the negatively charged foulant and membrane surface. Despite the repulsive forces, foulant deposition occurred due to interactions such as hydrogen bonding and van der Waals forces of attraction in the short range (0-0.5 nm), ionic

bonds in the long range (0.5-2 nm) and hydrophobic interactions [200, 201]. Ionic bonds are likely formed with the membrane surface despite repulsive forces as they form at distances larger than the Debye length, where the repulsive energy is most prominent. Additionally, higher NaCl concentrations in the actual fouling feed solution may result in the compression of the electrochemical double layer, resulting in a reduction of the repulsive energy barrier [202] and an increase in net attractive forces. The soft and flexible nature of the calcium alginate gel provides a further explanation for foulant deposition as it is continuously adsorbed on the membrane surface owing to a gain in conformational entropy.

From Figure 5.21 (a), it can be observed that the CTA surface was more negatively charged than TFC in the presence of Na^+ and Ca^{2+} , resulting in greater electrostatic repulsion with alginate. This could be a contributing factor towards its lower fouling propensity compared to TFC in FO mode as seen in Figure 5.10 (a). The zeta potential of the CTA top and bottom surfaces (Figure 5.21 (b)) are very similar, owing to the same polymeric material used, which corresponds well to the comparable fouling propensities of these surfaces (Figure 5.10 (a) and (b)).

Following the adsorption of foulant onto the membrane surface, subsequent fouling is likely governed by the free energy of cohesion between approaching alginate molecules and those already deposited on the membrane surface, contributing to the onset of foulant-foulant interaction [17]. It can be seen that once the foulant layer had been adsorbed onto the membrane surface, the zeta potential of all the surfaces were comparable at the ambient pH of the fouling solution (pH 6.8), i.e. they approached the surface charge of calcium alginate (-20 ± 2 mV). This indicates that a foulant layer had been adsorbed onto the membrane surface. Further, the similar surface charge post-foulant adhesion, infers that fouling on these membranes may be governed primarily by the initial interaction between the foulant and membrane surface.

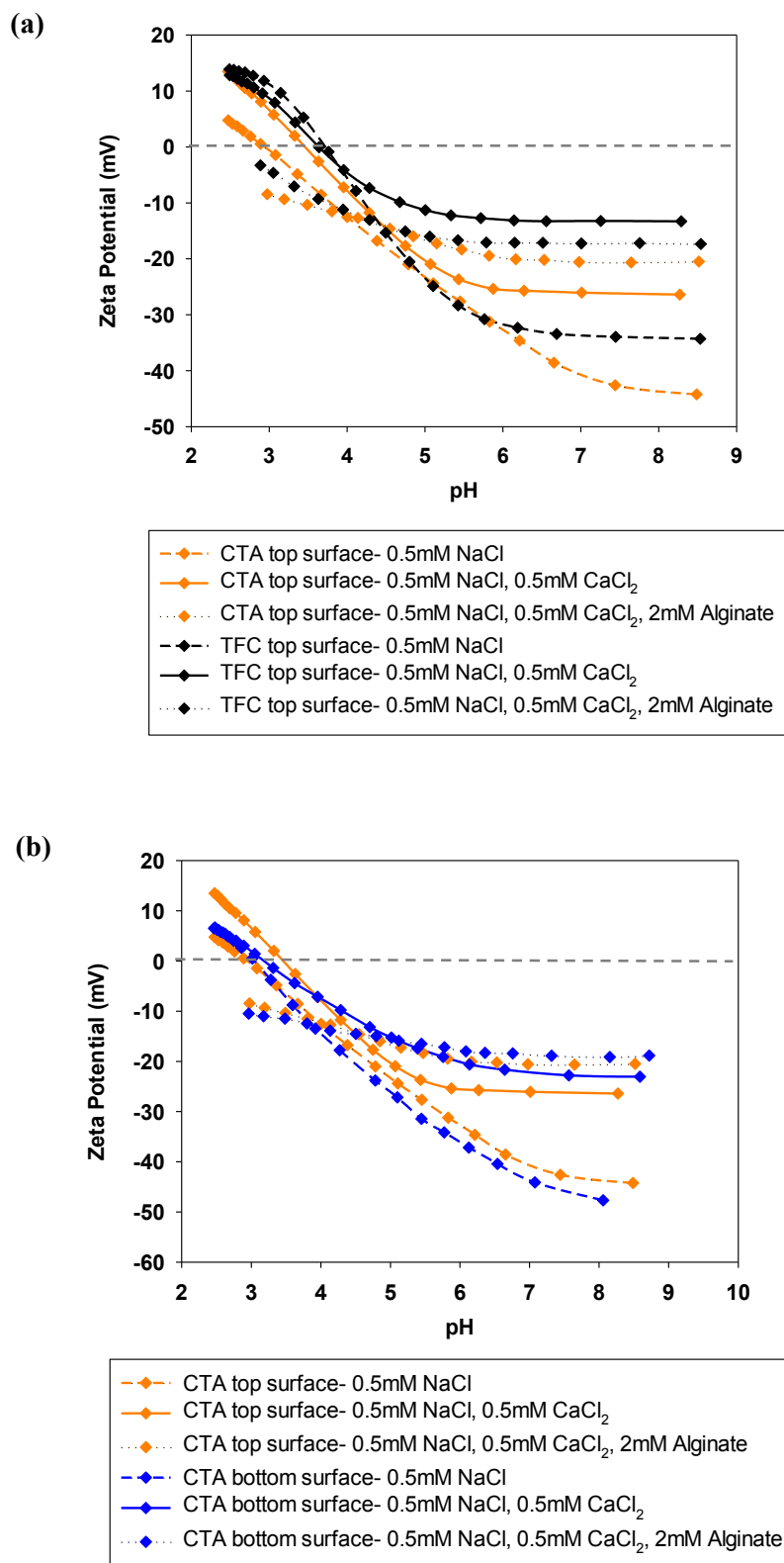


Figure 5.21: Zeta potential on (a) CTA and TFC top surface; (b) CTA top and bottom surfaces, as a function of pH with solutions representing baseline conditions (0.5 mM

NaCl), feed solution before (0.5 mM NaCl, 0.5 mM CaCl₂) and after foulant addition (0.5 mM NaCl, 0.5 mM CaCl₂, 2.0 mM Alginate).

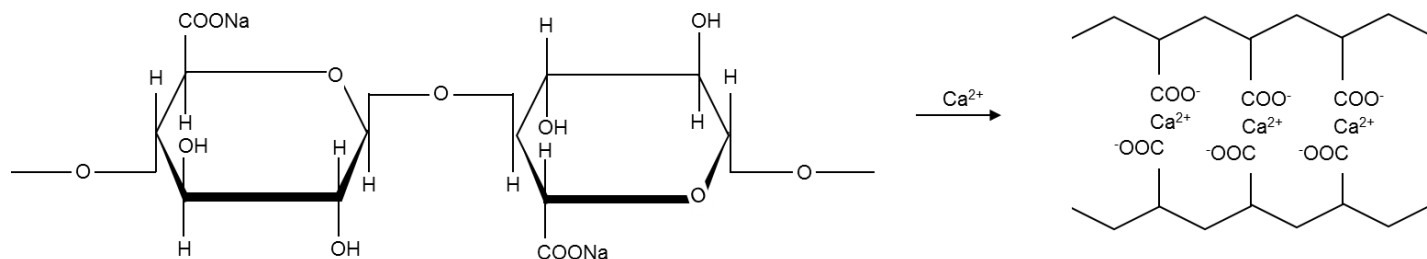


Figure 5.22: Structural formula of sodium alginate and calcium alginate, following the complexation of sodium alginate with Ca²⁺ ions. [Adapted from Ichiura et al. [203]].

5.3.3.3.4 Surface Chemical Heterogeneity

A study by Kim et al. has shown that surface chemical heterogeneity influences foulant deposition by introducing a higher area of favourable sites or patches for foulant adhesion [204]. The extent of chemical heterogeneity is related to the distribution of the atomic (or molecular) species and functional groups present on the membrane surface, which in turn affect surface composition and interactions between foulant and the surface [205].

The XPS results (Table 5.1) provide a good indication of the various functional groups present on the membrane surface which contribute to surface chemical heterogeneity. These results illustrate the presence of O-C=O groups on the TFC membrane surface (5.5% of the C1s spectra) which is characteristic of highly polar carboxylate groups available for ionic bonding with the foulant, thus enhancing the number of favourable sites for foulant adhesion. For the CTA membrane, the O-C=O group (24.9% of the C1s spectra) is associated with the acetate functional group and hence, exhibits a weaker ion-dipole interaction with the foulant at the fouling solution pH of 6.8. This further explains the greater fouling propensity on the TFC active surface compared to CTA. Additionally, the presence of excess unreacted amine groups on

the TFC membrane (5% of the N1s spectra) could generate favourable sites for foulant adhesion via electrostatic forces of attraction between the positively charged sites and negatively charged foulant. A molecular dynamic study on the interaction between a hydrated polyamide membrane and calcium alginate [201] showed that the probability of forming long-range (0.5-2 nm) ionic bridges between the negatively charged carboxylate ions on the alginate and the PA surface is over 80%. The rest of the binding sites involve direct PA-alginate interactions without metal ions. These include short-range (0-0.5 nm) hydrogen bonds between the hydroxyl group of the alginate molecule and carboxylate group of the PA layer, van der Waals forces of attraction and hydrophobic interactions.

5.3.4 Cleaning and Fouling Reversibility

Physical and chemical cleaning is a significant step in any membrane process to minimise fouling and extend the performance lifetime of a membrane. Investigating the cleaning behaviour of FO membranes enables the quantification of fouling reversibility, which subsequently provides information on the fouling propensity of these membranes.

The results for normalised flux decline after fouling and flux recovery after cleaning are presented in Figure 5.23. The CTA membrane in FO and PRO mode had high cleaning efficiencies and flux recoveries of 96% and 95% respectively. These results suggest a physical removal of the fouling layer as a result of the shear force generated by increased cross-flow. They also suggest that fouling by calcium alginate was mainly a result of adsorption on the active and support surfaces of the CTA membrane rather than a pore clogging mechanism.

The flux recovery of the TFC membrane after cleaning in FO mode was 85%, i.e. 10% lower compared to CTA. This suggests a greater adhesion of foulant on the TFC active surface, which can be attributed to factors such as surface roughness, surface charge, surface chemical heterogeneity and hydrodynamic effects i.e. the lack of shear in the ridge-and-valley structure of the PA layer, rendering cross-flow less effective on foulant removal in this region.

A previous study [201] suggested that due to the flexible gel-like behaviour of calcium alginate, the alginate gel may tend to adapt to the morphology of the polyamide membrane surface, thus increasing the contact area with the membrane. The packing density of the gel is distance dependent from the membrane surface, with a more compact gel formed adjacent to the surface due to the strong attraction between the foulant and the membrane. As suggested by this study, this “distance-dependent” density contributed to the weaker effects of cross-flow cleaning in removing the alginate from the PA surface.

Cleaning with cross-flow was not effective on the TFC membrane in PRO mode due to pore clogging. The reduced effects of cross-flow in the porous support renders shear force ineffective as a cleaning mechanism in this orientation with a flux recovery of only 37%. Hence, a more effective physical cleaning method had to be adopted which is presented in the following section.

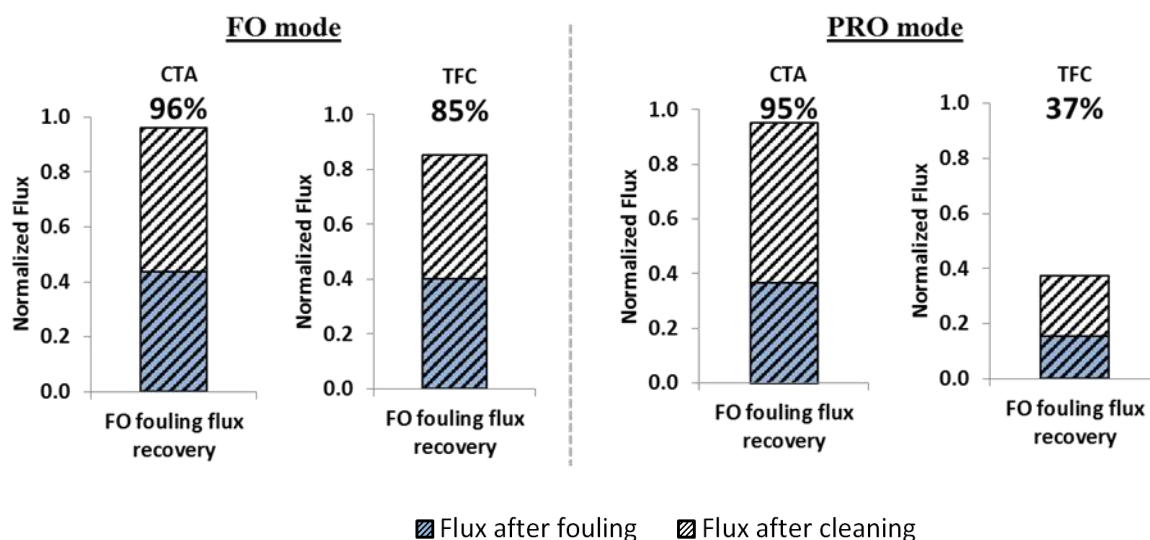


Figure 5.23: Flux recovery of fouled CTA and TFC membranes in FO and PRO mode, after cleaning with DIW at 60 L.h⁻¹ for 15 minutes. Flux after fouling is normalised by the initial flux of the fouling experiments, while flux after cleaning is normalised by the initial baseline flux of a pristine membrane.

5.3.5 Effect of TFC Membrane Support Structure

5.3.5.1 On Fouling and Cleaning Behaviour in PRO mode

As illustrated in the previous section, physical cleaning with increased cross-flow in PRO mode was ineffective in removing the foulant layer deposited in the porous support of the TFC membrane. Hence, backwashing was employed as an alternative cleaning method to improve flux recovery of the fouled membrane. Figure 5.24 (a-d) shows four fouling tests, each conducted over a period of 2 h, 5 h, 16 h and 27 h, respectively. Backwashing was performed after each fouling experiment. Results indicate that the amount of alginate accumulated in the porous support increased significantly in the first 10 hours of fouling and approached a steady state thereafter (Figure 5.24 (e)). The higher initial fluxes coupled with lack of shear in the porous support induced greater initial fouling. Interestingly, the onset of steady state flux observed after 10 hours of fouling (Figure 5.24 (d)) corresponds to the insignificant increase in the amount of foulant adsorbed within the support layer between 10 h and 27 h (Figure 5.24 (e)), suggesting that further fouling of the membrane had occurred minimally during this period.

The increase in the amount of foulant adsorbed over time had an effect on the degree of backwash flux required for fouling reversibility. As observed in the 2 h and 5 h fouling experiments, the efficiency of backwashing using the original fouling FS and DIW on the draw side decreased with time as more foulant was adsorbed within the porous support layer. This is quantitatively shown by the 87% flux recovery achieved after the 2 hour fouling test but only 65% recovered after 5 hours of fouling under the same cleaning conditions. However, when backwashing was conducted with 1 M NaCl as the FS, a higher backwash flux was achieved, resulting in almost 100% flux recovery. Using the same cleaning solution conditions, similar flux recoveries were observed for membranes fouled over 16 and 27 hours. For the membrane fouled over 27 hours, backwashing was conducted at a higher cross-flow rate of 60 L.h⁻¹ to ensure that foulant removed from the porous support was effectively cleaned off the membrane surface.

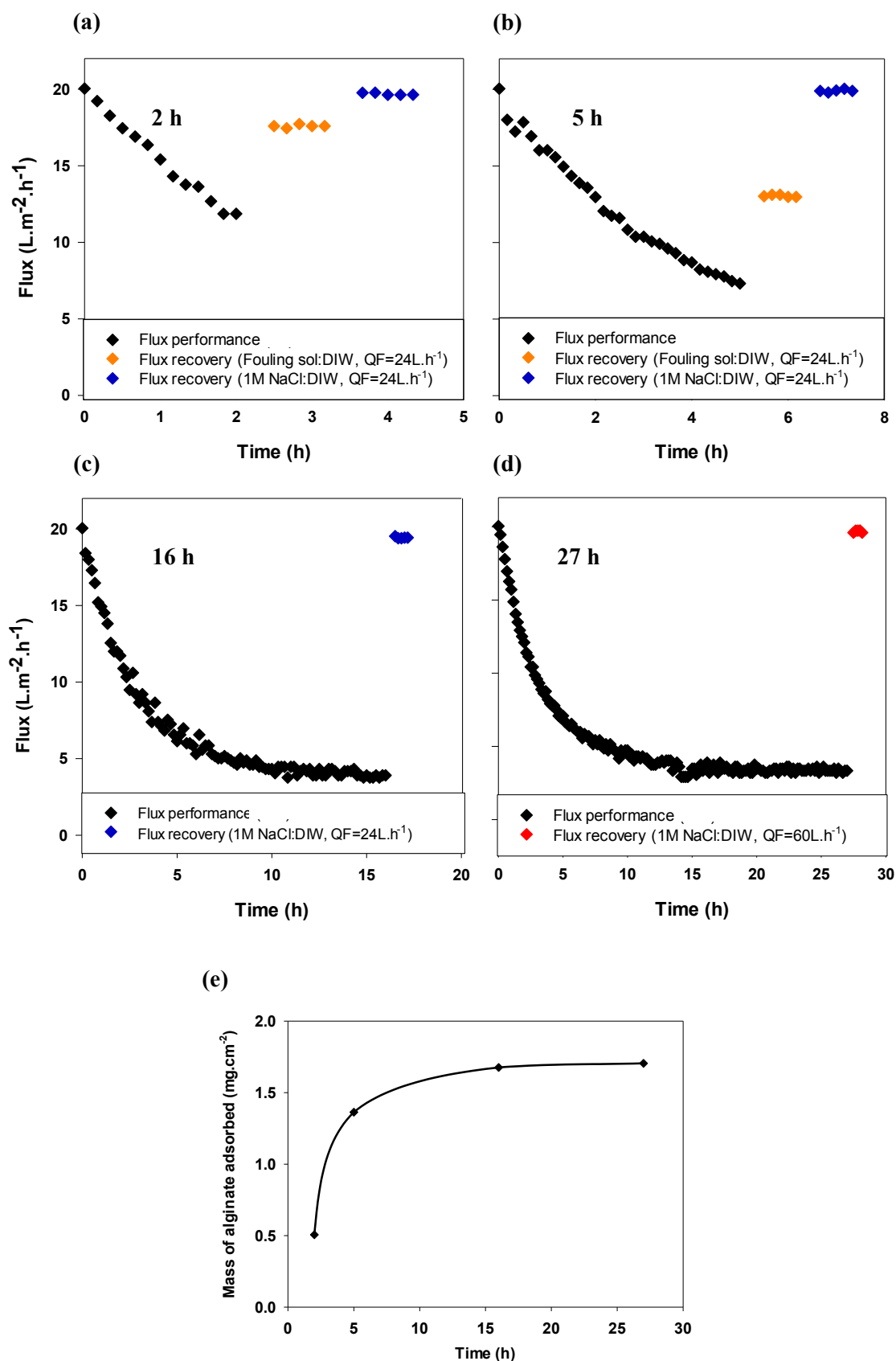


Figure 5.24: (a-d) Fouling behaviour and flux recovery of the HTI TFC membrane in PRO mode under various cleaning conditions at 2 h, 5 h, 16 h and 27 h, and (e) Specific mass of alginate adsorbed within the porous support at 2 h, 5 h, 16 h and 27 h of fouling in PRO mode.

5.3.5.2 On Critical Flux Behaviour in PRO mode

The onset of steady state behaviour observed in Figure 5.24 (d) and (e) after 10 hours of fouling, suggests that further fouling of the membrane occurred minimally during this period and to a negligible extent beyond 16 hours. The steady state flux behaviour observed may be influenced by a critical flux phenomenon (Figure 5.25). A critical flux experiment was performed by increasing DS concentration in predefined steps (analogous to pressure stepping for critical flux determination in MF and UF membranes), with a stepping duration of 30 minutes at each concentration step. 30 minutes was chosen to avoid excessive dilution of the DS and concentration of FS. Here, the weak form of critical flux is used which can be defined as the threshold flux above which significant fouling (i.e. flux decline from the baseline or foulant accumulation on the membrane) is experimentally observed [206]. The FO critical flux in this particular case was between 7.1 and 11.7 L.m⁻².h⁻¹, i.e. corresponding to the region whereby the water flux started to deviate from the baseline flux. This corresponds to a critical DS concentration between 0.25 and 0.50 M NaCl. The fluxes at the onset of steady state behaviour observed in Figure 5.24 (d) are below the critical flux value. Hence, flux decline in this region is no longer a function of membrane fouling and remains a consequence of osmotic dilution and concentration polarisation effects. At these low fluxes, the effect of cross-flow velocity likely exceeds permeation drag, thus preventing further foulant deposition within the porous support. Fouling reversibility was evaluated at the end of the fouling experiment following a backwashing step, by replacing the DS with DIW and FS with 1 M NaCl. The results show that fouling was highly reversible with a recovery of 98%.

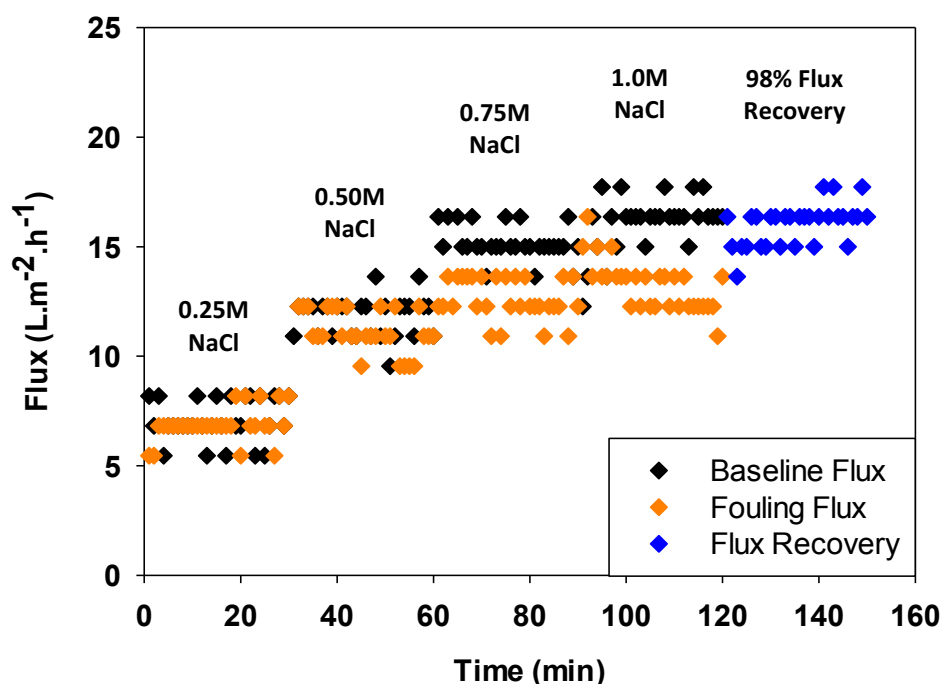


Figure 5.25: Flux behaviour of the TFC membrane in PRO mode with a 0.25 M-1.0 M NaCl DS and 50 mM NaCl FS. 200 mg.L⁻¹ alginate and 0.5 mM CaCl₂ were added to the fouling FS. DS concentration was increased in predefined steps, with a stepping duration of 30 min. Flux recovery was measured with a 50 mM NaCl FS and 1.0 M NaCl DS, following a backwashing step. A critical flux behaviour is observed between 0.25 M and 0.50 M DS.

5.4 Conclusion

Two FO membranes with varying chemical and structural properties were studied. The HTI TFC membrane was found to exhibit superior permeance and rejection performance compared to HTI CTA due to its favourable surface and structural properties. This could imply that thin film composite membranes with ideal structures tailored for FO use are a step forward in the development of high performance FO membranes in comparison to the integrally

asymmetric CTA membrane. However, this observation does not account for the performance under fouling conditions.

From the fouling study conducted with calcium alginate as a model organic foulant, it can be concluded that the TFC membrane performed poorly compared to CTA under fouling conditions in both orientations. In FO mode, the TFC active layer had a higher surface roughness and a lower negative charge resulting in greater fouling propensity. Additionally, the presence of carboxylate functional groups enhanced the number of favourable sites for foulant adhesion through ionic bonding. Other factors such as surface hydrophilicity and fouling density did not have a significant effect on the fouling propensity of these membranes. This implies that when designing TFC FO membranes with fouling mitigation properties, greater emphasis should be placed on i) reducing surface roughness whilst maintaining intrinsic membrane permeance, ii) modifying surface charge to enable greater electrostatic repulsion of the approaching foulant, and iii) minimising surface chemical heterogeneity. Comparable fouling densities were observed on the CTA and TFC active surfaces suggesting that stronger interactions between the foulant and the membrane surface do not necessarily lead to increased fouling density, which is likely a greater function of applied hydraulic forces such as in the case of RO.

In PRO mode, membrane surface properties played a less significant role compared to membrane structural properties in determining fouling behaviour. The highly asymmetric and open structure of the TFC support caused severe fouling as a result of pore clogging, exacerbated by the reduced effects of cross-flow within the porous support. Although pore clogging has most commonly been used to describe the fouling mechanism in FO supports, alginate fouling occurred as a surface phenomenon on the support layer of the CTA membrane. This was attributed to the smooth and dense surface of the CTA support coupled with the highly structured gel formed by calcium alginate upon aggregation. This observation indicates that the fouling mechanism on FO membranes is highly specific to the foulant size

and aggregation structure as well as the support pore size in relation to the foulant in question. Hence, FO supports of different structures and pore sizes may be selected for use depending on the type of foulant present in the feed water, in order to achieve a balance between superior flux performance and reduced fouling propensity when the PRO mode is utilised. If smaller and weakly aggregating foulants are used, then a trade-off between membrane performance and fouling mitigation would have to be achieved as the use of integrally asymmetric or double-skinned membranes with greatly improved fouling resistance, will be limited by their denser structures and enhanced ICP effects. Unless significant improvement is made to improve the structure and reduce ICP in these membranes, fouling mitigation will be at the expense of flux performance.

Due to the lower fouling propensity and nature of foulant deposition on the surface of the CTA membrane, physical cleaning with DI water and an increased cross-flow velocity was sufficient to achieve an almost complete flux recovery. The TFC membrane however, had poorer fouling reversibility and required backflushing with a sufficiently high driving force in PRO mode, in order to achieve comparable flux recoveries to CTA.

The fouling results imply that the successful application of FO would involve a diversification of membrane designs tailored to the type of feed solution used. The compromise between membrane performance as a result of membrane orientation used, and membrane fouling propensity, would have to be addressed by innovating improved structural properties of FO membranes such that ICP effects within the support of integrally asymmetric or double skinned membranes are mitigated. Alternatively, the successful reengineering of the polyamide surface on a highly open support can result in superior performance and minimal fouling in FO mode, which would be highly beneficial for treatment of raw feeds with high fouling potential.

The cleaning results prove that despite different mechanisms of fouling and quantities of foulant adsorbed in the FO membranes, FO is undoubtedly a resilient process with high

cleaning efficiencies and fouling reversibility. Hence, although most FO hybrid processes may not be competitive from an energetic perspective compared to RO, their high fouling reversibility may reduce or eliminate the need for chemical cleaning and pretreatment, which makes them an attractive prospect for use with challenging feeds.

Chapter 6

6 Towards Mitigating the Challenge of Internal Concentration

Polarisation²

6.1 Introduction

FO has a few potential benefits compared to conventional pressure driven membrane processes, such as its lower fouling propensity, potential to treat high salinity feeds and leverage low-cost thermal energy for draw solution (DS) recovery. Despite these advantages, which have been discussed in Chapter 4 and Chapter 5, any FO hybrid process with a membrane driven DS recovery stage, would require significant membrane areas due to the number of unit operations and stages required in both the FO and DS recovery stages. This would increase the capital cost required for FO hybrid systems, potentially rendering it uncompetitive with RO. One solution to reducing the FO footprint is to improve the productivity per m² of membrane. A major issue limiting productivity of current FO membranes is concentration polarisation, specifically internal concentration polarisation (ICP) observed within the porous structure of the support layer, which is reported to be mainly responsible for water flux decline [22, 50, 51, 207]. The severity and “self-limiting” behaviour of ICP have been discussed in Chapter 1 and Chapter 2, and is expressed in the models for water flux in forward osmosis, as illustrated in Equation 2.25 and Equation 2.26 of Chapter 2.

A number of publications have focused on limiting ICP effects by improving structural properties of the membrane support layer to reduce the so-called structural (S) parameter [22,

² I would like to acknowledge Jiang Zhiwei for his collaboration and contribution to the fabrication of the in-house membranes presented in this chapter, Santanu Karan for his support, and SEFAR Limited's (UK) Chris Sheridan for providing free samples of the Nylon 6,6 woven open mesh fabrics used in this work.

54, 62, 71, 99]. This is done essentially by making supports with improved porosity, pore interconnectivity, hydrophilicity and tortuosity approaching unity, whilst maintaining or reducing support thickness. However, many studies achieved only marginal improvements in flux. Additionally, membranes made by phase inversion of the support were limited by FO mode fluxes in the range of 18-25 L.m⁻².h⁻¹ for systems using DIW as the feed solution and up to 2 M NaCl as the draw solution, due to severe ICP [22, 51, 53].

Possibly the best performing FO membrane currently available in literature, the nanocomposite FO membrane (NC-FO) with a scaffold-like nanofiber support layer, exhibits improved tortuosity, porosity and thickness over conventional sponge-like and macroporous support layers [62]. The unique structure of the nanofiber support layer enabled improved fluxes and reduced ICP effects. The NC FO membrane achieved fluxes almost three times that of the commercial HTI TFC membrane in FO mode and double the flux in PRO mode, using DIW and 1 M NaCl as the feed and draw solution, respectively. Although this study along with others [71] are closing the gap in the ICP challenge, there is still room for further improvement.

This chapter investigates a novel method of fabricating FO membranes by interfacially polymerising a free-standing, salt rejecting polyamide (PA) film using a floating technique, and directly depositing this film onto an open mesh fabric. By doing this, the need for a phase inversion support is entirely eliminated. A commercially available Nylon 6,6 (N6,6) woven, open mesh fabric is used for its hydrophilicity, high tortuosity, precision engineered mesh and availability in a range of mesh sizes. The membranes were fabricated using mesh sizes ranging from 10 µm by 10 µm up to 25 µm by 25 µm to observe the effect of different mesh fabric supports on FO performance.

6.2 Materials and Methods

6.2.1 Chemicals and Materials

Nylon 6,6 (N6,6) precision woven open mesh fabrics were acquired from SEFAR Limited (UK). All solvents used in this work were HPLC grade. Methanol and hexane were purchased from VWR International Ltd., UK. Trimesoyl chloride (TMC) 98% and m-phenylenediamine (MPD) flakes $\geq 99\%$ were purchased from Sigma Aldrich, UK. MPD was purified under vacuum sublimation ($\sim 1 \times 10^{-2}$ mbar) at 75 °C fitted with a cold water trap and used fresh each time. Sodium chloride and acid fuschin were obtained from Sigma Aldrich, UK. Single crystal silicon wafers were purchased from Compart Technology Ltd. UK, and used as substrates for atomic force microscopy (AFM).

6.2.2 Membrane Preparation

The in-house FO composite membranes were fabricated by first interfacially polymerising a free-standing, salt rejecting polyamide (PA) layer using a controlled interfacial polymerisation technique, followed by deposition of the PA layer onto an N6,6 open mesh fabric by means of sucking under an applied vacuum. The properties of the N6,6 fabric used in this chapter are presented in Table 6.1.

The apparatus used for fabricating the FO membrane is shown in Figure 6.1. Two PA films with varying surface roughness were fabricated. The smoother PA film was fabricated using an MPD concentration of 3 wt%, TMC concentration of 0.15 wt% and a reaction time of 1 minute. The rougher PA film was fabricated with an MPD concentration of 6 wt%, TMC concentration of 0.3 wt% and a reaction time of 1 minute. A schematic of the interfacial reaction between TMC and MPD is shown in Figure B-1 of Appendix B. The free-standing film was formed by first pouring 25 ml of aqueous amine solution into a glass funnel (Advantec, Japan) with an effective diameter of 7.2 cm, followed by 25 ml of the TMC in hexane solution to create the interface (Figure 6.1). The timer was started as soon as the TMC solution was poured into

the funnel to record the polymerisation reaction time. After 1 minute reaction time, the vacuum pump was started and an applied vacuum of 10 mbar below atmosphere was used to suck the film onto the N6,6 mesh. The N6,6 mesh was clamped in the funnel and placed on the smooth side of a polypropylene nonwoven backing (Novatexx 2471, Freudenberg, Germany) for added support during PA film deposition. After depositing the film on the mesh support, excess TMC solution was discarded by pouring it out of the funnel. The PA film was subsequently cleaned with a sufficient amount of hexane to remove any remaining TMC and inhibit further reaction. The membrane was removed from the funnel, left to dry and stored at room temperature in a petri dish.

Fabric code	Mesh size (μm)	Open area (%)	Thickness (μm)
03-10/2	10.0	2.0	45.0
03-15/10	15.0	9.5	60.0
03-20/14	20.0	14.0	55.0
03-25/19	25.0	19.0	55.0

Table 6.1: Properties of the N6,6 open mesh fabrics used as membrane supports in this study.

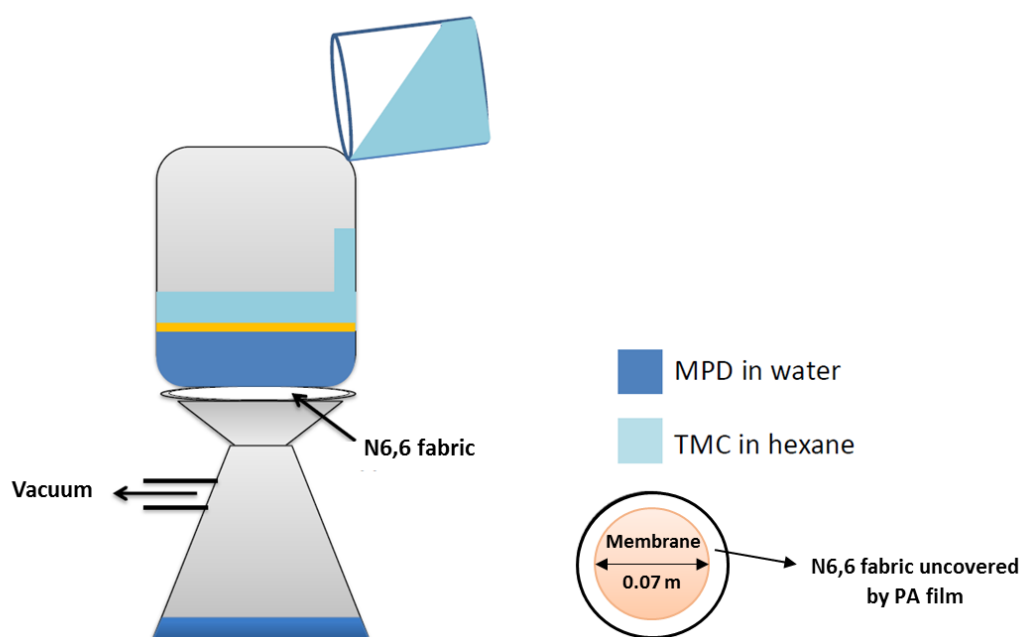


Figure 6.1: Schematic of the apparatus used for floating PA film formation and deposition onto a fabric support.

6.2.3 Commercial FO membranes

The commercial forward osmosis membranes used in this chapter for comparison of performance with in-house made membranes were obtained from Hydration Technology Innovations (HTI, Albany, OR). The HTI CTA membrane has an asymmetric structure and is made of cellulose triacetate supported by an embedded polyester mesh. The total thickness of the membrane is $\sim 50 \mu\text{m}$. The HTI TFC membrane resembles a typical TFC membrane with a tailor-made support structure to suit FO applications. A polyester mesh is embedded in the support for added mechanical strength. The total thickness of the membrane is $\sim 100 \mu\text{m}$. The TFC membrane was prewetted in 50% solution of methanol for 60 min to ensure that the membrane porous support is fully water saturated. SEM images of the cross-section and aerial views of the HTI CTA and TFC membranes are shown in Figure B-2 of Appendix B.

6.2.4 FO Test Solutions

Unless mentioned otherwise, the feed and draw solutions for the forward osmosis tests comprised DIW and 1 M NaCl solution, respectively. These compositions were selected to comply with the standard methodology for evaluating membrane performance in osmotically driven membrane processes [85], in order to provide the same basis for comparison with other membranes reported in literature.

6.2.5 Intrinsic Membrane Properties

The intrinsic pure water permeance (L_p) and salt rejection of the in-house membranes were obtained by performing RO tests in a cross-flow cell on the same free-standing PA film deposited onto an ultrafiltration (UF) polysulfone (PSf) support, using a method explained elsewhere [194]. The pure water permeance and salt rejection were calculated using Equation 5.1 and Equation 5.2 in Chapter 5.

RO tests were run with the PSf support instead of N6,6 open mesh fabric after initial tests on the N6,6 fabric proved unsuccessful, following defects formed in the PA film when tested under pressure. Permeance and rejection values reported were steady state values obtained under RO conditions after allowing for membrane compaction. Intrinsic pure water permeance was measured by permeating a DIW feed with an applied pressure of 20 bar. Salt rejection was determined by pressurising 2 g.L⁻¹ NaCl under the same applied pressure, and measuring the NaCl concentration in the permeate and retentate after a given time to satisfy the terms in Equation 5.2. Pure water permeance and salt rejection for the smooth PA film measured on the PSf support were 0.62 L.m⁻².h⁻¹.bar⁻¹ and 99.3%, respectively.

6.2.6 Membrane Characterisation

6.2.6.1 Scanning Electron Microscopy (SEM)

Arial and cross-sectional images of the membranes studied were taken with a high resolution, field-emission gun scanning electron microscope (FEGSEM), LEO Gemini 1525 (Karl Zeiss). For the cross-section images of the membranes, the samples were prepared by soaking in ethanol and freeze-fractured in liquid nitrogen to preserve the pore structure, before drying in air and carefully cut with a scissors to avoid any damage. Prior to imaging, the samples were coated with a 10 nm thick layer of chromium sputtered (Q150T turbo-pumped sputter coater, Quorum Technologies Ltd.) under an Ar atmosphere (2×10^{-2} mbar) to achieve a minimum conductivity for reliable SEM measurements.

6.2.6.2 X-ray Photoelectron Spectroscopy (XPS)

X-ray photoelectron spectroscopy (XPS) results conducted on a polyamide film made with 3 wt% MPD, 0.15 wt% TMC, was adapted from Karan et al.[194]. The sample was prepared by transferring the floating film onto a PLATYPUS™ gold coated silicon wafer. The XPS study was conducted by the Oxford Materials Characterisation Service and BegbrokeNano, Department of Materials, Oxford University. The survey spectra and core level XPS spectra were recorded from at least two different spots on the membrane surface of size 400 μm . 200 Watt unmonochromated Mg X-ray excitation was used. The analyser was operated at constant pass energy of 200 eV for wide scans and 20 eV for detailed scans. Data processing was performed using CasaXps.

6.2.6.3 Atomic Force Microscopy

A multimode 4 (Bruker, CA, USA) atomic force microscope (AFM), equipped with E – type or J – type piezzo scanner was used to measure surface roughness of the floating PA films. Free-standing PA fims were transferred onto silicon wafers and dried at room temperature

prior to measuring the surface roughness with AFM. Samples were attached onto the magnetic sample disk using double-sided adhesive tape. The images were captured under tapping mode using PointProbe® Plus silicon-SPM probes (PPP-NCH, Nanosensors™, Switzerland) with a typical tip radius of less than 7 nm. Cantilever resonance frequency was in the range of 204 – 497 kHz with a nominal spring constant of 42 N.m⁻¹. A sampling resolution of at least 512 points per line and a speed of 0.2 – 1 Hz were used. 'Gwyddion 2.38 SPM data visualization and analysis software' was used to analyse the AFM images.

6.2.6.4 UV Spectrometry

Acid Fuschin dye concentration was measured using a UV-VIS scanning spectrophotometer (UV-1800 Shimadzu, UK). The samples were assayed at 546 nm, against a blank. The dye concentration was measured to calculate dye rejection using Equation 5.2, in order to detect any defect or leakage through the membrane.

6.2.7 FO Experimental Setup

Figure 6.2 shows a schematic of the experimental setup used for the FO experiments in this chapter. This design was used instead of the setup in Chapter 5 (Figure 5.2 of Section 5.2.7) as the diameter of the FO cell used in Chapter 5 ($d = 7.5$ cm) was too large to accommodate the size of the membrane fabricated in this chapter ($d = 7.0$ cm). An attempt was made to use the aforementioned FO cell by sealing the additional N6,6 fabric area which was not covered by the membrane (Figure 6.1) to prevent leakage. However, best efforts to prevent the leak were unsuccessful. Hence, a new FO cell was designed with a smaller cell size to accommodate the entire membrane area and ensure there were no accessible areas prone to leakage (Figure 6.2 (b)). The simple design and operation of the apparatus also improved experimental efficiency. The new setup consists of a custom built Perspex FO cell with an open area of 12.6 cm² available for water permeation (Figure 6.2 (b)), attached to transparent

feed and draw solution channels. A stainless steel spacer with a mesh size of 1 mm was used in the feed and draw solution channels of the FO cell to enhance mass transfer and allow for good mixing as no recirculation was used in this setup. Mixing on both feed and draw sides were conducted with a magnetic stirrer set to a rotation speed of 400 rpm.

The height change in the column of fluid during the FO experiment was monitored using the level indicator on the feed and draw solution channels. The height change was converted into volume change and used to calculate water flux through the membrane:

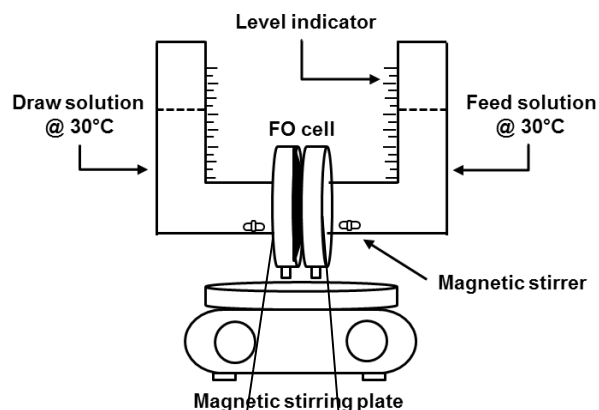
$$J_{P,FO_{t_i}} = \frac{(h_{t_i} - h_{t_{i-1}}) \cdot A_{channel}}{(t_i - t_{i-1}) \cdot A_m} = \frac{\Delta h_{t_i} \cdot A_{channel}}{\Delta t_i \cdot A_m} \text{ [unit: L} \cdot \text{m}^{-2} \cdot \text{h}^{-1}]$$

Equation 6.1

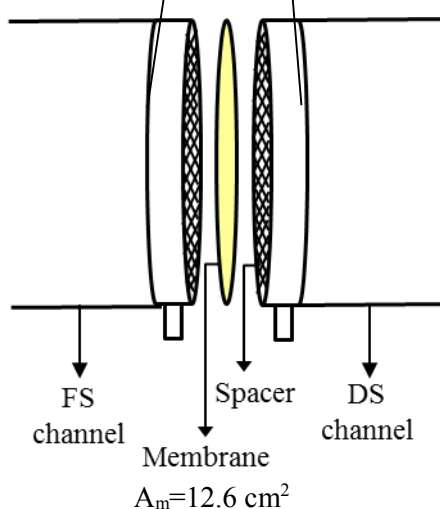
whereby, $J_{P,FO_{t_i}}$ is the FO permeate flux, Δh_{t_i} is the height change of the solution over a time interval, $A_{channel}$ is the cross sectional area of the FS and DS channel, A_m is the membrane area and Δt_i is the discrete time interval.

The feed and draw solutions were heated to 30 °C prior to starting the experiment.

A tracer dye, Acid Fuchsin, with a molar mass of 585.53 g.mol⁻¹ (Sigma Aldrich UK), was used in the feed solution to detect any leakage through the membrane (Figure B-3 of Appendix B). An overnight experimental run showed no visible tracer dye in the DS and UV measurements confirmed dye rejection was consistently above 99.3% for all experiments. Furthermore, NaCl rejection of the membranes was consistently maintained above 96.3% which is comparable to commercial FO membranes.



(a) Schematic of lab-scale U-tube FO experimental setup with level indicator for flux measurement.



(b) Schematic of U-tube FO cell configuration

Figure 6.2

In order to provide a baseline comparison of FO flux performance in the new U-tube setup (Figure 6.2) and the setup used in Chapter 5 (Figure 5.2), a standard FO experiment was conducted with the HTI TFC membrane in FO and PRO mode, using both setups. The FO tests show similar performance results for the HTI TFC membrane in either configuration (Figure 6.3). This indicates that the hydrodynamic conditions in both setups were similar and that results obtained using the U-tube apparatus can be directly compared to those obtained with the FO cross-flow setup in Chapter 5.

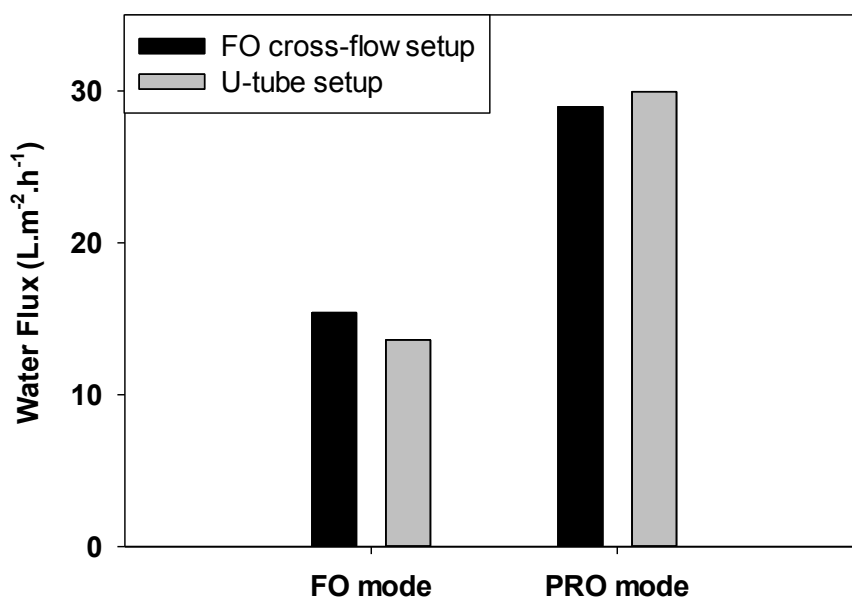


Figure 6.3: Comparison of the HTI TFC membrane flux performance using the FO cross-flow setup in Chapter 5 and the new U-tube experimental setup in this chapter. The membranes were tested in FO and PRO modes with DIW and 1 M NaCl as the feed and draw solutions, respectively.

6.2.8 FO Experimental Procedure

A new membrane coupon is loaded into the FO cell before each experiment. 200 ml of feed (DIW) and draw (1 M NaCl) solution were added to the feed and draw solution channels (Figure 6.2 (a)). The height of the column of fluid in the feed and draw channels were kept the same throughout the experiment by adjusting the DS volume accordingly as water permeated to the draw side. This is to ensure that water flux through the membrane was not affected by a transmembrane pressure difference and was only a function of osmotic driving force. The magnetic stirrer was set to a rotation speed of 400 rpm to promote good mixing in the feed and draw channels. Water flux was recorded at fixed time intervals by monitoring the height change in the feed channel (Equation 6.1) and an average value for initial flux was obtained. A

conductivity meter was used to monitor NaCl concentration in the feed and draw side to determine membrane rejection under FO conditions.

6.3 Results and Discussion

6.3.1 The Ideal Support Layer

The ideal support layer for an FO membrane (Figure 6.4) should possess low tortuosity and thickness, and be highly porous [95, 96] in order to minimise internal concentration polarisation. FO membranes fabricated by phase inversion have a mixed-structure support layer with a sponge-like layer sitting on top of porous macrovoids [54]. The tortuous structure of the sponge-like layer causes a resistance to mass transfer and limits water flux of these membranes. In order to address this bottleneck, an FO membrane with a PA film deposited on an N6,6 open mesh fabric of varying mesh size and effective mesh open areas, was fabricated. The open mesh fabric provides mechanical support and eliminates the need for a phase inversion support (Figure 6.5). The fabric was chosen for its good structural properties, including i) low tortuosity, ii) high mesh size, iii) reduced thickness, iv) availability in a range of open areas and v) hydrophilicity. The favourable structure of the support fabric is postulated to provide a good path for salt and water transport, thus mitigating ICP.

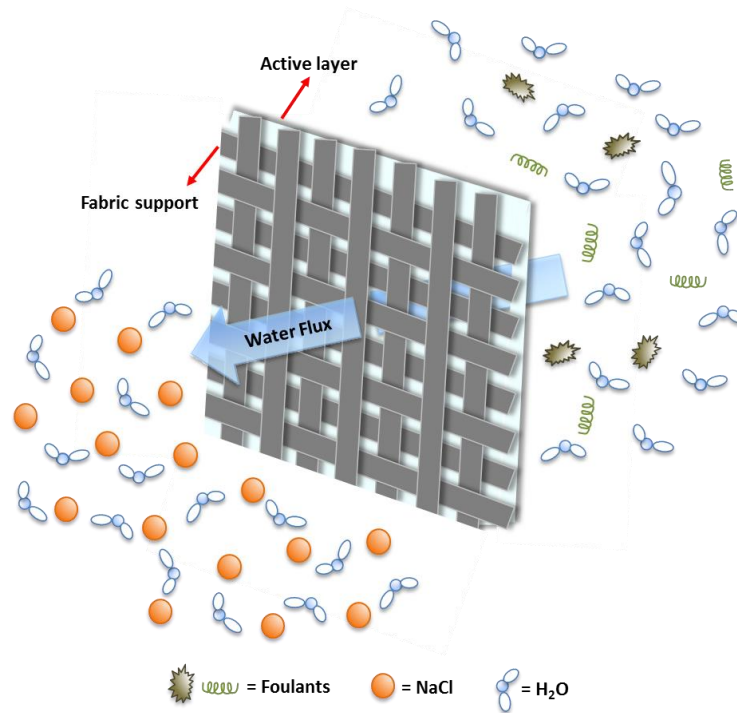


Figure 6.4: Schematic of an FO membrane with a dense active layer for rejection of foulants and salt ions, and an ideal support layer with low tortuosity, reduced thickness and high porosity to provide direct diffusion paths for water and salt transport.

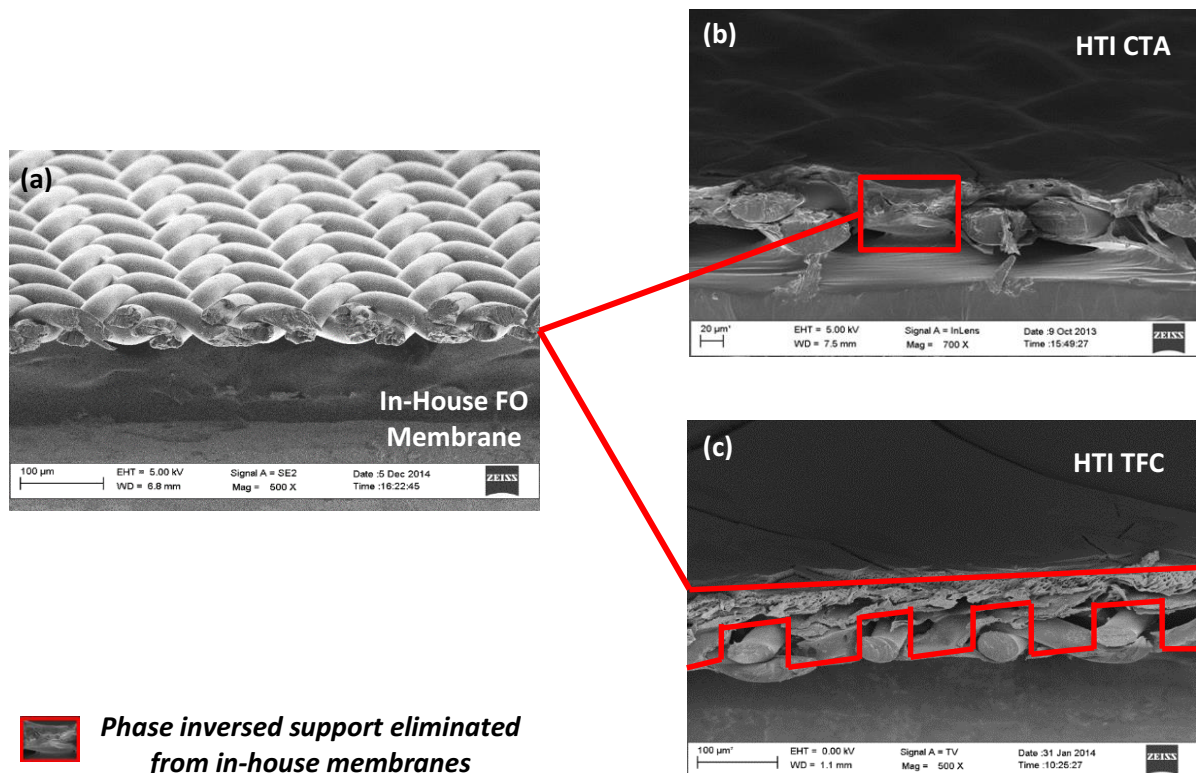


Figure 6.5: Cross-sectional SEM image showing the elimination of a phase inversion support in the (a) in-house fabricated FO membrane, compared to conventional phase-inversed membranes, such as the HTI (b) cellulose triacetate (CTA) and (c) thin film composite (TFC) FO membrane. The in-house fabricated membrane utilised an open mesh fabric to provide mechanical support, eliminating the need for a phase inversion support.

6.3.2 Membrane Characterisation

6.3.2.1 Scanning Electron Microscopy (SEM)

Figure 6.6 shows high resolution SEM images of an in-house FO membrane before and after PA film deposition on the N6,6 open mesh fabric. The PA film was synthesised using an MPD concentration of 3 wt%, TMC concentration of 0.15 wt% and a reaction time of 1 minute. The N6,6 fabric used had a mesh size of 15 μm and an effective open area of 10% available for

water transport. The remaining 90% of the fabric area consisted of the N6,6 fabric itself which was impermeable to water. Figure 6.6 (a) shows the N6,6 open mesh fabric prior to PA film deposition. It can be observed that the fabric consists of a precision engineered mesh structure. The large open mesh creates a direct path for salt and water transport and exhibits low tortuosity (Figure 6.6 (b)). Figure 6.6 (c) shows the membrane after PA film deposition. The PA film was deposited as a complete continuous film between the N6,6 fibres and open mesh, as shown in a higher magnification image in Figure 6.6 (d). An even higher magnification of the PA layer (Figure 6.6 (e)) shows an intermediately rough PA surface with the characteristic ridge-and-valley structure of the polyamide interspersed with smooth regions. A quantification of the surface roughness is given in Section 6.3.2.3. A cross-sectional image of the in-house membrane is shown in Figure 6.6 (f). The total thickness of the membrane is $\sim 60 \mu\text{m}$.

A comparison of the surface morphology of smoother (3 wt% MPD, 0.15 wt% TMC) and rougher (6 wt% MPD, 0.3 wt% TMC) PA films used in this work is presented in Figure 6.7. It can be observed that the rougher surface has a higher frequency of the protruding asperities.

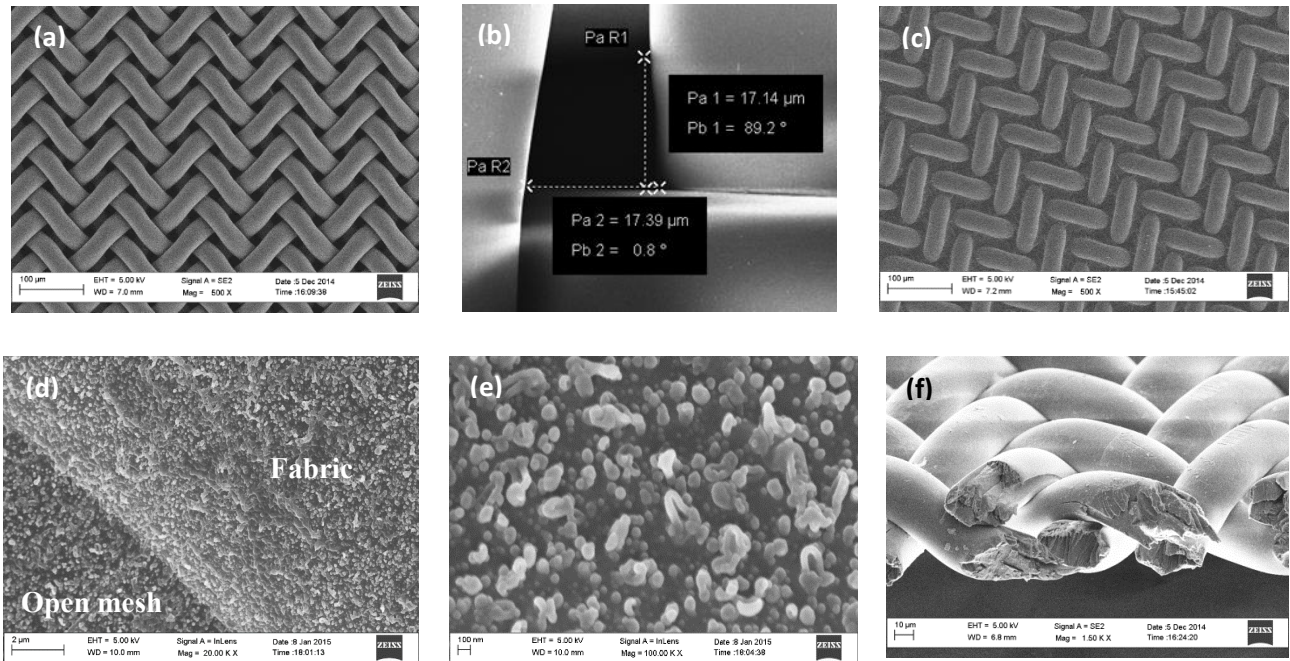


Figure 6.6: SEM image of a Nylon 6,6 support (mesh size = 15 μm and effective open area for water transport = 10% of total fabric), (a)-(b) before and (c) after of PA film deposition. The SEM image shows (a)-(b) a precision engineered open support with large mesh size and low tortuosity, and (c) a continuous PA film formed by interfacial polymerisation, physically adhered on the support. (d) A close-up showing a continuous PA film formed between a Nylon 6,6 fabric fibre and the open mesh. (e) Typical ridge-and-valley morphology of the interfacially polymerised PA film on the Nylon 6,6 mesh support. (f) Cross-sectional SEM image of the in-house membrane.

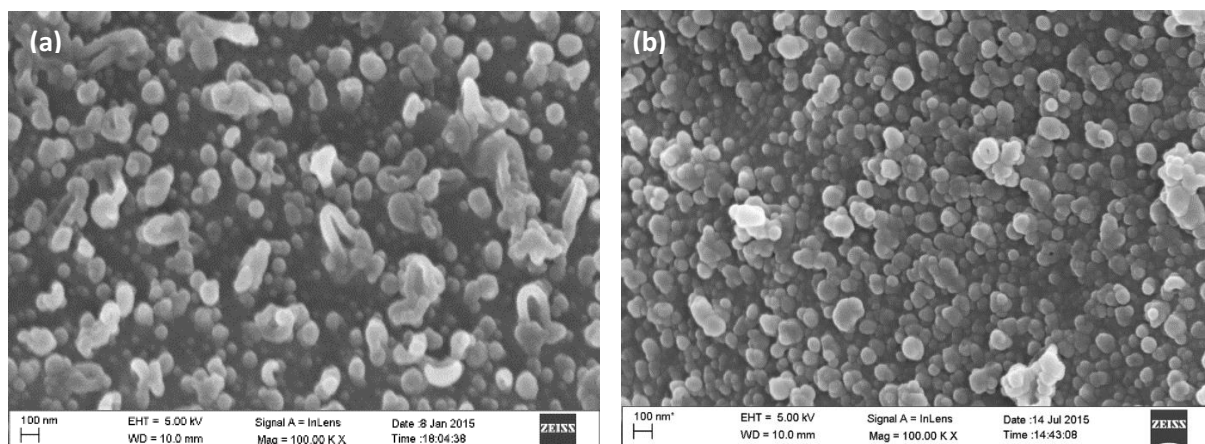


Figure 6.7: SEM image of the (a) smoother PA film formed with 3 wt% MPD and 0.15 wt% TMC, and (b) rougher PA film formed with 6 wt% MPD and 0.3 wt% TMC. Reaction times were fixed at 1 minute.

6.3.2.2 X-ray Photoelectron Spectroscopy (XPS)

Results for an XPS study conducted on the floating PA film made from 3 wt% MPD and 0.15 wt% TMC, was adapted from Karan et al. [194]. The floating film was fabricated under identical conditions as the PA film used in this work. The results presented in Table 6.2 reveal the signature amide and carboxyl groups which are typically present in a polyamide film, thus confirming that the floating method used successfully formed a PA layer.

Polyamide Film	C1s			O1s			N1s		
	Energy (eV)	Species	(%)	Energy (eV)	Species	(%)	Energy (eV)	Species	(%)
MPD 3%, TMC 0.15%	285.0	C-H, C-C, C=C	65.6						
	285.7	C-CONH, C-COO	12.6	532.0	N-C=O	74.5	398.5	R-NH ₂	4.3
	286.3	C-N	9.3	533.5	O-C=O	25.5	400.0	N-C=O	94.3
	288.2	N-C=O	9.3				401.7	R-N ⁺ H ₃	1.4
	288.8	O-C=O	3.2						

Table 6.2: XPS results of the polyamide floating film made from 3 wt% MPD and 0.15 wt% TMC. Binding energies and plausible species were determined from the deconvolution of C1s, O1s and N1s core level XPS spectra. [Adapted from Karan et al. [194]].

6.3.2.3 Atomic Force Microscopy

Surface roughness of the selective layer of the membranes studied in this work were measured by atomic force microscopy (AFM). AFM images of the PA films of the in-house membranes compared to a commercial HTI TFC membrane are shown in Figure 6.8 along with their root mean square (RMS) roughness values. The PA film in Figure 6.8 (a) was synthesised using an MPD concentration of 3 wt%, TMC concentration of 0.15 wt% and a reaction time of 1 minute. It can be seen that the PA film was smoother (RMS= 9.4 nm) compared to the HTI TFC membrane (RMS= 41.2 nm), indicating a lower surface area for permeation. The PA film synthesised with 6 wt% MPD, 0.3 wt% TMC is shown in Figure 6.8

(b). It can be observed that the film has an intermediate roughness, between the 3 wt% MPD floating film and the HTI TFC PA film. Although the smoother PA film formed (Figure 6.8 (a)) may reduce the effective area for water permeation, its relatively smooth surface is beneficial for fouling mitigation, as previously demonstrated in Chapter 5.

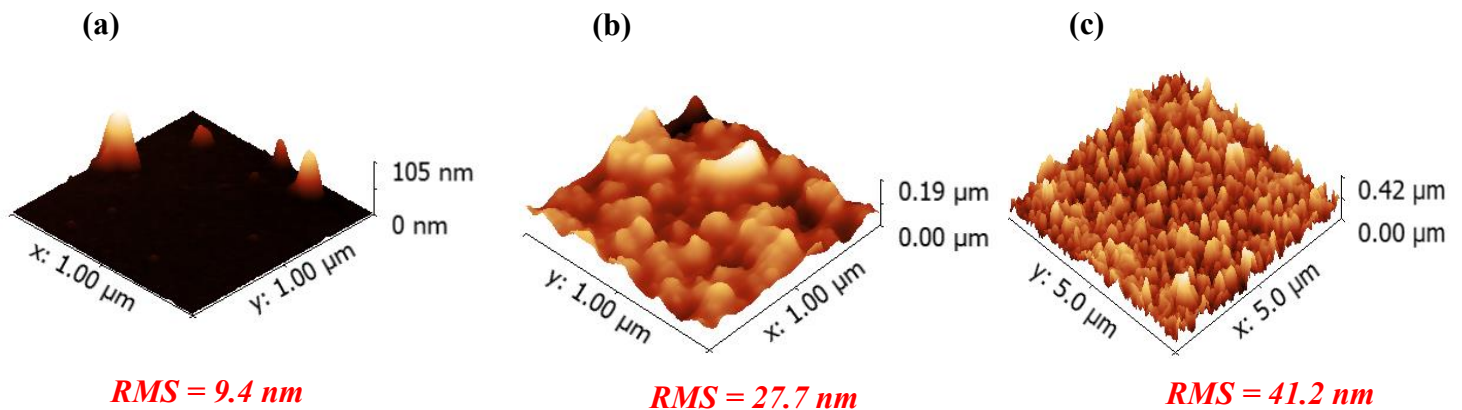


Figure 6.8: AFM images of the polyamide film with (a) 3 wt% MPD, 0.15 wt% TMC, (b) 6 wt% MPD, 0.3 wt% TMC and on (c) a commercial HTI TFC membrane.

6.3.3 FO Performance of In-House Membranes

Figure 6.9 shows the water flux and NaCl rejection data for FO experiments conducted with smooth (3 wt% MPD, 0.15 wt% TMC) and rough (6 wt% MPD, 0.3 wt% TMC) in-house membranes with effective mesh open areas of 0.3 cm², 1.3 cm² and 1.7 cm². The corresponding values for water flux and NaCl rejection are presented in Table 6.3.

A permeate flux was unobtainable for the in-house membrane with 2.3 cm² effective mesh open area in FO and PRO mode. Defects were detected in the membrane's PA film from NaCl conductivity measurements of the feed solution, which increased significantly during the experiment. These defects were likely formed when depositing the PA layer on the N6,6 mesh during membrane fabrication or when the membrane was loaded and tested in the FO cell. It

was challenging to form a defect-free PA film on the 2.3 cm² N6,6 mesh due to its high mesh size, measuring 25 μm × 25 μm.

Table 6.3 presents the membrane performance and structural properties of the in-house membranes, the highest performing FO membrane currently in literature (NC-FO) and commercial HTI membranes.

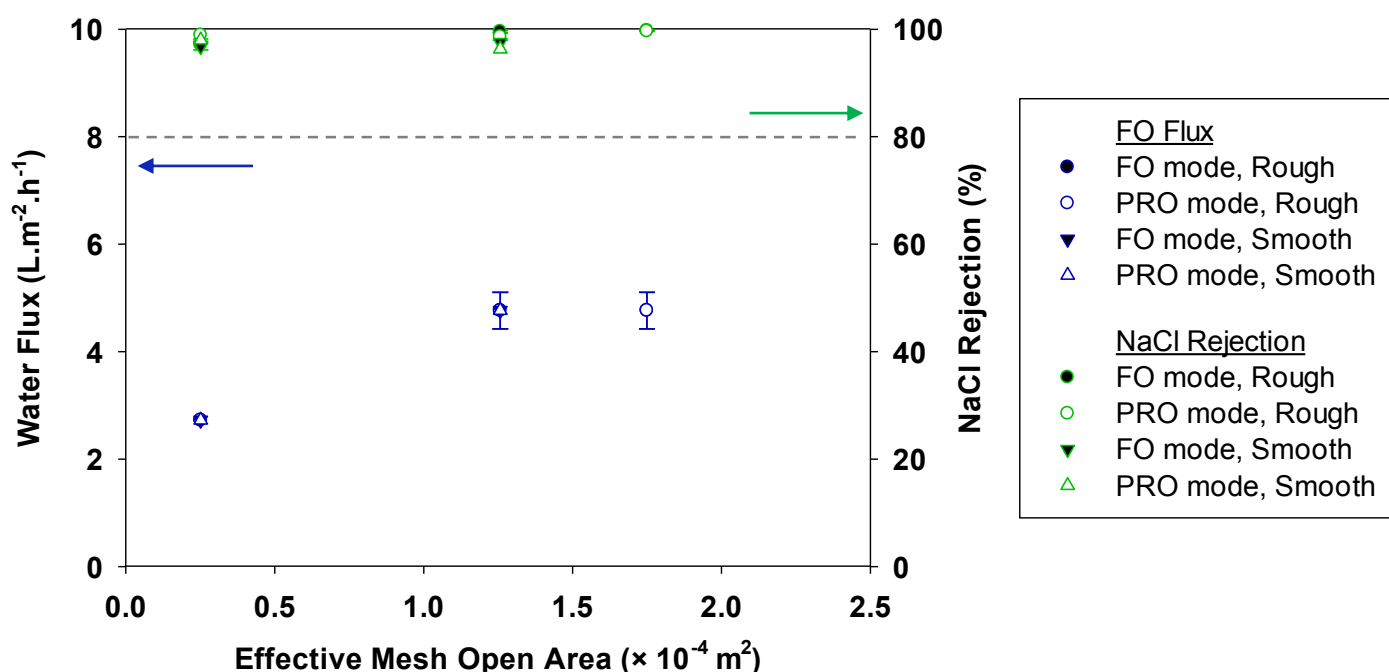


Figure 6.9: Water flux and NaCl rejection of in-house membranes made on i) 10 μm mesh size, 2% open area, ii) 15 μm mesh size, 10% open area and iii) 20 μm mesh size, 14% open area N6,6 fabrics; with corresponding effective mesh open areas of 0.3 cm², 1.3 cm² and 1.7 cm², respectively. DIW and 1 M NaCl were used as the feed and draw solutions. The in-house membranes made on 25 μm mesh size, 19% open area N6,6 fabric with a 2.3 cm² effective open area were prone to defects, hence a permeate flux was unobtainable.

Membrane		#1 N6,6-FO		#2 N6,6-FO		#3 N6,6-FO	#4 N6,6-FO	NC-FO	HTI CTA	HTI TFC
PA film roughness		Smooth	Rough	Smooth	Rough	Rough	Smooth	N/A	N/A	N/A
FO flux (L.m ⁻² .h ⁻¹)	FO mode	2.72±0.00	2.72	4.76	4.76±0.34	4.76±0.34	0	47	8	15
	PRO mode	2.72±0.00	2.72	4.76	4.76±0.34	4.76±0.34	0	52	18	29
NaCl rejection (%)	FO mode	96.8±0.6	97.1	97.5	99.6±0.2	99.8±0.1	N/A	N/A	99.4±0.1	99.3±0.1
	PRO mode	98.0±0.2	98.9	96.3	98.6±0.6	99.7±0.1	N/A	N/A	N/A	N/A
	RO	99.3±0.5*	N/A	99.3±0.5*	N/A	N/A	99.3±0.5*	97.0±1	97.7±0.05	99.0±0.02
Dye rejection (%)	FO mode	99.4±0.1	99.3	99.9	99.5±0.2	99.7	N/A	N/A	N/A	N/A
	PRO mode	99.7	99.3	99.9	99.5	99.8	N/A	N/A	N/A	N/A
RO Permeance (L.m ⁻² .h ⁻¹ .bar ⁻¹)		0.62±0.05*	N/A	0.62±0.05*	N/A	N/A	0.62±0.05*	1.70±0.1	1.05±0.02	3.07±0.07
Thickness (µm)		45		60		55	55	50	50	100
Porosity (%)		2		9.5		14	19	83	55	74
Tortuosity		~1		~1		~1	~1	1.33	7.63	5.26
'S' (µm)		2250		632		393	289	80	694	711

Table 6.3: Membrane performance and structural parameters of the in-house membranes and other FO membranes available in literature and commercially. #1 N6,6-FO, #2 N6,6-FO, #3 N6,6-FO and #4 N6,6-FO, refer to in-house FO membranes with 10 µm, 15 µm, 20 µm, 25 µm mesh size and 2%, 10%, 14%, 19% open area, respectively; with corresponding effective mesh open areas of 0.3 cm², 1.3 cm², 1.7 cm², 2.3 cm². NC-FO refers to a high performance nanofiber composite FO membrane with the highest performance data currently available in literature [62]. HTI CTA and HTI TFC are commercially available FO membranes. *RO permeance and rejection were measured on an ultrafiltration polysulfone support under 20 bar applied pressure. Lower permeance of the in-house membranes are partly attributed to the ageing of the UF support and compaction of the PA layer under pressure. Porosity (%) of the in-house membranes were calculated as the ratio of the open mesh volume available for permeation to the total mesh volume (i.e. open volume + volume occupied by N6,6 fabric). FO water flux, permeance and rejection were measured with a DIW FS and 1 M NaCl DS.

6.3.3.1 Factors Contributing to Performance Results following ICP Mitigation

6.3.3.1.1 The Low Flux Phenomenon

It can be observed from Figure 6.9 that there was effectively no difference in water flux for membranes tested in FO and PRO modes, thereby suggesting that membrane orientation did not have an effect on flux performance. This is a positive indication that ICP was greatly reduced or eliminated in these membranes due to the large mesh size and straight, less tortuous open channels of the N6,6 fabric allowing for direct diffusion of salt and water molecules throughout the support structure. However, it begs the question, why were the water fluxes low in the absence of ICP? This questions the widely accepted idea that high permeate fluxes can be achieved when ICP is eliminated.

To ensure that the low fluxes were not caused by poor wetting or trapped air in the N6,6 support, an in-house membrane was prewetted in 50% solution of methanol and its flux performance was compared to that of an unwetted membrane (Figure 6.10). In Chapter 5, it was shown that methanol pretreatment had a significant effect on improving flux performance of the HTI TFC membrane, whilst maintaining high salt rejection. However, as observed in Figure 6.10, there was effectively no difference in the performance of the in-house membrane before and after prewetting, suggesting that the N6,6 fabric support was already fully wetted by water prior to methanol pretreatment. Hence, the low fluxes obtained can be attributed to other factors.

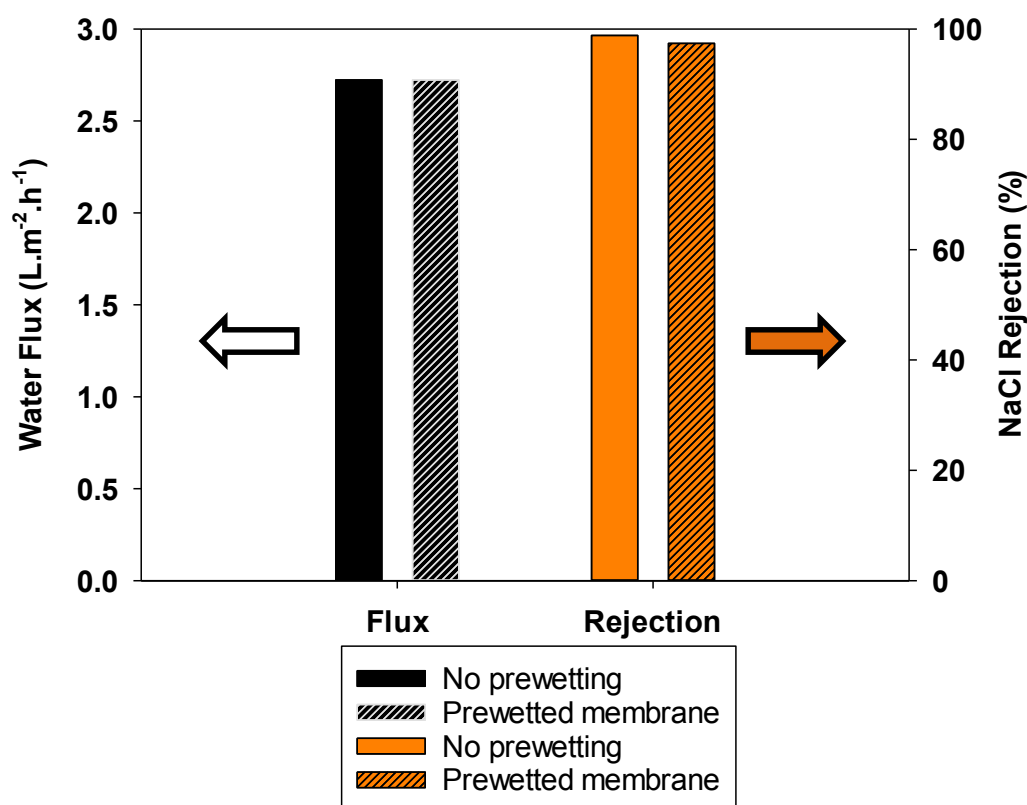


Figure 6.10: Water flux and NaCl rejection of an in-house membrane (10 μm mesh size and 2% open area), before and after prewetting with methanol. DIW and 1 M NaCl were used as the feed and draw solutions, respectively.

A few possible hypotheses are suggested to explain the low fluxes of the in-house membranes:

- i) The **effective mesh open area** had a limiting effect on water flux through the membrane, as the area of the PA film adhered on the mesh fabric may have been completely impermeable to water transport, suggesting that water transport may have only occurred through the PA film located directly above the open mesh area. Hence, although water flux was calculated by dividing the volumetric flow rate by the membrane area (i.e. 12.6 cm²), in reality only 0.3 cm², 1.3 cm², 1.7 cm² and 2.3 cm² of the total membrane area was available for water permeation through the 10 μm , 15 μm , 20 μm and 25 μm mesh size fabrics, respectively.

- ii) The **PA film** of the in-house membrane has a lower **surface area** for permeation compared to the commercial HTI TFC membrane. Karan et al. [194] described that the mechanism of formation of PA film at the bulk liquid interface (such as the in-house floating films), was different to that formed directly on an ultrafiltration support (e.g. HTI TFC membrane) under the same conditions, thus, yielding different film structures. As explained in [194], at the bulk interface, water provides a good heat sink to dissipate the heat generated from the interfacial reaction due to its high heat capacity. This prevents local temperature rises and interfacial instabilities in the organic phase (hexane), thus resulting in a relatively smooth film with a lower interfacial area formed under the interfacial tension of water and hexane [194]. In contrast, an interfacial reaction occurring on a support layer, is governed by a very thin water layer (not bulk water), forming an interface with hexane. Heat generated at the interface will be dissipated by heating up the hexane phase due to its low heat capacity. This causes local temperature rises and interfacial instabilities of the hexane phase, resulting in the crumpling up of the PA film, thus generating additional interfacial area and increasing surface roughness [194]. This can be inferred from the surface roughness the commercial HTI TFC PA layer which was higher than the rougher in-house floating PA film (6 wt% MPD, 0.3 wt% TMC) (Figure 6.8 (b) and (c)). It should be cautioned that AFM measurements of the HTI TFC membrane may be an underestimate of its actual surface roughness. As seen in Figure 6.8 (b) and (c), the height scale of the HTI TFC PA layer is larger than that of the in-house membrane (420 nm in height compared to 190 nm for the in-house rough membrane). Hence, when measuring surface roughness of the HTI TFC membrane, the AFM probe may not be able to access the smaller protuberances present in the underlying polyamide surface as illustrated in Figure 5.20 of Chapter 5. This means that the actual surface

roughness and interfacial area of the HTI TFC membrane is likely to be higher than indicated, compared to the rougher in-house membrane.

- iii) The actual **thickness of the PA film** formed at the bulk liquid interface using the floating method, was higher than the HTI TFC membrane. For PA films formed on a UF support, it is postulated that during the initial 'spontaneous' interfacial reaction occurring on the pico to nano-second time scale, the limited amount of MPD in contact with the support, along with its lower mobility within the pores of the support layer, results in a lower diffusion rate into the organic (hexane) phase. The interfacial reaction is hence, reaction rate dominated, whereby MPD molecules can only diffuse a short distance into the organic phase before the reaction takes place. This results in a thinner (albeit rougher) PA film being formed at the interface on the support layer. Further growth of the PA film is limited due to the film's resistance to MPD diffusion into the hexane layer. In contrast, for PA film formation at the bulk liquid interface (such as the in-house floating films), the high amount of MPD available in the bulk aqueous phase, allows for a higher rate of diffusion of MPD into the hexane layer. As the initial MPD diffusion rate exceeds the interfacial reaction rate, the MPD molecules can travel a longer distance into the hexane layer before reacting to form the interface. This results in a thicker PA film being formed at the bulk liquid interface.

6.3.3.1.2 Limiting Effect of the Polyamide Film

The results in Figure 6.9 reveal that the support fabric may have a limiting effect on flux at lower effective mesh open areas, as water flux increases initially before plateauing at higher open areas. An increase in permeate flux was observed when the effective mesh open area was increased from 0.3 cm² to 1.3 cm². However, despite a five-fold increase in the effective open area of the support fabric, water flux only approximately doubled. Moreover, there was

effectively no difference in permeate flux of the rough membranes between 1.3 cm² to 1.7 cm² effective open area despite an increase in the open area and a decrease in the 'S' parameter of the membranes (Table 6.3), suggesting a plateau was approached. This plateau infers that at higher mesh open areas, fluxes were governed primarily by diffusion through the PA film. In this event, the PA layer was behaving like a free-standing film on the N6,6 fabric support, with water freely permeating through the entire film area, limited only by the permeance of the film.

Transport of water through the PA film begins with the absorption of water into the film as a result of hydrogen bonds formed with the $-C=O$ and $-NH$ groups present. This is followed by the diffusion of water into the free volume (microvoids) of the film, which is a weakly hydrogen bonded interaction, in addition to strong hydrogen bonds formed between two carbonyl groups of the polyamide and water molecules [208]. Hydrogen bonds are also formed with the carboxyl groups present in the film, derived from unreacted acyl chloride groups during interfacial polymerisation. The desorption process which involves the release of water from the PA film, is just the opposite of absorption in terms of the interaction sequence between water and the polymer matrix [208]. Flux through the film may be limited by the absorption and desorption capacity of the PA film, in addition to diffusivity within the film. In order for water molecules to diffuse through the film, they will have to first absorb into the PA layer by forming moderate hydrogen bonds with the $-C=O$ and $-NH$ groups present on the surface. At high fluxes, the number of water molecules that can absorb on the PA surface at a given time (i.e. its affinity to the surface), may be limited by the number of binding sites (i.e. absorption capacity) present on the surface. Hence, a limiting permeance is reached when all the available absorption sites for water transport are water saturated. Furthermore, depending on the degree of crosslinking of the polymer, the maximum degree of swelling of the PA network by water may be approached at high fluxes [209]. Until the absorbed water molecules have diffused through the PA film, the absorption sites will not be available for the reabsorption of

new water molecules. Similarly, the desorption process may be limited by the desorption capacity of the PA surface facing the draw solution side. A molecular dynamic study by Xiang et al. [200] reported that the diffusivity of water decreases from $2.3 \times 10^{-9} \text{ m}^2.\text{s}^{-1}$ in bulk solution to $1.6 \times 10^{-9} \text{ m}^2.\text{s}^{-1}$ at the vicinity of the PA surface and $0.12 \times 10^{-9} \text{ m}^2.\text{s}^{-1}$ within the PA film itself, due to the aforementioned hydrogen bonding capacity of the film as well as the PA surface roughness and dynamic morphology changes in solution. The limiting permeance of the PA film corresponds to its maximum permeance, beyond which further increase in effective mesh open area will have no effect on water flux through the membrane, under the same driving force.

If it were true that the permeate fluxes through the higher open mesh areas were being governed by a free-standing PA film, then it is possible that water fluxes achieved with any FO membrane designed to greatly reduce or eliminate ICP, would eventually be limited by the permeance of the PA layer. As discussed previously in hypothesis (iii) of Section 6.3.3.1.1, the floating method used in this study may have resulted in a thicker PA film formed due to the reaction being governed by a higher rate of diffusion of MPD into the hexane layer. Moreover, it was observed that there was effectively no difference in water flux of the smooth and rough membranes in both orientations, suggesting that the floating PA film formed was relatively standard, independent of MPD concentration. There could be a trade-off between surface roughness and thickness of the PA film, whereby at higher MPD concentrations, the increase in surface roughness is compensated by the thicker film formed. Higher rates of diffusion into the hexane layer occur at higher MPD concentrations and hence, a thicker, albeit rougher, PA film could be formed at the bulk liquid interface, overall resulting in a similar performance compared to the smooth PA films fabricated using the same floating method.

Although the rougher membrane has more repeating units of protruding asperities, it may not necessarily mean that the available surface area for permeation is far greater than the smooth

membrane. From the SEM images in Figure 6.7, it can be seen that despite the lower surface roughness of the smoother PA film, the large protruding asperities observed (Figure 6.7 (a)) may potentially lead to higher surface areas. Hence, the overall area available for permeation for the smooth membrane may be higher than expected. This could be another reason for the similar flux performance of the smooth and rough PA films in Figure 6.9. Moreover, local permeances may differ at different locations on the PA film, depending on the available area for permeation, the degree of cross-linking, the flexibility of the PA chains etc. Hence, surface roughness alone does not provide a complete representation of the available area for permeation.

6.3.3.2 Rethinking the Structural Parameter – ICP Relationship

From Table 6.3, it can be seen that although the structural parameter of the HTI CTA membrane was comparable to the HTI TFC membrane, its fluxes were lower compared to the latter. This raises the question whether the 'S' parameter provides a good indication of the extent of resistance of the support layer to solute and water transport. Figure 6.11 illustrates how two supports may have the same overall 'S' parameter (i.e. equivalent porosity, thickness and tortuosity) but different solute diffusivities due to variation in the pore size. The ratio of pore size to pore length and solute diameter affects the ease with which a solute diffuses through the pore channel. For the same pore length (or support thickness) and solute diameter, the larger pore size allows for greater diffusivity of the solute, and hence, reduced ICP effects. A smaller pore size may cause hindered diffusion of the solute, if solute transport is retarded by the viscous drag of the solvent or an increased viscosity of fluid in the vicinity of the pore walls. Hence, if two structurally different supports have comparable 'S' parameters due to variations in their tortuosity, thickness and porosity, they may still exhibit different extents of ICP and water flux, as shown by the HTI CTA and TFC example. The finger-like morphology and large macroscopic pores around the mesh lines of TFC's support surface (Figure 5.4 (c) of Chapter 5) results in higher fluxes compared to the CTA membrane despite

exhibiting a greater thickness and comparable 'S' parameter to the latter. Hence, the 'S' parameter may not always provide a sufficiently good representation of ICP behaviour in the support layer, as one property of the support (e.g. pore size) may have a more dominating effect over another (e.g. support thickness).

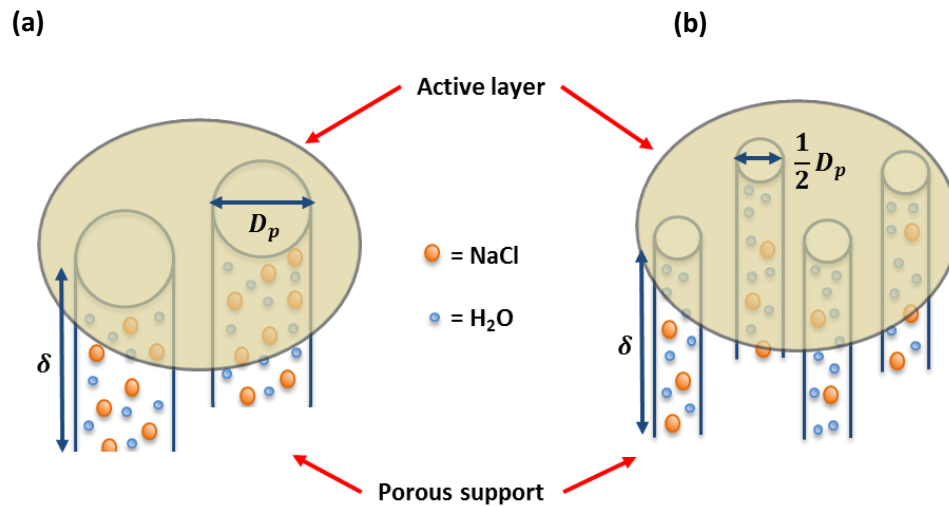


Figure 6.11: Schematic showing two membranes with identical 'S' parameter, i.e. equivalent thickness (δ), porosity (ε) and tortuosity ($\tau = 1$), but varying pore size (D_p). Figure (a) exhibits a larger pore size, allowing for higher solute diffusivities within the pore channel, whereas smaller pore sizes in (b) result in a lower solute diffusivity.

6.4 Conclusion

An investigation into a novel method for fabricating FO membranes was performed by interfacially polymerising a free-standing, salt rejecting polyamide (PA) film at the bulk interface, followed by deposition onto a Nylon 6,6 open mesh fabric by vacuum suction. The need for a phase inversion support was eliminated.

Results demonstrated that the membrane fabrication method resulted in the successful formation of defect-free, salt-rejecting FO membranes with greatly reduced or eliminated ICP. Water fluxes increased at lower effective mesh open areas and approached a steady state at higher open areas. It is believed that the N6,6 support mesh fabric has a limiting effect on permeate flux at lower effective mesh open areas. The effect of the fabric support becomes less significant at higher effective open areas, whereby permeate flux is primarily a function of diffusion through the PA film. In this region, the PA film behaves like a free-standing film, whereby flux is governed purely by the film's permeance.

The results led to the inference that the widely accepted idea of achieving high permeate fluxes when ICP is eliminated, is ultimately restricted by the structure and transport properties of the PA film. Despite greatly reducing or eliminating ICP in the in-house membranes, a surprisingly low flux was observed. It is proposed that this observation is attributed to the smoother and thicker structure of the floated PA film. It was also observed that there was no effective difference in the performance of smoother and rougher films indicating that there may be a trade-off between surface roughness and thickness of the PA films formed using the floating method. The relatively standard performance of these films is linked to the mechanism of film formation at the bulk interface. Hence, it is proposed that when designing FO membranes with ideal supports tailored to eliminate ICP, the focus should also be on tailoring the PA layer properties to achieve a highly permeable film without compromising selectivity.

Chapter 7

7 Overall conclusions

The increasing interest in forward osmosis (FO) as an emerging technology to provide a low-cost, low-energy alternative to conventional membrane separation processes, calls for an in depth investigation into the real potential of this technology and further clarity on its position in the current membrane market, specifically applications where FO can be successfully implemented, and where it does not have an added advantage over established membrane processes. In this concluding chapter, the research presented in this dissertation is summarised, based on the objectives defined in Chapter 3. The future directions are outlined in Chapter 8.

In Chapter 4, the position of FO as a commonly perceived low-energy process is clarified by performing a detailed modelling study on the specific energy consumption (SEC) of FO hybrid processes in desalination and comparing the results with its well-established counterpart, reverse osmosis (RO). It was discovered that contrary to popular belief, FO is not more energy efficient than RO due to the energy requirements of its draw solution (DS) recovery stage, which in many cases involving the use of a pressure-driven membrane process for DS regeneration, equals that of a standalone RO process. The simulation also compared the two processes on the basis of membrane area requirements with results indicating that FO hybrid processes required higher membrane footprints, which can be reduced if ICP within the support layer is greatly reduced or eliminated. A comparison between the standalone RO, and FO with nanofiltration (NF) draw solution (DS) recovery showed that there was practically no difference in SEC between the these two processes, and the same conclusion can be derived for other pressure driven membrane processes such as UF or RO, used in the DS recovery stage. It was also shown that currently available FO, RO and NF membranes are already operating close to the practical minimum energy required for separation of pure water from

seawater (i.e. the thermodynamic limit), hence even if any or all of the membranes considered, were perfect (i.e. had infinite permeance and 100% rejection), it would not improve the SEC significantly.

Although the results obtained suggested that the incorporation of FO in a membrane separation process cannot reduce the minimum energy of separation compared to a standalone RO process, FO-hybrid systems may still offer benefits over RO. The lower fouling propensity of FO compared to pressure driven membrane processes may reduce or eliminate the need for pre-treatment and chemical cleaning, hence saving on pretreatment costs. FO hybrid systems can provide energy cost savings with the use of alternative low-cost thermal energy to power the draw solution recovery stage. FO also presents an advantage over standalone RO in cases where the feed solution is challenging to treat due to high salinities, high fouling potential or the presence of specific contaminants. Furthermore, when used in applications whereby the diluted DS along with the concentrated feed are desired products, FO is truly a low energy process.

In Chapter 5, a potential benefit of FO over pressure-driven membrane processes was explored. The organic fouling propensity of two structurally and chemically different commercial HTI membranes, the cellulose triacetate (CTA) and more recently developed thin film composite (TFC) FO membrane, was investigated, using calcium alginate as a model foulant. Results revealed that although the TFC membrane exhibited superior intrinsic permeance compared to the CTA membrane, organic fouling with calcium alginate was more significant in the former, in both FO and PRO modes. In FO mode, fouling was a greater function of membrane surface properties compared to fouling layer properties, with some surface properties (e.g. surface roughness and surface chemical heterogeneity) having a more dominant effect on fouling than others (e.g. surface hydrophilicity). Due to the low variation in local cross-flow velocity across the membrane, a clear correlation between fouling density and cross-flow velocity was not observable. However, comparable fouling densities

were observed on the CTA and TFC membranes suggesting that there is not a strong correlation between foulant-membrane interaction and fouling density, which is likely a greater function of applied hydraulic forces such as in the case of RO.

In PRO mode, structural properties of the support played a more dominant role whereby fouling mechanism was specific to the foulant size and aggregation as well as the support pore size relative to the foulant. Whilst pore clogging was observed in the TFC membrane due to its highly asymmetric and porous support structure, fouling occurred as a surface phenomenon on the CTA membrane support layer attributed to its smooth and dense surface coupled with the highly structured gel formed by calcium alginate upon aggregation. In other words, the CTA membrane support structure was more symmetric in relation to the foulant (alginate) studied. Besides pore clogging, the severe fouling observed on the TFC membrane in PRO mode was due to a high specific mass of foulant adsorbed in its porous support.

It was observed that a trade-off between enhanced membrane performance and fouling mitigation is apparent in the membranes studied, with both membranes providing improvement in one aspect at the expense of the other. Hence, significant development in their surface and structural properties are needed to achieve high anti-fouling properties without compromising flux performance.

The cleaning results suggest physical cleaning was more effective on the CTA membrane, whereby increasing cross-flow velocity was sufficient to achieve an almost complete flux recovery. However, backflushing with a sufficiently high driving force was required for the TFC membrane to achieve comparable flux recoveries in PRO mode. In general, high fouling reversibility was observed on all the membranes studied despite different mechanisms of fouling and quantities of foulant adsorbed.

In Chapter 6, a novel method for fabricating FO membranes with significantly reduced or eliminated internal concentration polarisation (ICP) effects, was discussed. The fabrication method resulted in the successful formation of a defect-free, salt-rejecting FO membrane with the desired reduction in ICP effects, by means of eliminating the phase inversion support. The significant decline in ICP is attributed to high open mesh sizes and straight channels of the support fabric which exhibited minimal resistance to solute and water transport, hence allowing the effective concentration of draw solution at the membrane surface to equal that of the bulk solution. Despite successfully addressing the ICP challenge, it was observed that the support layer may still exhibit limiting effects on FO flux at low effective mesh open areas. It was also postulated that flux may be limited by the polyamide (PA) film morphology and transport properties itself, even if the support was no longer flux-limiting. A trade-off between surface roughness and thickness of the PA film was postulated, which is linked to the mechanism of film formation at the bulk interface. This trade-off resulted in a standard performance of the smoother and rougher films formed at the bulk interface.

Chapter 8

8 Future directions

The simulation work performed in Chapter 4 could be extended to include a wider selection of feed waters, such as high salinity and wastewater feeds, to provide a more rigorous survey of the SEC for different applications besides desalination. A wider selection of membranes, module design and operating conditions could be considered to investigate their influence on the SEC and membrane footprint of the processes studied. Further research into the design, operation and scale-up of FO modules with good mass transfer properties, will be useful in the evolution and successful implementation of this technology, besides providing a more practical basis for comparison of SEC and process performance with other currently available modules and membrane processes in industry.

The work conducted in Chapter 5 could be extended to include other organic foulants such as BSA and humic acid to represent fouling by protein and humic substances. It could also be extended to study inorganic fouling or the synergistic effects of organic and inorganic fouling of these membranes. Additionally, it would be useful to conduct these fouling studies under RO conditions to provide a comparison with the FO fouling behaviour. More specifically, a quantitative comparison of the fouling layer properties and their correlation with hydrodynamic conditions in FO and RO, can be performed, in order to gain a better understanding of the fouling mechanisms involved in these processes. For this purpose, the method for quantifying fouling density demonstrated in Chapter 5 can be applied to other foulants and fouling under RO conditions. Consequently, the density of the fouling layer in FO and RO can be compared. Non-invasive in situ fouling studies would be interesting to further the understanding of the kinetics and mechanism of fouling layer formation in FO, besides developing fouling models that may represent FO systems more effectively. Further, the development of anti-fouling surfaces (i.e. neutral, smooth, more homogeneous and hydrophilic with minimal carboxylic

functional groups) and modification of supports with anti-fouling properties, without compromising flux performance, are potential areas for future research. The design of novel membrane structures such as double-skinned membranes should also be explored further, to address the challenge of membrane asymmetry and pore-clogging in PRO mode. There is also scope for future work on the critical flux behaviour of FO membranes and their correlation with fouling behaviour. Finally, there is a need to investigate and optimise module design in FO to ensure that fouling propensity is minimised, as module configuration and spacer geometry can significantly influence the hydrodynamic conditions along the flow channels in these modules.

It is proposed for the work in Chapter 6 to be extended to include the fabrication of PA films using the floating method, on supports with higher percentage open areas or porosities, to further elucidate if the limited fluxes were attributed to the properties of the PA film. Supports with ideal tortuosities, higher porosities and comparable or lower thicknesses to the N6,6 fabric used in Chapter 6, such as alumina, polycarbonate, PTFE etc., can be investigated. Besides studying the effect of the support on flux performance of the membrane, the method of PA film formation can be improved to obtain a desired thinner but rougher film, and compare its performance to results obtained in Chapter 6. A better controlled formation of the PA film can be done by interfacially polymerising the PA layer on a sacrificial layer of (for e.g.) cadmium hydroxide nanostrands. The nanostrand layer can be removed by acid dissolution to obtain the desired membrane. This was previously demonstrated by Karan et al. [194] for the formation of ultrathin nanofilms for solvent permeation. This method of forming a PA film with controlled properties on any chosen support, can be used to systematically study the effect of support structure and PA film properties on the flux performance in FO, following the successful elimination of ICP. The effect of PA film thickness can also be investigated by proportionately decreasing the MPD and TMC concentrations from current values used in Chapter 6, to observe if thinner films can be successfully fabricated using the floating method and demonstrate improved permeance. The effect of PA film roughness on membrane

performance can also be studied to observe if there is a trade-off between surface roughness and concentration polarisation within the ridge-and-valley structure itself. Lastly, an investigation into the fouling behaviour of the membranes fabricated in Chapter 6 can be performed to observe the effects of surface roughness on fouling, specifically the extent to which FO fouling can be reduced on smooth PA surfaces.

Bibliography

1. Shaffer, D.L., J.R. Werber, H. Jaramillo, S.H. Lin, and M. Elimelech, *Forward osmosis: Where are we now?* Desalination, 2015. 356: p. 271-284.
2. Mi, B.X. and M. Elimelech, *Organic fouling of forward osmosis membranes: Fouling reversibility and cleaning without chemical reagents*. Journal of Membrane Science, 2010. 348(1-2): p. 337-345.
3. Mi, B. and M. Elimelech, *Chemical and physical aspects of organic fouling of forward osmosis membranes*. Journal of Membrane Science, 2008. 320(1-2): p. 292-302.
4. Achilli, A., T.Y. Cath, E.A. Marchand, and A.E. Childress, *The forward osmosis membrane bioreactor: A low fouling alternative to MBR processes*. Desalination, 2009. 239(1-3): p. 10-21.
5. Lee, S., C. Boo, M. Elimelech, and S. Hong, *Comparison of fouling behavior in forward osmosis (FO) and reverse osmosis (RO)*. Journal of Membrane Science, 2010. 365(1-2): p. 34-39.
6. Peter Nasr, H.S., *Forward osmosis: an alternative sustainable technology and potential applications in water industry*. Clean Techn Environ Policy, 2015.
7. Liu, Y.L. and B.X. Mi, *Combined fouling of forward osmosis membranes: Synergistic foulant interaction and direct observation of fouling layer formation*. Journal of Membrane Science, 2012. 407: p. 136-144.
8. Cornelissen, E.R., D. Harmsen, K.F. de Korte, C.J. Ruiken, J.J. Qin, et al., *Membrane fouling and process performance of forward osmosis membranes on activated sludge*. Journal of Membrane Science, 2008. 319(1-2): p. 158-168.
9. Holloway, R.W., A.E. Childress, K.E. Dennett, and T.Y. Cath, *Forward osmosis for concentration of anaerobic digester centrate*. Water Research, 2007. 41(17): p. 4005-4014.
10. Kim, Y., M. Elimelech, H.K. Shon, and S. Hong, *Combined organic and colloidal fouling in forward osmosis: Fouling reversibility and the role of applied pressure*. Journal of Membrane Science, 2014. 460: p. 206-212.
11. Mi, B.X. and M. Elimelech, *Gypsum Scaling and Cleaning in Forward Osmosis: Measurements and Mechanisms*. Environmental Science & Technology, 2010. 44(6): p. 2022-2028.
12. Mi, B.X. and M. Elimelech, *Silica scaling and scaling reversibility in forward osmosis*. Desalination, 2013. 312: p. 75-81.
13. Boo, C., M. Elimelech, and S. Hong, *Fouling control in a forward osmosis process integrating seawater desalination and wastewater reclamation*. Journal of Membrane Science, 2013. 444: p. 148-156.
14. Linares, R.V., S.S. Bucs, Z. Li, M. AbuGhdeeb, G. Amy, et al., *Impact of spacer thickness on biofouling in forward osmosis*. Water Research, 2014. 57: p. 223-233.
15. Hancock, N.T., P. Xu, M.J. Roby, J.D. Gomez, and T.Y. Cath, *Towards direct potable reuse with forward osmosis: Technical assessment of long-term process performance at the pilot scale*. Journal of Membrane Science, 2013. 445: p. 34-46.
16. Nguyen, N.C., S.S. Chen, H.Y. Yang, and N.T. Hau, *Application of forward osmosis on dewatering of high nutrient sludge*. Bioresour Technol, 2013. 132: p. 224-229.
17. Motsa, M.M., B.B. Mamba, A. D'Haese, E.M.V. Hoek, and A.R.D. Verliefde, *Organic fouling in forward osmosis membranes: The role of feed solution chemistry and membrane structural properties*. Journal of Membrane Science, 2014. 460: p. 99-109.
18. Yoon, H., Y. Baek, J. Yu, and J. Yoon, *Biofouling occurrence process and its control in the forward osmosis*. Desalination, 2013. 325: p. 30-36.

19. Li, Z.Y., V. Yangali-Quintanilla, R. Valladares-Linares, Q.Y. Li, T. Zhan, et al., *Flux patterns and membrane fouling propensity during desalination of seawater by forward osmosis*. *Water Research*, 2012. 46(1): p. 195-204.
20. She, Q.H., X. Jin, Q.H. Li, and C.Y.Y. Tang, *Relating reverse and forward solute diffusion to membrane fouling in osmotically driven membrane processes*. *Water Research*, 2012. 46(7): p. 2478-2486.
21. Parida, V. and H.Y. Ng, *Forward osmosis organic fouling: Effects of organic loading, calcium and membrane orientation*. *Desalination*, 2013. 312: p. 88-98.
22. Yip, N.Y., A. Tiraferri, W.A. Phillip, J.D. Schiffman, and M. Elimelech, *High Performance Thin-Film Composite Forward Osmosis Membrane*. *Environmental Science & Technology*, 2010. 44(10): p. 3812-3818.
23. Elimelech, M. and W.A. Phillip, *The future of seawater desalination: energy, technology, and the environment*. *Science*, 2011. 333(6043): p. 712-7.
24. Cath, T.Y., A.E. Childress, and M. Elimelech, *Forward osmosis: Principles, applications, and recent developments*. *Journal of Membrane Science*, 2006. 281(1-2): p. 70-87.
25. Zhao, S.F., L. Zou, C.Y.Y. Tang, and D. Mulcahy, *Recent developments in forward osmosis: Opportunities and challenges*. *Journal of Membrane Science*, 2012. 396: p. 1-21.
26. McCutcheon, J.R., R.L. McGinnis, and M. Elimelech, *A novel ammonia-carbon dioxide forward (direct) osmosis desalination process*. *Desalination*, 2005. 174(1): p. 1-11.
27. McGinnis, R.L. and M. Elimelech, *Global challenges in energy and water supply: the promise of engineered osmosis*. *Environmental Science & Technology*, 2008. 42(23): p. 8625-9.
28. Xie, M., L.D. Nghiem, W.E. Price, and M. Elimelech, *A Forward Osmosis-Membrane Distillation Hybrid Process for Direct Sewer Mining: System Performance and Limitations*. *Environmental Science & Technology*, 2013. 47(23): p. 13486-13493.
29. Zaviska, F. and L.D. Zou, *Using modelling approach to validate a bench scale forward osmosis pre-treatment process for desalination*. *Desalination*, 2014. 350: p. 1-13.
30. Bamaga, O.A., A. Yokochi, and E.G. Beaudry, *Application of forward osmosis in pretreatment of seawater for small reverse osmosis desalination units*. *Desalination and Water Treatment*, 2009. 5(1-3): p. 183-191.
31. Zhao, S.F., L.D. Zou, and D. Mulcahy, *Brackish water desalination by a hybrid forward osmosis-nanofiltration system using divalent draw solute*. *Desalination*, 2012. 284: p. 175-181.
32. Altaee, A., A. Mabrouk, and K. Bourouni, *A novel Forward osmosis membrane pretreatment of seawater for thermal desalination processes*. *Desalination*, 2013. 326: p. 19-29.
33. Altaee, A., A. Mabrouk, K. Bourouni, and P. Palenzuela, *Forward osmosis pretreatment of seawater to thermal desalination: High temperature FO-MSF/MED hybrid system*. *Desalination*, 2014. 339: p. 18-25.
34. Xie, M., L.D. Nghiem, W.E. Price, and M. Elimelech, *Comparison of the removal of hydrophobic trace organic contaminants by forward osmosis and reverse osmosis*. *Water Research*, 2012. 46(8): p. 2683-2692.
35. Coday, B.D., B.G.M. Yaffe, P. Xu, and T.Y. Cath, *Rejection of Trace Organic Compounds by Forward Osmosis Membranes: A Literature Review*. *Environmental Science & Technology*, 2014. 48(7): p. 3612-3624.
36. Kim, C., S. Lee, H.K. Shon, M. Elimelech, and S. Hong, *Boron transport in forward osmosis: Measurements, mechanisms, and comparison with reverse osmosis*. *Journal of Membrane Science*, 2012. 419: p. 42-48.
37. Shaffer, D.L., N.Y. Yip, J. Gilron, and M. Elimelech, *Seawater desalination for agriculture by integrated forward and reverse osmosis: Improved product water quality for potentially less energy*. *Journal of Membrane Science*, 2012. 415: p. 1-8.

38. Hoover, L.A., W.A. Phillip, A. Tiraferri, N.Y. Yip, and M. Elimelech, *Forward with Osmosis: Emerging Applications for Greater Sustainability*. Environmental Science & Technology, 2011. 45(23): p. 9824-9830.
39. McGinnis, R.L. and M. Elimelech, *Energy requirements of ammonia-carbon dioxide forward osmosis desalination*. Desalination, 2007. 207(1-3): p. 370-382.
40. Cath, T.Y., N.T. Hancock, C.D. Lundin, C. Hoppe-Jones, and J.E. Drewes, *A multi-barrier osmotic dilution process for simultaneous desalination and purification of impaired water*. Journal of Membrane Science, 2010. 362(1-2): p. 417-426.
41. Shokri, J., P. Ahmadi, P. Rashidi, M. Shahsavari, A. Rajabi-Siahboomi, et al., *Swellable elementary osmotic pump (SEOP): an effective device for delivery of poorly water-soluble drugs*. Eur J Pharm Biopharm, 2008. 68(2): p. 289-97.
42. Wang, C.Y., H.O. Ho, L.H. Lin, Y.K. Lin, and M.T. Sheu, *Asymmetric membrane capsules for delivery of poorly water-soluble drugs by osmotic effects*. Int J Pharm, 2005. 297(1-2): p. 89-97.
43. McGovern, R.K. and J.H. Lienhard, *On the potential of forward osmosis to energetically outperform reverse osmosis desalination*. Journal of Membrane Science, 2014. 469: p. 245-250.
44. McGinnis, R.L., J.R. McCutcheon, and M. Elimelech, *A novel ammonia-carbon dioxide osmotic heat engine for power generation*. Journal of Membrane Science, 2007. 305(1-2): p. 13-19.
45. Wang, K.Y., T.S. Chung, and J.J. Qin, *Polybenzimidazole (PBI) nanofiltration hollow fiber membranes applied in forward osmosis process*. Journal of Membrane Science, 2007. 300(1-2): p. 6-12.
46. Wang, K.Y., Q. Yang, T.S. Chung, and R. Rajagopalan, *Enhanced forward osmosis from chemically modified polybenzimidazole (PBI) nanofiltration hollow fiber membranes with a thin wall*. Chemical Engineering Science, 2009. 64(7): p. 1577-1584.
47. Gerstandt, K., K.V. Peinemann, S.E. Skilhagen, T. Thorsen, and T. Holt, *Membrane processes in energy supply for an osmotic power plant*. Desalination, 2008. 224(1-3): p. 64-70.
48. Yang, Q., K.Y. Wang, and T.S. Chung, *A novel dual-layer forward osmosis membrane for protein enrichment and concentration*. Separation and Purification Technology, 2009. 69(3): p. 269-274.
49. Yang, Q., K.Y. Wang, and T.S. Chung, *Dual-Layer Hollow Fibers with Enhanced Flux As Novel Forward Osmosis Membranes for Water Production*. Environmental Science & Technology, 2009. 43(8): p. 2800-2805.
50. Chou, S.R., L. Shi, R. Wang, C.Y.Y. Tang, C.Q. Qiu, et al., *Characteristics and potential applications of a novel forward osmosis hollow fiber membrane*. Desalination, 2010. 261(3): p. 365-372.
51. Wang, R., L. Shi, C.Y.Y. Tang, S.R. Chou, C. Qiu, et al., *Characterization of novel forward osmosis hollow fiber membranes*. Journal of Membrane Science, 2010. 355(1-2): p. 158-167.
52. Su, J.C., Q. Yang, J.F. Teo, and T.S. Chung, *Cellulose acetate nanofiltration hollow fiber membranes for forward osmosis processes*. Journal of Membrane Science, 2010. 355(1-2): p. 36-44.
53. Wang, K.Y., R.C. Ong, and T.S. Chung, *Double-Skinned Forward Osmosis Membranes for Reducing Internal Concentration Polarization within the Porous Sublayer*. Industrial & Engineering Chemistry Research, 2010. 49(10): p. 4824-4831.
54. Tiraferri, A., N.Y. Yip, W.A. Phillip, J.D. Schiffman, and M. Elimelech, *Relating performance of thin-film composite forward osmosis membranes to support layer formation and structure*. Journal of Membrane Science, 2011. 367(1-2): p. 340-352.
55. Zhang, S., K.Y. Wang, T.S. Chung, H.M. Chen, Y.C. Jean, et al., *Well-constructed cellulose acetate membranes for forward osmosis: Minimized internal concentration polarization with an ultra-thin selective layer*. Journal of Membrane Science, 2010. 360(1-2): p. 522-535.

56. Arena, J.T., B. McCloskey, B.D. Freeman, and J.R. McCutcheon, *Surface modification of thin film composite membrane support layers with polydopamine: Enabling use of reverse osmosis membranes in pressure retarded osmosis*. *Journal of Membrane Science*, 2011. 375(1-2): p. 55-62.
57. Sairam, M., E. Sereewatthanawut, K. Li, A. Bismarck, and A.G. Livingston, *Method for the preparation of cellulose acetate flat sheet composite membranes for forward osmosis-Desalination using MgSO₄ draw solution*. *Desalination*, 2011. 273(2-3): p. 299-307.
58. Saren, Q., C.Q. Qiu, and C.Y.Y. Tang, *Synthesis and Characterization of Novel Forward Osmosis Membranes based on Layer-by-Layer Assembly*. *Environmental Science & Technology*, 2011. 45(12): p. 5201-5208.
59. Setiawan, L., R. Wang, K. Li, and A.G. Fane, *Fabrication of novel poly(amide-imide) forward osmosis hollow fiber membranes with a positively charged nanofiltration-like selective layer*. *Journal of Membrane Science*, 2011. 369(1-2): p. 196-205.
60. Yu, Y., S. Seo, I.C. Kim, and S. Lee, *Nanoporous polyethersulfone (PES) membrane with enhanced flux applied in forward osmosis process*. *Journal of Membrane Science*, 2011. 375(1-2): p. 63-68.
61. Zhang, S., K.Y. Wang, T.S. Chung, Y.C. Jean, and H.M. Chen, *Molecular design of the cellulose ester-based forward osmosis membranes for desalination*. *Chemical Engineering Science*, 2011. 66(9): p. 2008-2018.
62. Song, X.X., Z.Y. Liu, and D.R.D.L. Sun, *Nano Gives the Answer: Breaking the Bottleneck of Internal Concentration Polarization with a Nanofiber Composite Forward Osmosis Membrane for a High Water Production Rate*. *Advanced Materials*, 2011. 23(29): p. 3256-+.
63. Qiu, C., L. Setiawan, R. Wang, C.Y.Y. Tang, and A.G. Fane, *High performance flat sheet forward osmosis membrane with an NF-like selective layer on a woven fabric embedded substrate*. *Desalination*, 2012. 287: p. 266-270.
64. Wang, K.Y., T.S. Chung, and G. Amy, *Developing thin-film-composite forward osmosis membranes on the PES/SPSf substrate through interfacial polymerization*. *Aiche Journal*, 2012. 58(3): p. 770-781.
65. Chou, S.R., R. Wang, L. Shi, Q.H. She, C.Y. Tang, et al., *Thin-film composite hollow fiber membranes for pressure retarded osmosis (PRO) process with high power density*. *Journal of Membrane Science*, 2012. 389: p. 25-33.
66. Bui, N.N. and J.R. McCutcheon, *Hydrophilic Nanofibers as New Supports for Thin Film Composite Membranes for Engineered Osmosis*. *Environmental Science & Technology*, 2013. 47(3): p. 1761-1769.
67. Lu, X.L., S.R.V. Castrillon, D.L. Shaffer, J. Ma, and M. Elimelech, *In Situ Surface Chemical Modification of Thin-Film Composite Forward Osmosis Membranes for Enhanced Organic Fouling Resistance*. *Environmental Science & Technology*, 2013. 47(21): p. 12219-12228.
68. Wang, Y.Q., R.W. Ou, Q.Q. Ge, H.T. Wang, and T.W. Xu, *Preparation of polyethersulfone/carbon nanotube substrate for high-performance forward osmosis membrane*. *Desalination*, 2013. 330: p. 70-78.
69. Emadzadeh, D., W.J. Lau, and A.F. Ismail, *Synthesis of thin film nanocomposite forward osmosis membrane with enhancement in water flux without sacrificing salt rejection*. *Desalination*, 2013. 330: p. 90-99.
70. Goh, K.L., L. Setiawan, L. Wei, W.C. Jiang, R. Wang, et al., *Fabrication of novel functionalized multi-walled carbon nanotube immobilized hollow fiber membranes for enhanced performance in forward osmosis process*. *Journal of Membrane Science*, 2013. 446: p. 244-254.
71. Stillman, D., L. Krupp, and Y.H. La, *Mesh-reinforced thin film composite membranes for forward osmosis applications: The structure-performance relationship*. *Journal of Membrane Science*, 2014. 468: p. 308-316.

72. Castrillon, S.R.V., X.L. Lu, D.L. Shaffer, and M. Elimelech, *Amine enrichment and poly(ethylene glycol) (PEG) surface modification of thin-film composite forward osmosis membranes for organic fouling control*. *Journal of Membrane Science*, 2014. 450: p. 331-339.
73. Hu, M. and B.X. Mi, *Layer-by-layer assembly of graphene oxide membranes via electrostatic interaction*. *Journal of Membrane Science*, 2014. 469: p. 80-87.
74. Ong, R.C., T.S. Chung, J.S. de Wit, and B.J. Helmer, *Novel cellulose ester substrates for high performance flat-sheet thin-film composite (TFC) forward osmosis (FO) membranes*. *Journal of Membrane Science*, 2015. 473: p. 63-71.
75. Tian, E.L., H. Zhou, Y.W. Ren, Z.A. Mirza, X.Z. Wang, et al., *Novel design of hydrophobic/hydrophilic interpenetrating network composite nanofibers for the support layer of forward osmosis membrane*. *Desalination*, 2014. 347: p. 207-214.
76. Wei, R., S. Zhang, Y. Cui, R.C. Ong, T.S. Chung, et al., *Highly permeable forward osmosis (FO) membranes for high osmotic pressure but viscous draw solutes*. *Journal of Membrane Science*, 2015. 496: p. 132-141.
77. Huang, Y.B., H.Y. Jin, H. Li, P. Yu, and Y.B. Luo, *Synthesis and characterization of a polyamide thin film composite membrane based on a polydopamine coated support layer for forward osmosis*. *Rsc Advances*, 2015. 5(128): p. 106113-106121.
78. Emadzadeh, D., W.J. Lau, M. Rahbari-Sisakht, H. Ilbeygi, D. Rana, et al., *Synthesis, modification and optimization of titanate nanotubes-polyamide thin film nanocomposite (TFN) membrane for forward osmosis (FO) application*. *Chemical Engineering Journal*, 2015. 281: p. 243-251.
79. Li, X.S., S.R. Chou, R. Wang, L. Shi, W.X. Fang, et al., *Nature gives the best solution for desalination: Aquaporin-based hollow fiber composite membrane with superior performance*. *Journal of Membrane Science*, 2015. 494: p. 68-77.
80. Park, M.J., S. Phuntsho, T. He, G.M. Nisola, L.D. Tijing, et al., *Graphene oxide incorporated polysulfone substrate for the fabrication of flat-sheet thin-film composite forward osmosis membranes*. *Journal of Membrane Science*, 2015. 493: p. 496-507.
81. Lu, P., S. Liang, L. Qiu, Y.S. Gao, and Q. Wang, *Thin film nanocomposite forward osmosis membranes based on layered double hydroxide nanoparticles blended substrates*. *Journal of Membrane Science*, 2016. 504: p. 196-205.
82. Shen, L., S. Xiong, and Y. Wang, *Graphene oxide incorporated thin-film composite membranes for forward osmosis applications*. *Chemical Engineering Science*, 2016. 143: p. 194-205.
83. Han, G., B.W. Zhao, F.J. Fu, T.S. Chung, M. Weber, et al., *High performance thin-film composite membranes with mesh-reinforced hydrophilic sulfonated polyphenylenesulfone (sPPSU) substrates for osmotically driven processes*. *Journal of Membrane Science*, 2016. 502: p. 84-93.
84. Dabaghian, Z., A. Rahimpour, and M. Jahanshahi, *Highly porous cellulosic nanocomposite membranes with enhanced performance for forward osmosis desalination*. *Desalination*, 2016. 381: p. 117-125.
85. Cath, T.Y., M. Elimelech, J.R. McCutcheon, R.L. McGinnis, A. Achilli, et al., *Standard Methodology for Evaluating Membrane Performance in Osmotically Driven Membrane Processes*. *Desalination*, 2013. 312: p. 31-38.
86. Ren, J. and J.R. McCutcheon, *A new commercial thin film composite membrane for forward osmosis*. *Desalination*, 2014. 343: p. 187-193.
87. Loeb S, S.S., *Sea Water Demineralization by Means of an Osmotic Membrane*. *Advances in Chemistry Series*, 1963(38): p. 117-132.
88. Achilli, A. and A.E. Childress, *Pressure retarded osmosis: From the vision of Sidney Loeb to the first prototype installation - Review*. *Desalination*, 2010. 261(3): p. 205-211.

89. Achilli, A., T.Y. Cath, and A.E. Childress, *Power generation with pressure retarded osmosis: An experimental and theoretical investigation*. Journal of Membrane Science, 2009. 343(1-2): p. 42-52.
90. Baker, R.W., *Membrane technology and applications*. 2nd ed ed2004, Chichester: Wiley. x, 538 p.
91. Mulder, M., *Basic principles of membrane technology*. 2nd ed1996, Dordrecht ; Boston: Kluwer Academic. 564 p.
92. McCutcheon, J.R. and M. Elimelech, *Influence of concentrative and dilutive internal concentration polarization on flux behavior in forward osmosis*. Journal of Membrane Science, 2006. 284(1-2): p. 237-247.
93. McCutcheon, J.R., R.L. McGinnis, and M. Elimelech, *Desalination by ammonia-carbon dioxide forward osmosis: Influence of draw and feed solution concentrations on process performance*. Journal of Membrane Science, 2006. 278(1-2): p. 114-123.
94. Wei, J., C.Q. Qiu, C.Y.Y. Tang, R. Wang, and A.G. Fane, *Synthesis and characterization of flat-sheet thin film composite forward osmosis membranes*. Journal of Membrane Science, 2011. 372(1-2): p. 292-302.
95. McCutcheon, J.R. and M. Elimelech, *Modeling water flux in forward osmosis: Implications for improved membrane design*. Aiche Journal, 2007. 53(7): p. 1736-1744.
96. Loeb, S., L. Titelman, E. Korngold, and J. Freiman, *Effect of porous support fabric on osmosis through a Loeb-Sourirajan type asymmetric membrane*. Journal of Membrane Science, 1997. 129(2): p. 243-249.
97. McCutcheon, J.R. and M. Elimelech, *Influence of membrane support layer hydrophobicity on water flux in osmotically driven membrane processes*. Journal of Membrane Science, 2008. 318(1-2): p. 458-466.
98. Widjojo, N., T.S. Chung, M. Weber, C. Maletzko, and V. Warzelhan, *The role of sulphonated polymer and macrovoid-free structure in the support layer for thin-film composite (TFC) forward osmosis (FO) membranes*. Journal of Membrane Science, 2011. 383(1-2): p. 214-223.
99. Bui, N.N., M.L. Lind, E.M.V. Hoek, and J.R. McCutcheon, *Electrospun nanofiber supported thin film composite membranes for engineered osmosis*. Journal of Membrane Science, 2011. 385(1-2): p. 10-19.
100. Phillip, W.A., J.S. Yong, and M. Elimelech, *Reverse Draw Solute Permeation in Forward Osmosis: Modeling and Experiments*. Environmental Science & Technology, 2010. 44(13): p. 5170-5176.
101. Tiraferri, A., N.Y. Yip, A.P. Straub, S.R.V. Castrillon, and M. Elimelech, *A method for the simultaneous determination of transport and structural parameters of forward osmosis membranes*. Journal of Membrane Science, 2013. 444: p. 523-538.
102. Hancock, N.T. and T.Y. Cath, *Solute Coupled Diffusion in Osmotically Driven Membrane Processes*. Environmental Science & Technology, 2009. 43(17): p. 6769-6775.
103. McGinnis, R.L., N.T. Hancock, M.S. Nowosielski-Slepowron, and G.D. McGurgan, *Pilot demonstration of the NH₃/CO₂ forward osmosis desalination process on high salinity brines*. Desalination, 2013. 312: p. 67-74.
104. Achilli, A., T.Y. Cath, and A.E. Childress, *Selection of inorganic-based draw solutions for forward osmosis applications*. Journal of Membrane Science, 2010. 364(1-2): p. 233-241.
105. Hoek, E.M.V. and M. Elimelech, *Cake-enhanced concentration polarization: A new fouling mechanism for salt-rejecting membranes*. Environmental Science & Technology, 2003. 37(24): p. 5581-5588.
106. Wang, Y.N., F. Wicaksana, C.Y. Tang, and A.G. Fane, *Direct Microscopic Observation of Forward Osmosis Membrane Fouling*. Environmental Science & Technology, 2010. 44(18): p. 7102-7109.

107. Zhao, S.F., L.D. Zou, and D. Mulcahy, *Effects of membrane orientation on process performance in forward osmosis applications*. *Journal of Membrane Science*, 2011. 382(1-2): p. 308-315.
108. Zodrow, K.R., M.E. Tousley, and M. Elimelech, *Mitigating biofouling on thin-film composite polyamide membranes using a controlled-release platform*. *Journal of Membrane Science*, 2014. 453: p. 84-91.
109. Morra, M., *On the molecular basis of fouling resistance*. *Journal of Biomaterials Science-Polymer Edition*, 2000. 11(6): p. 547-569.
110. Kang, G.D. and Y.M. Cao, *Development of antifouling reverse osmosis membranes for water treatment: A review*. *Water Research*, 2012. 46(3): p. 584-600.
111. Rana, D. and T. Matsuura, *Surface Modifications for Antifouling Membranes*. *Chemical Reviews*, 2010. 110(4): p. 2448-2471.
112. Chekli, L., S. Phuntsho, H.K. Shon, S. Vigneswaran, J. Kandasamy, et al., *A review of draw solutes in forward osmosis process and their use in modern applications*. *Desalination and Water Treatment*, 2012. 43(1-3): p. 167-184.
113. Tan, C.H. and H.Y. Ng, *A novel hybrid forward osmosis - nanofiltration (FO-NF) process for seawater desalination: Draw solution selection and system configuration*. *Desalination and Water Treatment*, 2010. 13(1-3): p. 356-361.
114. Phuntsho, S., H.K. Shon, S. Hong, S. Lee, and S. Vigneswaran, *A novel low energy fertilizer driven forward osmosis desalination for direct fertigation: Evaluating the performance of fertilizer draw solutions*. *Journal of Membrane Science*, 2011. 375(1-2): p. 172-181.
115. Kessler, J.O. and C.D. Moody, *Drinking-Water from Sea-Water by Forward Osmosis*. *Desalination*, 1976. 18(3): p. 297-306.
116. Kravath, R.E. and J.A. Davis, *Desalination of Sea-Water by Direct Osmosis*. *Desalination*, 1975. 16(2): p. 151-155.
117. Stache, K.D., (DE), *Apparatus for transforming sea water, brackish water, polluted water or the like into a nutritious drink by means of osmosis*, 1989, DD-Dynamic Devices Ltd. (London, GB2): United States.
118. Ling, M.M. and T.S. Chung, *Desalination process using super hydrophilic nanoparticles via forward osmosis integrated with ultrafiltration regeneration*. *Desalination*, 2011. 278(1-3): p. 194-202.
119. Ling, M.M. and T.S. Chung, *Novel dual-stage FO system for sustainable protein enrichment using nanoparticles as intermediate draw solutes*. *Journal of Membrane Science*, 2011. 372(1-2): p. 201-209.
120. Ling, M.M., K.Y. Wang, and T.S. Chung, *Highly Water-Soluble Magnetic Nanoparticles as Novel Draw Solutes in Forward Osmosis for Water Reuse*. *Industrial & Engineering Chemistry Research*, 2010. 49(12): p. 5869-5876.
121. Ge, Q.C., J.C. Su, T.S. Chung, and G. Amy, *Hydrophilic Superparamagnetic Nanoparticles: Synthesis, Characterization, and Performance in Forward Osmosis Processes*. *Industrial & Engineering Chemistry Research*, 2011. 50(1): p. 382-388.
122. Chung, T.S., S. Zhang, K.Y. Wang, J.C. Su, and M.M. Ling, *Forward osmosis processes: Yesterday, today and tomorrow*. *Desalination*, 2012. 287: p. 78-81.
123. Bamaga, O.A., A. Yokochi, B. Zabara, and A.S. Babaqi, *Hybrid FO/RO desalination system: Preliminary assessment of osmotic energy recovery and designs of new FO membrane module configurations*. *Desalination*, 2011. 268(1-3): p. 163-169.
124. Li, D., X.Y. Zhang, J.F. Yao, Y. Zeng, G.P. Simon, et al., *Composite polymer hydrogels as draw agents in forward osmosis and solar dewatering*. *Soft Matter*, 2011. 7(21): p. 10048-10056.
125. Kim, T.W., Y. Kim, C. Yun, H. Jang, W. Kim, et al., *Systematic approach for draw solute selection and optimal system design for forward osmosis desalination*. *Desalination*, 2012. 284: p. 253-260.

126. Ge, Q.C., M.M. Ling, and T.S. Chung, *Draw solutions for forward osmosis processes: Developments, challenges, and prospects for the future*. Journal of Membrane Science, 2013. 442: p. 225-237.
127. Rubinstein, M. and R.H. Colby, *Polymer physics* 2003, Oxford ; New York: Oxford University Press. xi, 440 p.
128. Zhao, S.A.F. and L.D. Zou, *Relating solution physicochemical properties to internal concentration polarization in forward osmosis*. Journal of Membrane Science, 2011. 379(1-2): p. 459-467.
129. Boo, C., Y.F. Khalil, and M. Elimelech, *Performance evaluation of trimethylamine-carbon dioxide thermolytic draw solution for engineered osmosis*. Journal of Membrane Science, 2015. 473: p. 302-309.
130. Ge, Q.C., J.C. Su, G.L. Amy, and T.S. Chung, *Exploration of polyelectrolytes as draw solutes in forward osmosis processes*. Water Research, 2012. 46(4): p. 1318-1326.
131. Stone, M.L., A.D. Wilson, M.K. Harrup, and F.F. Stewart, *An initial study of hexavalent phosphazene salts as draw solutes in forward osmosis*. Desalination, 2013. 312: p. 130-136.
132. Stone, M.L., C. Rae, F.F. Stewart, and A.D. Wilson, *Switchable polarity solvents as draw solutes for forward osmosis*. Desalination, 2013. 312: p. 124-129.
133. Wilson, A.D. and F.F. Stewart, *Structure-function study of tertiary amines as switchable polarity solvents*. Rsc Advances, 2014. 4(22): p. 11039-11049.
134. Wijmans, J.G. and R.W. Baker, *The Solution-Diffusion Model - a Review*. Journal of Membrane Science, 1995. 107(1-2): p. 1-21.
135. Tang, C.Y.Y., Q.H. She, W.C.L. Lay, R. Wang, and A.G. Fane, *Coupled effects of internal concentration polarization and fouling on flux behavior of forward osmosis membranes during humic acid filtration*. Journal of Membrane Science, 2010. 354(1-2): p. 123-133.
136. Lin, S.H., N.Y. Yip, T.Y. Cath, C.O. Osuji, and M. Elimelech, *Hybrid Pressure Retarded Osmosis-Membrane Distillation System for Power Generation from Low-Grade Heat: Thermodynamic Analysis and Energy Efficiency*. Environmental Science & Technology, 2014. 48(9): p. 5306-5313.
137. Shaffer, D.L., L.H.A. Chavez, M. Ben-Sasson, S.R.V. Castrillon, N.Y. Yip, et al., *Desalination and Reuse of High-Salinity Shale Gas Produced Water: Drivers, Technologies, and Future Directions*. Environmental Science & Technology, 2013. 47(17): p. 9569-9583.
138. Greenlee, L.F., D.F. Lawler, B.D. Freeman, B. Marrot, and P. Moulin, *Reverse osmosis desalination: Water sources, technology, and today's challenges*. Water Research, 2009. 43(9): p. 2317-2348.
139. Antony, A., J.H. Low, S. Gray, A.E. Childress, P. Le-Clech, et al., *Scale formation and control in high pressure membrane water treatment systems: A review*. Journal of Membrane Science, 2011. 383(1-2): p. 1-16.
140. Fritzmann, C., J. Lowenberg, T. Wintgens, and T. Melin, *State-of-the-art of reverse osmosis desalination*. Desalination, 2007. 216(1-3): p. 1-76.
141. Cunningham, V.L., S.P. Binks, and M.J. Olson, *Human health risk assessment from the presence of human pharmaceuticals in the aquatic environment*. Regulatory Toxicology and Pharmacology, 2009. 53(1): p. 39-45.
142. Zhu, A.Z., P.D. Christofides, and Y. Cohen, *Effect of Thermodynamic Restriction on Energy Cost Optimization of RO Membrane Water Desalination*. Industrial & Engineering Chemistry Research, 2009. 48(13): p. 6010-6021.
143. Avlonitis, S., W.T. Hanbury, and M. Benboudinar, *Spiral Wound Modules Performance - an Analytical Solution .1*. Desalination, 1991. 81(1-3): p. 191-208.
144. Avlonitis, S., W.T. Hanbury, and M.B. Boudinar, *Spiral Wound Modules Performance - an Analytical Solution .1*. Desalination and Water Re-Use : Proceedings of the Twelfth International Symposium, Vol 1, 1991. 125: p. 191-208.

145. Avlonitis, S.A., M. Pappas, and K. Moutesidis, *A unified model for the detailed investigation of membrane modules and RO plants performance*. Desalination, 2007. 203(1-3): p. 218-228.
146. Beca, J., *Pharmaceutical discharge: Zero discharge for pharma plant*. Filtration & Separation, 2007. 44(6): p. 40-41.
147. Benboudinar, M., W.T. Hanbury, and S. Avlonitis, *Numerical-Simulation and Optimization of Spiral-Wound Modules*. Desalination, 1992. 86(3): p. 273-290.
148. Geraldes, V., N.E. Pereira, and M.N. de Pinho, *Simulation and optimization of medium-sized seawater reverse osmosis processes with spiral-wound modules*. Industrial & Engineering Chemistry Research, 2005. 44(6): p. 1897-1905.
149. Rautenbach, R. and W. Dahm, *Design and Optimization of Spiral-Wound and Hollow Fiber Ro-Modules*. Desalination, 1987. 65(1-3): p. 259-275.
150. van der Meer, W.G.J. and J.C. van Dijk, *Theoretical optimization of spiral-wound and capillary nanofiltration modules*. Desalination, 1997. 113(2-3): p. 129-146.
151. Villafafila, A. and I.M. Mujtaba, *Fresh water by reverse osmosis based desalination: simulation and optimisation*. Desalination, 2003. 155(1): p. 1-13.
152. Fethi, K., *Optimization of energy consumption in the 3300 m³/d RO Kerkennah plant*. Desalination, 2003. 157(1-3): p. 145-149.
153. Nemeth, J.E., *Innovative system designs to optimize performance of ultra-low pressure reverse osmosis membranes*. Desalination, 1998. 118(1-3): p. 63-71.
154. Wilf, M., *Design consequences of recent improvements in membrane performance*. Desalination, 1997. 113(2-3): p. 157-163.
155. Cardona, E., A. Piacentino, and F. Marchese, *Energy saving in two-stage reverse osmosis systems coupled with ultrafiltration processes*. Desalination, 2005. 184(1-3): p. 125-137.
156. Cote, P., S. Siversns, and S. Monti, *Comparison of membrane-based solutions for water reclamaton and desalination*. Desalination, 2005. 182(1-3): p. 251-257.
157. Qiu, C.Q., S.R. Qi, and C.Y.Y. Tang, *Synthesis of high flux forward osmosis membranes by chemically crosslinked layer-by-layer polyelectrolytes*. Journal of Membrane Science, 2011. 381(1-2): p. 74-80.
158. Peshev, D. and A.G. Livingston, *OSN Designer, a tool for predicting organic solvent nanofiltration technology performance using Aspen One, MATLAB and CAPE OPEN*. Chemical Engineering Science, 2013. 104: p. 975-987.
159. Water, P.I. 2012-2013; Available from: <http://puretecwater.com/what-is-reverse-osmosis.html#recovery>.
160. Robinson, R.A. and R.H. Stokes, *Electrolyte solutions; the measurement and interpretation of conductance, chemical potential, and diffusion in solutions of simple electrolytes*. 2d ed 1959, London,,: Butterworths. xv, 571 p.
161. Heyrovská, R., *Physical electrochemistry of strong electrolytes based on partial dissociation and hydration - Quantitative interpretation of the thermodynamic properties of NaCl(aq) from "zero to saturation"*. Journal of the Electrochemical Society, 1996. 143(6): p. 1789-1793.
162. Choi, B.B., Y.J. Choi, J.S. Choi, S. Lee, and H.J. Oh, *Energy management in submerged microfiltration systems by optimum control of aeration*. Desalination, 2009. 247(1-3): p. 233-238.
163. Schock, G. and A. Miquel, *Mass-Transfer and Pressure Loss in Spiral Wound Modules*. Desalination, 1987. 64: p. 339-352.
164. Sagiv, A., A.H. Zhu, P.D. Christofides, Y. Cohen, and R. Semiat, *Analysis of forward osmosis desalination via two-dimensional FEM model*. Journal of Membrane Science, 2014. 464: p. 161-172.
165. Lee, J., B. Kim, and S. Hong, *Fouling distribution in forward osmosis membrane process*. Journal of Environmental Sciences-China, 2014. 26(6): p. 1348-1354.

166. Shim, S.M. and W.S. Kim, *A numerical study on the performance prediction of forward osmosis process*. Journal of Mechanical Science and Technology, 2013. 27(4): p. 1179-1189.
167. FilmTec, D. *Steps to Design an RO/NF Membrane System*. Available from: http://www.dowwaterandprocess.com/support_training/literature_manuals/lm_techinfo/designstps.htm.
168. <http://www.htiwater.com/contact/index.html>. [cited 2014 13 June].
169. *Mutual Diffusion-Coefficients in Aqueous-Electrolyte Solutions (Technical Report)*. Pure and Applied Chemistry, 1993. 65(12): p. 2614-2640.
170. Feinberg, B.J., G.Z. Ramon, and E.M.V. Hoek, *Thermodynamic Analysis of Osmotic Energy Recovery at a Reverse Osmosis Desalination Plant*. Environmental Science & Technology, 2013. 47(6): p. 2982-2989.
171. Li, M.H., *Minimization of Energy in Reverse Osmosis Water Desalination Using Constrained Nonlinear Optimization*. Industrial & Engineering Chemistry Research, 2010. 49(4): p. 1822-1831.
172. Li, M.H., *Reducing specific energy consumption in Reverse Osmosis (RO) water desalination: An analysis from first principles*. Desalination, 2011. 276(1-3): p. 128-135.
173. Liu, C., K. Rainwater, and L.F. Song, *Energy analysis and efficiency assessment of reverse osmosis desalination process*. Desalination, 2011. 276(1-3): p. 352-358.
174. Liu, C., K. Rainwater, and L.F. Song, *Calculation of energy consumption for crossflow RO desalination processes*. Desalination and Water Treatment, 2012. 42(1-3): p. 295-303.
175. Oi, B.W., Y. Wang, S.C. Xu, Z.C. Wang, and S.C. Wang, *Operating Energy Consumption Analysis of RO Desalting System: Effect of Membrane Process and Energy Recovery Device (ERD) Performance Variables*. Industrial & Engineering Chemistry Research, 2012. 51(43): p. 14135-14144.
176. Wilf, M. and M.K. Schierach, *Improved performance and cost reduction of RO seawater systems using UF pretreatment*. Desalination, 2001. 135(1-3): p. 61-68.
177. Technology, W. 2010 [cited 2013; Available from: <http://www.watertechnonline.com/articles/what-to-look-for-in-desalination-pumps>.
178. Corporation, F. *Desalination Bulletin*. 2012 [cited 2013; Available from: <http://www.flowserve.com/files/Files/Literature/FPD/fpd-10-ea4.pdf>.
179. David Cohen-Tanugi, R.K.M., Shreya H. Dave, John H. Lienhard and Jeffrey C. Grossman*, *Quantifying the potential of ultra-permeable membranes for water desalination*. Energy & Environmental Science, 2014(3): p. 1134-1141.
180. Cohen-Tanugi, D. and J.C. Grossman, *Water Desalination across Nanoporous Graphene*. Nano Letters, 2012. 12(7): p. 3602-3608.
181. Zhu, A.H., A. Rahardianto, P.D. Christofides, and Y. Cohen, *Reverse osmosis desalination with high permeability membranes - Cost optimization and research needs*. Desalination and Water Treatment, 2010. 15(1-3): p. 256-266.
182. Organization, W.H. *Guidelines for drinking-water quality*. 1996 March 2013]; 2nd ed. Vol. 2:[Available from: http://www.who.int/water_sanitation_health/dwq/ammonia.pdf.
183. Mazlan, N.M.P., D.; Livingston, A.G., *Energy Consumption for Desalination - A Comparison of Forward Osmosis with Reverse Osmosis, and the Potential for Perfect Membranes*. Desalination, 2015. 377: p. 138-151.
184. (HTI), H.T.I. *HTI'S New Thin Film Forward Osmosis Membrane in Production*. 2012; Available from: <http://www.htiwater.com/news/press-room/content/2012/press-HTI-HTIThinFilmMembrane042512.pdf>.
185. Desalination.com. *TFC FO elements now available*. 2012; Available from: <http://www.desalination.com/wdr/48/17/tfc-fo-elements-now-available>.
186. Nguyen, T.P.N., B.M. Jun, J.H. Lee, and Y.N. Kwon, *Comparison of integrally asymmetric and thin film composite structures for a desirable fashion of forward osmosis membranes*. Journal of Membrane Science, 2015. 495: p. 457-470.

187. Xie, M., J. Lee, L.D. Nghiem, and M. Elimelech, *Role of pressure in organic fouling in forward osmosis and reverse osmosis*. Journal of Membrane Science, 2015. 493: p. 748-754.
188. Characklis, W.G. and K.C. Marshall, *Biofilms*. Wiley series in ecological and applied microbiology 1990, New York: Wiley. xvii, 796 p.
189. Choi, H., K. Zhang, D.D. Dionysiou, D.B. Oerther, and G.A. Sorial, *Influence of cross-flow velocity on membrane performance during filtration of biological suspension*. Journal of Membrane Science, 2005. 248(1-2): p. 189-199.
190. Peeva, L.G., E. Gibbins, S.S. Luthra, L.S. White, R.P. Stateva, et al., *Effect of concentration polarisation and osmotic pressure on flux in organic solvent nanofiltration*. Journal of Membrane Science, 2004. 236(1): p. 121-136.
191. Robinson, R.A. and R.H. Stokes, *Electrolyte solutions, the measurement and interpretation of conductance, chemical potential, and diffusion in solutions of simple electrolytes*. 2d ed 1959, London,: Butterworths Scientific Publications. 559 p.
192. Freger, V., *Swelling and morphology of the skin layer of polyamide composite membranes: An atomic force microscopy study*. Environmental Science & Technology, 2004. 38(11): p. 3168-3175.
193. Zhang, S., F.J. Fu, and T.S. Chung, *Substrate modifications and alcohol treatment on thin film composite membranes for osmotic power*. Chemical Engineering Science, 2013. 87: p. 40-50.
194. Karan, S., Z.W. Jiang, and A.G. Livingston, *Sub-10 nm polyamide nanofilms with ultrafast solvent transport for molecular separation*. Science, 2015. 348(6241): p. 1347-1351.
195. Kolev, V. and V. Freger, *Hydration, porosity and water dynamics in the polyamide layer of reverse osmosis membranes: A molecular dynamics study*. Polymer, 2014. 55(6): p. 1420-1426.
196. Mukherjee, D., A. Kulkarni, and W.N. Gill, *Chemical treatment for improved performance of reverse osmosis membranes*. Desalination, 1996. 104(3): p. 239-249.
197. Gorgojo, P., M.F. Jimenez-Solomon, and A.G. Livingston, *Polyamide thin film composite membranes on cross-linked polyimide supports: Improvement of RO performance via activating solvent*. Desalination, 2014. 344: p. 181-188.
198. Hoek, E.M.V., S. Bhattacharjee, and M. Elimelech, *Effect of membrane surface roughness on colloid-membrane DLVO interactions*. Langmuir, 2003. 19(11): p. 4836-4847.
199. Lee, S. and M. Elimelech, *Relating organic fouling of reverse osmosis membranes to intermolecular adhesion forces*. Environmental Science & Technology, 2006. 40(3): p. 980-987.
200. Xiang, Y., Y.L. Liu, B.X. Mi, and Y.S. Leng, *Hydrated Polyamide Membrane and Its Interaction with Alginate: A Molecular Dynamics Study*. Langmuir, 2013. 29(37): p. 11600-11608.
201. Xiang, Y., Y.L. Liu, B.X. Mi, and Y.S. Leng, *Molecular Dynamics Simulations of Polyamide Membrane, Calcium Alginate Gel, and Their Interactions in Aqueous Solution*. Langmuir, 2014. 30(30): p. 9098-9106.
202. Mara, D.D. and N.J. Horan, *Handbook of water and wastewater microbiology* 2003, London ; San Diego: Academic Press. ix, 819 p.
203. Hideaki Ichiura, M.M., Masaki Takahashi, Noriyoshi Nishida, Takamitsu Igaue, Takayoshi Konishi,, *Method for producing functional material, functional material, sheet-like structure and sanitary product* 2013, Unicharm Corporation: Japan.
204. Youngjin Kim, S.L., Jihoon Kuk, Seungkwon Hong, *Surface chemical heterogeneity of polyamide RO membranes: Measurements and implications*. Desalination, 2015. 367: p. 154-160.
205. Swain, P.S. and R. Lipowsky, *Contact angles on heterogeneous surfaces: A new look at Cassie's and Wenzel's laws*. Langmuir, 1998. 14(23): p. 6772-6780.
206. Bacchin, P., P. Aimar, and R.W. Field, *Critical and sustainable fluxes: Theory, experiments and applications*. Journal of Membrane Science, 2006. 281(1-2): p. 42-69.

207. Mehta, G.D. and S. Loeb, *Internal Polarization in the Porous Substructure of a Semipermeable Membrane under Pressure-Retarded Osmosis*. *Journal of Membrane Science*, 1978. 4(2): p. 261-265.
208. Jin, Y., W. Wang, and Z.H. Su, *Spectroscopic study on water diffusion in aromatic polyamide thin film*. *Journal of Membrane Science*, 2011. 379(1-2): p. 121-130.
209. Jr., P.J.F.J.R., *Statistical Mechanics of Cross-Linked Polymer Networks II. Swelling*. *J. Chem. Phys.*, 1943(11): p. 521-526.

9 Appendices

Appendix A (Chapter 4)

Appendix A 1

Process Model for RO Desalination

$$Q_F - Q_R - Q_P = 0 \quad \text{Equation A 1}$$

$$Q_F X_{F,NaCl} - Q_R X_{R,NaCl} - Q_P X_{P,NaCl} = 0 \quad \text{Equation A 2}$$

$$Q_P = \frac{L_p A_m \left[\Delta P - \theta \left(\frac{X_{M,NaCl}}{v_M} - \frac{X_{P,NaCl}}{v_P} \right) R_g T \right]}{v_P} \quad \text{Equation A 3}$$

$$X_{P,NaCl} v_M = X_{M,NaCl} v_P (1 - R) \quad \text{Equation A 4}$$

$$\frac{X_{M,NaCl}}{v_M} = \left(\frac{X_{R,NaCl}}{v_R} - \frac{X_{P,NaCl}}{v_P} \right) \exp \left[\frac{(Q_P/A_m) v_P}{k} \right] + \frac{X_{P,NaCl}}{v_P} \quad \text{Equation A 5}$$

It should be noted that $X_{P,NaCl} = 0$ in the simulation since NaCl rejection is assumed to be 100%. The applied transmembrane pressure, ΔP , is calculated as a function of pressure drop as shown in Appendix A 2 whereby $\Delta P_{(i)} = P_{out(i-1)} - 10^5$ (Pa), whereby (i) is the i^{th} element in series down the flow path of the feed.

Note that Equation A 3 is a rearrangement of Equation 2.8 in Chapter 2, which describes water flux across a membrane under RO conditions. Whereas, Equation A 4 is a rearrangement of Equation 5.2 in Chapter 5, describing solute rejection of the membrane.

Appendix A 2

Model for Pressure Drop in a Typical 8-inch by 40-inch Spiral Wound FilmTec (SW30HR-380) RO Module [148]

$$\begin{aligned} \frac{dP_f}{dx} &= 2.4 \times 6.23 \left(\frac{9.35 \times 10^{-4} \cdot v_f \cdot 1025}{\mu} \right)^{-0.3} \frac{1025 \cdot v_f^2}{2(9.35 \times 10^{-4})} \\ &= 15.14 \left(\frac{v_f}{\mu} \right)^{-0.3} \times 548128.34 v_f^2 \end{aligned}$$

$$= 8300817 \times \mu^{0.3} \times \nu_f^{1.7}$$

$$P_{out}(i) = P_{in}(i + 1)$$

$$= P_{in}(i) - 8300817 \cdot c_1 (\mu(i + 1)^{0.3}) \cdot c_2 (\nu_f(i + 1)^{1.7}) \cdot dx$$

Equation A 6

The absolute pressure at the exit of the module, P_{out} i.e. at the exit of the last infinitesimal element, was calculated using Equation F 6, whereby c_1 and c_2 are constants. The step size was sufficiently small to ensure no significant effect of its value on the overall pressure drop along the module.

Appendix A 3

Process Model for FO with NF recovery Desalination

$$A_m \frac{Q_{PP} \times \nu_{H_2O}}{L_P} \times \left[\frac{\left[\left(\phi_{MgSO_4} \frac{X_{P,MgSO_4}}{\nu_P} - \phi_{MgSO_4} \frac{X_{D,MgSO_4}}{\nu_D} \right) \exp[-(Q_{PP}/A_m) \nu_{PP} K] - \left(\phi_{NaCl} \frac{X_{F,NaCl}}{\nu_F} - \phi_{NaCl} \frac{X_{R,NaCl}}{\nu_R} \right) \exp\left[\frac{(Q_{PP}/A_m) \nu_{PP}}{k}\right] \right] R_g T}{\ln \left[\frac{\left(\phi_{MgSO_4} \frac{X_{P,MgSO_4}}{\nu_P} \right) \exp[-(Q_{PP}/A_m) \nu_{PP} K] - \left(\phi_{NaCl} \frac{X_{F,NaCl}}{\nu_F} \right) \exp\left[\frac{(Q_{PP}/A_m) \nu_{PP}}{k}\right]}{\left(\phi_{MgSO_4} \frac{X_{D,MgSO_4}}{\nu_D} \right) \exp[-(Q_{PP}/A_m) \nu_{PP} K] - \left(\phi_{NaCl} \frac{X_{R,NaCl}}{\nu_R} \right) \exp\left[\frac{(Q_{PP}/A_m) \nu_{PP}}{k}\right]}} \right]} = 0$$

Equation A 7

$$Q_P - Q_{PP} - Q_D = 0$$

Equation A 8

$$Q_R + Q_{PP} - Q_F = 0$$

Equation A 9

$$(X_{R,NaCl} \cdot Q_R) - (X_{F,NaCl} \cdot Q_F) = 0$$

Equation A 10

$$(X_{P,MgSO_4} \cdot Q_P) - (X_{D,MgSO_4} \cdot Q_D) = 0$$

Equation A 11

The osmotic pressure difference in the FO stage (Equation A 7 and Equation 4.4 of Chapter 4) was calculated using an approach analogous to one which involves mass transfer between two phases such as in the case of absorption. In this case, driving force is expressed in terms of concentration differences, just as in FO whereby osmotic pressure is a function of concentration. The permeate flow that occurs across an FO membrane between the feed and

draw solutions is analogous to the mass transfer that takes place at the interface in an absorber. In Equation A 7, the log mean driving force was used as an approximation for the osmotic pressure difference across the membrane. This implies that a linear profile was assumed for the function: (osmotic pressure in draw solution channel) vs. (osmotic pressure in feed solution channel) along the FO module. In reality, the profile is not exactly linear as the flowrates are variable along the feed and draw solution channels of the module. However, as there are currently no specifications available on the geometry and flow configurations of commercial FO modules, the log mean osmotic pressure approach was used as an adequate estimate given the present limitations.

When calculating the log mean osmotic pressure difference, it is assumed that all permeate from the feed channel is transferred to the draw channel i.e. no mass is lost to the surroundings. A constant total mass flowrate is also assumed based on the law of conservation of mass, as the total mass flowrate into the FO stage must be equal to the total mass flowrate exiting system:

$$Q_F + Q_D = Q_P + Q_R$$

Equation A 12

For the valid use of the log mean approach, steady flow conditions, no phase change and a constant membrane permeance are also assumed.

Note that Equation A 7 is a rearrangement of Equation 2.26 in Chapter 2, which describes water flux across the membrane in FO mode.

Single-Stage NF

The process model used for single-stage NF for draw solution recovery is the same as RO (Appendix A 1) with the NaCl solute in RO replaced by MgSO₄ in NF and the corrected van't Hoff factor for the MgSO₄ solution being $\phi = 1.2$.

Appendix A 4

Method of Calculation Used to obtain the Gain in Energy Savings (G_{SEC}) for the two-stage RO Relative to the Single-Stage RO [142].

$$G_{SEC} = \frac{SEC_{1RO}}{\pi_0} f_{ES}$$

Where $\pi_0 = \pi_{NaCl@35g.l^{-1}}$ and the fractional energy savings,

$$f_{ES} = \frac{SEC(1RO) - SEC(2ROs)}{SEC(1RO)}$$

The penalty due to the increase in membrane area (P_{SMC}) is calculated using the following equation [142]:

$$P_{SMC} = \frac{m_{norm}}{\frac{1}{1-Y} - \frac{1}{Y} \ln\left(\frac{1}{1-Y}\right)} \times \left(\frac{A_{mem,1} + A_{mem,2}}{A_{mem,1RO}} - 1 \right)$$

Where m_{norm} (calculated for desalination as ~ 0.1) is a dimensionless membrane price which is independent of RO operating conditions calculated using:

$$m_{norm} = \frac{m}{L_p(\pi_0)^2} \times \left(\frac{A_{mem,1} + A_{mem,2}}{A_{mem,1RO}} - 1 \right)$$

Where m is the amortized membrane price per unit area, given by:

$$m = \frac{m_A \beta}{\epsilon}$$

Where m_A ($\text{£.m}^{-2}.\text{h}^{-1}$) is the amortized membrane unit cost selected at 100 £.m^{-2} assuming a membrane life of 5 years, β ($\text{Pa.m}^3.\text{kWh}^{-1}$) is the conversion factor calculated as $1.557 \times 10^6 \text{ Pa.m}^3.\text{kWh}^{-1}$ and ϵ_p (£.kWh^{-1}) is the energy price selected at the current average standard price of 0.15 £.kWh^{-1} [142].

The overall cost savings was calculated as follows:

$$\text{Overall cost savings} = G_{SEC} - P_{SMC}$$

Appendix A 5**Calculation of Energy Consumption for the FO-UF Process using Nanoparticles (NPs) as the Draw Solution**

Osmotic pressure of 35 g.L⁻¹ NaCl = 24.29 bar

At 75% recovery for FO,

$$\pi_{NaCl,exit} = \frac{24.29}{0.25} = 97.16 \text{ bar}$$

$$\pi_{DS,in} = 97.16 + 2 = 99.16 \text{ bar}$$

$$\pi_{DS,exit} = 99.16 \times 0.25 = 24.79 \text{ bar}$$

At 75% recovery for UF, $\pi_{reconcentrated NP} = \frac{24.79}{0.25} = 99.16 \text{ bar}$

$$\Delta P_{required} \approx 100 \text{ bar}$$

SEC_{UF}

$$= \frac{\Delta P(\text{Pa}) \times 1(\text{h})}{Y \times 3600(\text{s}) \times 1000}$$

$$= \frac{100 \times 10^5(\text{Pa}) \times 1(\text{h})}{0.75 \times 3600(\text{s}) \times 1000}$$

$$= 3.70 \text{ kWh.m}^{-3}$$

In the presence of an ERD at 100% efficiency,

$SEC_{UF,recovered}$

$$= \Delta P \times \frac{Q_R}{Q_P}$$

$$= \frac{100 \times 10^5(\text{Pa}) \times \frac{1}{3} \times 1(\text{h})}{3600(\text{s}) \times 1000}$$

$$= 0.9259 \text{ kWh.m}^{-3}$$

Whereby,

$$\frac{Q_R}{Q_P} = \frac{0.25 \times Q_F}{0.75 \times Q_F} = \frac{1}{3}$$

$$\Rightarrow SEC_{UF,ERD}$$

$$= 3.7 - 0.9259$$

$$= 2.77 \text{ kWh.m}^{-3}$$

Total SEC for FO-UF

$$= 2.77 + 0.07$$

$$= \mathbf{2.84 \text{ kWh.m}^{-3}}$$

Assuming UF pretreatment prior to FO stage with an SEC of 0.33 kWh.m^{-3} ,

$$SEC_{FO-UF} = 2.84 + 0.33 = \mathbf{3.2 \text{ kWh.m}^{-3}}$$

Appendix A 6

Calculation of Energy Consumption for the Recovery of MNPs using a Magnetic Field

$$\text{Permeate flowrate, } Q_P = \frac{50(\text{mL})}{30(\text{min})} = 1 \times 10^{-4} \frac{\text{m}^3}{\text{h}}$$

SEC

$$= \frac{\text{Magnetic Power}}{Q_P}$$

$$= \frac{187 \text{ (W)}}{1 \times 10^{-4} \left(\frac{\text{m}^3}{\text{h}} \right)}$$

$$= \mathbf{1870 \text{ kWh.m}^{-3}}$$

Appendix A 7

Pressure drop profile along eight spiral wound (SW) modules in series (Section 4.3.2)

The pressure drop profile based on the model used in Section 4.2.2.1.2 is shown in Figure A-1. Considering the maximum allowable feed flowrate for the module FilmTec SW30HR-380 of $18 \text{ m}^3 \cdot \text{h}^{-1}$ and operating below the maximum operating pressure of 69 bar, it can be observed that the highest ΔP_{loss} attained per element at the maximum feed flowrate was 1.63 bar (Figure A-2). This result indicates that in order to operate the 8" by 40" SW30HR-380 module below the operating limits for pressure drop of 1 bar, a feed flowrate of $13 \text{ m}^3 \cdot \text{h}^{-1}$ and below would be required. The contribution of pressure drop in comparison with the applied pressure i.e. $\frac{\Delta P_{\text{loss}}}{\Delta P}$ was small i.e. in the order of 10^{-2} , which is within the range calculated for an SWRO process with similar process conditions as shown in a study by Zhu et al., thus verifying these model results [142].

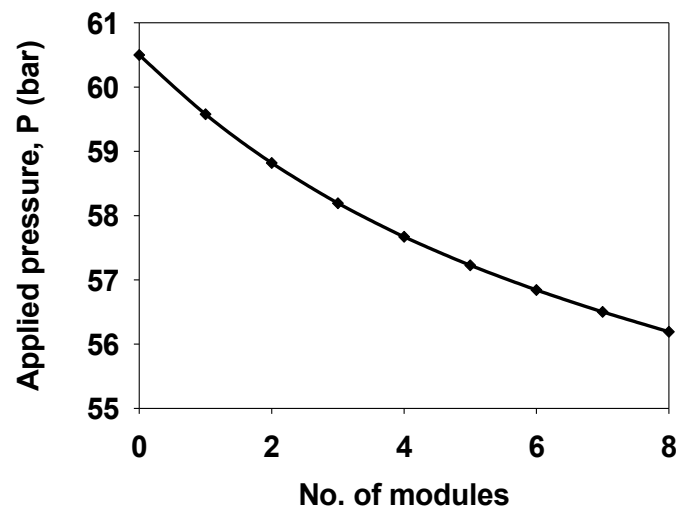


Figure A- 1: Profile of applied pressure along eight spiral wound elements in a series at a feed flow rate, $Q_F=12.85 \text{ m}^3 \cdot \text{h}^{-1}$, $A_m=35 \text{ m}^2$ per element, $\Delta P=59.5 \text{ bar}$.

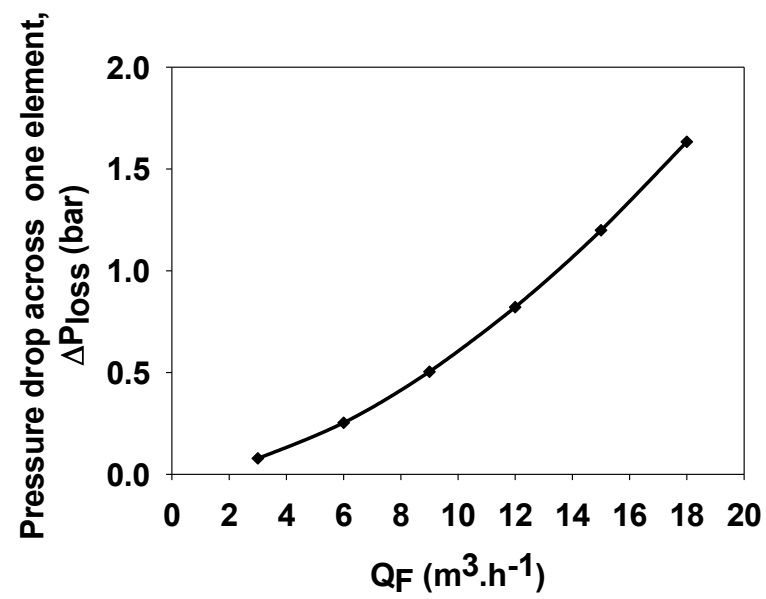


Figure A- 2: Pressure drop across a single spiral wound element with varying feed flowrates. $L_m=1$ m, $A_m=35$ m^2 , $\Delta P=59.5$ bar.

Comparison of retentate flowrate and applied pressure for 2:1 and 3:2 RO configurations (Section 4.3.2).

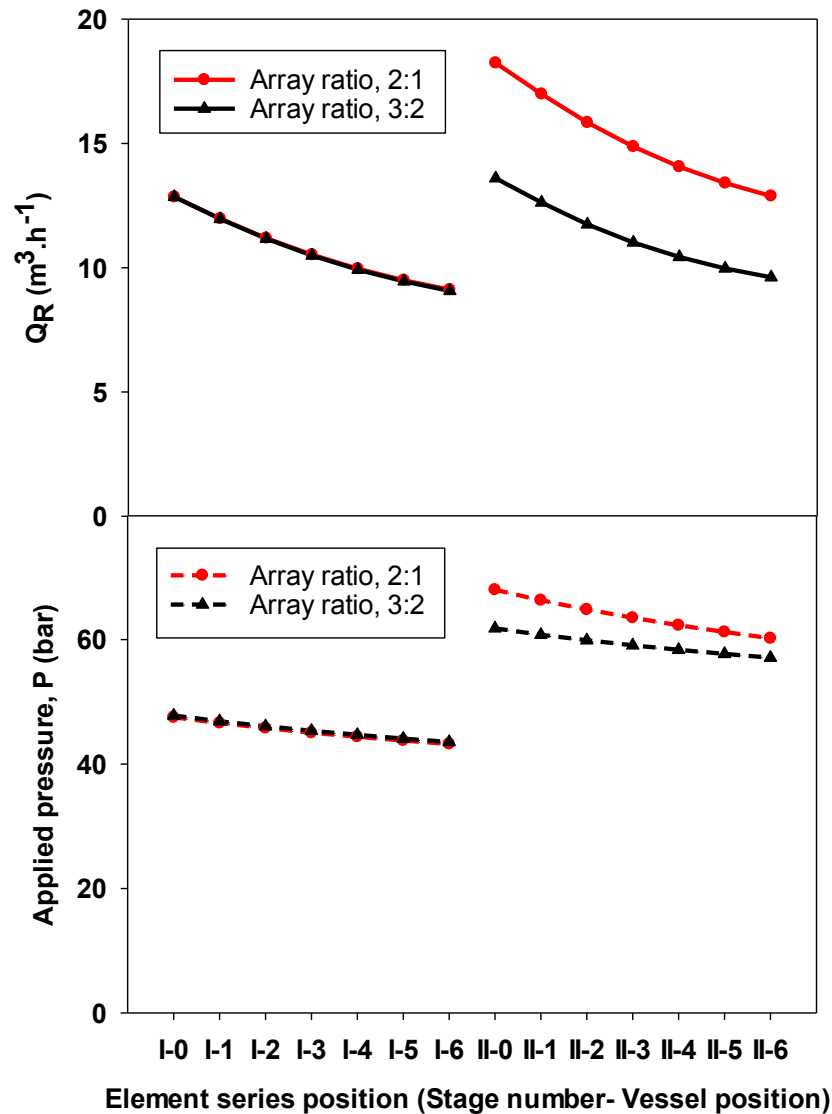


Figure A- 3: Variation of retentate flowrate and applied pressure along twelve elements in a series in a 2:1 and 3:2 array of six-element pressure vessels. Product recovery=50%, Q_F per pressure vessel for the 1st stage=12.85 m³.h⁻¹.

Process scale-up for a single-stage RO configuration (Section 4.3.3)

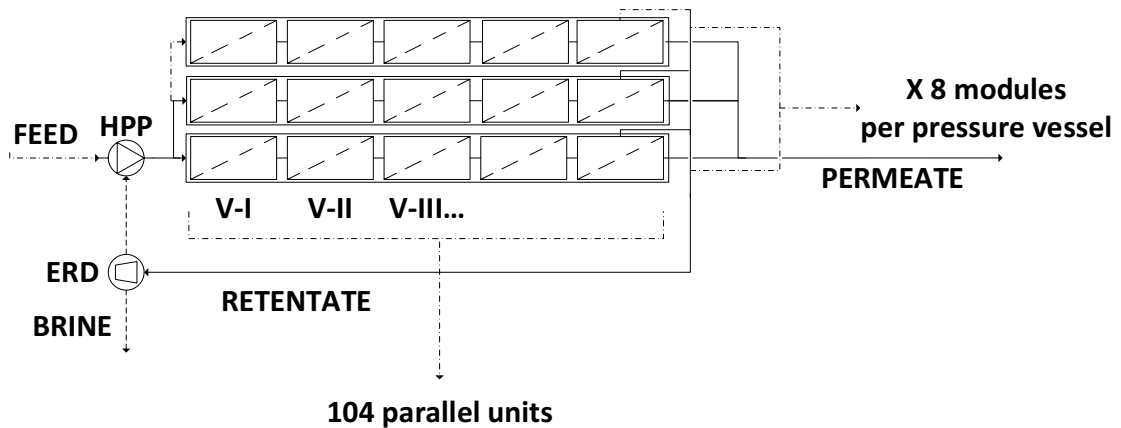


Figure A- 4: Process scale-up for a single-stage RO configuration with 8 modules per pressure vessel for 50% product recovery. For a scale-up to $Q_p=666 \text{ m}^3 \cdot \text{h}^{-1}$, 104 parallel units are required with a specific membrane area of $A_{m,s}=43.57 \text{ [m}^2(\text{m}^3 \cdot \text{h}^{-1})^{-1}]$.

Process scale-up for a two-stage RO configuration (Section 4.3.3)

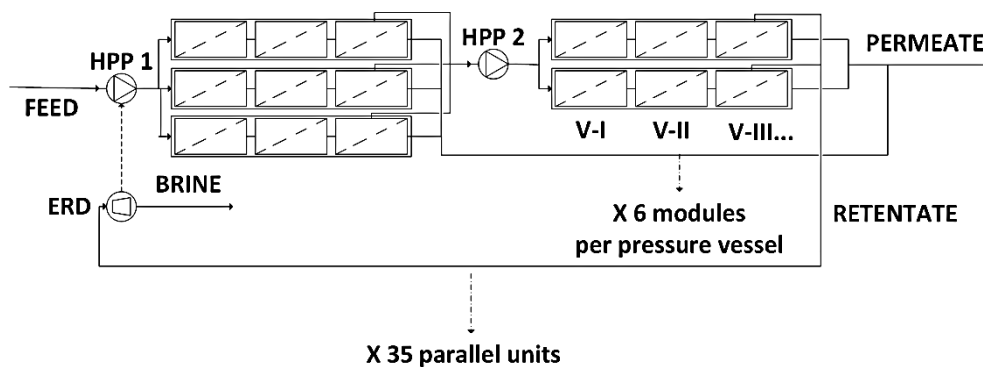


Figure A- 5: Process scale-up for a two-stage tapered RO configuration with 6 modules per pressure vessel for 75% product recovery. For scale-up to $Q_p=666 \text{ m}^3 \cdot \text{h}^{-1}$, 35 parallel units are required with a specific membrane area of $A_{m,s}=54.47 \text{ [m}^2(\text{m}^3 \cdot \text{h}^{-1})^{-1}]$.

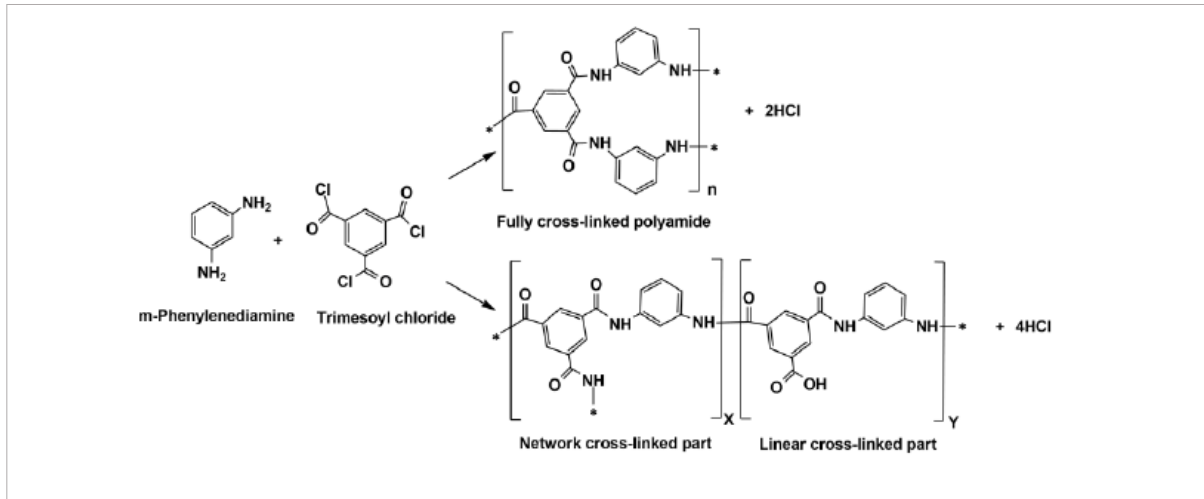
Appendix B (Chapter 6)**Schematic of the interfacial reaction between TMC and MPD (Section 6.2.2)**

Figure B- 1: Interfacial reaction of m-phenylenediamine (MPD) with trimesoyl chloride (TMC) and formation of network and linear cross-linked polyamide nanofilm. [Reprinted from Karan et al. [194]].

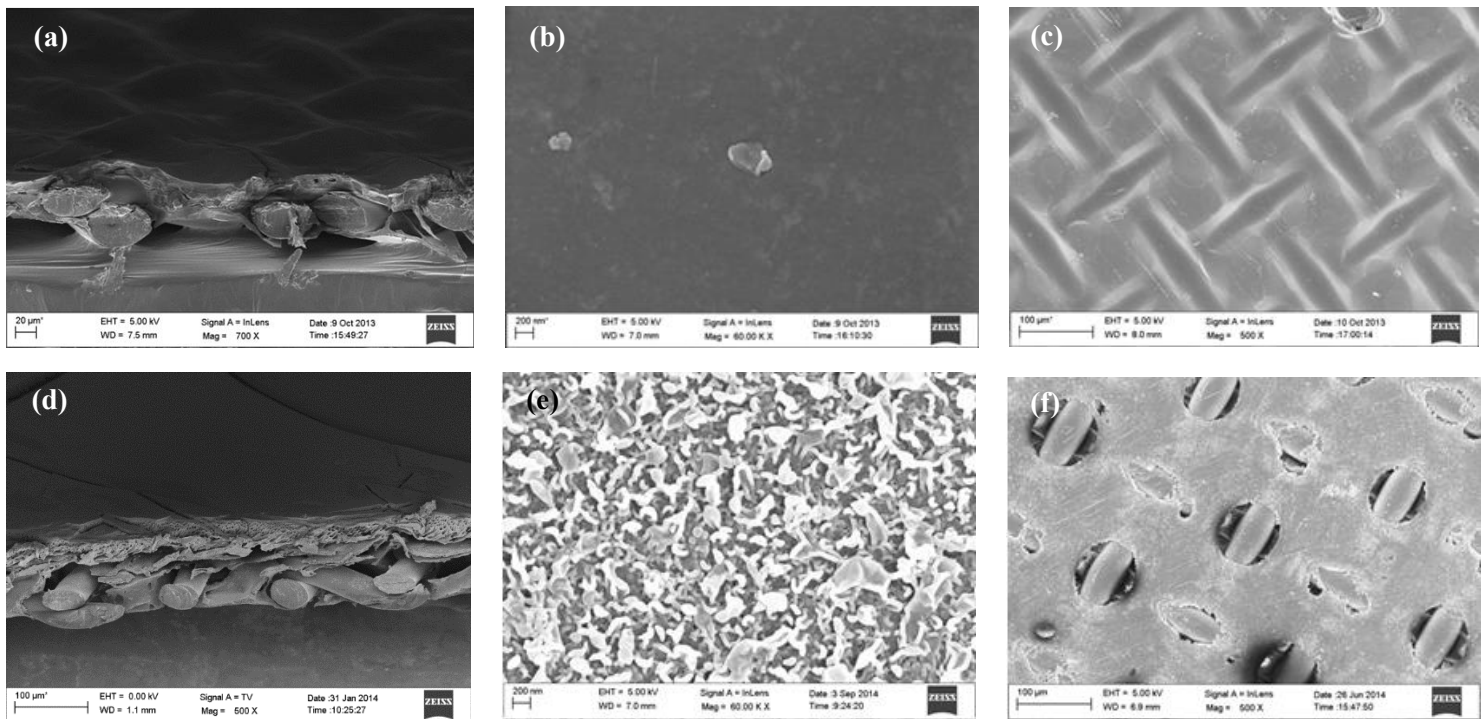
SEM images of cross-section and aerial views of HTI CTA and TFC membranes (Section 6.2.3)

Figure B- 2: SEM micrographs of commercial HTI membranes: (a-c) cross-section, top and bottom surface of HTI CTA membrane, and (d-f) cross-section, top and bottom surface of HTI TFC membrane.

FO U-tube apparatus with Acid Fuchsin tracer dye in the feed solution to detect any leakage through the membrane (Section 6.2.7)

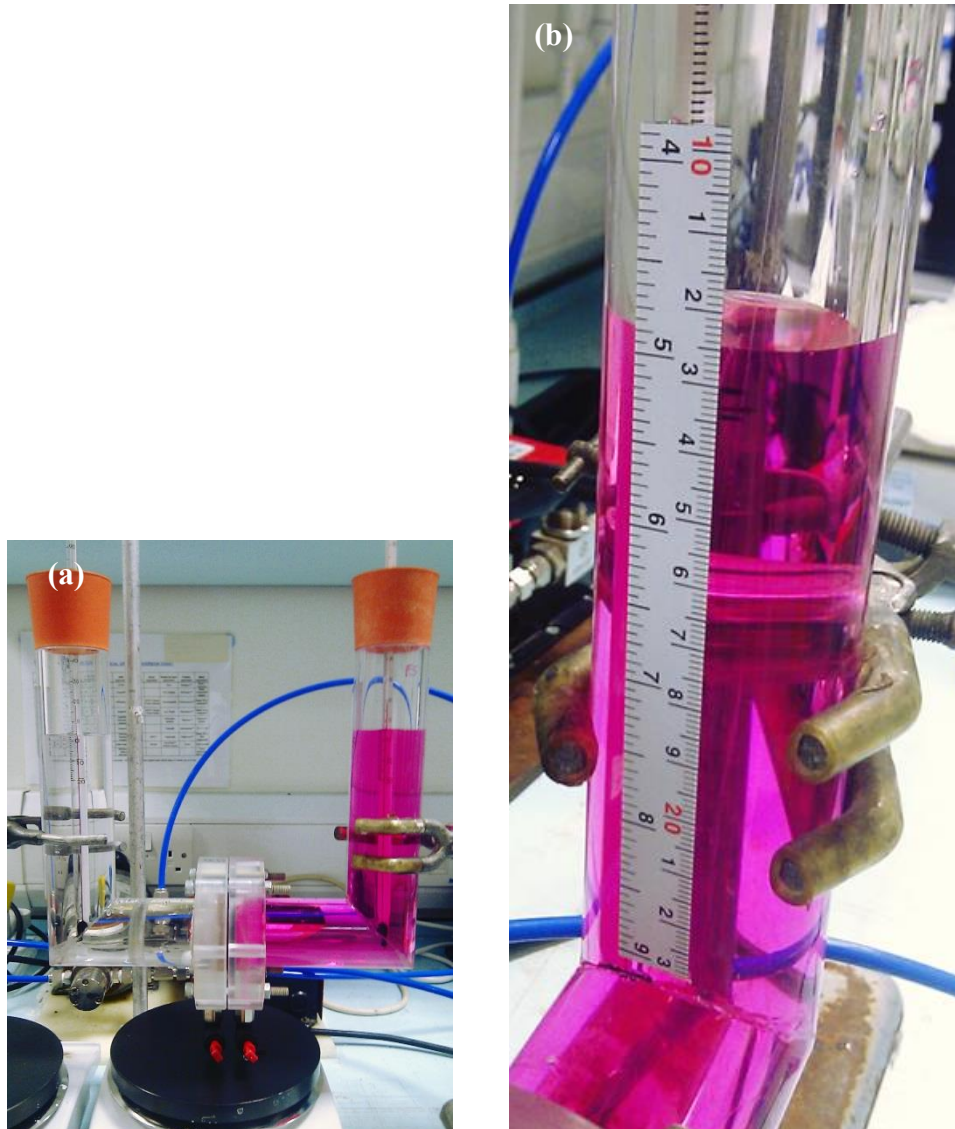
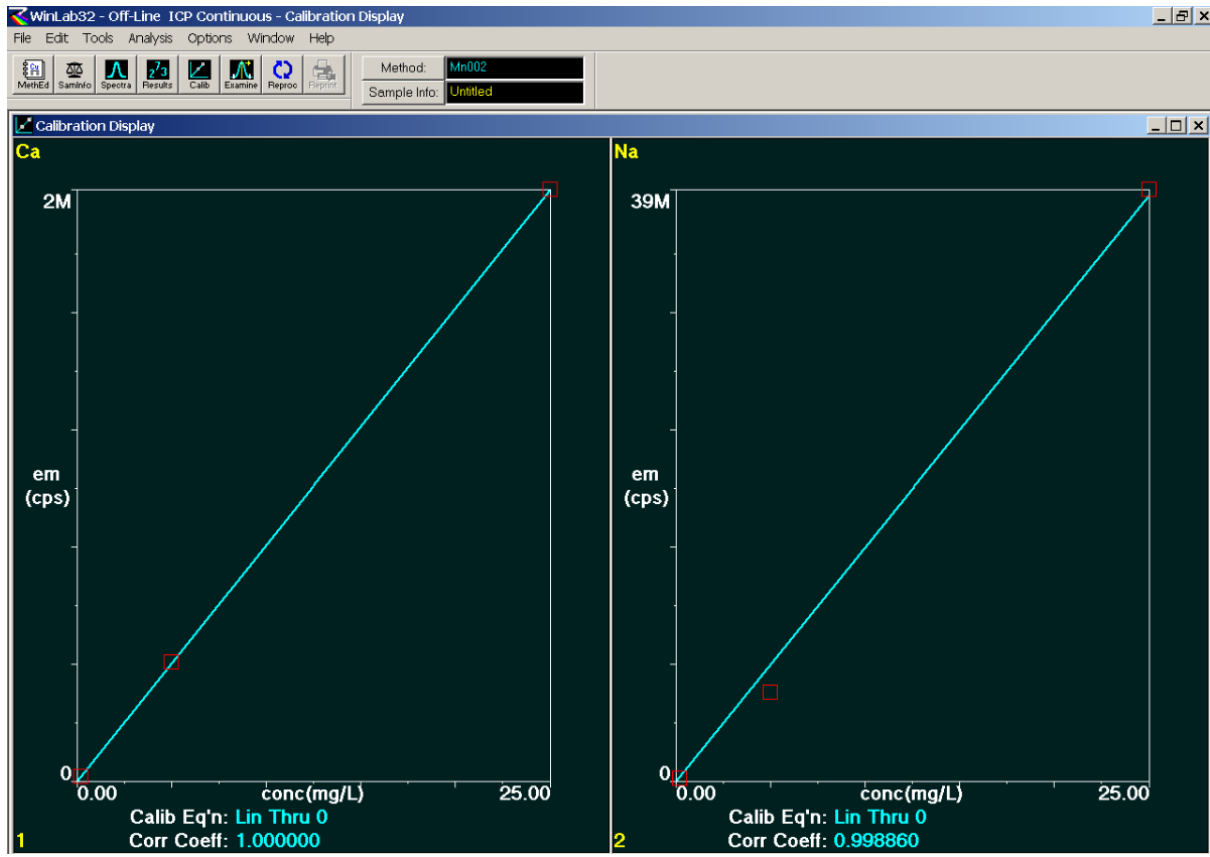


Figure B- 3: (a) U-tube apparatus with Acid Fuchsin tracer dye in the FS to indicate any leaks through the membrane. An overnight experimental run showed no visible tracer dye in the DS and UV measurements showed dye rejection was consistently > 99.3%. (b) Level indicator to monitor height change in the column of fluid during FO experiment.

Appendix C

Inductively Coupled Plasma (ICP) calibration for Na⁺ and Ca²⁺ samples (Chapter 5)



Method: Mn002

Page 1

Date: 03/12/2013 11:08:53

=====
Analysis BegunStart Time: 03/12/2013 09:29:00
Logged In Analyst: user
Spectrometer Model: Optima 2000Plasma On Time: 03/12/2013 09:28:26
Technique: ICP Continuous
Autosampler Model: AS-90plus

Sample Information File:

Batch ID:
Results Data Set: PC010813
Results Library: C:\pe\user\Results\Results.mdb=====
Method LoadedMethod Name: Mn002
IEC File:
Method Description: Na MgMethod Last Saved: 06/11/2013 11:26:44
MSF File:=====
Sequence No.: 1Sample ID: Calib Blank 1
Analyst:
Initial Sample Wt:
Dilution:

Autosampler Location:

Date Collected: 03/12/2013 09:29:04
Data Type: Original
Initial Sample Vol:
Sample Prep Vol:=====
Replicate Data: Calib Blank 1

Repl#	Analyte	Net Intensity	Corrected Intensity	Conc.	Calib. Units	Analysis Time
1	Ca	-760.1	-760.1	[0.00]	mg/L	09:29:34
1	Na	-8242.1	-8242.1	[0.00]	mg/L	09:30:02
2	Ca	-749.2	-749.2	[0.00]	mg/L	09:29:43
2	Na	-8326.3	-8326.3	[0.00]	mg/L	09:30:08
3	Ca	-875.6	-875.6	[0.00]	mg/L	09:29:50
3	Na	-6961.4	-6961.4	[0.00]	mg/L	09:30:12

=====
Mean Data: Calib Blank 1

Analyte	Mean Corrected Intensity	Std.Dev.	RSD	Conc.	Calib. Units
Ca	-794.9	70.02	8.81%	[0.00]	mg/L
Na	-7843.3	764.87	9.75%	[0.00]	mg/L

=====
Sequence No.: 2Sample ID: Calib Blank 1
Analyst:
Initial Sample Wt:
Dilution:

Autosampler Location:

Date Collected: 03/12/2013 09:55:29
Data Type: Original
Initial Sample Vol:
Sample Prep Vol:=====
Replicate Data: Calib Blank 1

Repl#	Analyte	Net Intensity	Corrected Intensity	Conc.	Calib. Units	Analysis Time
1	Ca	-601.9	-601.9	[0.00]	mg/L	09:55:58
1	Na	8141.4	8141.4	[0.00]	mg/L	09:56:24
2	Ca	-500.5	-500.5	[0.00]	mg/L	09:56:05
2	Na	5986.5	5986.5	[0.00]	mg/L	09:56:29
3	Ca	-448.1	-448.1	[0.00]	mg/L	09:56:13
3	Na	6960.6	6960.6	[0.00]	mg/L	09:56:33

=====
Mean Data: Calib Blank 1

Analyte	Mean Corrected Intensity	Std.Dev.	RSD	Conc.	Calib. Units
Ca	-516.8	78.19	15.13%	[0.00]	mg/L
Na	7029.5	1079.09	15.35%	[0.00]	mg/L

=====
Sequence No.: 3Sample ID: Sample001
Analyst:
Initial Sample Wt:

Autosampler Location:

Date Collected: 03/12/2013 10:08:00
Data Type: Original
Initial Sample Vol:

Method: Mn002 Page 2 Date: 03/12/2013 11:08:53

Dilution: Sample Prep Vol:

Replicate Data: Sample001

Repl#	Analyte	Net Intensity	Corrected Intensity	Calib. Conc. Units	Sample Conc. Units	Analysis Time
1	Ca	396704.5	397221.3			10:08:29
1	Na	5934397.8	5927368.3			10:08:45
2	Ca	396025.7	396542.5			10:08:34
2	Na	5912420.4	5905390.9			10:08:49
3	Ca	398900.6	399417.5			10:08:37
3	Na	5775095.5	5768066.0			10:08:52

Mean Data: Sample001

Analyte	Mean Corrected Intensity	Calib. Conc. Units	Std.Dev.	Sample Conc. Units	Std.Dev.	RSD
Ca	397727.1				1502.74	0.38%
Na	5866941.8				86331.12	1.47%

Analysis Begun

Start Time: 03/12/2013 10:10:23
 Logged In Analyst: user
 Spectrometer Model: Optima 2000

Plasma On Time: 03/12/2013 09:28:26
 Technique: ICP Continuous
 Autosampler Model: AS-90plus

Sample Information File:

Batch ID:
 Results Data Set: HTI 11, 14, 18, 19
 Results Library: C:\pe\user\Results\Results.mdb

Sequence No.: 1

Sample ID: Calib Blank 1

Analyst:
 Initial Sample Wt:
 Dilution:

Autosampler Location:

Date Collected: 03/12/2013 10:10:23

Data Type: Original
 Initial Sample Vol:
 Sample Prep Vol:

Replicate Data: Calib Blank 1

Repl#	Analyte	Net Intensity	Corrected Intensity	Calib. Conc. Units	Analysis Time
1	Ca	-730.6	-730.6	[0.00] mg/L	10:10:52
1	Na	3866.6	3866.6	[0.00] mg/L	10:11:20
2	Ca	-775.5	-775.5	[0.00] mg/L	10:11:01
2	Na	3563.2	3563.2	[0.00] mg/L	10:11:26
3	Ca	-732.3	-732.3	[0.00] mg/L	10:11:09
3	Na	2938.1	2938.1	[0.00] mg/L	10:11:31

Mean Data: Calib Blank 1

Analyte	Mean Corrected Intensity	Std.Dev.	RSD	Calib Conc. Units
Ca	-746.1	25.45	3.41%	[0.00] mg/L
Na	3456.0	473.49	13.70%	[0.00] mg/L

Sequence No.: 2

Sample ID: 1

Analyst:
 Initial Sample Wt:
 Dilution:

Autosampler Location:

Date Collected: 03/12/2013 10:12:22

Data Type: Original
 Initial Sample Vol:
 Sample Prep Vol:

Replicate Data: 1

Repl#	Analyte	Net Intensity	Corrected Intensity	Calib. Conc. Units	Analysis Time
1	Ca	15313.0	16059.2	[0.20] mg/L	10:12:50
1	Na	180508.3	177052.4	[0.20] mg/L	10:13:18
2	Ca	15064.9	15811.0	[0.20] mg/L	10:12:59
2	Na	188266.3	184810.3	[0.20] mg/L	10:13:22
3	Ca	15480.4	16226.5	[0.20] mg/L	10:13:06
3	Na	180715.7	177259.7	[0.20] mg/L	10:13:26

Method: Mn002

Page 3

Date: 03/12/2013 11:08:53

Mean Data: 1

Analyte	Mean Corrected Intensity	Std.Dev.	RSD	Conc.	Calib Units
Ca	16032.2	209.02	1.30%	[0.20]	mg/L
Na	179707.5	4420.42	2.46%	[0.20]	mg/L

Sequence No.: 3

Sample ID: 2

Analyst:

Initial Sample Wt:

Dilution:

Autosampler Location:

Date Collected: 03/12/2013 10:13:36

Data Type: Original

Initial Sample Vol:

Sample Prep Vol:

Replicate Data: 2

Repl#	Analyte	Net Intensity	Corrected Intensity	Conc.	Calib. Units	Analysis Time
1	Ca	396923.8	397669.9	[5.00]	mg/L	10:14:05
1	Na	5931365.2	5927909.2	[5.00]	mg/L	10:14:22
2	Ca	395332.2	396078.3	[5.00]	mg/L	10:14:09
2	Na	5964441.8	5960985.8	[5.00]	mg/L	10:14:26
3	Ca	399058.6	399804.7	[5.00]	mg/L	10:14:13
3	Na	5951105.6	5947649.7	[5.00]	mg/L	10:14:29

Mean Data: 2

Analyte	Mean Corrected Intensity	Std.Dev.	RSD	Conc.	Calib Units
Ca	397851.0	1869.78	0.47%	[5.00]	mg/L
Na	5945514.9	16641.32	0.28%	[5.00]	mg/L

Sequence No.: 4

Sample ID: 3

Analyst:

Initial Sample Wt:

Dilution:

Autosampler Location:

Date Collected: 03/12/2013 10:14:44

Data Type: Original

Initial Sample Vol:

Sample Prep Vol:

Replicate Data: 3

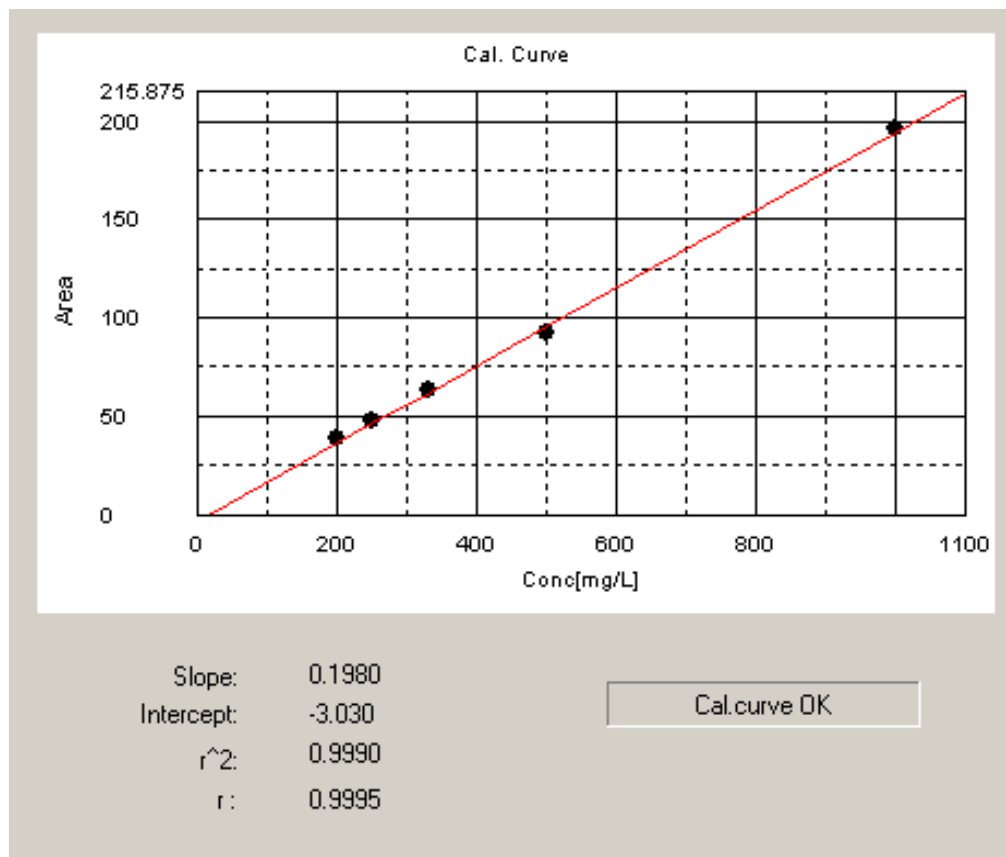
Repl#	Analyte	Net Intensity	Corrected Intensity	Conc.	Calib. Units	Analysis Time
1	Ca	1983193.3	1983939.4	[25.00]	mg/L	10:15:13
1	Na	39314537.0	39311081.0	[25.00]	mg/L	10:15:27
2	Ca	1926236.6	1926982.7	[25.00]	mg/L	10:15:17
2	Na	39940964.2	39937508.2	[25.00]	mg/L	10:15:34
3	Ca	2036495.2	2037241.3	[25.00]	mg/L	10:15:20
3	Na	38962961.6	38959505.6	[25.00]	mg/L	10:15:39

Mean Data: 3

Analyte	Mean Corrected Intensity	Std.Dev.	RSD	Conc.	Calib Units
Ca	1982721.1	55139.37	2.78%	[25.00]	mg/L
Na	39402698.3	495396.39	1.26%	[25.00]	mg/L


Calibration Summary

Analyte	Stds.	Equation	Intercept	Slope	Curvature	Corr. Coef.	Reslope
Ca	3	Lin Thru 0	0.0	79320	0.00000	1.000000	
Na	3	Lin Thru 0	0.0	1561000	0.00000	0.998860	

Appendix D**Total Organic Carbon (TOC) calibration curve for alginate concentration analysis
(Chapter 5)**

Appendix E- Product data sheets**HTI CTA membrane**

HTI OsMem™ CTA-ES Membrane



Features:

- The OsMem™ CTA-ES Membrane is HTI's fouling resistant and most chlorine resistant FO membrane with an embedded support.
- The OsMem™ CTA-ES Membrane is used in all spiral-wound FO elements that use CTA (Expedition, HydroWell, and 2521FO-CTA, 4040FO-CTA, and 8040FO-CTA).
- The OsMem™ CTA-ES Membrane is cast on 40" (1-m) wide rolls.
- The OsMem™ CTA-ES Membrane coupons are shipped "dry," where vegetable-based glycerin replaces the water.

Typical FO Performance (Rejection Layer Contacting Feed):

- Water Permeation: 4.5 GFD (gallons per square foot each day) (7.7 LMH – liters per square meter each hour)
- Salt Rejection: 99.4% as defined in Test Conditions

Test Conditions: **Feed:** 1 gpm (4 lpm) tap water feed at 77°F (25°C) fed at the bottom into a 4" (100 mm) by 0.13" (3.2 mm) open channel with an initial volume of 0.40 gal (1.5 L) and an exit pressure of 5 psi (35 kPa).
Draw: 7 gph (26 lph) 1 M NaCl (58.5 g/L) at the bottom at 2 psi (15 kPa) feed into a 4" (100 mm) by 0.06" (1.5 mm) channel of three 20-mil (0.5 mm) directional permeate spacers with the membrane-contacting spacer with channels parallel to the flow and the other two with channels perpendicular to the flow with an initial volume of 0.13 gal (0.5 L).
Membrane Area: 0.22 ft² (0.020 m²)
Rejection: $\{1 - [(mol\ NaCl\ transferred\ to\ feed)/(L\ water\ removed)]/(1\ M)\}$

Typical uPRO* Performance (Rejection Layer Contacting Draw Solution):

- Water Permeation: 7 GFD (gallons per square foot each day) (12 LMH – liters per square meter each hour)
- Salt Rejection: 99.4% as defined in Test Conditions

Test Conditions: **Feed:** 7 gph (26 lph) tap water at the bottom at 2 psi (15 kPa) feed into a 4" (100 mm) by 0.06" (1.5 mm) channel of three 20-mil (0.5 mm) directional permeate spacers with the membrane-contacting spacer with channels parallel to the flow and the other two with channels perpendicular to the flow with an initial volume of 0.26 gal (1.0 L).
Draw: 1 gpm (4 lpm) 1 M NaCl (58.5 g/L) at 77°F (25°C) fed at the bottom into a 4" (100 mm) by 0.13" (3.2 mm) open channel with an initial volume of 0.2 gal (0.8 L) and an exit pressure of 5 psi (35 kPa).
Membrane Area: 0.22 ft² (0.020 m²)
Rejection: $\{1 - [(mol\ NaCl\ transferred\ to\ feed)/(L\ water\ removed)]/(1\ M)\}$
***uPRO:** unpressurized Pressure Retarded Osmosis membrane orientation

Hydration Technology Innovations
2484 Ferry St. SW Albany, OR 97322 USA 541-917-3335 info@htiwater.com

HTI OsMem™ CTA-ES Membrane 130916
http://www.htiwater.com

HTI OsMem™ CTA-ES Membrane (page 2)



Operating Limits and Guidelines:

- | | |
|--|--|
| <ul style="list-style-type: none"> • Membrane Requirements | Membrane coupons are shipped in glycerin. Should be soaked in water for 30 minutes prior to use. After glycerin extraction, membrane must be kept moist at all times. Do not allow to freeze. Exercise care in handling. |
| <ul style="list-style-type: none"> • Membrane Type | Cellulose Triacetate (CTA) with embedded polyester screen support |
| <ul style="list-style-type: none"> • Maximum Operating Temperature | 160°F (71°C) |
| <ul style="list-style-type: none"> • Maximum Transmembrane Pressure | 10 psi (70 kPa), if supported |
| <ul style="list-style-type: none"> • pH Range | 3 to 8 |
| <ul style="list-style-type: none"> • Maximum Chlorine | 2 ppm |
| <ul style="list-style-type: none"> • Cleaning Guidelines | Use only cleaning chemicals approved for CA/CTA RO membranes |
| <ul style="list-style-type: none"> • Storage Guidelines | After wetting, store out of direct sunlight with a couple mL of water |

FO Membrane Notes:

The membrane is initially cast on rolls. On a roll, the rejection layer is to the inside of the roll and is the shiny side; on drying, the membrane will curl towards the rejection layer.

FO membranes behave similarly to RO membranes in that dissolved gases are not rejected well. Their ions are rejected, but the (often small) fraction that exists as a dissolved gas is not rejected. Small polar, water-soluble organics, such as urea, methanol, and ethanol, are also not rejected well.

Brief Startup Description:


If the process is being run with the draw solution contacting the rejection layer (uPRO), make sure that there is water in the cell on the supported side to draw from. Start the pump on the unsupported side. Adjust the flowrate with the inlet valve and the exit pressure to 5 psi (35 kPa) with the exit valve. Start the side with the membrane support and adjust to the desired inlet pressure of 2 psi (15 kPa). Monitor volume or weight changes, temperature, and concentrations with time.

Brief Shutdown Descriptions:

Turn off the pumps and drain the high osmotic pressure solution first. Then drain the low osmotic pressure solution. Rinsing is recommended. The membrane can be stored in the cell – preferably drained.

HTI TFC membrane

HTI OsMem™ TFC-ES Membrane



Features:

- The OsMem™ TFC-ES Membrane is HTI's fastest and highest rejecting FO membrane.
- The OsMem™ TFC-ES Membrane is used in all spiral-wound FO elements that use TFC.
- The OsMem™ TFC-ES Membrane is cast on 40" (1-m) wide rolls.
- The OsMem™ TFC-ES Membrane coupons are shipped "dry," where vegetable-based glycerin replaces the water.

Typical FO Performance (Rejection Layer Contacting Feed): AL-F1

- Water Permeation: 11 GFD (gallons per square foot each day) (18 LMH – liters per square meter each hour)
- Salt Rejection: 99.4% as defined in Test Conditions

Test Conditions: **Feed:** 1 gpm (4 lpm) tap water feed at 77°F (25°C) fed at the bottom into a 4" (100 mm) by 0.2" (5 mm) open channel with an initial volume of 0.40 gal (1.5 L) and an exit pressure of 10 psi (40 kPa). **Draw:** 20 gph (75 lph) 1 M NaCl (58.5 g/L) at the bottom at 6 psi (40 kPa) feed into a 4" (100 mm) by 0.06" (1.5 mm) channel of three 20-mil (0.51-mm) epoxy-coated permeate spacer with the bottom two oriented normal to flow and the membrane-contacting spacer parallel to the flow with an initial volume of 0.13 gal (0.5 L). **Membrane Area:** 0.22 ft² (0.020 m²) **Rejection:** $\{1 - [(\text{mol NaCl transferred to feed})/(\text{L water removed})]/(1 \text{ M})\}$

Typical uPRO* Performance (Rejection Layer Contacting Draw Solution): AL-D3


- Water Permeation: 21 GFD (gallons per square foot each day) (36 LMH – liters per square meter each hour)
- Salt Rejection: 99.4% as defined in Test Conditions

Test Conditions: **Feed:** 20 gph (75 lph) tap water at the bottom at 6 psi (40 kPa) feed into a 4" (100 mm) by 0.06" (1.5 mm) channel of three 20-mil (0.51-mm) epoxy-coated permeate spacer with the bottom two oriented normal to flow and the membrane-contacting spacer mounted parallel to the flow with an initial volume of 0.26 gal (1.0 L). **Draw:** 1 gpm (4 lpm) 1 M NaCl (58.5 g/L) at 77°F (25°C) fed at the bottom into a 4" (100 mm) by 0.2" (5 mm) open channel with an initial volume of 0.2 gal (0.8 L) and an exit pressure of 10 psi (70 kPa). **Membrane Area:** 0.22 ft² (0.020 m²) **Rejection:** $\{1 - [(\text{mol NaCl transferred to feed})/(\text{L water removed})]/(1 \text{ M})\}$ ***uPRO:** unpressurized Pressure Retarded Osmosis membrane orientation

Hydration Technology Innovations
2484 Ferry St. SW Albany, OR 97322 USA 541-917-3335 info@htewater.com

HTI OsMem™ TFC-ES Membrane 130927
http://www.htewater.com

HTI OsMem™ TFC-ES Membrane (page 2)



Operating Limits and Guidelines:

<ul style="list-style-type: none"> • Membrane Requirements • Membrane Type • Maximum Operating Temperature • Maximum Transmembrane Pressure • pH Range • Maximum Chlorine • Cleaning Guidelines • Storage Guidelines 	<p>Membrane coupons are shipped in glycerin. Should be soaked in water for 30 minutes prior to use. After glycerin extraction, membrane must be kept moist at all times. Do not allow to freeze. Exercise care in handling.</p> <p>Thin-Film Composite (TFC) with embedded polyester screen support</p> <p>160°F (71°C)</p> <p>10 psi (70 kPa), if supported</p> <p>2 to 11</p> <p><0.1 ppm</p> <p>Use only cleaning chemicals approved for TFC RO membranes</p> <p>When initially received, the membrane is dry. Leave in sealed bag and out of direct sunlight. After a piece has been used, store that piece out of direct sunlight with a couple mL of water in a sealed bag.</p>
--	--

FO Membrane Notes:

The membrane is initially cast on rolls. On a roll, the rejection layer is to the inside of the roll and is the shiny side; on drying, the membrane will curl towards the rejection layer.

FO membranes behave similarly to RO membranes in that dissolved gases are not rejected well. Their ions are rejected, but the (often small) fraction that exists as a dissolved gas is not rejected. Small polar, water-soluble organics, such as urea, methanol, and ethanol, are also not rejected well.

Brief Startup Description:

If the process is being run with the draw solution contacting the rejection layer (uPRO), make sure that there is water in the cell on the supported side to draw from. Start the pump on the unsupported side. Adjust the flowrate with the inlet valve and the exit pressure to 10 psi (70 kPa) with the exit valve. Start the side with the membrane support and adjust to the desired inlet pressure of 6 psi (40 kPa). Monitor volume or weight changes, temperature, and concentrations with time.

Brief Shutdown Description:

Turn off the pumps and drain the high osmotic pressure solution first. Then drain the low osmotic pressure solution. Rinsing is recommended. The membrane can be stored in the cell – preferably drained.

Hydration Technology Innovations
2484 Ferry St. SW Albany, OR 97322 USA 541-917-3335 info@htiwater.com

HTI OsMem™ TFC-ES Membrane 130927
http://www.htiwater.com

Nylon 6-6 open mesh fabric

SEFAR NITEX
03-10/2Datenblatt
Data Sheet

Fasermaterial <i>Fibre Material</i>	PA 6.6, monofilament
Bindung <i>Weave Pattern</i>	2:2 Köper 2:2 twill weave
Boil-over Bubble Point [mmWS] <i>Boil-over Bubble Point [in.H₂O]</i>	540-660 21.0-26.0
Luftdurchlässigkeit [(l(n)/m ² s) bei 2 mbar <i>Air Permeability [(l(n)/m²s) at 2 mbar</i> <i>Air Permeability [scfm/sq.ft.] at 1/2" H₂O</i>	100-200 13.5-28.0
Siebfeinheit [n/cm] <i>Mesh Count [n/cm]</i> <i>Mesh Count [n/inch]</i>	190 483
Drahtdurchmesser [µm] <i>Wire Diameter [µm]</i>	28
Offene Fläche [%] <i>Open Area [%]</i>	~ 2
Dicke [µm] <i>Thickness [µm]</i>	45
Gewicht [g/m ²] <i>Weight [g/m²]</i> <i>Weight [oz/sq.yd]</i>	40 1.18
Ausrüstung <i>Finish</i>	Kalandriert Calendered

SEFAR NITEX 03-15/10

Datenblatt Data Sheet

Fasermaterial
Fibre Material

PA 6.6, monofilament

Bindung
Weave Pattern

**2:2 Köper
2:2 twill weave**

Maschenweite [μm]
Mesh Opening [μm]

15 +/- 2.0 s: max. 1.5

Siebfeinheit [n/cm]
Mesh Count [n/cm]
Mesh Count [n/inch]

**202.0
513.1**

Drahtdurchmesser [μm]
Wire Diameter [μm]

35

Offene Fläche [%]
Open Area [%]

9.5

Dicke [μm]
Thickness [μm]

60

Gewicht [g/m^2]
Weight [g/m^2]
Weight [oz/sq.yd]

**40
1.18**

Ausrüstung
Finish

**stabilisiert
stabilized**

SEFAR NITEX 03-20/14

Datenblatt Data Sheet

Fasermaterial
Fibre Material

PA 6.6, monofilament

Bindung
Weave Pattern

**2:2 Köper
2:2 twill weave**

Maschenweite [μm]
Mesh Opening [μm]

20 +/- 3.0 s: max. 1.5

Siebfeinheit [n/cm]
Mesh Count [n/cm]
Mesh Count [n/inch]

**188
478**

Drahtdurchmesser [μm]
Wire Diameter [μm]

34

Offene Fläche [%]
Open Area [%]

14

Dicke [μm]
Thickness [μm]

55

Gewicht [g/m^2]
Weight [g/m^2]
Weight [oz/sq.yd]

**35
1.03**

Ausrüstung
Finish

**Stabilisiert
Stabilized**

SEFAR NITEX 03-25/19

Datenblatt Data Sheet

Fasermaterial
Fibre Material

PA 6.6, monofilament

Bindung
Weave Pattern

**2:2 Köper
2:2 twill weave**

Maschenweite [μm]
Mesh Opening [μm]

25 +/- 3.0 s: max. 1.5

Siebfeinheit [n/cm]
Mesh Count [n/cm]
Mesh Count [n/inch]

**174.0
442.0**

Drahtdurchmesser [μm]
Wire Diameter [μm]

33

Offene Fläche [%]
Open Area [%]

19

Dicke [μm]
Thickness [μm]

55

Gewicht [g/m^2]
Weight [g/m^2]
Weight [oz/sq.yd]

**30
0.89**

Ausrüstung
Finish

**Stabilisiert
Stabilized**
